

METROLOGY OF MESOSCALE  
BALLAST PARTICLE  
DYNAMICS USING KLI-PI

---

**FEBRUARY 2019**



UNIVERSITEIT VAN PRETORIA  
UNIVERSITY OF PRETORIA  
YUNIBESITHI YA PRETORIA

# **METROLOGY OF MESOSCALE BALLAST PARTICLE DYNAMICS USING KLI-PI**

**ANDRÉ BROEKMAN**

**A dissertation submitted in partial fulfilment of the requirements for the degree of**

**MASTER OF ENGINEERING (TRANSPORTATION ENGINEERING)**

**In the**

**FACULTY OF ENGINEERING, BUILT ENVIRONMENT AND INFORMATION  
TECHNOLOGY**

**UNIVERSITY OF PRETORIA**

**FEBRUARY 2019**

# METROLOGY OF MESOSCALE BALLAST PARTICLE DYNAMICS USING KLI-PI

**ANDRÉ BROEKMAN**

**Supervisor:** Professor P.J. Gräbe  
**Department:** Civil Engineering  
**University:** University of Pretoria  
**Degree:** Master of Engineering (Transportation engineering)

At first glance the operational performance of ballast appears trivial in its simplicity. However, various mechanisms affect the short and long term performance of the ballast and in turn, the response of the track structure, both on a *macroscopic* scale considering the track structure as an entity and on a discrete particle level or *mesoscale*. The nature and geometry of the material itself creates difficulty in instrumenting the ballast directly and analytical solutions of the track structure in three dimensions require complex numerical models. The importance of experimental studies to establish the influence of the granular fabric on both the static and quasi-static deformational response of granular materials has been repeatedly highlighted by other researchers. A three-dimensional, half-space model is extremely difficult, if not impossible, to be developed for the theoretical investigation of complex ballast vibrations. This information contributes to the fundamental understanding of mechanical behaviour of granular media.

The proliferation of low cost Micro-Electro-Mechanical Systems (MEMS) has evolved the science of metrology through the introduction of a new class of instruments, known as “smart ballast”, for use in railway and transportation research applications. These instruments are able to quantify both the micro- and macroscopic dynamic response of railway ballast. Such a smart ballast prototype, named Kli-Pi, has been developed by the author. The name is derived from the Afrikaans word “klippie”, which is synonymous with the description of “small rock”. The instrument provides sufficient resolution and fidelity to investigate the relationship between ballast translation and rotation in three spatial dimensions for both laboratory and in-service track environments. Using multiple Kli-Pis

arranged in succession, the dynamic performance and characteristics (for both the time and frequency domain) of ballast in both laboratory and field environments can be remotely monitored in real-time. Statistical parameters and energy metrics are formulated to compare and quantify the measured laboratory and field characteristics of ballast.

Through this research, Kli-Pi has been developed to provide valuable information surrounding the rotations and deflections in three dimensions, dominant frequencies and harmonics of the track components, indirect observations of principal stress rotations (PSR) and the underlying probabilistic micromechanics and statistical nature of the mesoscale ballast dynamics. Contrary to traditional deterministic mechanics, the probabilistic nature of the material does not conform to uniform-strain assumptions. Probabilistic behaviour governs the particle deflections where instances of alternating positive and negative strain are observed in the vertical direction. For both the laboratory and field experiments investigated, the largest component of the energy was concentrated along the vertical direction, parallel to the direction of the load. The passage of the locomotives coincided with significant longitudinal and lateral forces from the tractive effort, the influence of which extended to the subballast interface. Kli-Pi provided the necessary sensitivity to observe changes in the skeletal structure or “fabric” of the ballast and the influence of impact loads. Finally, the kinetic energy of each Kli-Pi was quantified which relates statistical parameters such as standard deviation and skewness with the particle coordination number (CN) and relative degrees of confinement. Of all the statistics investigated to quantify the ballast dynamics, the mechanical work proved to be the most suitable descriptor, exemplifying the fundamental, probabilistic response of ballast subjected to dynamic loading conditions.

# DECLARATION

I, the undersigned hereby declare that:

- I understand what plagiarism is and I am aware of the University's policy in this regard;
- The work contained in this dissertation is my own original work;
- I did not refer to work of current or previous students, lecture notes, handbooks or any other study material without proper referencing;
- Where other people's work has been used this has been properly acknowledged and referenced;
- I have not allowed anyone to copy any part of my dissertation;
- I have not previously in its entirety or in part submitted this dissertation at any university for a degree.

**Signature of student:**



**Name of student:**

**André Broekman**

**Student number:**

**u13025059**

**Date:**

**11 February 2019**

# ACKNOWLEDGEMENTS

I wish to express my appreciation to the following organisations and persons who made this project dissertation possible:

- a) Transnet Freight Rail is thanked for sponsoring the Chair in Railway Engineering at the University of Pretoria.
- b) Professor P.J. Gräbe, my project supervisor, for his guidance and support.
- c) The following persons are gratefully acknowledged for their assistance during the course of the study:
  - i) Staff from the Department of Civil Engineering: Mr. Timothy Jideani, Mr. Rikus Kock, Mrs. Adri Scholtz, Mrs. Hayley Boks, Professor Gerhard Heymann and Professor Wynand (JvdM) Steyn, Head of the Department of Civil Engineering, University of Pretoria.
  - ii) Mr. Sean Kruger, Makerspace coordinator at the University of Pretoria
  - iii) Ken Burns, TinyCircuits CEO & co-founder.
  - iv) My family for their encouragement and support during the study.

# TABLE OF CONTENTS

1	INTRODUCTION .....	1-1
1.1	Background.....	1-1
1.2	Objectives of the Study.....	1-2
1.3	Scope of the Study .....	1-2
1.4	Methodology.....	1-3
1.5	Organisation of the Dissertation .....	1-4
2	LITERATURE REVIEW .....	2-1
2.1	Introduction .....	2-1
2.2	Track Structure .....	2-3
2.3	Emerging Sensor Technologies .....	2-6
2.3.1	Wireless Sensor Platforms .....	2-7
2.3.2	Inertial Navigation Systems.....	2-8
2.3.3	MEMS Instrumentation .....	2-9
2.4	Continuum Mechanics of Granular Materials .....	2-11
2.4.1	Permanent Strain.....	2-11
2.4.2	Fouling.....	2-13
2.4.3	Principal Stress Rotation and Confining Stress .....	2-13
2.5	Micromechanics of Granular Materials .....	2-14
2.5.1	Discrete Element Modelling .....	2-14
2.5.2	Entropy .....	2-17
2.5.3	Probability Density Functions .....	2-18
2.5.4	Smart Ballast.....	2-19
2.5.5	SmartRock Laboratory Testing.....	2-23
2.5.6	SmartRock Numerical Model Comparison.....	2-25
2.6	Discussion.....	2-26
3	KLI-PI DEVELOPMENT .....	3-1
3.1	Introduction .....	3-1
3.2	Conceptual Design.....	3-2
3.3	Sensor Platform .....	3-2
3.4	IMU assembly and Configuration .....	3-5
3.4.1	External Enclosure.....	3-5
3.4.2	Power Source.....	3-6

3.4.3	Auxiliary Power Control.....	3-7
3.4.4	Software Configuration .....	3-9
3.5	Network Configuration and Deployment .....	3-10
3.5.1	User Interface .....	3-11
3.5.2	Access Point .....	3-12
3.6	Calibration of the IMU .....	3-13
3.6.1	Calibration Validation .....	3-14
3.6.2	Accuracy and Noise Characteristics .....	3-19
3.7	3D Shell Design and Manufacturing .....	3-20
3.7.1	Shell Design (Blender) .....	3-20
3.7.2	3D Printing .....	3-21
3.7.3	Coordinate Frame .....	3-23
3.8	Stress Testing.....	3-24
3.9	Discussion.....	3-25
4	EXPERIMENTAL WORK .....	4-1
4.1	Laboratory Testing.....	4-1
4.2	Field Testing.....	4-3
4.3	Typical Results .....	4-7
4.3.1	Displacement .....	4-8
4.3.2	Rotation .....	4-8
5	DISCUSSION OF THE RESULTS.....	5-1
5.1	Modes of Translation and Rotation .....	5-2
5.1.1	Laboratory Testing.....	5-2
5.1.2	Field Testing.....	5-4
5.2	Mechanical Work and Energy Methods .....	5-7
5.3	Cumulative Displacements and Rotations .....	5-12
5.4	Statistical Descriptors .....	5-15
5.4.1	Displacement .....	5-15
5.4.2	Rotation .....	5-18
5.4.3	Mechanical Work.....	5-20
6	CONCLUSIONS AND RECOMMENDATIONS .....	6-1
6.1	Conclusions .....	6-1
6.1.1	Kli-Pi Development and Implementation.....	6-1
6.1.2	Mesoscale Behaviour of Discrete Ballast Particles .....	6-2
6.1.3	Energy Principles and Statistical Descriptors.....	6-3

6.2	Recommendations.....	6-4
7	REFERENCES .....	7-1
A	APPENDIX .....	A-1
A.1	IMU Calibration Derivation and Procedure.....	A-1
A.1.1	Tri-axis Accelerometer .....	A-1
A.1.2	Tri-axis Gyroscope .....	A-3
A.1.3	Calibration Procedure .....	A-6
A.2	Software Analysis and Implementation.....	A-8
A.2.1	Calibration and Orientation Methods .....	A-8
A.2.2	Filtering Considerations.....	A-11
A.2.3	Approximation and Integration Methods.....	A-12
A.2.4	Frequency Domain Transformation.....	A-13
A.2.5	Peak Identification.....	A-14
A.3	Laboratory Testing Graphs .....	A-15
A.4	Field Testing Graphs.....	A-42
A.5	Summary of Displacement Statistics .....	A-78
A.6	Summary of Rotation Statistics .....	A-79
A.7	Summary of Work Statistics.....	A-80
A.8	Network Configuration Details.....	A-81
A.8.1	AP & IP Credentials .....	A-81
A.8.2	AP Configuration.....	A-81
A.8.3	USB AP Peripheral .....	A-84
A.8.4	Ubilinux AP & Non-AP Mode Selection .....	A-84
A.8.5	Ubilinux system time.....	A-84
A.9	Electrical Configuration.....	A-85

## LIST OF TABLES

Table 2-1: Summary of analytic methods and frequencies of interest for ballast studies.....	2-28
Table 3-1: Comparison between the calibrated and uncalibrated IMU accelerometer .....	3-14
Table 3-2: Frequency selection for calibration and validation of the accelerometer.....	3-16
Table 3-3: Summary of the IMU accuracy for measured and derived parameters .....	3-19
Table 4-1: Summary of variables used to calculate the maximum wheel load (adapted from Jideani, 2018).....	4-2
Table 4-2: Static instrument orientation before and after train passage .....	4-6

### APPENDIX

Table A-1: Peak-to-Peak displacement comparison for the laboratory test (all Kli-Pis).....	A-78
Table A-2: Peak-to-Peak displacement comparison for the field test (all Kli-Pis).....	A-78
Table A-3: Peak-to-Peak rotation comparison for the laboratory test (all Kli-Pis) .....	A-79
Table A-4: Peak-to-Peak rotation comparison for the field test (all Kli-Pis) .....	A-79
Table A-5: Peak-to-Peak work comparison for the laboratory test (all Kli-Pis).....	A-80
Table A-6: Peak-to-Peak work comparison for the field test (all Kli-Pis).....	A-80

# LIST OF FIGURES

Figure 2-1: Contribution to track settlement from different formation strata (Selig & Walters, 1994)	2-2
Figure 2-2: Frequency contribution of vehicle, track and soil interactions (Kouroussis et al., 2015)	2-5
Figure 2-3: The body and global frames of reference (Woodman, 2007)	2-8
Figure 2-4: Electrically conductive cantilevered vibratory member affixed to the substrate (Nathanson H.C & Wickstrom R.A., 1968)	2-9
Figure 2-5: Top view of the sensing element and the equivalent electrical model (Lemkin & Bernhard, 1999)	2-10
Figure 2-6: Implementation detail of a dully decoupled 3D gyroscope (Kempe, 2011)	2-11
Figure 2-7: Cyclic tensile strain in a granular material with no tensile capacity (Li et al., 2015b)	2-12
Figure 2-8: Force chain development for uncrushable ballast particles (Lobo-Guerrero. & Vallejo, 2006)	2-12
Figure 2-9: $\beta$ -contour plot for a train velocity of 200 km/h (Zhang et al., 2016)	2-15
Figure 2-10: Vector plot for ballast (a) displacement, (b) velocity and (c) accelerations (Zhang et al., 2016)	2-16
Figure 2-11: Vertical particle displacement comparison as a function of longitudinal position and depth (Zhang et al., 2016)	2-16
Figure 2-12: Comparison of frequency spectra of ballast accelerations; theoretical model (solid line) and measured data (dashed line) (Zhai et al., 2004)	2-19
Figure 2-13: Power spectrum density of measured ballast vibrating for vertical accelerations (Aikawa, 2009)	2-20
Figure 2-14: Fourier transform for (a & b) vertical sleeper and (c) ballast particle accelerations (Milne et al., 2016a)	2-21
Figure 2-15: Comparative, long-term displacements of sleeper performance for the same track over a four week period (Milne et al., 2016b)	2-22
Figure 2-16: Illustration of the “SmartRock” internal unit and accompanying protective shell (Liu et al., 2016a)	2-23
Figure 2-17: Translational accelerations for horizontal (x & y-axis) and vertical directions (z-axis) (left to right) (Liu et al., 2016a)	2-24

Figure 2-18: Rotational accelerations about horizontal (x & y-axis) and vertical directions (z-axis) (left to right) (Liu et al., 2016a).....	2-24
Figure 2-19: Comparative vertical (left), horizontal (middle) and angular peak acceleration (right) measurements between laboratory testing and DEM (Liu et al., 2016a).....	2-26
Figure 3-1: Intel Edison placed next to a LEGO figurine for size comparison (Yoctopuce, 2015) ....	3-4
Figure 3-2: Assembly of the mounting bracket and Intel Edison platform .....	3-6
Figure 3-3: TinyDuino stack with the proto shield visible .....	3-7
Figure 3-4: Nordic application facilitating communication with the TinyDuino .....	3-8
Figure 3-5: Proposed network interface, configuration and deployment.....	3-11
Figure 3-6: Raspberry Pi user interface controller with visible Ethernet cable .....	3-12
Figure 3-7: Raspberry Pi access point with visible Ethernet cable and a rechargeable USB power supply.....	3-13
Figure 3-8: Calibration of the IMU tri-axis accelerometer for 1 G acceleration .....	3-14
Figure 3-9: Box test configuration with the IMU (center) and the LDVT (left, not shown) bracket	3-15
Figure 3-10: Frequency dependent load cycle deflection comparison between the LVDT and the IMU .....	3-17
Figure 3-11: Frequency dependent deflection differences between the LVDT and the IMU .....	3-17
Figure 3-12: Calibration of the IMU tri-axis gyroscope for varying angular velocities.....	3-18
Figure 3-13: Blender design of the Kli-Pi shell.....	3-21
Figure 3-14: MakerBot print preview of the internal shell structure .....	3-22
Figure 3-15: Four assembled Kli-Pi instruments used for the experiments.....	3-23
Figure 3-16: Force-strain relationship for the shell subject to uniaxial, static loading.....	3-25
Figure 4-1: Kli-Pi 2 and 1 positioned at depths of 100 mm (left) and 250 mm (right) in the ballast box .....	4-3
Figure 4-2: Instrumented section of track; view towards South-Western direction .....	4-4
Figure 4-3: Installation of Kli-Pi 1 and 3 just below the ballast and sleeper respectively.....	4-5
Figure 4-4: Wi-Fi AP with both the Ethernet cable and Kli-Pi 4 visible.....	4-6
Figure 4-5: Time-domain deflection: all axes of Kli-Pi 1 (laboratory test, detailed) .....	4-9
Figure 4-6: Time-domain deflection: all axes of Kli-Pi 3 (field test, detailed) .....	4-9

Figure 4-7: Time-domain deflection: Z-axes of all Kli-Pis (laboratory test, detailed) .....	4-10
Figure 4-8: Time-domain deflection: Z-axis of all Kli-Pis (field test, detailed).....	4-10
Figure 4-9: Time-domain displacement matrix: Kli-Pi 1 (laboratory test, detailed) .....	4-11
Figure 4-10: Time-domain displacement matrix: Kli-Pi 3 (field test, detailed) .....	4-11
Figure 4-11: Time-domain rotation: all axes of Kli-Pi 2 (laboratory test, detailed).....	4-12
Figure 4-12: Time-domain rotation: all axes of Kli-Pi 3 (field test, detailed).....	4-12
Figure 4-13: Time-domain rotation: Z-axis of all Kli-Pis (laboratory test, detailed) .....	4-13
Figure 4-14: Time-domain rotation: X-axis of all Kli-Pis (field test, detailed).....	4-13
Figure 4-15: Time-domain rotation matrix: Kli-Pi 1 (laboratory test, detailed).....	4-14
Figure 4-16: Time-domain rotation matrix: Kli-Pi 3 (field test, detailed).....	4-14
Figure 5-1: Spectrographic deflection: Z-axis of Kli-Pi 2 (laboratory test) .....	5-3
Figure 5-2: Spectrographic displacement: Z-axis of Kli-Pi 3 (field test) .....	5-5
Figure 5-3: Spectrographic rotation: X-axis of Kli-Pi 3 (field test).....	5-6
Figure 5-4: Work energy response of all Kli-Pis (laboratory test) .....	5-9
Figure 5-5: Work energy response of all Kli-Pis (laboratory test, detailed).....	5-9
Figure 5-6: Work response of all Kli-Pis (field test) .....	5-10
Figure 5-7: Work response of all Kli-Pis (field test, detailed).....	5-10
Figure 5-8: Kinetic energy response of all Kli-Pis (field test).....	5-11
Figure 5-9: Potential energy response of all Kli-Pis (field test) .....	5-11
Figure 5-10: Cumulative displacement of all Kli-Pis (field and laboratory test).....	5-14
Figure 5-11: Cumulative rotation of all Kli-Pis (field and laboratory test) .....	5-14
Figure 5-12: Displacement: mean for all axes (field and laboratory test) .....	5-17
Figure 5-13: Displacement: coefficient of variance for all axes (field and laboratory test) .....	5-17
Figure 5-14: Displacement: skewness for all axes (field and laboratory test).....	5-17
Figure 5-15: Rotation: mean for all axes (field and laboratory test).....	5-19
Figure 5-16: Rotation: coefficient of variance for all axes (field and laboratory test) .....	5-19
Figure 5-17: Rotation: skewness for all axes (field and laboratory test) .....	5-19
Figure 5-18: Mechanical work: minimum, mean maximum (field and laboratory test).....	5-21

Figure 5-19: Mechanical work: standard deviation, coefficient of variance (CoV) and skewness (field and laboratory test) .....	5-21
--	------

## APPENDIX

Figure A-1: Misalignment between non-orthogonal sensors axes and the platform frame (Skog & Händel, 2006) .....	A-1
Figure A-2: Calibration tool assembly with a rotating platform about the hinge .....	A-7
Figure A-3: Relationship between vectors in Euclidian geometry and quaternions (Kuipers, 2000)... A-10	
Figure A-4: Time-domain deflection: X-axis of all Kli-Pis (laboratory test, detailed) .....	A-17
Figure A-5: Time-domain deflection: Y-axis of all Kli-Pis (laboratory test, detailed) .....	A-17
Figure A-6: Time-domain deflection: Z-axis of all Kli-Pis (laboratory test) .....	A-18
Figure A-7: Time-domain deflection: Y-axis of all Kli-Pis (laboratory test) .....	A-18
Figure A-8: Time-domain deflection: all axes of Kli-Pi 3 (0mm, laboratory test) .....	A-19
Figure A-9: Spectrographic acceleration: Z-axis of Kli-Pi 2 (350mm, laboratory test) .....	A-19
Figure A-10: Spectrographic deflection: Z-axis of Kli-Pi 2 (350mm, laboratory test) .....	A-20
Figure A-11: Spectrographic deflection: X-axis of Kli-Pi 2 (350mm, laboratory test) .....	A-20
Figure A-12: Spectrographic deflection: Y-axis of Kli-Pi 2 (350mm, laboratory test) .....	A-21
Figure A-13: Time-domain rotation: all axes of Kli-Pi 1 (500mm, laboratory test) .....	A-21
Figure A-14: Time-domain rotation: all axes of Kli-Pi 2 (350mm, laboratory test) .....	A-22
Figure A-15: Time-domain rotation: all axes of Kli-Pi 3 (0mm, laboratory test) .....	A-22
Figure A-16: Time-domain rotation: all axes of Kli-Pi 1 (500mm, laboratory test) .....	A-23
Figure A-17: Time-domain rotation: all axes of Kli-Pi 3 (0mm, laboratory test) .....	A-23
Figure A-18: Time-domain displacement matrix: Kli-Pi 1 (500mm, laboratory test) .....	A-24
Figure A-19: Time-domain displacement matrix: Kli-Pi 1 (500mm, laboratory test, detailed) .....	A-25
Figure A-20: Time-domain displacement matrix: Kli-Pi 2 (350mm, laboratory test) .....	A-26
Figure A-21: Time-domain displacement matrix: Kli-Pi 2 (350mm, laboratory test, detailed) .....	A-27
Figure A-22: Time-domain displacement matrix: Kli-Pi 3 (0mm, laboratory test) .....	A-28

Figure A-23: Time-domain displacement matrix: Kli-Pi 3 (0mm, laboratory test, detailed) .....	A-29
Figure A-24: Time-domain rotation matrix: Kli-Pi 1 (500mm, laboratory test) .....	A-30
Figure A-25: Time-domain rotation matrix: Kli-Pi 1 (500mm, laboratory test, detailed).....	A-31
Figure A-26: Time-domain rotation matrix: Kli-Pi 2 (350mm, laboratory test) .....	A-32
Figure A-27: Time-domain rotation matrix: Kli-Pi 2 (350mm, laboratory test, detailed).....	A-33
Figure A-28: Time-domain rotation matrix: Kli-Pi 3 (0mm, laboratory test) .....	A-34
Figure A-29: Time-domain rotation matrix: Kli-Pi 3 (0mm, laboratory test, detailed).....	A-35
Figure A-30: Time-domain displacement: all Kli-Pis (laboratory test, 60 degrees).....	A-36
Figure A-31: Time-domain displacement: all Kli-Pis (laboratory test, 120 degrees).....	A-37
Figure A-32: Time-domain displacement: all Kli-Pis (laboratory test, 210 degrees).....	A-38
Figure A-33: Time-domain rotation: all Kli-Pis (laboratory test, 60 degrees) .....	A-39
Figure A-34: Time-domain rotation: all Kli-Pis (laboratory test, 120 degrees) .....	A-40
Figure A-35: Time-domain rotation: all Kli-Pis (laboratory test, 210 degrees) .....	A-41
Figure A-36: Time-domain deflection: X-axis of all Kli-Pis (field test, detailed) .....	A-45
Figure A-37: Time-domain deflection: Y-axis of all Kli-Pis (field test, detailed) .....	A-45
Figure A-38: Time-domain deflection: X-axis of all Kli-Pis (field test) .....	A-46
Figure A-39: Time-domain deflection: Y-axis of all Kli-Pis (field test) .....	A-46
Figure A-40: Time-domain rotation: X-axis of all Kli-Pis (field test).....	A-47
Figure A-41: Time-domain rotation: Y-axis of all Kli-Pis (field test).....	A-47
Figure A-42: Time-domain deflection: Z-axis of all Kli-Pis (field test, impact load).....	A-48
Figure A-43: Time-domain rotation: X-axis of all Kli-Pis (field test, impact load).....	A-48
Figure A-44: Spectrographic acceleration: Z-axis of Kli-Pi 1 (550mm, field test) .....	A-49
Figure A-45: Spectrographic acceleration: Z-axis of Kli-Pi 1 (550mm, field test, detailed).....	A-49
Figure A-46: Spectrographic displacement: Z-axis of Kli-Pi 1 (550mm, field test, detailed).....	A-50
Figure A-47: Spectrographic displacement: X-axis of Kli-Pi 3 (250mm, field test, detailed) .....	A-50
Figure A-48: Spectrographic displacement: Y-axis of Kli-Pi 3 (250mm, field test, detailed) .....	A-51
Figure A-49: Spectrographic displacement: Z-axis of Kli-Pi 3 (250mm, field test, detailed).....	A-51
Figure A-50: Spectrographic displacement: X-axis of Kli-Pi 1 (550mm, field test, detailed) .....	A-52

Figure A-51: Spectrographic acceleration: Z-axis of Kli-Pi 3 (250mm, field test) .....	A-52
Figure A-52: Spectrographic acceleration: Z-axis of Kli-Pi 4 (0mm, field test) .....	A-53
Figure A-53: Spectrographic rotation: X-axis of Kli-Pi 4 (0mm, field test, detailed).....	A-53
Figure A-54: Spectrographic rotation: X-axis of Kli-Pi 1 (550mm, field test, detailed).....	A-54
Figure A-55: Spectrographic rotation: Y-axis of Kli-Pi 1 (550mm, field test, detailed).....	A-54
Figure A-56: Spectrographic rotation: Z-axis of Kli-Pi 1 (550mm, field test, detailed) .....	A-55
Figure A-57: Spectrographic rotation: X-axis of Kli-Pi 3 (250mm, field test, detailed).....	A-55
Figure A-58: Time-domain displacement matrix: Kli-Pi 1 (550mm, field test).....	A-56
Figure A-59: Time-domain displacement matrix: Kli-Pi 1 (550mm, field test, detailed) .....	A-57
Figure A-60: Time-domain displacement matrix: Kli-Pi 2 (400mm, field test).....	A-58
Figure A-61: Time-domain displacement matrix: Kli-Pi 2 (400mm, field test, detailed) .....	A-59
Figure A-62: Time-domain displacement matrix: Kli-Pi 3 (250mm, field test).....	A-60
Figure A-63: Time-domain displacement matrix: Kli-Pi 3 (250mm, field test, detailed) .....	A-61
Figure A-64: Time-domain displacement matrix: Kli-Pi 4 (0mm, field test).....	A-62
Figure A-65: Time-domain displacement matrix: Kli-Pi 4 (0mm, field test, detailed) .....	A-63
Figure A-66: Time-domain rotation matrix: Kli-Pi 1 (550mm, field test).....	A-64
Figure A-67: Time-domain rotation matrix: Kli-Pi 1 (550mm, field test, detailed).....	A-65
Figure A-68: Time-domain rotation matrix: Kli-Pi 2 (400mm, field test).....	A-66
Figure A-69: Time-domain rotation matrix: Kli-Pi 2 (400mm, field test, detailed).....	A-67
Figure A-70: Time-domain rotation matrix: Kli-Pi 3 (250mm, field test).....	A-68
Figure A-71: Time-domain rotation matrix: Kli-Pi 3 (250mm, field test, detailed).....	A-69
Figure A-72: Time-domain rotation matrix: Kli-Pi 4 (0mm, field test).....	A-70
Figure A-73: Time-domain rotation matrix: Kli-Pi 4 (0mm, field test, detailed).....	A-71
Figure A-74: Time-domain displacement: all Kli-Pis (field test, 60 degrees).....	A-72
Figure A-75: Time-domain displacement: all Kli-Pis (field test, 120 degrees).....	A-73
Figure A-76: Time-domain displacement: all Kli-Pis (field test, 210 degrees).....	A-74
Figure A-77: Time-domain rotation: all Kli-Pis (field test, 60 degrees) .....	A-75
Figure A-78: Time-domain rotation: all Kli-Pis (field test, 120 degrees) .....	A-76

Figure A-79: Time-domain rotation: all Kli-Pis (field test, 210 degrees) .....	A-77
Figure A-80: Electrical connectors for the interface board .....	A-85
Figure A-81: Electrical design of the interface board.....	A-86

## **LIST OF ABBREVIATIONS**

ADC	Analog to Digital Converter
BLE	Bluetooth Low Energy
CoV	Coefficient of Variance
CSV	Comma Separated Variable
DFT	Discrete Fourier Transform
DoF	Degree of Freedom
DPS	Degrees per Second
eMMC	embedded Multi-Media Controller
FC	Fouling Content
FFT	Fast Fourier Transform
GPIO	General Purpose Input Output
IC	Integrated Circuit
IDE	Integrated Development Environment
IHHA	International Heavy Haul Association
IMU	Inertial Measurement Unit
mJ	milli-Joule
LAN	Local Area Network
LiPo	Lithium-ion Polymer
LoRa	Long Range (communication)
LVDT	Linear Variable Differential Transformer
MCU	Micro Controller Unit
MEMS	Micro-Electro Mechanical System
OS	Operating System
PSSH	Parallel Secure Shell
PLA	Polylactic Acid
RAM	Random Access Memory
RPM	Rotations per Minute
SHM	Structural Health Monitoring
SoC	System on Chip
SSH	Secure Shell
TFR	Transnet Freight Rail
WEF	World Economic Forum
WSSN	Wireless Smart Sensor Networks

## LIST OF SYMBOLS

$\psi$	Yaw
$\theta$	Pitch
$\phi$	Roll
$G$	Acceleration unit equivalent to $9.81 \text{ m/s}^2$
$\theta$	Surface friction angle
$\theta'$	Effective surface friction angle
$\sigma_3$	Confining stress
$\sigma_1$	Compressive stress
$\Lambda_a$	Cost function for accelerometer calibration
$\Gamma$	Cost function for gyroscope calibration
$\omega_{P,k}$	Angular vector for the body (platform) frame
$\omega_{S,k}$	True angular vector for the sensor frame
$S_g$	Scale factor matrix for the gyroscope
$M_g$	Misalignment correction matrix for the gyroscope
$a_{P,k}$	Acceleration vector for the body (platform) frame
$a_{S,k}$	True acceleration vector for the sensor frame
$S_a$	Scale factor matrix for the accelerometer
$M_a$	Misalignment correction matrix for the accelerometer
$k$	Shape parameter (Weibull)
$\lambda$	Scale factor (Weibull)
$q$	Quaternion vector
$\dot{\omega}$	Angular velocity vector
$H$	Information entropy (Shannon)
$H_m$	Normalised information entropy measure of disorder
$U_K$	Kinetic energy
$U_P$	Potential energy
$m$	Mass
$E$	Young's Modulus of the material

# 1 INTRODUCTION

## 1.1 BACKGROUND

At first glance the operational performance of ballast appears trivial in its simplicity. However, various mechanisms affect the short and long term performance of the ballast and in turn, the response of the track structure, both on a *macroscopic* scale considering the track structure as an entity and on a discrete particle level or *mesoscale*. The nature and geometry of the material itself creates difficulty in instrumenting the ballast directly and analytical solutions of the track structure in three dimensions require complex numerical models. Rucker (1982) concluded that a three-dimensional, half-space model is extremely difficult, if not impossible, to be developed for the theoretical investigation of complex ballast vibrations. Without continuous, accurate and reliable quantitative measurements of the operating condition of railway infrastructure, cost-effective maintenance to minimize the life cycle cost of these infrastructure projects will not be realized. Maintenance operations in particular can benefit from investigating the interrelationship between ballast particle dynamics and track characteristics.

For the past three decades, industry and academia have experimented and improved upon an increasing number of versatile and more powerful wireless sensor platforms for the purpose of structural health monitoring (Lynch & Loh, 2006), driven by the low cost and improved performance of different sensor technologies. The continuous evolution and widespread application of these instruments in civil engineering structures provide monitoring solutions and cost-savings not possible before. MEMS (Micro-Electro-Mechanical System) devices have recently evolved to provide versatile, miniaturized sensors that are capable of measuring accelerations ranging from fractions of the Earth's gravitational field, up to 400 *G* (STMicroelectronics, 2013a). These devices borrow similar operating principles from strain gauges, LVDTs (Linear Variable Differential Transformer) and piezoelectric transducers (Nathanson & Wickstrom, 1965). Zhai et al. (2004) is one of the earliest examples to directly instrument the ballast with a uniaxial MEMS sensor. More recently, Liu et al. (2005, 2016a, 2016b, 2016c) demonstrated the successful implementation of the aptly named "SmartRock" for investigating the dynamic ballast behaviour in greater detail for both translation and rotations in three dimensions.

Existing investigation methods and instruments are however limited in its ability to instrument ballast and track structures subjected to harsh environmental and operating conditions with sufficient sampling frequencies. Furthermore, where instruments such as SmartRock excels in its propensity as a “smart ballast” instrument leveraging wireless sensor technologies, the short range communication system and modest sampling rate lacks the necessary fidelity and resolution to resolve and quantify the dominant modes of ballast movement and rotation under representative field conditions.

## **1.2 OBJECTIVES OF THE STUDY**

The main objectives of the study are summarised as follows:

- The realization of a smart ballast instrument (Kli-Pi) that builds and improves upon existing instrumentation to measure the dominant modes of ballast translations and rotations with sufficient resolution and frequency.
- To quantify the representative dynamic response (time and frequency domain) of ballast for both laboratory and field environments about all degrees of freedom.
- To investigate the application of descriptive statistics and energy principles to formulate new metrics for comparing and quantifying the measured experimental and field performance of ballast.

## **1.3 SCOPE OF THE STUDY**

The focus of the study is the investigation of ballast dynamics, limited to short term field testing and simplified laboratory box tests. Both time and frequency domain characteristics were investigated for different depths of instrumentation. A novel smart ballast instrument was designed and constructed (Kli-Pi) for the experiments to measure the ballast dynamics. Only short term field trials were conducted, with the objective of gathering data that is representative of the track performance at a single interval of time. The influence of ballast particle characteristics, ballast fouling and changes in particle geometry did not form part of this research project. All experimental work was based on heavy haul train specifications, technology and characteristic operational conditions.

## 1.4 METHODOLOGY

The study is broadly divided into two main sections that follow upon one another:

- The development and fabrication process of Kli-Pi, a smart ballast prototype designed to measure mesoscale ballast behaviour. The instrument was designed and constructed against a desired set of criteria as determined from the literature review, improving upon existing research efforts and technical specifications of smart ballast, implementing MEMS-based inertial measurement units (IMU's). This encompasses the methodical process of instrument design, assembly, programming, calibration, testing and implementation.
- The analysis and interpretation of data and information gathered from small scale, representative laboratory and field testing to investigate the interrelationship between the translation and rotations in three dimensions. This includes investigating the movement and orientation patterns in three dimensions - angular rotations and linear displacements – and simplified energy considerations. Both the time and frequency domains were investigated for characteristic information pertaining to the position within the track structure of each Kli-Pi. For both the instrument operations and data analytics, Python scripts were implemented and developed by the author to ensure accuracy and operational transparency of the results that can additionally be scaled and adapted for improvements of smart ballast platforms in the future.

## 1.5 ORGANISATION OF THE DISSERTATION

The report consists of the following chapters:

- Chapter 1 serves as the introduction to the dissertation, outlining the objectives, scope, methodology and organisation of the research project.
- Chapter 2 contains a discussion of literature related to different instrumentation methods, existing knowledge on the dynamic behaviour of ballast – both in the macro- and mesoscale domain - and the emergence of “smart ballast” instrumentation to study ballast dynamics.
- Chapter 3 provides the detailed development and calibration process of Kli-Pi, a prototype smart ballast instrument that can be used to directly measure the ballast dynamics with a sufficient level of accuracy and resolution to address the research objectives.
- Chapter 4 covers the experimentation process that comprises both laboratory box tests and field testing using the Kli-Pi platform.
- Chapter 5 discusses the results of the analyses, their significance and implications in the broader context of the functional role of ballast in the track structure.
- Chapter 6 concludes with a summary of the addressed research objectives as stated in Chapter 1. Recommendations for future research activities that can augment and elaborate on the results of the research are summarised.
- Chapter 7 lists the referenced literature.
- Appendix A provides additional information consisting of graphs, software implementation and analysis, electrical wiring and the operating specifications of Kli-Pi.

## 2 LITERATURE REVIEW

### 2.1 INTRODUCTION

At the opening of the most recent International Heavy Haul Association (IHHA) conference, hosted in Cape Town, South Africa during September 2017, Dr. Cheryl Martin, head of the Centre of Global Industries at the World Economic Forum (WEF) stressed the uncertainty in emerging technologies that underpins the fourth industrial revolution such as Augmented Reality (AR), 3D printing technologies and smart infrastructure (Smith, 2017). Klar et al. (2016) defines “smart infrastructure” as: “*an emerging field of study dealing with the development and large-scale embedment of hi-tech sensors in traditional civil engineering structures, and concurrently, with the collecting and meaningful interpretation of raw signals*”. Noting that the focus of the next IHHA conference to be hosted in Norway during 2019 is focused on the “Railways 4.0” paradigm, it becomes imperative that the railway industry exploit disrupting technologies that can provide increasingly safer, economical and efficient railway operations.

A recent report by the U.S. Department of Transportation (2010) stated that nearly two thirds of the capital allocated to bridge and road infrastructure was spent on system enhancements and rehabilitation (\$56.6 billion) compared to only \$33.6 billion for system expansion during 2008. Assessing the performance of extensive civil infrastructure in a cost effective manner provides the opportunity for enhanced policy decisions and budget allocations, reducing inconvenience to the public and most importantly, promoting public safety. Visual inspection by qualified personnel remains the favoured method for evaluation of infrastructure. This is tied to significant financial cost and human resources both of which are under strain with extensive and ageing infrastructure networks. It is widely recognised that the majority of maintenance is related to the deterioration of track geometry. Repeated dynamic wheel loading degrades the performance of ballast through inter-particle attrition, weathering of the material and fouling. Together with the settlement of the underlying earthworks, ballast layers are tamped, replaced and relevelled on a periodic basis to maintain the track and ballast stability. The majority of track settlement can be attributed to the settlement of ballast (Figure 2-1).

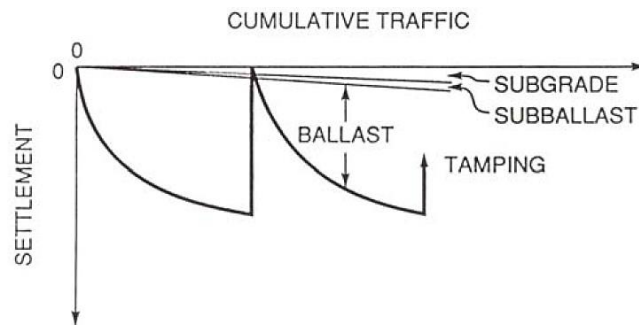


**Figure 2-1: Contribution to track settlement from different formation strata (Selig & Walters, 1994)**

Limited information is however available on the in-situ condition and performance of ballast without expensive excavation operations and complete track occupation. There exists an increasing need to better understand the effects of different ballast characteristics on the track performance that is subjected to dynamic loading conditions. Instrumentation provides accurate, quantitative information of track parameters through the measurement of physical quantities such as displacement. To systematically and continually assess the health of a railway track, more cost effective monitoring solutions are required. Ideally, a relationship describing the ballast particle dynamics and track stability is desired for optimizing maintenance, operations and track construction techniques. Audley & Andrews (2013) summarizes their discussion on the availability of track deterioration models: *“It is clear from looking at the existing track geometry models that there remains a need for better understanding of the degradation process to be established, which can support the development of accurate models, based on historical data. This model needs to be capable of including the effects of maintenance models”*. Cowin & Satake (1979) noted the importance of experimental studies to quantify the influence of the granular fabric on both the static and quasi-static deformational response of granular materials. This information contributes to the fundamental understanding of mechanical behaviour of granular media.

The literature review broadly differentiates between ballast mechanics viewed from a deterministic, continuum or *macroscopic* perspective and probabilistic, micromechanics or *mesoscale* behaviour. Some of the most critical factors that govern the dynamic behaviour and response of ballast are reviewed, covering field, laboratory and numerical studies. These interrelated behavioural components are discussed and reviewed with the objective of investigating the interrelationship between macro and mesoscale ballast behaviour, through the direct instrumentation of ballast particles. Finally, existing and developing measurement technologies for ballast investigation are reviewed, including wireless sensor platforms, inertial navigation systems and MEMS-based instrumentation.

## 2.2 TRACK STRUCTURE

Any railway track structure must be designed to provide safe and economical train transportation with the structure serving as a stable guide-way of appropriate vertical and horizontal alignment and its associated components providing the required performance under the various environmental and loading conditions as was designed for (Selig & Walters, 1994). The granular material response stems from the complex interaction of dynamic loading conditions, stress rotations and progressive settlement of the track structure. A traditional track structure can be divided in two main functional components, each with its own subset of components:

- Superstructure
  - Rail
  - Fastener
  - Pad
  - Sleeper
- Substructure
  - Ballast
  - Subballast
  - Subgrade

For ballast to fulfil its intended functions, the ballast layer must be constructed to an adequate thickness with the correct particle size distribution. The thickness should be specified based on the structural capacity of the track to ensure that it can withstand and distribute the applied train loading to an acceptable stress level, such that the subgrade will not deform excessively over the expected life of the track. The ballast provides resiliency, absorbs the applied loading energy, aids in the drainage of surface precipitation, provides voids for the storage of fouling material and aids in the arrangement of the track geometry during maintenance. Shape, angularity, surface texture and the level of compaction are important attributes of the ballast that affect the performance of the ballast. The applied force is a combination of both the static and superimposed dynamic or quasi-static force; the static load is determined by the mass of both the train and the track superstructure while the dynamic component is dependent on the condition of the track (defects, irregularities and an absence of contact between the sleeper and the ballast) and the velocity of the train. Lateral and horizontal forces are imposed on the ballast, although quantification of these forces presents its own difficulties (Selig & Walters, 1994).

The subballast is the granular layer that separates the ballast and the subgrade and consists of broadly graded gravel and sand. The gradation resists the interpenetration of the ballast and the subgrade material that can result in pumping of fine material to the surface and prevents subgrade attrition from the ballast above. The layer further reduces the traffic induced stress to a tolerable level at the top of the subgrade. The track substructure consists of the foundation layers that need to adequately support the track superstructure uniformly. It consists of either placed or natural soil (fill) or rock upon which the subballast layer rests.

Energy consisting of a combination of frequencies is transmitted throughout the track structure, with certain frequency bands attributed and differentiated according to vehicle, track and soil components (Figure 2-2). Lower frequencies are associated with longer wavelengths that are predominantly associated with the train geometry (Kouroussis et al., 2015). These include the inter-axle, inter-bogie and sleeper spacing dimensions. Intermediate frequencies are characteristic of soil and ballast layers, with higher frequencies attributed to track and rail effects and properties. For investigation of ballast dynamics, the maximum frequency cut-off of interest is around 250 Hz. The first resonance frequency for vertical vibration between the ballast and the sleeper is in the range of 50 – 300 Hz.

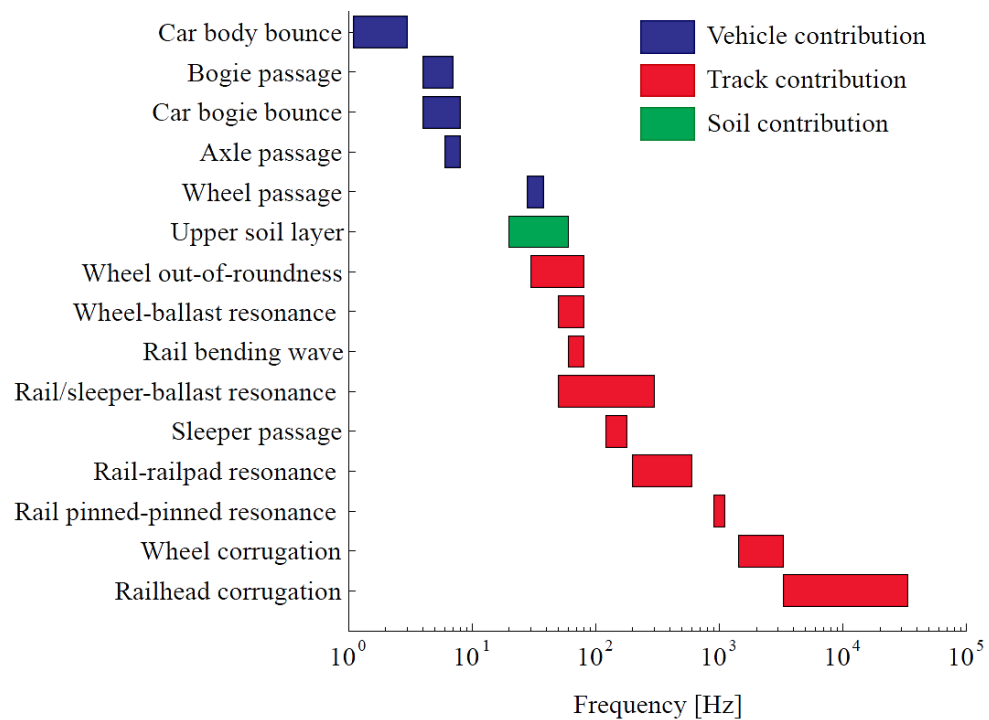


**Figure 2-2: Frequency contribution of vehicle, track and soil interactions (Kouroussis et al., 2015)**

Lamas-Lopez et al. (2017) reported that the accuracy between a fixed LVDT and accelerometer is in the region of 20% over a wide range of train speeds for peak-to-peak displacement values. The two varieties of instruments provide a means to quantify the displacement response with depth of the entire track structure. The authors summarised typical displacements encountered that can be expected for different granular layers:

- Sleeper: 0.8 *mm* for locomotive, 0.5 *mm* for coaches
- Subballast (700 *mm* depth): 0.4 *mm* for locomotive, 0.3 *mm* for coaches
- Subgrade (900 *mm* depth): 0.2 *mm* for locomotive, 0.1 *mm* for coaches

## 2.3 EMERGING SENSOR TECHNOLOGIES

It is clear that measurement instrumentation plays a valuable role in railway applications to quantify the performance of the various track components. Different types of instrumentation are suited for different types of components under study. The importance of ballast and its associated functions for a well performing track is well understood, although instruments to directly measure and quantify the ballast behaviour have been few and far between, given the associated technical and practical difficulties. The particles themselves are relatively small with irregular geometry and are allowed limited freedom of movement and rotations about all three dimensions, complicating efforts to accurately instrument them. All the ballast particles, with the exception of the particles at the surface, are surrounded and obscured from visual observation. Any instrumentation that incorporates wires for the supply of electrical power or communications is subject to attrition if placed within the structure in addition to changing the surrounding interlock behaviour of the particles. The instruments themselves have to be small enough to be representative in size and shape of a typical particle if the behaviour at a particulate level is to be mimicked, requiring spatial alignment of the body frame to the global or track coordinate frame as the unbound continuum shifts over time.

Structural Health Monitoring (SHM) is an engineering paradigm for the application of new and emerging sensor technologies that can rapidly identify and quantify the onset and extent of structural damage (Lynch & Loh, 2006). A variety of sensors can be installed on a structure that records the sensor data either locally, or transmits the data to a centralized storage location for both long and short term analysis. The advent of wireless sensor networks have greatly increased the nodal densities at which structures can be instrumented due to significant cost savings compared to a wired network. For example, the cost of instrumenting the Bill Emerson Memorial Bridge with 86 wired accelerometers was \$1.3 million or \$15,000 per node (Çelebi, 2006). The notion of a wireless “sensor” has evolved to be more accurately defined as the combination of mobile computing, low-power, wireless communication and the sensor itself, in a stand-alone *platform* - Wireless Smart Sensor Networks (WSSN). These sensors utilize recent advances in semiconductor manufacturing technology to include miniaturized, solid state sensor technologies. The addition of mobile computing allows for localized data processing and autonomy.

### 2.3.1 Wireless Sensor Platforms

Wireless sensors require an appropriate interface through which the analog signals can be transformed into digital form for processing by a microprocessor. The quality is affected by the specification of the resolution, sampling rate and the number of data channels available to the analog-to-digital converter (ADC). A radio transceiver is typically employed for wireless communication and data transfer. Unlicensed radio frequencies of 2.4 GHz and 5 GHz are the most commonly used with different protocols such as 802.11 (commonly referred to as Wi-Fi), with Bluetooth and ZigBee operating on the same frequency band.

Some early examples of successful wireless monitoring systems are that of Straser and Kiremidjian (1998) that was specifically designed for the monitoring of civil structures. For early applications in geotechnical and pavement engineering applications, whereby the physical footprint of the device is the primary design constraint, Bennett et al. (1999) employed a cylindrical form factor for thermal and strain measurements of thin, flexible asphalt surfacings. Nejikovsky & Keller (2000) developed an on-board monitoring system that successfully identified and monitored excessive lateral acceleration that results in excessive cant levels on passenger rail cars along the Pacific North-West. Currently the largest limitation in the prolific adoption of these new technologies is the low-density battery technologies that power the devices for a relatively short period of time.

### 2.3.2 Inertial Navigation Systems

Woodman (2007) defines inertial navigation as “a self-contained navigation technique in which measurements provided by accelerometers and gyroscopes are used to track the position and orientation of an object relative to a known starting point, orientation and velocity”. Self-contained inertial measurement units (IMUs) contain three orthogonal accelerometers and gyroscopes for full spatial orientation. The accelerometers quantify linear or translational acceleration and the gyroscopes either angular acceleration or angular velocity depending on the kind of sensor. Gyroscopes are initialized before navigation commences to align the body and global frames. Illustrated in Figure 2-3, the gyroscope (body frame) provides a relative frame of reference for orientation that can be compared to the initial frame of reference (global frame) at any point in time or space. Two classes of inertial configurations are differentiated: stable platform and strapdown. A stable platform is isolated from any external perturbations using a system of mechanical gimbals with the inertial sensors fixed to the free platform. Relative angles are recorded and the position is determined through double integration of accelerometer readings. A rigid system by comparison fixes the sensors directly to the body frame. Accelerometer readings first have to be transformed back to the global frame before the body position can be determined.

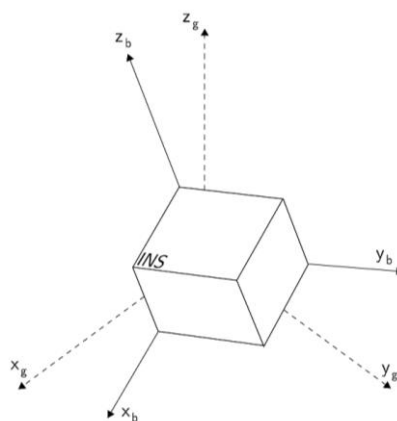


**Figure 2-3: The body and global frames of reference (Woodman, 2007)**

### 2.3.3 MEMS Instrumentation

Nathanson & Wickstrom (1965) conceived the idea of a Micro-Electro-Mechanical System (MEMS) based device for the purpose of frequency tuning for radio equipment. These devices are constructed using traditional semiconductor and integrated circuit (IC) fabrication techniques to create moving mechanical elements that measure micrometres in size (Figure 2-4).

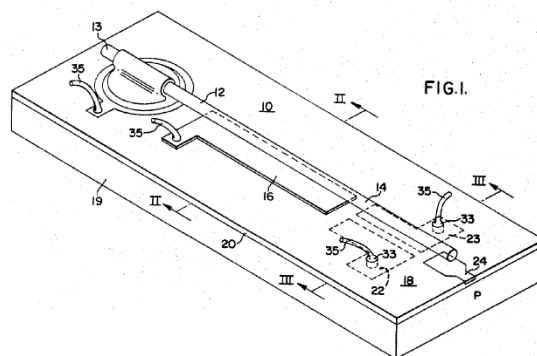


**Figure 2-4: Electrically conductive cantilevered vibratory member affixed to the substrate (Nathanson H.C & Wickstrom R.A., 1968)**

This technology has evolved to create versatile, miniaturized sensors able to measure accelerations ranging from that of the earth's gravitational field, up to 400  $G$  (STMicroelectronics, 2013a). These devices are shock resistant (up to 10,000  $G$ ), consume very little electrical current during operation and have substantially lowered in cost due to the proliferation of smartphones using these sensors for enhanced user interfaces. These devices borrow similar operating principles from strain gauges, LVDTs and piezoelectric transducers. Even though the devices cannot match the performance characteristics of optic-based systems, Titterton & Weston (2004) highlight the advantages of MEMS-based sensors:

- Small size
- Low weight
- Rugged construction
- Low power consumption
- Short start-up time
- High volume production yield inexpensive units

Lemkin & Bernhard (1999) describe the typical construction and operation of such a device. Changes in acceleration of the substrate or anchor that is fixed to the sensor enclosure induce an unbalanced force (Figure 2-5). A spring mounted proof mass displaces in the opposite direction to that of the accelerating substrate and anchor point. The proof mass is situated within a comb-like matrix of complimentary stationary elements, forming a variable capacitive half bridge. A force balance accelerometer is attained through application of a negative feedback loop that applies a restoring force proportional to the offset, to restore the proof mass to its original, centred position. This minimizes excessive deflections and resulting non-linear effects while maintaining an appropriate dynamic range. Advanced resonant sensors incorporate changes to the resonance frequencies, phases or resonance amplitudes from the accelerations of the mechanical transducer to attain larger signal-to-noise ratios and dynamic range (Kempe, 2011).

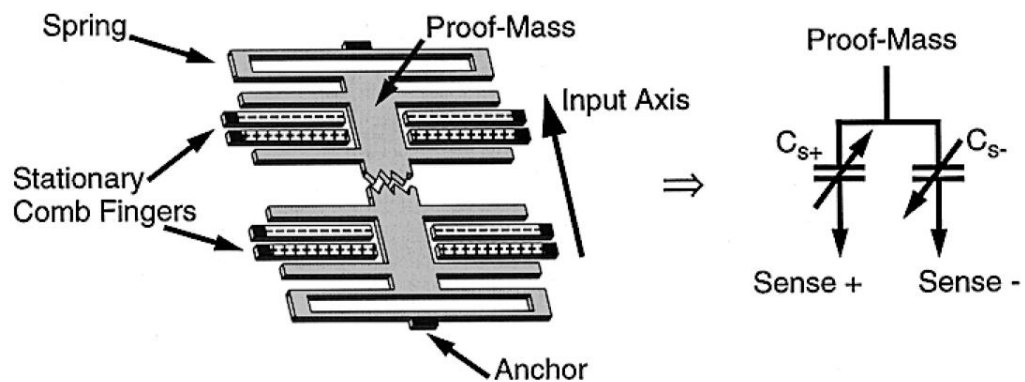


**Figure 2-5: Top view of the sensing element and the equivalent electrical model (Lemkin & Bernhard, 1999)**

Similarly, gyroscopic or angular velocities can also be measured through the use of MEMS fabrication technologies. The Coriolis force generated from a rotating, non-inertial system of coordinates is used to determine the angular velocity (Kempe, 2011). Unlike high accuracy navigational applications, the Earth's rotation vector can be ignored with its surface acting as the inertial system reference. So-called "rate" gyroscopes use the Coriolis force as a coupling mechanism between the mass movement and the platform's rotation (body frame) with respect to the Earth (global frame). Multiple degree of freedom (DoF) gyroscopes make use of more complex, multiple platform and proof mass arrangements (Figure 2-6) to maximize the space efficiency.

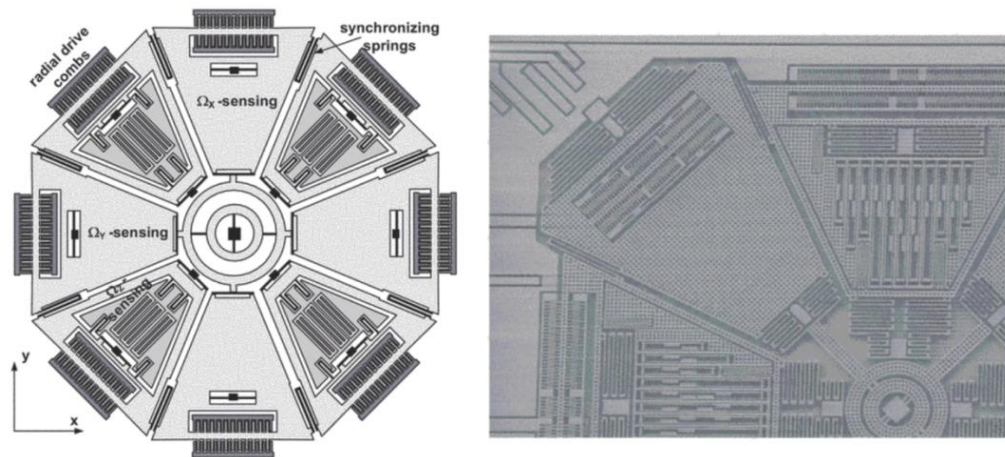


**Figure 2-6: Implementation detail of a dully decoupled 3D gyroscope (Kempe, 2011)**

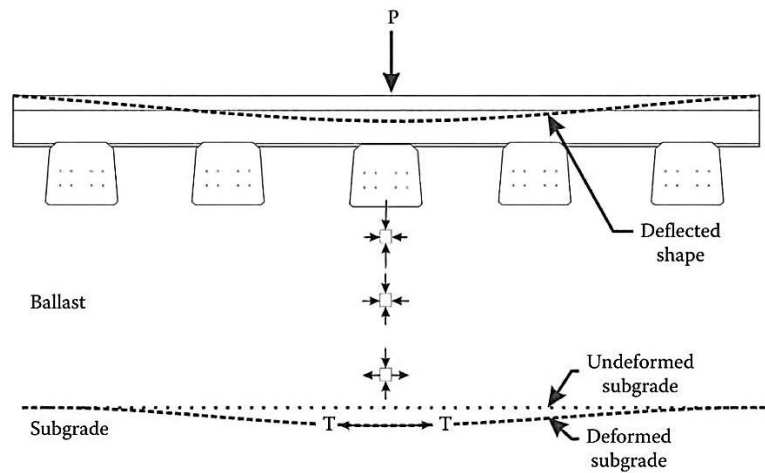
## 2.4 CONTINUUM MECHANICS OF GRANULAR MATERIALS

This section emphasises ballast investigation from a continuum or deterministic viewpoint. It is a combination of research involving laboratory, field measurements and numerical models. This pertains to the effects of permanent strain, fouling, stress rotation and confinement.

### 2.4.1 Permanent Strain

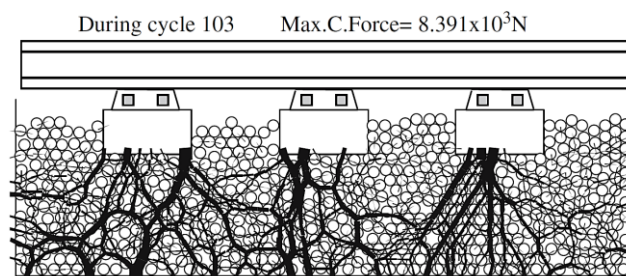
Permanent strain is thought to occur due to the breakage of ballast particles in addition to the repeated rearrangement of particles. With an increasing number of repeated load cycles, the ballast interlocks into an increasingly tighter or more confined arrangement. With sufficient compaction, the ballast layer gains adequate strength to support the load from above without undergoing excessive plastic deformation. This process relies on a simplified ratcheting mechanism in conjunction with deformation of the ballast layer. The ballast situated in the bottom tends to spread laterally in the absence of adequate confinement, mitigating the benefit of the interlocking process.

Figure 2-7 illustrates the ballast layer subdivided into three distinct zones. Load transfer from the sleeper to the ballast is equivalent to typical triaxial compression. The middle layer experiences higher levels of confinement with a corresponding reduction in vertical stress. The lowest layer develops incremental tension with an increasing number of load cycles. This zone in particular is prone to the particles rearranging and spreading, with newly created voids filled with particles falling from above.



**Figure 2-7: Cyclic tensile strain in a granular material with no tensile capacity (Li et al., 2015b)**

Lobo-Guerrero & Vallejo (2006) found that even if only a minority of particles break, the associated increase in permanent strain is substantial. For typical maintenance activities such as tamping of the ballast - periodically disturbing the particle arrangement - the shear resistance reduces by up to 40% and lateral resistance up to 60% (Tutumluer et al., 2006). Comparing uncrushable ballast with that incorporating the breakage model, the permanent deformation after only 200 load cycles increased from 33.8 mm to 51.2 mm. Particle breakage was predominantly concentrated directly underneath the sleepers. The development of force chains illustrates the absence of strength contribution from the crib ballast in addition to the irregular pattern of force distribution (Figure 2-8). Cundall & Strack (1979) also illustrated the “columns” that carry the major principal stresses that are periodically altered with particle rearrangement and breakage.



**Figure 2-8: Force chain development for uncrushable ballast particles (Lobo-Guerrero, & Vallejo, 2006)**

### 2.4.2 Fouling

The progressive addition of fine material that occupies the voids of ballast, origination from spilled cargo (coal and iron ore dust), inter-ballast attrition or the pumping of fines from the subballast due to cyclic loading, is known as fouling. Fouling degrades the general performance of the track and inhibits the drainage of surface water. Selig & Waters (1994) defined the fouling content (FC) as the sum of the mass of material percentage passing both the 4.75 mm and 0.075 mm sieve sizes. Haung et al. (2009) established that at a 15% FC threshold, statistically significant reductions in strength were observed. For fully fouled ballast at 35% moisture content, friction angles could be as low as the friction angle of the fouled material itself – likely due to the absence of the stone-matrix support. The inter-particle shear strength is a function of both the normal contact force and the surface friction angle, defining the Mohr-Coulomb failure criterion. For a contact shear force exceeding the contact shear strength, particles will slip and slide relative to one another. Huang & Tutumluer (2011) investigated how particle characteristics should be altered for discrete element model (DEM) applications to include the functional, altered effects of fouled ballast. Using this information for a half-track model with fouled material confined to the extent of the rails, the centre portion of ballast was found to have an increased level of confinement with displacements predominantly in the vertical direction, whereas the majority of the shear failure sliding surface is located in the shoulder section, specifically the bottom portion. The shoulder ballast experiences increased displacement along the shearing direction which ultimately leads to more settlement.

### 2.4.3 Principal Stress Rotation and Confining Stress

Stresses resulting from the combination of traffic and the track structure, particularly the ballast and subballast, are complex considering the three dimensional geometry. The effects of principal stress rotation (PSR) resulting from cyclic loading has a significant effect on both the long term cumulative (Gräbe & Clayton, 2009) and the rate (Lekarp et al., 2000) of permanent deformation. For ballast in close proximity to the sleeper, the significant stresses in the vertical plane limit any effective development of PSR (Lim, 2004). The volume or quantity of soil that is subject to PSR is dependent on the Young's modulus of both the ballast and the underlying subgrade with the most unfavourable combination of stresses occurring near the mid-depth of the subballast. Major principal stresses can potentially be rotated by up to  $\pm 90^\circ$  depending on the coefficient of earth pressure at rest ( $K_0$ ). The influence of PSR on the permanent axial strain is evident when comparing the results of cyclic loading both with and without the effects of PSR. An increase in the effective principal stress ratio rapidly

increases the rate of permanent deformation. The PSR can be described as a combination of three distinct mechanisms (Gräbe & Clayton, 2009):

1. For shallow depths and single axle configurations, longitudinal PSR occurs between two successive sleepers.
2. Transverse PSR are located at the ends of the sleeper.
3. For a higher axle count per bogie, the influence of PSR extends deeper down into the formation.

## **2.5 MICROMECHANICS OF GRANULAR MATERIALS**

Theories pertaining to elasticity and plasticity are generally employed to model the response to loading when investigating of the granular structure from a continuum or macroscopic point of view. This observed structural response is the combined contribution of all the constituent track components, including the discrete granular particles and voids among them. To better understand the micromechanics or *mesoscale* behaviour of the discrete granular material, adapted solutions and implementations of instrumentation and numerical methods are required. Contrary to continuum mechanics, micromechanics of granular materials fully accounts for the discrete nature of granular materials. Finite element modelling (FEM) and more recently, discrete element modelling (DEM), are the two dominant numerical methods used for the modelling and study of ballast. These are viable alternatives to field testing and monitoring, though the granular nature of the particles and the significant number thereof add to the complexity of selecting the appropriate numerical model. With the addition of smart sensors and miniaturized MEMS-based sensors, new avenues of research have recently been explored.

### **2.5.1 Discrete Element Modelling**

Numerical studies using either FEM or DEM contribute to the understanding of the dynamic response and underlying mechanics of ballast and railway structures. The use of numerical models in railway engineering is well established, extending beyond the isolated track superstructure with the inclusion of train-track interaction dynamics. Few, if any, satisfactory constitutive relationships exist that can accurately describe the complex behaviour of a discrete medium; thus followed the application of explicit numerical methods. The foundation for Discrete Element Modelling (DEM) resulted from the work of Cundall & Strack (1979) for the simulation of dynamic, rigid (discs and spheres) particle systems

undergoing large displacements and rotations, compared to Finite Element Modelling (FEM) where a continuum, divided into a finite number of subdomains, averages particle properties.

Zhang et al. (2016) presented a comprehensive DEM analysis on the dynamic behaviour of ballast for high-speed railway (HSR) applications. Results indicate that ballast particles experience the most significant stresses within the first 200 mm underneath the sleepers. Acceleration frequencies are concentrated not only below the 100 Hz region but also in the medium frequency range of 150 – 300 Hz. Although the computational overhead is substantially reduced to accelerate the simulations, the 2D DEM model is unable to calculate the particle packing, void distribution and calculation of stresses. A dimensionless variable  $\beta$  is introduced that relates the ratio of principle stresses of the particle to that of the average value for the three principal stresses. Figure 2-9 illustrates the  $\beta$ -contour plot for a train velocity of 200 km/h.

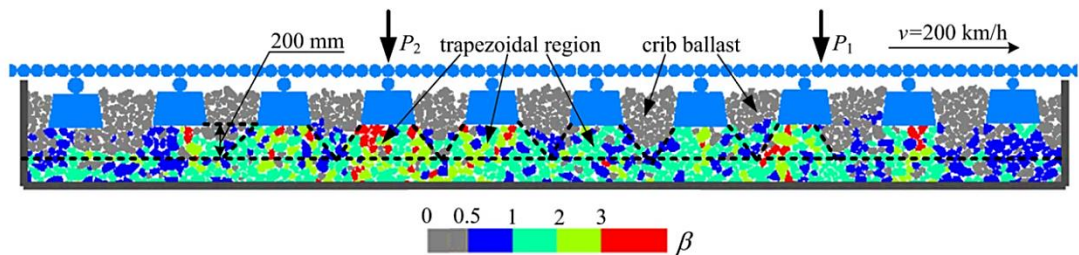


**Figure 2-9:  $\beta$ -contour plot for a train velocity of 200 km/h (Zhang et al., 2016)**

It is clear that the crib ballast experiences small forces with the force chains predominantly residing below the sleeper under the frustum-shaped loading zones, similar to that of Figure 2-8. The alternating  $\beta$ -values underneath the sleeper illustrate the PSR as the wheel loads move successively over a particular point. The particle accelerations illustrate irregular spatial distributions, though the displacement and velocity vector plot show a clear agreement with the expected direction of displacement (Figure 2-10). If the displacement of a particle is compared over successive points along the direction of movement, a circular movement pattern is produced. On a particle-by-particle basis, the spatial distribution illustrates that the longitudinal discontinuity of the ballast lead to non-uniform vertical displacements (Figure 2-11). This alternating pattern of vertical displacement, together with the longitudinal displacement in front and behind the bogie resulting from PSR, contributes to the circular movement pattern of the particles. The magnitude of the ballast particle displacements is comparatively small with maximum amplitudes approaching 200  $\mu\text{m}$ . The highest frequency spectral densities were found to correlate with the velocity of the train and the geometry

(inter-axle and bogie spacing). The third dominant acceleration frequency appeared at nearly ten times the first dominant (inter-axle) frequency. No particle breakage is taken into account for this model, nor is information provided pertaining to particle rotation.

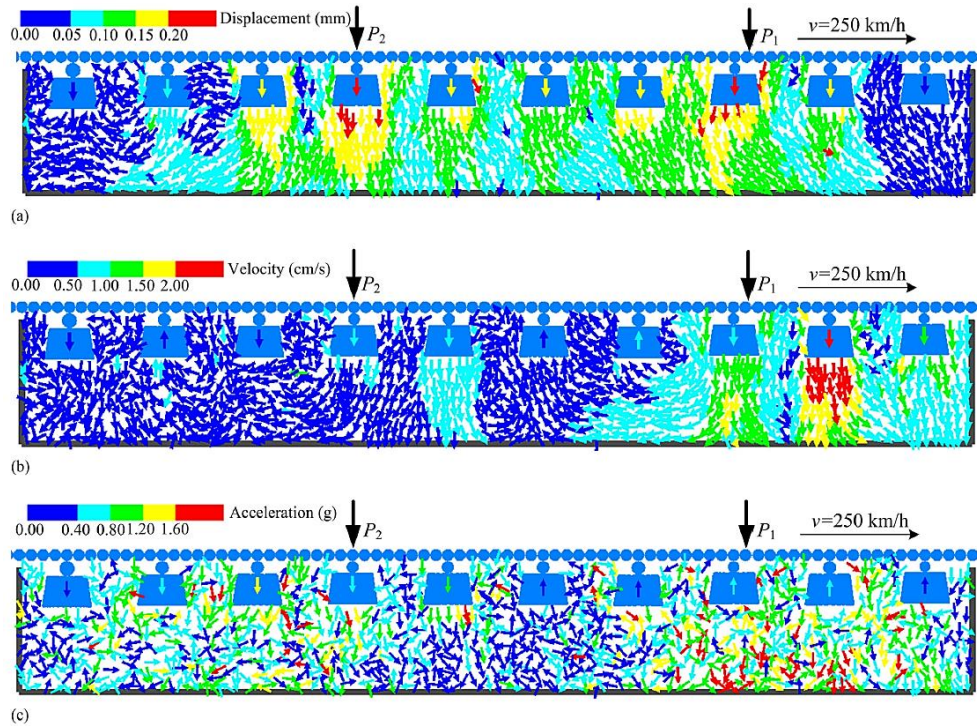


**Figure 2-10: Vector plot for ballast (a) displacement, (b) velocity and (c) accelerations (Zhang et al., 2016)**

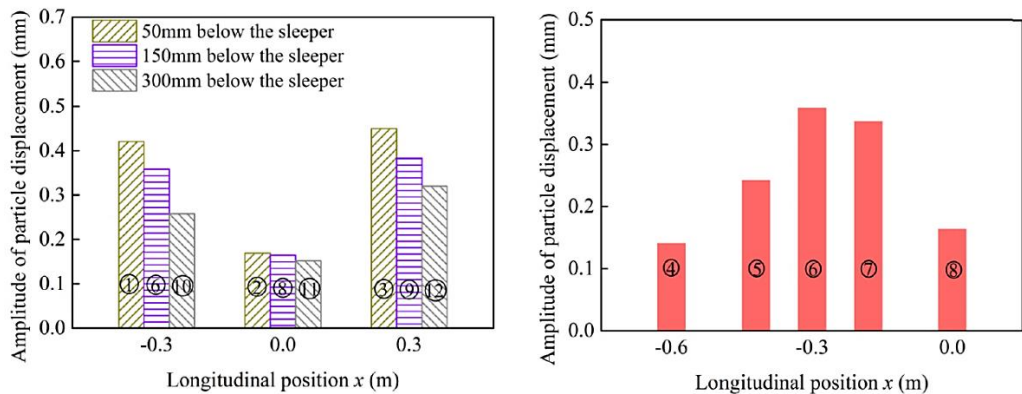


**Figure 2-11: Vertical particle displacement comparison as a function of longitudinal position and depth (Zhang et al., 2016)**

Recent research efforts have replaced the spherical particle shapes generally used in DEM to more representative non-convex particles found in civil engineering applications (Wilke et al., 2016). Representative ballast geometry and its associated characteristics can be quantitatively defined using imaging methods (Indraratna et al., 2011) or with laser scanning technologies (Mvelase et al., 2012). Compared to a spherical model, fewer particles are required than with the fusion of convex polyhedra.

## 2.5.2 Entropy

Information entropy, first described by Shannon (1948), is a measure of the quantity or randomness of the information contained in a given dataset, related to the number of different micro-states that can be realized for a particular probability distribution. This measure is not related to whether the information has any value or meaning and is independent of the spatial arrangement of the information. Information entropy is only concerned with the information content and structure. Information entropy can assume multiple definitions depending on the context of its application. For pure information, the entropic content can be viewed as the weighted average of the information of all possible outcomes. For physical systems this can be said to evolve from one configuration to another, with the latter entailing a higher probability than the former. A change in entropy corresponds to a change in the information contained within a given sample drawn from a probability distribution.

Results from Brown (1978) indicated that granular media tend to evolve to a state of maximum entropy. This observation enables the description of the stress state and deformational behaviour with statistical approaches. A modified formula for Shannon's statistical descriptor (Shi et al., 1998) used in geologic materials is given by Equation 2-1.

$$H_m = - \sum_{i=1}^n P_i \log_n P_i \quad (\text{Equation 2-1})$$

The parameter  $H_m$  describes a normalised measure of disorder through the alteration of base- $i$  to base- $n$ . Evans & Brown (2014) illustrated that through the maximization of entropy of microstate behaviour, a representative macroscopic response can be predicted.

### 2.5.3 Probability Density Functions

Cowin & Satake (1979) summarised their findings where statistical approaches, such as the application of information entropy, hold the potential to relate the continuum concepts of granular media to the mesoscale behaviour of the discrete components. Kitamura (1980) summarises this potential statistical approach: “*Furthermore, it is shown that the discontinuous motions largely contribute to the deformation process of particulate material, and the method to quantitatively estimate the discontinuous motions is proposed based on the probabilistic considerations for the motions of particles*”.

The *deterministic* nature of granular materials stem from the mechanical response founded on the laws of mechanics. This is despite the paradoxical observation that many features, such as contact forces and displacements, are best described in *statistical* terms (Rothenburg & Kruyt, 2009). Small variations in the local mesoscale environments provide variations in the strain distribution even with uniform loading and strain conditions. The authors hypothesized that the relative displacements of particles, with identical contact orientations, are independent outcomes of a random variable with a corresponding conditional probability density. This method provides the desired micromechanical constitutive relation. Using entropy maximization methods, it was proven that the shape of the probability density function is that of a Gaussian distribution. Furthermore, the moduli can be approximated using the uniform stress (lower bound) and uniform strain (upper bound). Considering coordination numbers ( $CN$ ) instead, this theory remains valid for loose systems ( $4 < CN < 5$ ) while uniform-strain assumptions are used for dense systems ( $5.5 < CN < 6$ ). This argument may explain the change in character of the probability density functions, from exponential to Gaussian, when the confining stress is increased (Kruij & Rothenburg, 2002). This phenomenon was found both experimentally and from simulations by Makse et al. (2000). It can be proven that the entropy of a Gaussian distribution is equal to  $H = \frac{1}{2} \ln(2\pi e \sigma^2)$ .

### 2.5.4 Smart Ballast

With the growth of smart sensor technologies and the recent attempts to merge these sensor platforms with physical ballast particles, it is appropriate to refer to this new concept as “smart ballast”. An example of the earliest attempts to directly instrument a ballast particle is that by Zhai et al. (2004). The authors proposed a five-parameter model for the analysis of ballast vibration, finding good agreement between simulations and field test results. Zhai et al. conducted a comparative test in which a modified uniaxial accelerometer was placed directly beneath the rail centre line, 150 mm below the bottom of the sleeper. Good agreement was found between the proposed model and the field measurements for the vertical accelerations (Figure 2-12). The resonance frequency of the ballast is situated between 80 Hz and 100 Hz. The shearing and damping parameters between the adjacent sleeper and ballast sections appear to have a significant influence on the magnitude of the calculated accelerations, due to the continuous interlocking and coupling nature of the granular particles. These results are in close agreement with Li et al. (2015a), observing that the first fundamental frequency is between 50 Hz and 210 Hz.

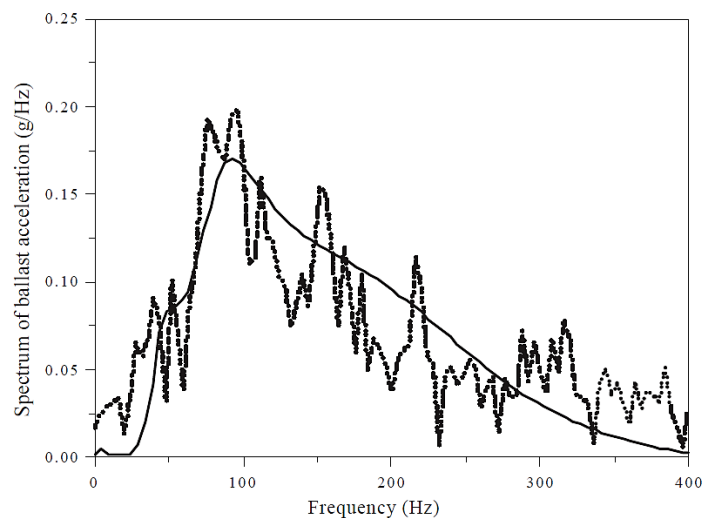


**Figure 2-12: Comparison of frequency spectra of ballast accelerations; theoretical model (solid line) and measured data (dashed line) (Zhai et al., 2004)**

Aikawa (2009) extended this idea by embedding two piezo-resistive, tri-axial MEMS accelerometers (Hitachi Metals H48D) in a ballast analogue. The two sensors were spaced an arbitrary distance apart with the axes orientated collinearly to differentiate between linear and rotational acceleration. The void was filled with resin to form a waterproof shell around the electronics and seal off the wires. The smart ballast was installed directly beneath a sleeper, 150 mm below the bottom of the sleeper, similar to that of Zhai et al. (2004). High frequency, vertical translational accelerations of 300 – 400 Hz preceded the rapidly attenuated 50 – 100 Hz components (Figure 2-13). Additionally, the rotational components exemplified a similar frequency spectrum to that of the translational accelerations, though these were rapidly attenuated together with the high frequency translational components. The information provided from this study was limited to information along the vertical axis (the axis aligned parallel to the earth’s gravitational field).

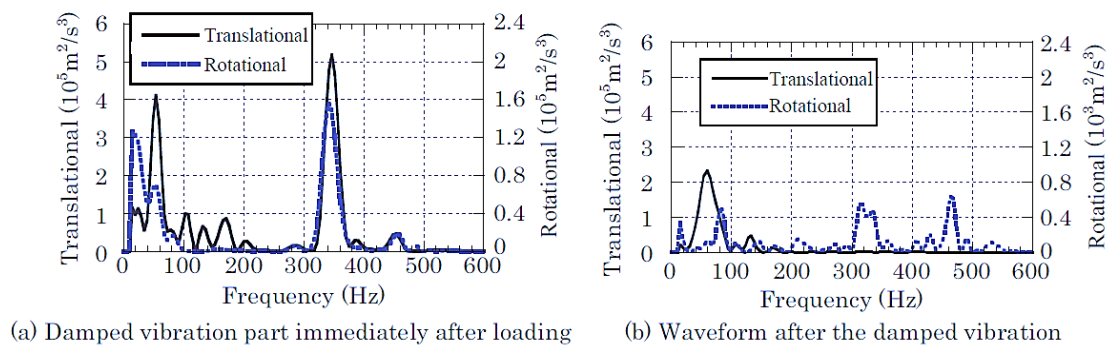


**Figure 2-13: Power spectrum density of measured ballast vibrating for vertical accelerations (Aikawa, 2009)**

For train velocities approaching 400 km/h, ballast exhibits a tendency to become airborne through a combination of track bed vibration and air flow patterns – the mechanics of which is not well understood. Milne et al. (2016a) investigated this phenomenon using smart ballast with an integrated 3-axis MEMS accelerometer (Analog Devices ADXL345) enclosed in a small waterproof enclosure, measuring only 23 × 32.5 × 7.6 mm in size. Each of the sensor’s axes was aligned with the global frame (track coordinate system). Ballast particles passing the 50 mm sieve were hollowed to accommodate the sensor platform and sealed with an epoxy resin. Four of these smart ballast particles were placed on the surface of the crib ballast. Geophones fixed to the sleeper provided comparative data between the track bed and the superstructure.

The measured orientation of the smart ballast before and after each train remained unaltered and was assumed constant. The longitudinal acceleration was greater than that in the lateral direction, possibly due to airflow from the underbody of the train. No measurements indicated that the upward accelerations exceeded that of gravitational acceleration, which indicated that ballast uplift and subsequent flight did not occur. Frequency spectra indicated that for frequencies above 60 Hz, the amplitude of ballast accelerations was larger than that of the sleeper. Again, the acceleration energy for ballast was concentrated around 80 – 120 Hz (Figure 2-14).

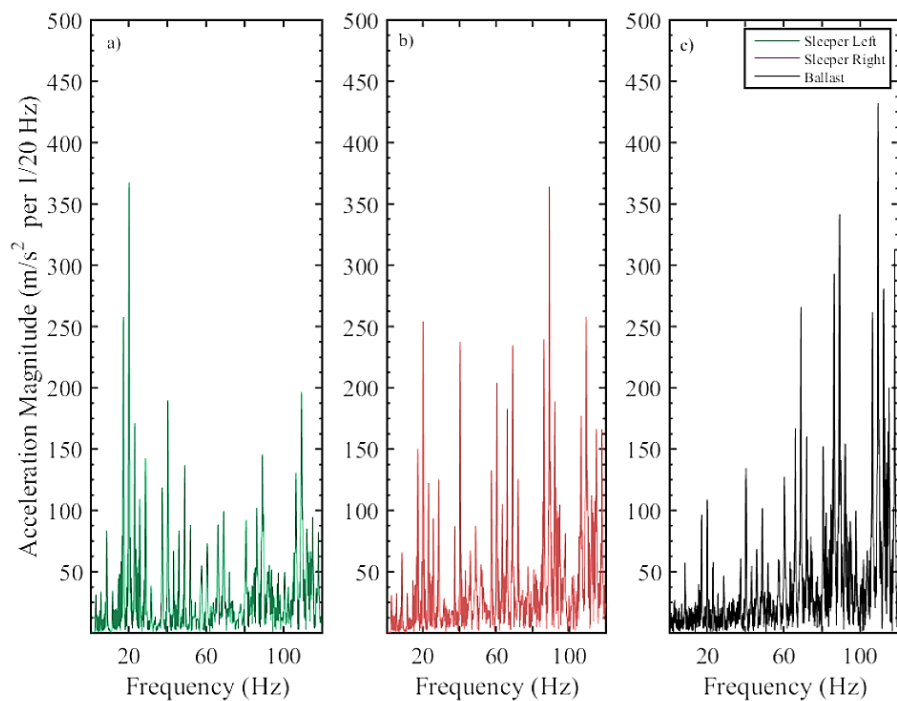


**Figure 2-14: Fourier transform for (a & b) vertical sleeper and (c) ballast particle accelerations (Milne et al., 2016a)**

Given the proven performance history of traditional instrumentation, MEMS-based technologies can be calibrated against these instruments for quantifying the reliability to support wider adoption toward self-monitoring smart infrastructure (Milne et al., 2016b). The results suggest that MEMS-based devices provide sufficient accuracy and reliability with field trials providing comparable displacements compared to the more expensive geophones. An actuator excited the respective sensors with a sinusoidal waveform at a fixed frequency, for 1 Hz increments, from 1 to 5 Hz. For higher frequencies an electrodynamic shaker provided excitation frequencies that varied from 5 to 45 Hz. A Butterworth bandpass filter

(0.8 – 8 Hz) in conjunction with integration was used to obtain comparative displacements. For a train velocity of 230 km/h and a sampling rate of 500 Hz, the deflections agree broadly with some minor variations in the frequency response. For a full data set of 24 train passes over the course of a day, the mean characteristic displacement is in close agreement: 0.27 mm and 0.28 mm for the geophone and accelerometer respectively. The relative standard deviation was 5% and 11% respectively. The potential for long term application is clear when deployed over a long period of time as illustrated by Figure 2-15, a characteristic made possible by the lower cost and longevity that is lacking with existing instrumentation. Trends are clearly visible and identifiable when comparing the dynamic sleeper displacements at two different sections of the same track. As noted by the authors, only one of the potential statistical parameters is considered to describe the passage of a train – current MEMS technologies allow for 5 additional DoF that have yet to be investigated.

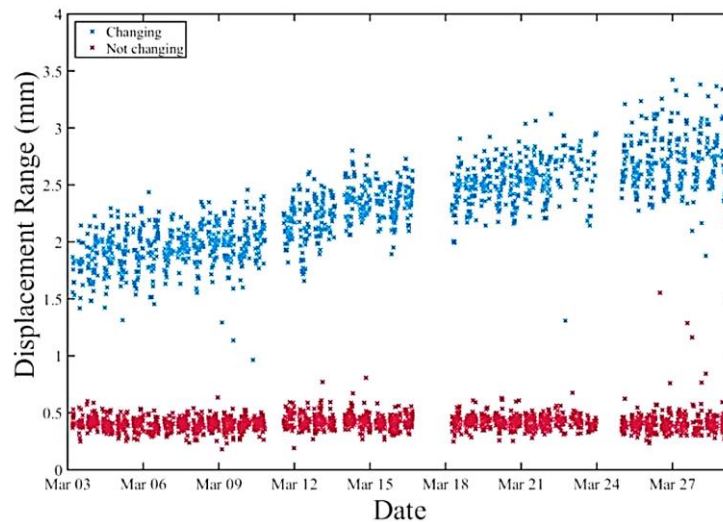


**Figure 2-15: Comparative, long-term displacements of sleeper performance for the same track over a four week period (Milne et al., 2016b).**

### 2.5.5 SmartRock Laboratory Testing

Liu et al. (2016a) developed a proprietary instrument aptly named “SmartRock”, to investigate ballast behaviour beneath a sleeper (Figure 2-16). The nominal dimensions of the device are  $60 \times mm$   $60 mm \times 60 mm$ .

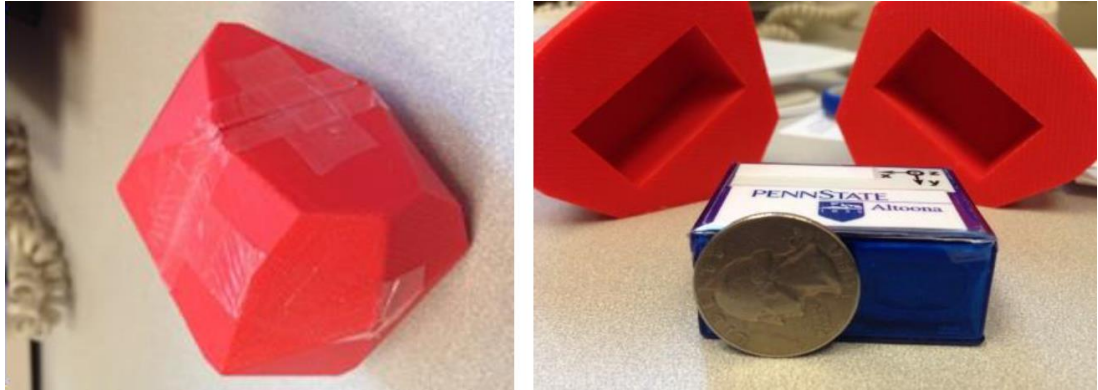


**Figure 2-16: Illustration of the “SmartRock” internal unit and accompanying protective shell (Liu et al., 2016a)**

The SmartRock is equipped with a 9 DoF MEMS-based IMU – a tri-axis accelerometer, tri-axis gyroscope and tri-axis magnetometer for measuring magnetic field intensity. Measurements are transmitted using Bluetooth to a centralized computer. Three-dimensional (3D) additive printing was used for construction of the surrounding protective shell to encase and protect the electronics inside the pseudo-particle. The stiffness and density were chosen to resemble realistic parameters as this influences the moment of inertia. Even though the IMU IC is capable of  $500 \text{ Hz}$  sampling rates, the choice of Bluetooth for communication severely limits the throughput to only  $64 \text{ Hz}$  according to the authors. For initial verification of the SmartRock instrument, a simplified box test was conducted whereby a single SmartRock was placed  $250 \text{ mm}$  beneath the centre of a sleeper. A  $1 \text{ Hz}$ ,  $65 \pm 65 \sin(2\pi t) \text{ kN}$  load was adopted for this test for 500 loading cycles. An increase in translational particle acceleration can be observed for the initial 130 cycles as rearrangement and densification ensues following the start of the test, subsequently decreasing as the ballast interlocks with adjacent particles. Horizontal translational and angular accelerations never reached a stable state, with a series of peaks present throughout the duration of the test (Figure 2-17 and Figure 2-18). Only peak acceleration values are reported for this test with no illustration or discussion regarding particle dynamics on individual loading cycles.

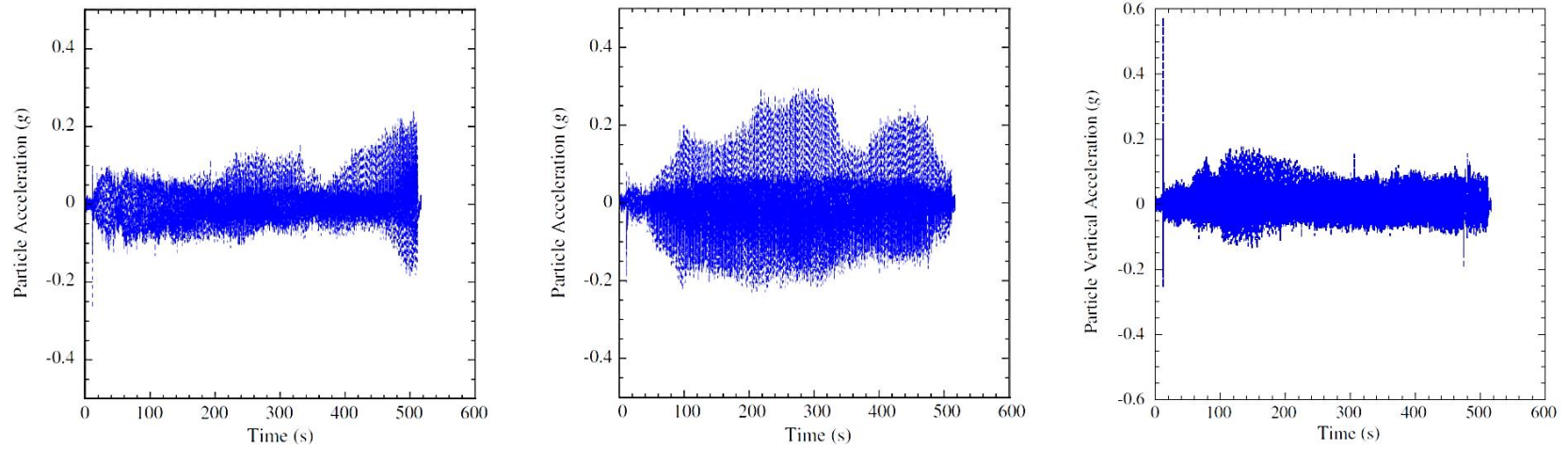


**Figure 2-17: Translational accelerations for horizontal (x & y-axis) and vertical directions (z-axis) (left to right) (Liu et al., 2016a)**

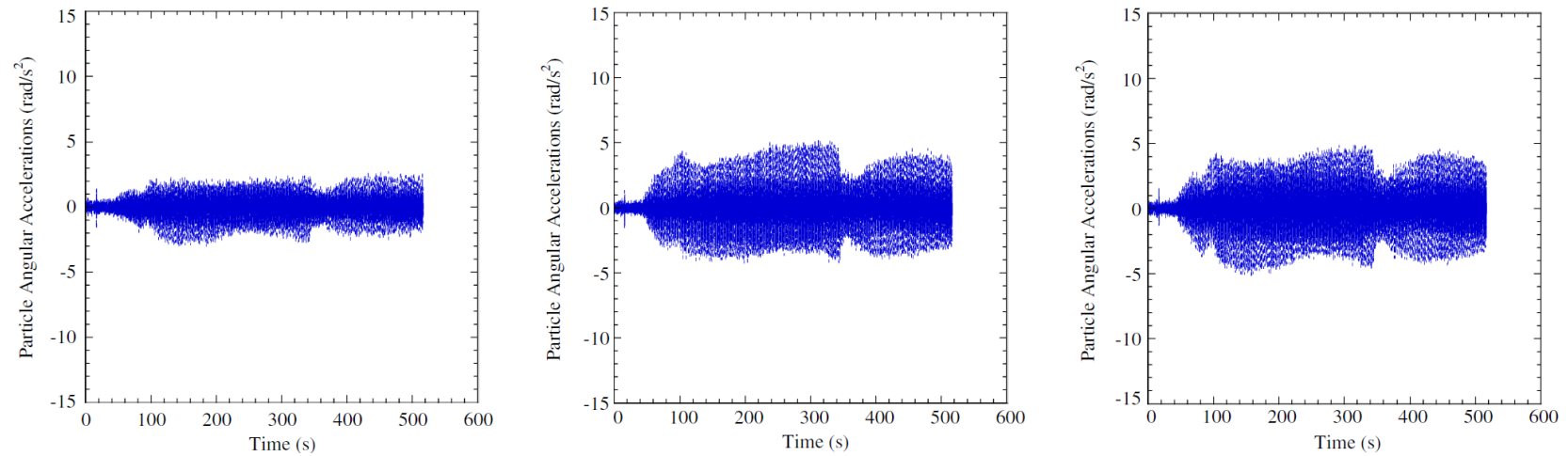


**Figure 2-18: Rotational accelerations about horizontal (x & y-axis) and vertical directions (z-axis) (left to right) (Liu et al., 2016a)**

Additionally, Liu et al. (2016b) investigated the effect of moving the SmartRock to different depths beneath a concrete sleeper for the same loading conditions as the simplified box test. The SmartRock was placed either in the middle or at the edge with respect to the sleeper's longitudinal profile. Only peak accelerations are investigated due to the chosen sampling rate of 4 Hz. Using laboratory box tests, the main conclusions reached is summarised:

- For cyclic loading, the SmartRock underwent both translational and rotational dynamics.
- Rotation was observed together with horizontal translation.
- An increase in the variation and amplitude by an order of magnitude for the rotations at the edge of the sleeper compared to the centre position.
- Ballast movement significantly reduces with increasing depth.

Lastly, Liu et al. (2016c) included ballast reinforcement in the form of a geogrid, shaped in an equilateral triangular pattern with a 60 mm × 60 mm aperture size to increase the degree of interlocking among the ballast particles. Significant changes were observed with the inclusion of the geogrid. Both the initial and accumulated vertical displacement throughout the test was substantially reduced with the included geogrid. The resilient deformation remained similar at the end of the 500 cycle test. The steady-state stiffness was achieved rapidly using the geogrid (after 100 cycles) whereas the unreinforced ballast only progressively gained an increase in stiffness. Rotation and translational accelerations of the SmartRock effectively ceased entirely when constrained with the geogrid, eliminating the random-walk behaviour observed prior to reinforcement. To summarise, reductions in excess of 80% were observed for nearly all quantitative measurements of the SmartRock.

### **2.5.6 SmartRock Numerical Model Comparison**

Liu et al. (2016a) compared the results between SmartRock measurements and a representative DEM model (BLOKS3D) for peak horizontal, vertical and angular accelerations for the same set of 500 load cycles (Figure 2-19). The same general behavioural trends can be observed comparing the two different methods, though the magnitudes thereof were disparate to an extent (Figure 2-19, left). No detailed information regarding individual loading cycles were presented or compared for a particular case. Liu et al. (2015) concluded that the particle shape, angularity, elongation and surface texture exhibited different long-term settlement and acceleration behaviour when comparing two

completely different DEM test cases. If there is a lack of confinement at the edge of the sleeper, a decrease in resistance to movement will be experienced by the particles. Figure 2-19 (middle) illustrates this decrease in effective stiffness resulting in continual lateral accelerations that is observed from the SmartRock. Liu et al. (2018) successfully demonstrated the possibility of using the SmartRock platform to calibrate DEM models for improved accuracy.

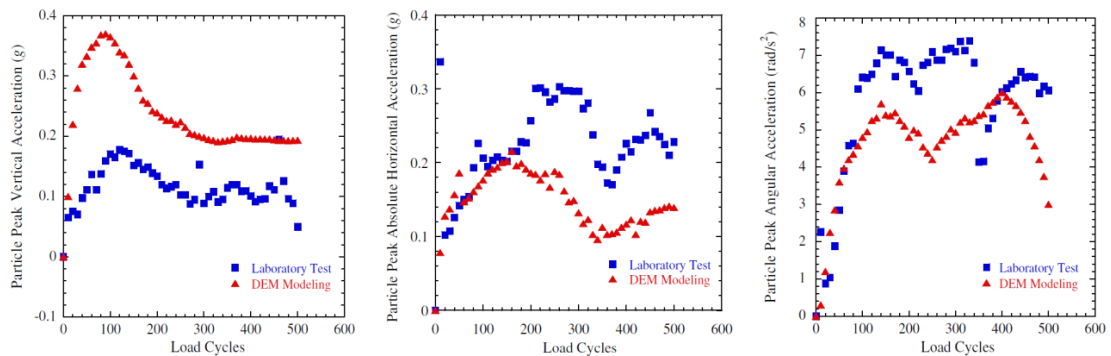


**Figure 2-19: Comparative vertical (left), horizontal (middle) and angular peak acceleration (right) measurements between laboratory testing and DEM (Liu et al., 2016a)**

## 2.6 DISCUSSION

At first glance the operational performance of ballast appears trivial in its simplicity. However, effects and principles operating over a range of dimensional scales affect the short and long term performance of the ballast and in turn, the track structure. The nature of the material itself creates difficulty in instrumenting the particles directly, with the three dimensional geometry of the track structure requiring complex numerical models. There appears to be a transition in the macroscopic behaviour after a period of compaction, beyond which particle breakage accelerates the rate of permanent strain accumulation. With the addition of fouling material, the centre portion of the ballast had an increased level of confinement with displacements predominantly in the vertical direction. This is in contrast to the shear failure sliding surface being located in the shoulder section, specifically the bottom portion of the shoulder ballast. This increased displacement along the shearing direction leads to progressive settlement. Added complexity arises from maintenance activities reducing the shear and lateral resistance up to half its original capacity.

It is clear that the vibrational characteristics of ballast, subject to dynamic loading, can be expressed as a function of both train and track geometry for both translational and rotational modes of displacement and rotation respectively. Table 2-1 summarises the most important findings from the various authors surrounding frequencies of interest. Smart ballast is able to provide information on the spread and variance of amplitudes of the vibrations. Increased horizontal accelerations / lateral movement at the edge of the sleeper accompany the larger angular accelerations as compared to the middle of the sleeper; a phenomenon that 2D DEM numerical models lack. Negligible contributions to the strength are mobilized by the crib ballast with the force chains predominantly residing below the sleeper under the trapezoidal-shaped loading zones.

The complex regime of PSR in three dimensions varies with depth, track and train geometry, soil properties and at discontinuities such as the sleeper ends as is also evident from the studies using SmartRock. The variation of principal stresses with depth illustrate that the permanent settlement cannot be expected to be uniform throughout the layer. Deformational characteristics associated with the rotation of principal stress should in theory be observable when measuring the particles at a high level of detail - a rolling, rotational motion as the shear strength is mobilized with the vertical load from the train wheel moving horizontally over the surface. The relative location of the ballast particles relative to the sleeper location will dictate the dominant directions of movement and rotation.

Rucker (1982) has already concluded that the three-dimensional half-space model is extremely difficult if not impossible to be applied in engineering for the theoretical investigation on ballast vibrations. The correlation of measured data to the calculated receptance values is one of the few methods available that can determine the ballast properties. The addition of DEM models have provided more quantitative results for various factors that affect the ballast behaviour, though this is not without limitations. More accurate representations of the particle geometry provide increased accuracy for dilating and contracting responses for DEM applications at the cost of significant increases in runtime.

**Table 2-1: Summary of analytic methods and frequencies of interest for ballast studies**

Author	Type of Analysis	Relevant Points of Interest
Zhai et al. (2004)	Field testing Analytical methods	The resonance frequency of the ballast is situated between 80 Hz and 100 Hz.
Aikawa (2009)	Field testing	High frequency, vertical translational accelerations of 300 – 400 Hz precedes the rapidly attenuated 50 – 100 Hz components.
Kouroussis et al. (2015)	Analytical methods	The first resonance frequency for vertical vibration between the ballast and the sleeper is in the range of 50 – 300 Hz.
Li et al. (2015)	Analytical methods	First fundamental frequency is between 50 Hz and 210 Hz.
Milne et al. (2016a)	Field testing	For frequencies above 60 Hz, the amplitude of ballast accelerations is larger than that of the sleeper. Again, the acceleration energy for ballast is concentrated around 80 – 120 Hz (Figure 2-14).
Liu et al. (2016c)	Laboratory testing	Only peak-to-peak measurements, indicating measured, indicating history dependant behaviour (Figure 2-18).
Zhang et al. (2016)	DEM analysis	Acceleration frequencies are concentrated not only below the 100 Hz region but also in the medium frequency range of 150 – 300 Hz ; The highest frequency spectral densities were found to correlate with the velocity of the train and the geometry (inter-axle and bogie spacing).

Currently the research focus remains on the vertical response measurements, neglecting the additional five DoF data sets that are available with the introduction of MEMS IMUs.

MEMS accelerometers have been proven to provide good conformance over a range of frequencies, from 1 Hz up to half the frequency of interest (Milne et al., 2016). The introduction of SmartRock is the first stepping stone in the instrumentation of ballast. This has however remained confined to laboratory studies with particles viewed in isolation. The focus has remained on the short term evolution of accelerations and measuring only peak values, partly due to limitations in wireless communications bandwidth and the requirement for auxiliary systems to both capture the data stream and provide electrical power. Research to date has neither investigated nor measured in detail the inter-relationship between the additional degrees of freedom for each load cycle subjected to a representative distribution of dynamic excitation. An instrument that can survive the hostilities of large dynamic forces, accelerations and adverse moisture conditions, operating for extended periods of time without any physical disturbance or interference, is desired. There is a clear need to increase the number of smart ballast particles that can provide representative track data, bridging the understanding of complex ballast performance for field conditions.

To quote Dr. Cheryl Martin's closing remarks from the IHHA 2017 conference regarding the potential of these new and disruptive technologies: *"The question is what the potential will be for the rail industry. It is no longer a question of whether there will be disruption in the industry, but the question is when it will take place and what the impact will be. There will be changes to what is being moved and who moves it."*

## **3 KLI-PI DEVELOPMENT**

### **3.1 INTRODUCTION**

This chapter discusses the developmental and calibration process of a smart ballast prototype IMU unit named “Kli-Pi”. The name “Kli-Pi” is derived from the Afrikaans word for “small rock”; conveying the key notion of a device shaped in the form of a small rock or ballast particle. Kli-Pi comprises two main components: a stand-alone internal unit containing all the necessary electronics for the IMU and the 3D printed external exoskeleton or shell, which can be easily joined together to protect the IMU when embedded in geotechnical or railway structures subjected to large forces. The software implementation and methodology used to obtain the required information and results from the raw data sets, are comprehensively presented in Appendix A.2. This chapter is chronologically structured as follows:

- Conceptual design and the desired performance characteristics
- Choice of sensor platform(s) and architecture
- IMU assembly and configuration
- Network configuration and deployment
- Calibration of the IMU
- 3D shell design and manufacturing
- Stress testing of the various components
- Conclusions

## 3.2 CONCEPTUAL DESIGN

The SmartRock concept from Liu et al. (2016) illustrates the versatility of an IMU that is designed for complete wireless operation. However, the lack of data storage on the device itself and limited sampling rate, provide the opportunity to create an improved sensor platform. For Kli-Pi, the following characteristics are required:

- Wireless operation and communication that is not dependent on auxiliary systems for data storage. The IMU should be incorporated as part of an existing peripheral hardware platform to reduce the development time and cost.
- Sufficient sampling rates for all the DoF. From the literature it is clear that ballast frequencies in the mid-range (80 – 120 Hz) are present. The Nyquist frequency provides a lower bound of 250 Hz that is required to resolve these frequencies.
- Optimized power consumption for extended battery operation. Switching the processor on and off remotely allows the Kli-Pi to remain embedded within the track structure for an extended period of time.
- Wireless charging. While the technology is still in its infancy with respect to implementation, integrating the technology in the design can enable investigation of its viability for future prototypes.
- A small physical size that should conform to the ballast gradation requirements, i.e. passing through a 73 mm sieve size (Transnet Freight Rail, 1998).
- The combination of the IMU and surrounding 3D printed shell should be strong enough to withstand the inter-particle forces. Protection against dust and moisture penetration should form part of the material selection and geometry in the design of Kli-Pi.

## 3.3 SENSOR PLATFORM

With the rapid pace of technological development and reduction in the effective cost of computing, a number of small, commercially available computer platforms have been developed during the last decade. The Arduino microcontroller and Raspberry Pi microcomputer in particular have transformed the way individuals can access powerful resources at a small cost without requiring advanced engineering or technical skills. The computing platforms are largely differentiated by their level of performance: the Arduino is a power efficient microcontroller with application for small, embedded projects. The Raspberry Pi caters for projects requiring more computer resources and runs a dedicated Linux distro as the operating system (OS). Alongside the hardware exist active communities

dedicated to improving both the hardware and software functionalities, extending and modifying the platforms for their own needs or projects. These expansion boards are commonly referred to as “shields” that extend and add additional functionality to the platform. Pin-compatible interconnections stack the boards vertically in a series configuration, increasing only the volume and not the footprint of the system.

Recently, the distinction between these discrete groups has become vague; Arduino provides a variety of products with both microcontrollers and microcomputers coexisting. The Raspberry Pi foundation has led efforts to the development of a smaller board (Zero) for the cost of \$5 aimed at embedded applications. The challenge in developing the Kli-Pi is choosing the platform that best fits the project requirements. From the literature it appears as though most authors have opted for microcontroller systems that are small and power efficient, with limited functional capabilities regarding the attainable sampling rate. Kli-Pi requires a platform with a small footprint with shields that can add additional storage space for data, a 9 DoF IMU sensor and the capability to condition the power received from a rechargeable battery. Even though Bluetooth offers lower power requirements than Wi-Fi, the bandwidth and ease of interface for a small sized network outweighs the disadvantages. At the time of writing, the combination of availability, cost and speed of software development positioned the Intel Edison platform as the most suitable and viable choice for the project. The Edison platform (Figure 3-1) is a combination of a microcontroller and microcomputer system on chip (SoC) in a small form factor ( $35\text{ mm} \times 25\text{ mm} \times 4\text{ mm}$ ) with the flexibility of supporting either the Yocto Linux or Ubinlinux distro as the OS. The primary hardware specifications of importance are as follows (Intel, 2016):

- CPU: Intel Atom, 32-bit, 500 *Mhz*, dual-core, dual-thread
- MCU: Intel Quark @ 100 *Mhz*
- RAM: 1 *Gb* LPDDR3 POP
- Storage: 4 *Gb* eMMC (embedded Multi-Media Controller) Flash
- Communication: Wi-Fi: 802.11 *a/b/g/n*, 2.4 *GHz* & 5 *GHz* | Bluetooth 4.0
- Power supply: 3.3 – 4.5 *V* (100 *mA* @ 3.3 *V* & 100 *mA* @ 1.8 *V*)
- GPIO: 40 pin interface supporting: UART, I2C, I2S, SPI, USB 2.0 & SD card storage
- Connector: Hirose DF40 series

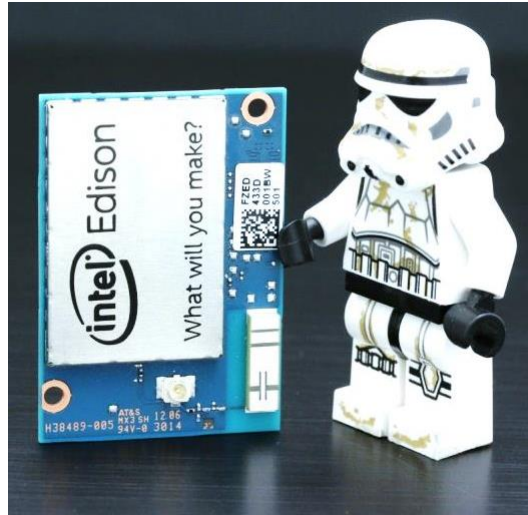


**Figure 3-1: Intel Edison placed next to a LEGO figurine for size comparison (Yoctopuce, 2015)**

SparkFun, an online hobbyist store specializing in electronics that is based in the United States (Boulder, Colorado), supplies both the Intel Edison and develops the shields as part of their product range. The shields connect in a vertical formation with 2 *mm* standoff screws providing structural rigidity. For Kli-Pi, the following shields were incorporated:

- Battery shield: an interface managing the power distribution to the rest of the platform, with the option of adding a rechargeable lithium-ion polymer (LiPo) battery. A micro-B USB connector allows for power delivery and serial communication to a computer.
- SD card shield: a standard microSD card interface accommodating mountable storage for expansive, non-volatile data storage.
- 9 DoF shield: the heart of the instrument – a LSM9DS0 9 DoF MEMS IMU sensor orthogonally aligned to the shield.

### 3.4 IMU ASSEMBLY AND CONFIGURATION

The IMU sensor (STMicroelectronics, 2013b) features the following specifications for the respective tri-axis sensors:

- Accelerometer:  $\pm 2, 4, 6, 8, 16 G$  | 1600 Hz maximum sampling rate / axis
- Gyroscope:  $\pm 245, 500, 2000 \text{ }^\circ/s$  | 760 Hz maximum sampling rate / axis
- Magnetometer:  $\pm 2, 4, 8, 12 Gauss$  | 95 Hz maximum sampling rate / axis
- Integrated 16-bit ADC

An I2C communication protocol simplifies the interface for a variety of programming languages and sensors alike. The I2C bus supports a 400 kHz bandwidth allowing for sufficient data transfer speeds from the sensors to the processor. For this project, the software development was restricted to Python for both data acquisition and processing. All the acquired data is initially stored in the random access memory (RAM) before being transferred to the SD card. Should the IMU unit be either damaged during testing or disconnected from the power supply, the data stored on the SD card has a high probability of recovery. A suitable enclosure had to be selected that would protect the electronics, allow for the transmission of 2.4 GHz communications, resist penetration of water and dust and integrate the wireless charger and battery.

#### 3.4.1 External Enclosure

A rectangular, 3 mm thick general purpose ABS enclosure, measuring 40 mm  $\times$  56 mm  $\times$  81 mm in size, provides adequate space and mounting rigidity for all the components. The enclosure is designed for limited protection against dust and splashes of water from any direction (Ingress Protection 54 rating). To attach the Edison platform to the bottom of the enclosure, a suitable mounting bracket was designed using Blender, an open source suite of animation software. A MakerBot Replicator served as the 3D printed using PLA (Polylactic acid) filament. The bracket is glued to the enclosure, with the four standoff screws secured in the corresponding mounting holes (Figure 3-2). A small pedestal protrudes from the bracket directly underneath the IMU IC. The narrow 1.8 mm space provides enough clearance for a 2 mm piece of aluminium, measuring 10 mm  $\times$  10 mm in size, to securely make contact with the IMU IC. A small amount of thermal compound was applied at the contact interface. This configuration restricts the IMU from vibrating and lowers the thermal variance, significantly

reducing thermal noise. The combination of the proximity of the IMU sensor to the centre of mass of the Kli-Pi, together with the small angular velocities recorded in subsequent tests, ensures that centripetal acceleration can be considered arbitrarily small when compared to the performance of the sensor.

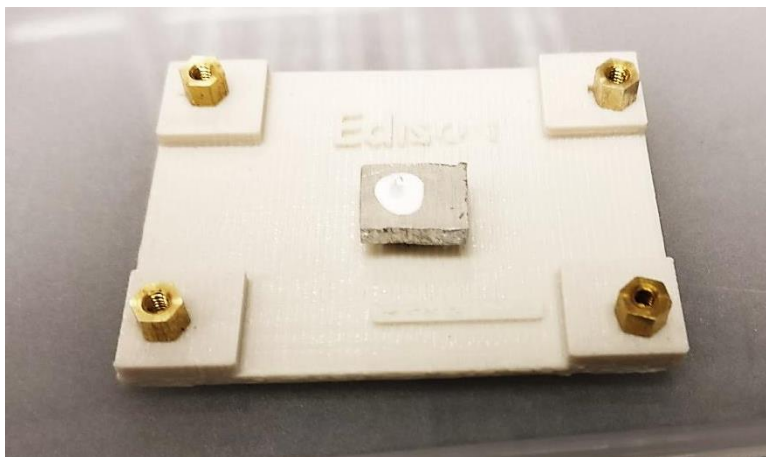


**Figure 3-2: Assembly of the mounting bracket and Intel Edison platform**

### 3.4.2 Power Source

Rechargeable LiPo batteries provide high power densities, various form factors, a wide range of operational temperature ranges, built-in short circuit protection, a satisfactory number of recharging cycles and are relatively inexpensive. Due to limited stock availability, two 1000 *mAh* cells were wired in a parallel (1S2P) configuration to provide an effective 2000 *mAh*, 3.7 *V* battery. The battery shield provides a constant recharging current of 500 *mA* for an effective 4 *h* recharging time. The introduction of wireless induction charging methods had limited success due to the distance between the transmission coil and the enclosure material. Wireless induction remains limited to a small separation distance between the coils for sufficient coupling to be realised. The Edison itself requires only 500 *mW* of power on average in an idle state. The maximum runtime is approximately 12 *h* with the Wi-Fi enabled, which is sufficient for laboratory and short-term testing. For extended periods of time over days or weeks, periodically retrieving the Kli-Pis for recharging remain impractical. Wireless power transmission over the distance of a few meters is not (yet) possible, thus some form of low power auxiliary battery control system is required.

### 3.4.3 Auxiliary Power Control

As mentioned, Arduino is a popular platform among hobbyists for its ease of use, versatility and low cost. Even the smallest of standard format Arduino products will be physically too large to fit alongside the Edison platform in the enclosure. Arduino is however an open source platform whereby anyone is able to access the circuit designs and the ability to manufacture their own PCB. The company TinyCircuits based in the United States (Akron, Ohio), designs and manufactures their own version of the Arduino UNO called the TinyDuino. The PCB footprint measures  $20\text{ mm} \times 20\text{ mm}$  in size, with a complete stack of 4 shields measuring  $15\text{ mm}$  tall (Figure 3-3). The TinyDuino platform used for Kli-Pi consists of the following shields:

- Processor shield: an AVR ATmega328p microcontroller (8 MHz clock speed, 2 kb of SRAM and 32 kb of Flash storage) with support for a 2.7V – 5.5 V rechargeable battery.
- Programming shield: the USB-to-serial IC controls the communications between the integrated development environment (IDE) and the microcontroller. This enables the bidirectional data transfer and flashing of new firmware, also referred to as sketches.
- Bluetooth shield: the Bluetooth Low Energy (BLE) shield facilitates wireless, power efficient, bidirectional communication using the Bluetooth 4.0 protocol.
- Proto shield: ideal for prototyping and interfacing with other devices, this shield exposes all the general purpose input/output (GPIO) and power supply pins.

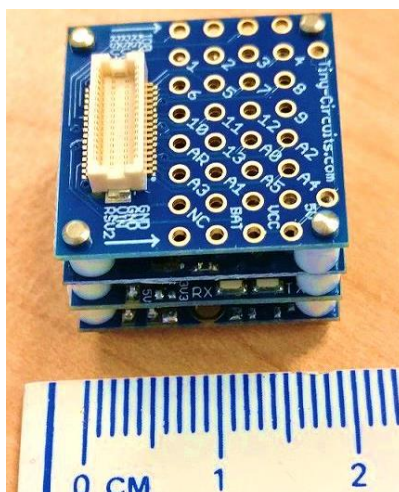


**Figure 3-3: TinyDuino stack with the proto shield visible**

The Arduino IDE software is compatible with the TinyDuino allowing seamless integration with existing programming services. The required software libraries to interface with the BLE shield are provided freely on GitHub. The IC (nRF8001) that controls the Bluetooth communication is manufactured by Nordic whom also supplies a complimentary Android and iOS application. Simple text commands can be sent through the application that toggles the GPIO pins and relays information back to the user. The digital pins control a power switch IC (AP22802) that relays power to the Edison stack. Appendix A.9 provides a schematic of the electrical configuration. A simple application interface was configured with additional features for the user (Figure 3-4):

- On/Off: toggles the power enable pin on and off that in turn connects or disconnects the power to the Edison platform.
- State: provide the power state feedback on whether the power enable pin is currently high or low (on or off).
- Battery Voltage: measure the current battery Voltage to estimate the battery charge remaining. Although the accuracy can only be specified to within 10%, this nonetheless provides an indication of the recharging process of the battery or a possible electrical short.
- Timer: a periodic on/off command after a predetermined, user-specified period of time has passed.

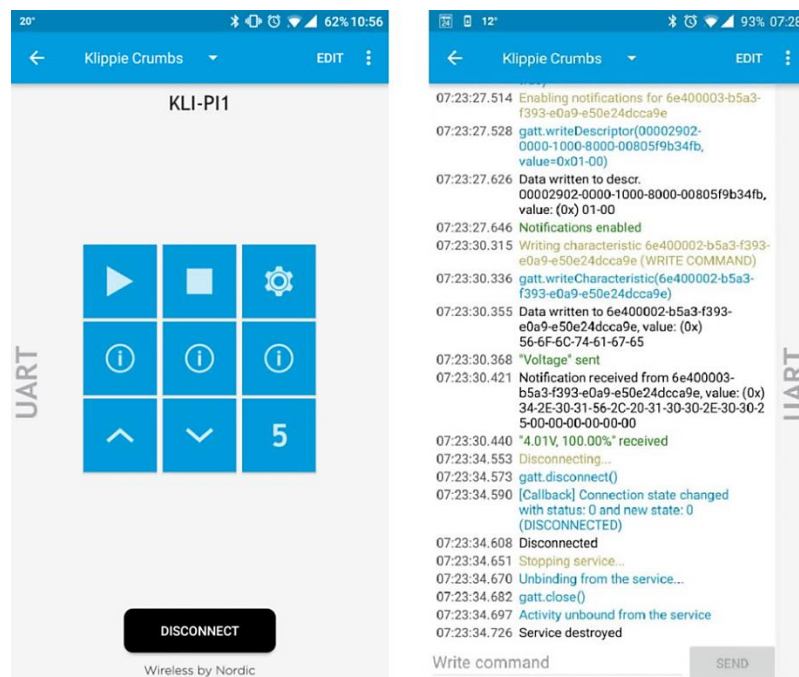


**Figure 3-4: Nordic application facilitating communication with the TinyDuino**

The TinyDuino is configured to default to a power saving state when not processing any commands received from the Bluetooth interface. The Bluetooth connection remains active even in this configuration as the Bluetooth module is controlled by an independent microcontroller. In this configuration, the current consumption as measured from the battery terminals is  $400 \mu A$ . Accounting for minimum operating Voltage levels and self-discharge of the battery, a standby time of 3 months for a Kli-Pi prototype unit was achieved. This dextrous combination of operating and standby capacities exceeds the functional requirements. With an adequate regime of battery management where only periodic measurements are recorded, an extended, in-situ installation is viable.

#### **3.4.4 Software Configuration**

The Edison is preinstalled with the Linux Yocto distro. After the Edison is powered on, the default root user account is accessed through a serial terminal. For easy network access, the default network AP credentials are configured (Chapter 3.5). Every time the power supply is cycled for the Edison platform, through the TinyDuino, the Linux OS boots the system along with the requisite configuration files – this only occurs once by default, including any attempt to connect to the default network AP. To ensure connectivity regardless of the AP status, a daemon service was created to ensure that the network manager scans for the network every 30 s. The daemon is configured as a start-up service.

After a successful connection is established with the wireless network, the Edison can initiate a user defined script to configure and record data from the IMU. A simplified Python script interfaces with the IMU and configures the required registers, setting the sampling rate and full scale. Using Python, a maximum of 3,000 data samples per second can be recorded to the RAM in the form of an array. This capacity is divided among the sensors such that the data from each axis of the accelerometer and that of the gyroscope is sampled at 500 Hz each. After the predetermined number of samples has been captured, the data is stored in a comma separated variable (CSV) file on the SD card for post processing.

### 3.5 NETWORK CONFIGURATION AND DEPLOYMENT

For a scalable system that can accommodate additional Kli-Pis, the design and deployment of a simplified computer network becomes a necessity. System services are implemented that initiates during the boot process, configuring the communication interfaces and network settings automatically. The Kli-Pi interface is configured to operate in either:

1. Access Point (AP) Mode, whereby the user connects to the Wi-Fi hotspot established by the Edison. Only a single Kli-Pi can be connected to a computer or smartphone at any one time. This works well for demonstration purposes.
2. As a client device, where the Edison connects to a preconfigured AP. The number of Kli-Pis in the network is limited by the AP. A maximum of 255 Kli-Pis can be connected using a standard network address scheme.

From experience gained with laboratory and field testing, the latter configuration was preferred. The network should be accommodating to the typical field conditions that can be experienced – inclement weather such as high daytime temperatures, rain and dust and lack of reliable electrical power. The Kli-Pis themselves were placed in close proximity to one another, owing to the track geometry. From a safety perspective, the user should be situated a safe distance away from the track without any of the hardware interfering with train operations. The Kli-Pis require a centralized AP, with its own dedicated electrical power source and environmental protection, in close proximity to the track through which the Kli-Pis can connect to the network. The AP in turn is accessed by the user using an Ethernet cable some distance away with either a tablet or laptop computer. The AP assigns static internet protocol (IP) addresses to the each of the Kli-Pis based on the MAC address, uniquely identifying each device in the network. For the purposes of this project, no consideration is given to the integration of internet or cloud based services. The proposed network is visually illustrated in Figure 3-5. The IP configuration and access credentials are provided in the appendix (Appendix A.8).

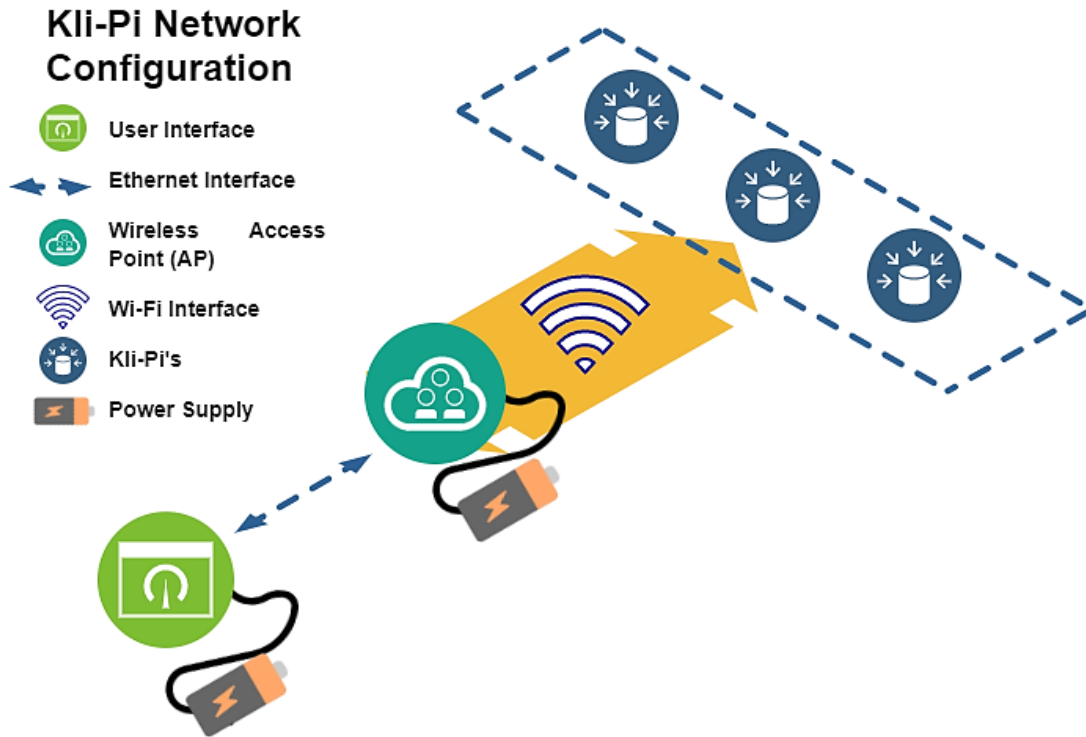


**Figure 3-5: Proposed network interface, configuration and deployment.**

### 3.5.1 User Interface

Both the user interface and the wireless AP are adapted for the Raspberry Pi 3 platform. The small size and 5 V power interface makes it ideal for powering the devices from a low cost power bank typically used for smartphones. For modular mobility, the Raspberry Pi platform is paired with a touchscreen and protective case for the user interface (Figure 3-6). Combined with a 10,000 mAh power bank, 18 h of continuous operation is viable with a combined power consumption of only 1.5 W. The user interface is configured with a static IP address that falls within the same local area network (LAN) as that of the AP. The Ethernet cable connects directly both the user interface and the AP. From the user interface a secure shell (SSH) connection is established with the AP that is configured with its own static IP. This in effect gives direct access to the array of Kli-Pis as though the user is directly interfacing with the AP.

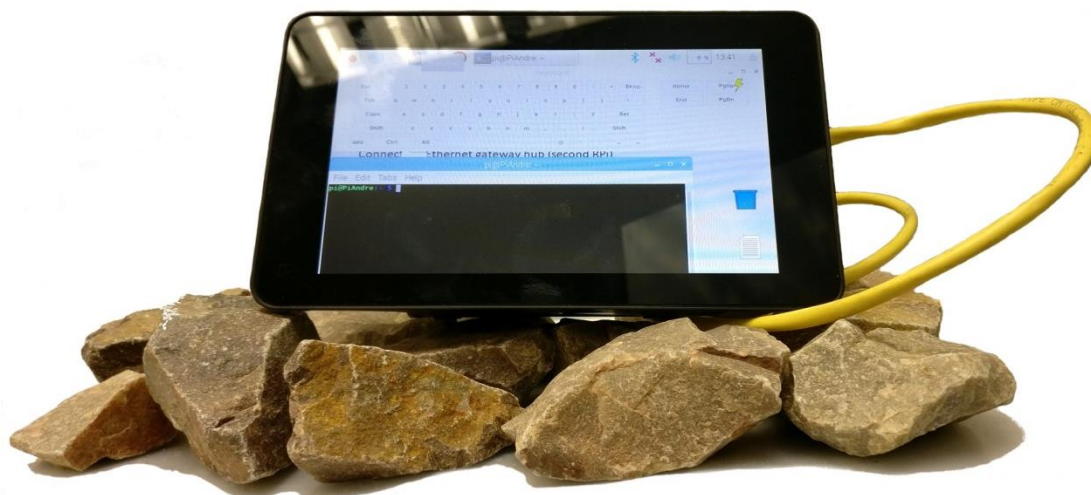


**Figure 3-6: Raspberry Pi user interface controller with visible Ethernet cable**

### **3.5.2 Access Point**

The AP provides a direct connection to communicate with the Kli-Pi (Figure 3-7). The AP is configured to assign static IP addresses to the array of Kli-Pis based on the unique MAC address associated with each device's Wi-Fi controller. For enhanced security and ease of access, certificate authentication is implemented that allows for the execution of commands directly from the AP without the need to provide user credentials. Parallel SSH (PSSH) allows for sending an identical command, initiating the recording of data in this situation, to all the devices on the network. It should be noted that this method does not ensure time synchronisation among the devices; post processing is required to align the data along the time axis. The AP is housed in a small plastic enclosure, placed in an inverted orientation as to allow any precipitation to run off. Adequate space is provided to place the power bank with adhesive to the inverted floor of the enclosure. The container is securely placed on the surface of the ballast in close proximity to the Kli-Pis to ensure a stable Wi-Fi connection is established and maintained. Even though it is possible to directly interface with the TinyDuino BLE through the Raspberry Pi AP, software inefficiencies dictate that the smartphone application is better suited for this aspect.



**Figure 3-7: Raspberry Pi access point with visible Ethernet cable and a rechargeable USB power supply**

### **3.6 CALIBRATION OF THE IMU**

MEMS devices are subjected to a wide range of environmental and intrinsic error sources. Bias stability, scale factors, temperature sensitivity, nonlinearity, intrinsic noise, axis misalignment, hysteresis, self-heating, resistor noise, electromagnetic interference and ADC clock jitter are the main sources of errors (Zaiss, 2012). Each error can be largely eliminated with its own calibration procedure. Even though the list of shortcomings and technical difficulties seem daunting when designing a high performance instrument, various simplifications and measures can be applied. The largest sources of errors – non-unity scale factors, bias and cross axis sensitivity - are the only errors addressed in this study. Temperature effects are minimized as part of the instrument design process (Chapter 3.4.1).

Traditional calibration procedures for IMU sensors require a specialized mechanical platform, comparing the measurements to highly accurate inertial gyroscopes and a calibrated gravitational field. Skog & Händel (2006) describe a general framework for calibrating a low-cost IMU where the need for a mechanical platform to accelerate the sensor platform is not required. A cost model or function is formulated to acquire the vector of unknown coefficients through Newton's Method. The derivation of the calibration procedure, the calibration procedure itself and the accuracy and noise characteristics of the IMU (Broekman, 2017a) are discussed in detail in Appendix A.1. The calibration validation is discussed in Chapter 3.6.1.

### 3.6.1 Calibration Validation

Both the accelerometer and gyroscope were assessed for both static and dynamic excitation. For the static test, the IMU was orientated in 50 random configurations and the static gravitational acceleration recorded (Figure 3-8). The gravity vector is calculated using Pythagoras’s Theorem to account for all the components of the measured acceleration vector about the axes. Table 3-1 illustrates how the implementation of the calibration factors improves the accuracy and minimizes the variance when taking measurements. The calibrated mean value is situated substantially closer to the true gravitational vector with the standard deviation reduced by nearly 90%.

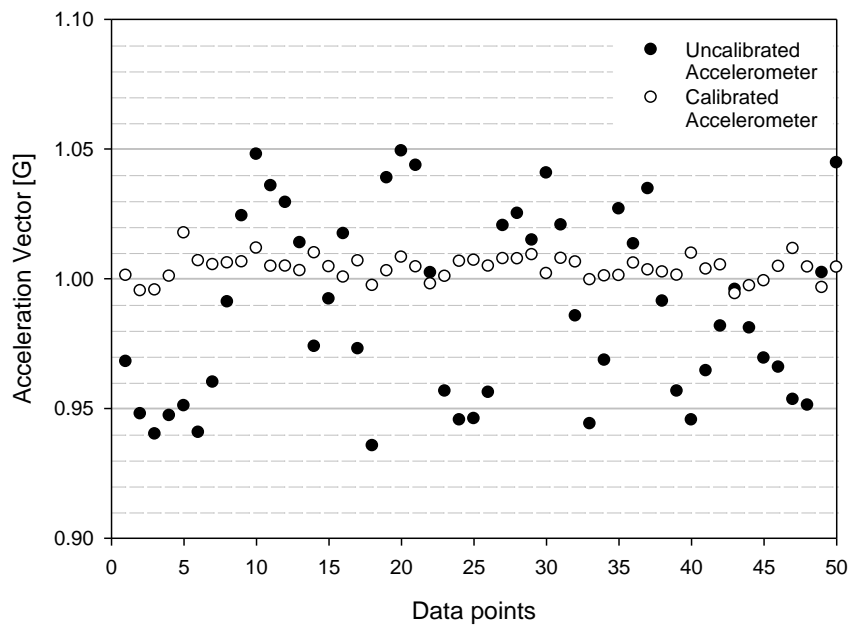


Figure 3-8: Calibration of the IMU tri-axis accelerometer for 1 G acceleration

Table 3-1: Comparison between the calibrated and uncalibrated IMU accelerometer

Parameter	Uncalibrated [G]	Calibrated [G]
Minimum Value	0.936	0.994
Maximum Value	1.049	1.018
Mean	0.989	1.004
Standard Deviation	$35.88 \times 10^{-3}$	$4.643 \times 10^{-3}$
Accuracy	$64.43 \times 10^{-3}$	$5.883 \times 10^{-3}$
Coefficient of Variance	$36.30 \times 10^{-3}$	$4.624 \times 10^{-3}$

To fully calibrate the accelerometer for dynamic excitation, two aspects require consideration: the first, applying the new calibration factors; the second, determining the appropriate frequency spectra that define the dynamic range of the instrument as discussed by Milne et al. (2016b). A small scale laboratory box test was utilized for this purpose (Figure 3-9) measuring 1200 mm long, 650 mm wide and 300 mm deep. The IMU was fixed to the sleeper with epoxy glue with a corresponding LVDT functioning as the reference for measuring the true displacement. As part of the data post processing and analysis procedure, discussed in Appendix A.2, a Butterworth bandpass filter was implemented to remove the unwanted frequencies and any DC bias. As noted by Milne et al. (2016b), a lower and upper bound of 0.8 Hz and half the sampling frequency respectively, produced the most accurate measurements. By comparing the deflection data of the LVDT to the IMU accelerometer, the optimal selection of cut-off frequencies can be determined. Using a 500 kN capacity hydraulic actuator with an applied cyclic force of 90 kN, a wide range of frequencies was investigated as summarised in Table 3-2. Each frequency corresponds to a corresponding train velocity depending on the train's geometry. For each frequency the cyclic load was applied over a 10 minute period. To compare displacements with one another, the accelerometer acceleration was calculated through numerical double integration using a second order Lagrange polynomial (Appendix A.3).



**Figure 3-9: Box test configuration with the IMU (center) and the LDVT (left, not shown) bracket**

**Table 3-2: Frequency selection for calibration and validation of the accelerometer**

Frequency [Hz]	Effective Train Velocity [km/h]	Load Cycles
1	7	300
2.5	17	1500
4	26	2400
6	40	3600
9	60	5400
12	80	7200

Both the displacements, as measured by the LVDT and the IMU, can be compared for a single, representative loading cycle at a specific frequency (Figure 3-10), as outlined in Table 3-2. A bandpass filter of 4 Hz – 200 Hz for the acceleration data was found to be the most accurate over the range of loading frequencies tested which also eliminates the low frequency bias and drift. From the graph it is clear that the displacements are nearly identical for both instruments for frequencies higher than 6 Hz over the entire loading cycle. Frequencies between 4 Hz and 6 Hz produced acceptable correlations with underestimation of the deflection becoming prevalent, even though this frequency was at the cut-off frequency of the filter. For frequencies below 1 Hz, insignificantly small accelerations were measured. This is in part due to the performance limitations of the sensor. The implications of these results are related to the train velocities above which the measured data will be representative of the ballast dynamics. For train velocities exceeding 26 km/h, producing dominant frequencies above 4 Hz, an accurate representation of the accelerations is measured since the dominant frequencies are above the lower bound threshold of the bandpass filter. The accuracy for each discrete frequency can also be expressed as the deviation of the deflection, either as an under- or overestimation, compared to the LVDT (Figure 3-11). Again, small differences are observed for the higher frequencies compared to the lower frequencies. The level of underestimation of the true deflection increases with a decrease in frequency. These results are in agreement with that of Milne et al. (2016b).

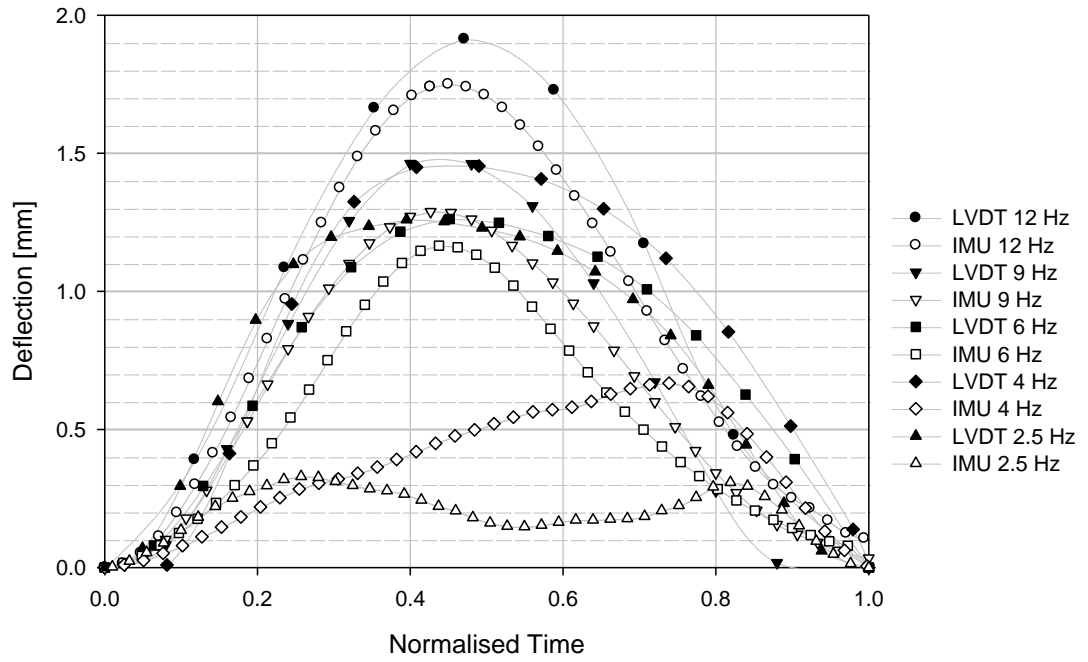


**Figure 3-10: Frequency dependent load cycle deflection comparison between the LVDT and the IMU**

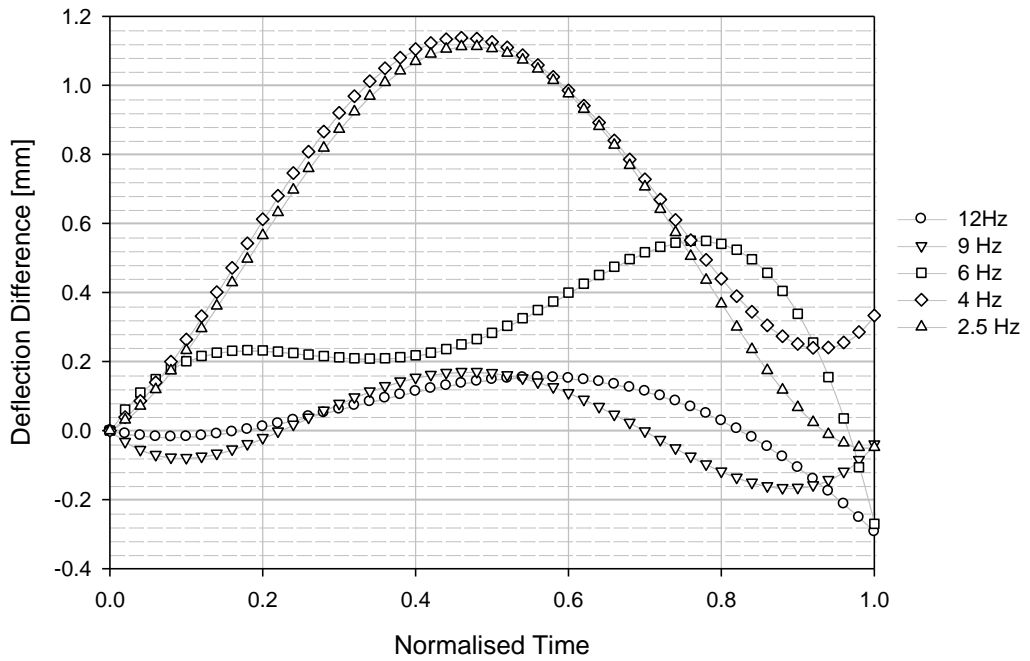


**Figure 3-11: Frequency dependent deflection differences between the LVDT and the IMU**

For the gyroscope a range of dynamic measurements were compared using a digitally controlled lathe (HAAS TL-1). Each of the three axes of the IMU was aligned parallel to the axis of rotation of the lathe. A total of four rotational velocities were investigated - 10, 30, 60 and 80 rotations per minute (RPM) – which is within the FS range of 500 degrees per second (DPS) used for field testing (Broekman, 2017a). The constant velocity provided by the lathe was compared to the values reported by the IMU, both with and without the calibration factors applied (Figure 3-12). With the calibration factors applied, the measured values reflect both an increased accuracy and a mean that is situated closer to the true value, compared to the uncalibrated measurements. This can be attributed to the adjustment of the non-unity scale factors of the  $E_{g1}$  matrix (Appendix A.1.3). Compared to the accelerometer, the adjustment of the scale factors for the gyroscope are significantly higher.

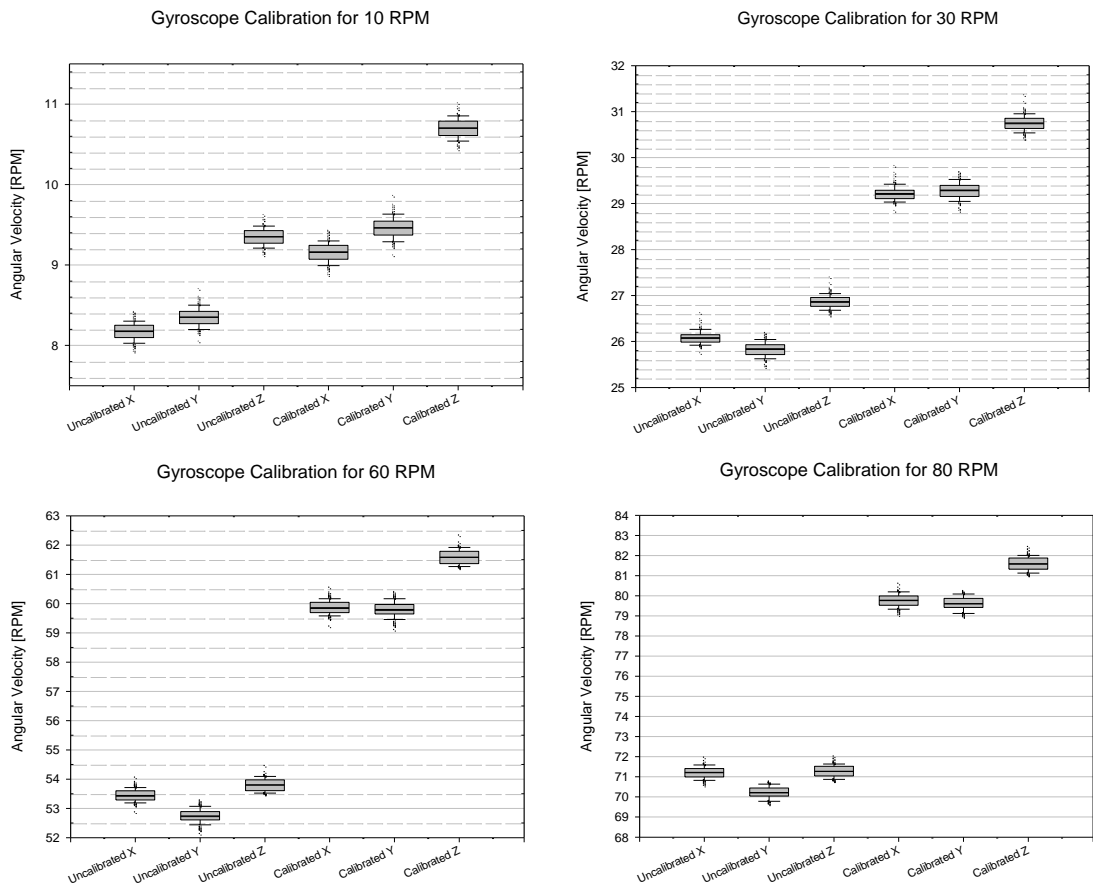


**Figure 3-12: Calibration of the IMU tri-axis gyroscope for varying angular velocities**

### 3.6.2 Accuracy and Noise Characteristics

For any transducer not subjected to any form of excitation, electrical and thermal noise will produce random variations. Depending on the performance and application of a given instrument, the level of noise limits the degree of accuracy which can be achieved. Similarly, the noise characteristics of the IMU can be determined under static conditions by recording measurements with the hydraulic actuator powered off. Using a 95% confidence interval for a sample comprising of 30,000 measurements, the accuracy for both the accelerometer and gyroscope are quantified for each respective axis (Table 3-3). The derived parameters obtained through integration methods are formulated in the same manner.

**Table 3-3: Summary of the IMU accuracy for measured and derived parameters**

IMU Parameter		Axis		
		X	Y	Z
Accelerometer	Acceleration [m/s <sup>2</sup> ]	$\pm 106 \times 10^{-3}$	$\pm 153 \times 10^{-3}$	$\pm 220 \times 10^{-3}$
	Velocity [m/s]	$\pm 973 \times 10^{-6}$	$\pm 1.08 \times 10^{-3}$	$\pm 2.14 \times 10^{-3}$
	Displacement [m]	$\pm 24.2 \times 10^{-6}$	$\pm 21.2 \times 10^{-6}$	$\pm 51.6 \times 10^{-6}$
Gyroscope	Velocity [deg/s]	$\pm 714 \times 10^{-3}$	$\pm 770 \times 10^{-3}$	$\pm 642 \times 10^{-3}$
	Attitude [deg]	$\pm 5.18 \times 10^{-3}$	$\pm 5.76 \times 10^{-3}$	$\pm 4.64 \times 10^{-3}$

### **3.7 3D SHELL DESIGN AND MANUFACTURING**

The IMU on its own does not provide the representative surface friction, angularity or the interlocking potential of ballast. With the electronics firmly glued to the inside of the enclosure, the addition of a secondary layer of protection acts as a sacrificial barrier providing additional strength, wear resistance and irregular, angular geometric features. Using Blender, a suitable shell was designed for the desired functionality and manufacturing technologies available.

#### **3.7.1 Shell Design (Blender)**

Blender is suited for the modelling of the required features and details of the shell around the enclosure. The enclosure is represented as a hexahedron with the corresponding measurements and the shell as an icosphere (simplicial polytype). The chosen rectangular geometry is similar to that of the internal enclosure to minimize the total volume of the final instrument. A smaller sensor platform and power source will allow for a smaller and more organic ballast shape. The icosphere with its vertices is iteratively scaled, adjusted and subdivided to completely surround the enclosure with a sufficient thickness, integrating both convex and nonconvex geometrical features. The enclosure geometry is subtracted from the shell to create the required void for the IMU. The shell is divided in half with a cut and groove profile providing a frictional interlock mechanism. The orientation axes, unit number and any other additional text and features are subtracted (etched) from the face of the shell (Figure 3-13). These recessed features are less prone to abrasion and wear. The final shell design is corroborated to conform to the manifold requirements before a digital file is exported for 3D printing. The digital nature of the design procedure allows for additional numerical and FEM analyses of the mechanical strength and behaviour.

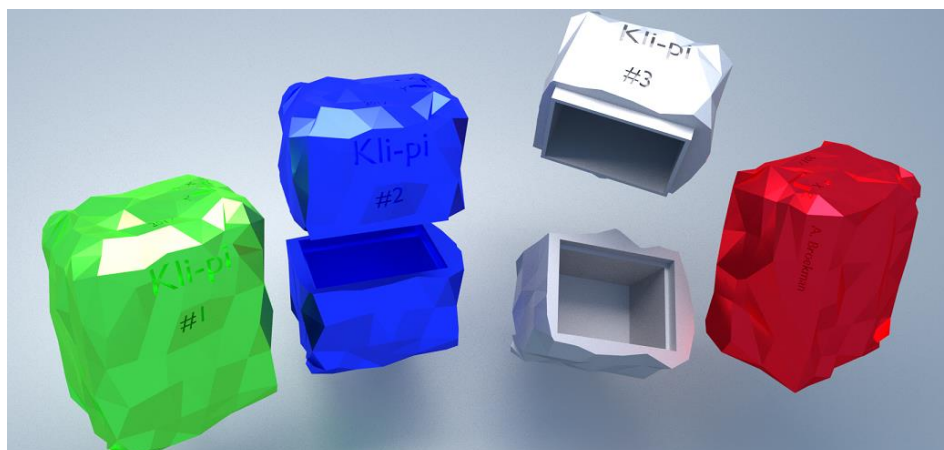


**Figure 3-13: Blender design of the Kli-Pi shell**

### 3.7.2 3D Printing

Additive manufacturing technologies are uniquely suited for the creation of intricate and complex geometries in addition to the lower cost and development time. 3D printing was chosen not only for its suitability to produce the desired geometry, but also the material properties. Kli-Pi's implementation of wireless communication requires minimal attenuation of the electromagnetic radiation through the surrounding material. The selection of PLA provides suitable transmission properties and mechanical strength. The stress-strain response is characterized by an anisotropic, non-linear, viscoelastic response relationship that varies with age and exposure to moisture (Bergstrom et al., 2013). Even though the material does soften slightly in the presence of water, the yield strength remains largely unaffected. The strength and Young's modulus of the PLA is in the order of 40 MPa and 1 GPa respectively with a glass transition temperature above 60°C. The following colour scheme (Figure 3-15) was employed for the 4 Kli-Pis used in the experimental work (Chapter 4):

- Kli-Pi 1: Blue
- Kli-Pi 2: Grey
- Kli-Pi 3: Green
- Kli-Pi 4: Red

The Ultimaker Cura software package was used for slicing the model, whereby the digital model is reconstructed using a large set of numerical control (NC) operations. The 3D printer fabricates the model by depositing the heated plastic filament in successive layers. For the shell, a triangular infill pattern provides a truss-like structure for increased rigidity and minimizing the amount of raw material required (Figure 3-14). The outer shell, measuring four layers thick, provides increased resistance against puncturing from the adjacent ballast. Through experimentation, the optimal printing scale was found to be 102.5% , accommodating the thermal shrinkage and non-uniform deposition of material, in addition to providing an interference fit with the IMU enclosure. All four shells were printed at the University of Pretoria’s Makerspace (Broekman, 2017b) on a RoboBeast PLA printer, using filament manufactured by Wanhao. The assembled Kli-Pi prototypes are illustrated in Figure 3-15. Each Kli-Pi can be uniquely identified by its colour to avoid incorrect order and can also be corroborated with photographs after testing has taken place. The total mass of the shell and the IMU together is 400 grams. This value is used as the mass for the mechanical energy calculations (Chapter 5.2).

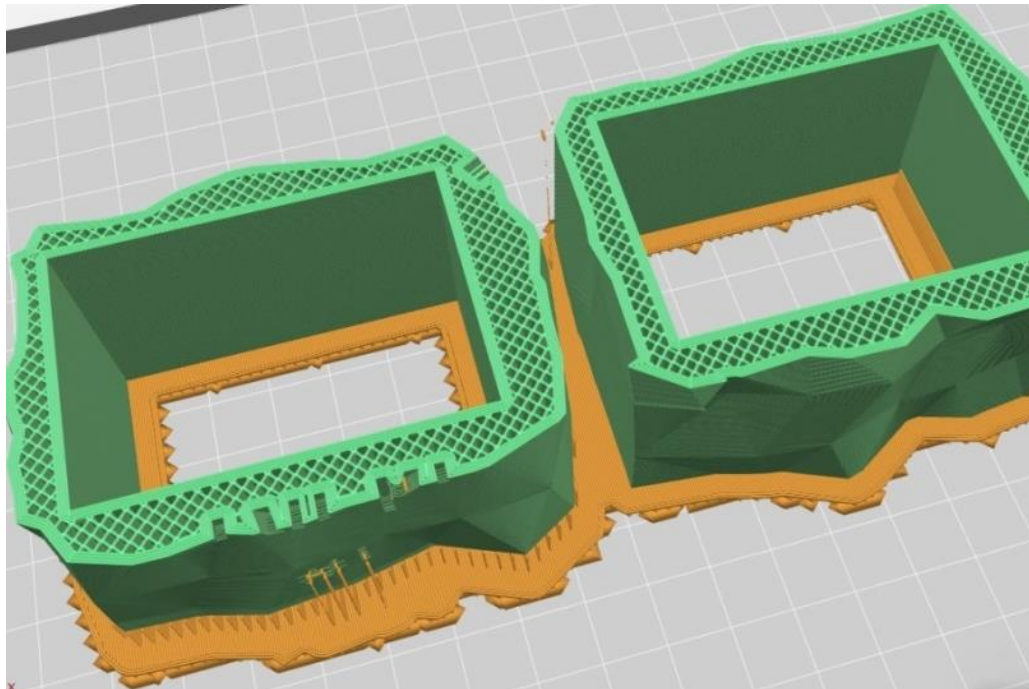


**Figure 3-14: MakerBot print preview of the internal shell structure**



**Figure 3-15: Four assembled Kli-Pi instruments used for the experiments**

### **3.7.3 Coordinate Frame**

For any orientation of the IMU, the gravitational vector can only be used to align the body and global frame's z-axis parallel to one another. However, due to the strong magnetic field associated with the electrified track, the IMU's magnetometer cannot be used to fully align the body and global coordinate frames. During installation the shell is used as a reference to align the yaw-axis ( $xy$ -plane) with respect to the track or global frame. The body frame coordinate system followed during the installation and experimentation process is as follow:

- Longitudinal | parallel to the direction of the rails |  $x$ -axis or roll ( $\phi$ )
- Lateral | parallel to the long axis of the sleepers |  $y$ -axis or pitch ( $\theta$ )
- Vertical | parallel to the gravitational vector |  $z$ -axis or yaw ( $\psi$ )

### 3.8 STRESS TESTING

Any instrument should be designed to withstand the most enduring and extreme environmental conditions that can occur. Concentrated point loads within the ballast matrix, moisture and extreme levels of acceleration are relevant for this study. The choice of PLA for the shell ensures that no brittle fractures or punctures occur, owing to the large degree of elasticity. One top half of the shell, with the top and bottom polished perpendicularly using a circular saw, was subjected to static loading. The results corroborated the findings of Bergstrom et al. (2013) regarding the mechanical properties of the PLA (Figure 3-16). Even though the distinction between the elastic and plastic deformation is not clear, linear-elastic behaviour is observed for a force in excess of 30 *kN* for a strain of 4%. For a strain exceeding 6%, the material exhibited plastic strain with no significant fractures or cracks visible. The test was terminated at a strain of 16% with no excessive cracking or brittle failure visible.

For short term monitoring applications, both the enclosure and the shell should provide penetration resistance to precipitation from both the surface and the subballast. During field testing, intensive rain storms saturated the fouled ballast to the extent that one of the Kli-Pis was submerged underneath 150 *mm* of water for a period of one hour. The shell provided sufficient protection with the enclosure emerging dry after the shell had been removed. This scenario also illustrated the inability of the communication signals to penetrate through the water as the signal radiation is absorbed. In addition to the field testing, the IMU was subjected to a continuous acceleration of 50 *G* over the period of an hour in a geotechnical centrifuge (Jacobsz et al., 2014) to assess the resilience of both the instrument and the MEMS IMU.

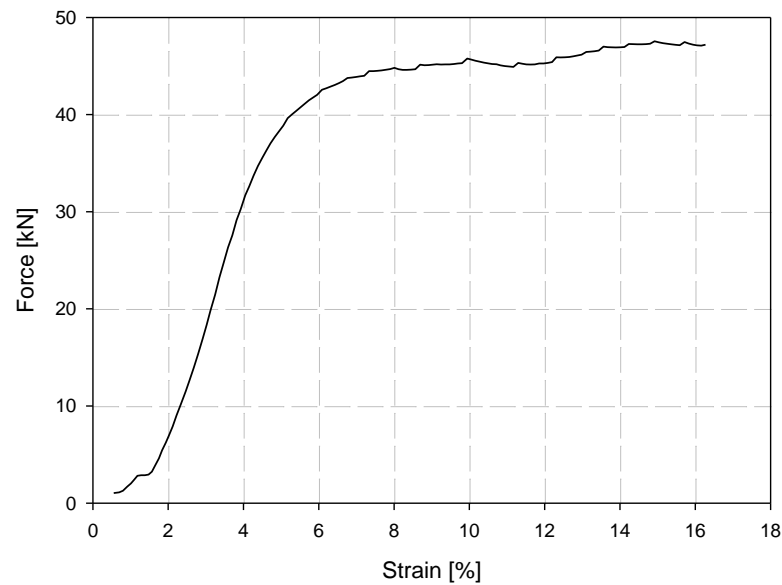


**Figure 3-16: Force-strain relationship for the shell subject to uniaxial, static loading**

### 3.9 DISCUSSION

This chapter discussed the design methodology, design, construction, calibration and field testing of Kli-Pi, a smart ballast prototype. The desired performance characteristics and functionality were incorporated as part of the design methodology to meet the objectives set out during the conceptual design phase. The performance characteristics of Kli-Pi was methodically tested, quantified and compared with traditional instrumentation to develop a high-performance instrument capable of measuring the dynamic response of ballast under both laboratory and field conditions (Broekman, 2018). With the Kli-Pi prototypes and peripheral systems configured and calibrated, field testing and experimentation as set out in Chapter 4 was conducted using Kli-Pi. Analysis and discussion of these measurements are discussed in Chapter 5.

## 4 EXPERIMENTAL WORK

Both small scale laboratory experiments and field application testing were incorporated as part of this study. These two different testing environments provided important and relevant information pertaining to addressing the research objectives.

### 4.1 LABORATORY TESTING

The small-scale laboratory box test, as detailed in Chapter 3.6.1 for the purposes of calibration validation, formed part of this testing regime. Selective sampling provided the required data for calibration as set out in Chapter 3.6. In addition to the Kli-Pi unit fixed to the surface of the sleeper, an additional two Kli-Pi prototypes formed part of the instrumentation design, positioned at depths of 100 *mm* and 250 *mm* from the surface beneath the sleeper (Figure 4-1), or 350 *mm* and 500 *mm* respectively when measured from the invert level of the sleeper. Numbering of the Kli-Pis is arranged in increasing sequence from the lowest point in the structure, starting from number 1, incrementing through to number 3 that is fixed to the sleeper.

Clean ballast, conforming to the S406 specifications of Transnet Freight Rail (1998), was used for the laboratory experiment. The ballast was progressively layered, tamped and levelled by hand to ensure a uniform density and packing arrangement. Due to the box test consisting of only one half of a sleeper, the instruments were positioned directly below the rail seat where maximum corresponding stresses would be expected in the field. The 300 *mm* depth of ballast is representative of typical railway formations. Even though this depth is significantly less than that employed by Liu et al. (2016b) for SmartRock, quantitative comparisons can be drawn between the two experiments.

The hydraulic actuator was configured for load control for representative stresses between the ballast and sleeper interface. The biggest difference between this experimental configuration and that of Liu et al. (2016b) is the actuation frequency. Results from Chapter 3.6.1 indicate the need for actuation frequencies higher than 4 *Hz*, compared to the 1 *Hz* actuation frequency chosen by Liu et al. (2016b). The authors did not state the frequency band over which the SmartRock instrument provides accurate measurements or whether the device's calibration was verified. For the purposes of this study, only the 12 *Hz* actuation frequency is investigated. This represents the highest kinetic energy with additional shakedown prior to data acquisition. Table 3-2 provides a summary of the actuation frequency and number of

load cycles applied with the box test configuration. Table 4-1 provides a summary of the dynamic wheel load variables. A maximum rail seat load ( $q_r$ ) of 92 kN was used for the laboratory test.

**Table 4-1: Summary of variables used to calculate the maximum wheel load (adapted from Jideani, 2018)**

Parameter	Value	Unit
Axle load (heavy haul)	26	Tonnes
Static wheel load, $P_{static}$	127.53	kN
Vehicle speed, $V$	70	km/h
$\eta$	1.07	
Track condition, $\delta$	0.2	
$t$	2	
Dynamic impact factor, $\phi$	1.429	
Dynamic wheel load, $P_{dyn}$	182.2	kN
Sleeper spacing	650	mm
Load distribution factor	50.4	%
Maximum rail seat load, $q_r$	92	kN



**Figure 4-1: Kli-Pi 2 and 1 positioned at depths of 100 mm (left) and 250 mm (right) in the ballast box**

## **4.2 FIELD TESTING**

The field test was conducted on 6 December 2017 near the Komati power station/ Broodsnyersplaas (26°04'32.9"S 29°30'17.8"E), located in the Mpumalanga province of South Africa. A summary of the specification for the heavy haul coal line railway section instrumented is provided by Gräbe & Clayton (2009):

- Track gauge: 1,067 *mm*
- Sleepers: PY concrete
- Axle load: 26 *t/axle*
- Sleeper spacing: 650 *mm*
- Ballast depth: 300 *mm*
- Subballast & subgrade material depth: 900 *mm*
- Year of completion: 1976

From visual observations, this section of track appeared to have been in service for a number of years. The majority of the PY sleepers were dated between the late 1970s and early 1980s, with a relatively high level of fouling. The track alignment consisted of a large radius curve with one double line and an adjacent single line. The right-hand track section of the double line was instrumented (Figure 4-2). For the duration of testing, the trains were travelling in a South-Western direction (increasing kilometers). The positive gradient resulted in trains slowing down during their passage past this point. Short bouts of rain led to the saturation of the layers. The water table was positioned approximately 100 mm above the Kli-Pi positioned in the subballast during retrieval of the instruments. This was in part due to the terrain channelling the water and moist soil conditions from prior precipitation the weeks before.



**Figure 4-2: Instrumented section of track; view towards South-Western direction**

The track was instrumented with 4 Kli-Pi instruments. The body coordinate frame was kept consistent with the convention as detailed in Chapter 3.7.3. All the instruments were positioned below one of the sleepers, directly beneath sleeper edge (Figure 4-3). This method allows for minimal disturbance to the ballast and reduces the time required to install and remove the instruments. For each Kli-Pi, the ballast stones were positioned during installation around the instruments to provide confinement and interlocking among the adjacent particles. In addition, with the forces distributed in the shape of a frustum, the instruments were located such that all instruments would be subjected to the highest

concentration of stress. The positioning of the Kli-Pis at the edge of the sleeper coincides with the position where significant Principal Stress Rotation (PSR) is expected to occur. With distance measured relative to the top of the sleeper, the invert level of each numbered Kli-Pi and its position within the structure is summarized as follow:

- Kli-Pi 4: 0 *mm* – Top surface of the sleeper for measurement reference
- Kli-Pi 3: 250 *mm* – Top of the ballast, 10 *mm* below the bottom of the sleeper surface (Figure 4-3, right)
- Kli-Pi 2: 400 *mm* – Middle of the ballast layer
- Kli-Pi 1: 550 *mm* - Subballast-ballast interface (Figure 4-3, left)



**Figure 4-3: Installation of Kli-Pi 1 and 3 just below the ballast and sleeper respectively**

The Wi-Fi AP point was positioned above the column of Kli-Pis, adjacent to the sleeper (Figure 4-4). The small enclosure was inverted and wrapped with a thin plastic cover to prevent the ingress of moisture. The Ethernet cable protruded from the inverted lid and connected to the user interface controller situated a safe distance away from the railway tracks (Figure 4-2). Only a single train pass was recorded during the test for all 4 instruments; the accumulation of water around the instruments as a result of a downpour prevented wireless signal transmissions, severing communications with the Wi-Fi AP. The focus of the analysis

remained on the concurrent data collected from all 4 Kli-Pi instruments. Due to the poor visibility during the passage of the train, the only information available of the train consist was the class 10E locomotives. From the data analysis, 6 locomotives and 100 loaded wagons were identified. From the frequency spectra, the wagon class could be derived. The passage of the train did not affect the orientation of the ballast. Table 4-2 compares the pitch and roll (orientation) of the instruments before and after the passage of the train.

**Table 4-2: Static instrument orientation before and after train passage**

Kli-Pi	Initial Orientation [deg]		Final Orientation [deg]	
	Roll	Pitch	Roll	Pitch
1	1	9	2	9
2	-8	-1	-8	-1
3	-8	10	-8	7
4	0	-6	1	-6



**Figure 4-4: Wi-Fi AP with both the Ethernet cable and Kli-Pi 4 visible**

### 4.3 TYPICAL RESULTS

Both single load cycles and short term load cycling representative of typical field conditions were investigated. Data was acquired in the form accelerations and rotational velocity. Displacements and orientation (attitude) representations were acquired through integration procedures of the acceleration and rotational velocity data respectively. Typical results obtained are presented in Chapter 4.3.1 and Chapter 4.3.2. Differences and similarities can be visually distinguished between the two experiments, highlighting the different dynamic response associated with each experiment. A discussion of the results obtained follows in Chapter 5. The graphs illustrate the typical displacement and rotation response of:

1. A single Kli-Pi positioned within the ballast matrix (comparing all the axes).
2. All Kli-Pis about a specific axis or DoF (comparing the laboratory and field experiment).

Additionally, an effective method to summarize and visualize the rotation and displacement data in three dimensions is through the introduction of scatter matrix graphs. Each of the four dimensions (one axis of time and three for the spatial dimensions) can be graphed as a function of all the dimensions, generating a  $4 \times 4$  matrix of *scatter* graphs. Importantly, the scales for the spatial dimensions are kept consistent for all the Kli-Pis for a particular test, together with the colour scheme (Chapter 3.7.2) used throughout this document to uniquely identify the Kli-Pi instruments. The markers are semi-transparent to identify the density and extent of variation for a given time span. This method provides three key pieces of visual information:

1. Time-spatial information, providing a time-history of the data, with each axis graphed separately to avoid the overlap of data.
2. Spatial-spatial information, providing different orthogonal viewports or projections of a pair of DoF.
3. The diagonal elements do not contain any meaningful information (the variable is graphed as a function of itself). This scatter matrix element is instead replaced by the probability density function (PDF) distribution of data points in the form of a histogram. The PDF of the X, Y and Z axes are typically in the form of a Gaussian distribution. The time-axis will always be an ideal uniform distribution as each equidistant data point of the time axis occurs only once in the sample. This information forms the precursor to the statistical analysis of the data (Chapter 5.4).

### **4.3.1 Displacement**

Figure 4-5 and Figure 4-6 illustrate the deflection response about all three Cartesian axes of Kli-Pi 1 (laboratory test) and Kli-Pi 3 (field test) respectively.

Figure 4-7 and Figure 4-8 illustrate the deflection response about the Z-axis for all Kli-Pis (laboratory and field test).

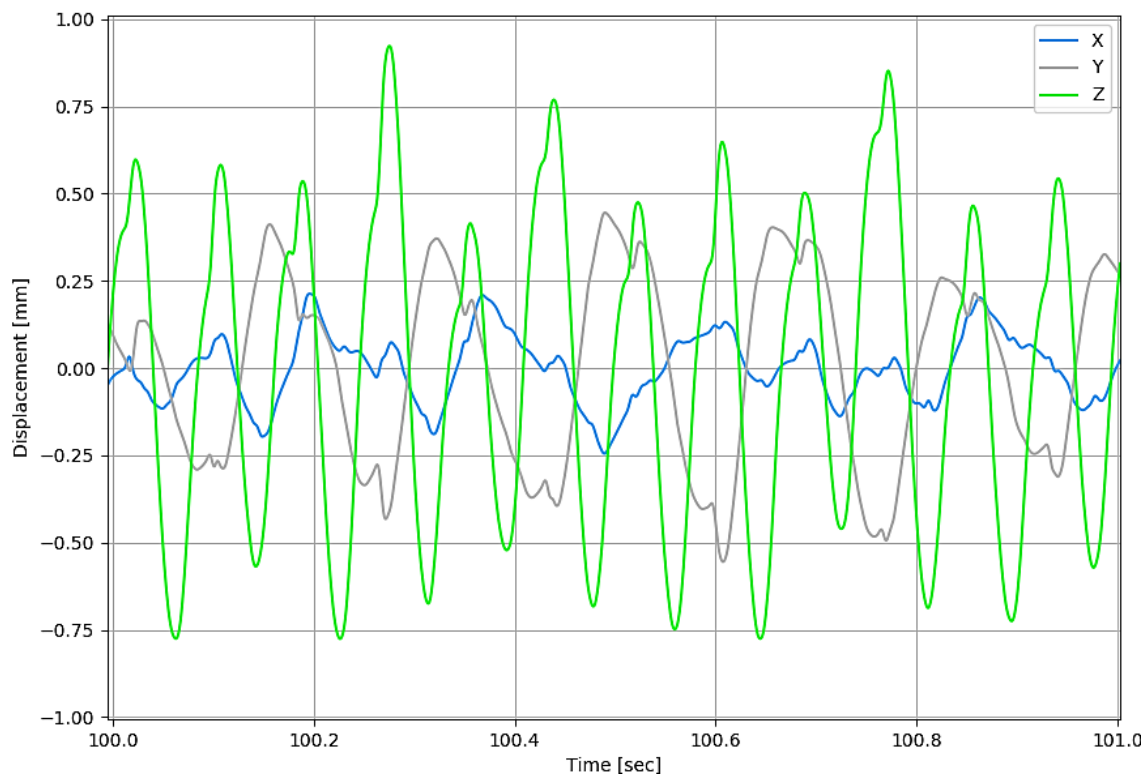
The matrix of scatter graphs for Kli-Pi 1 (laboratory test) is illustrated in Figure 4-9 while the matrix of scatter graphs for Kli-Pi 3 (field test) is illustrated in Figure 4-10.

### **4.3.2 Rotation**

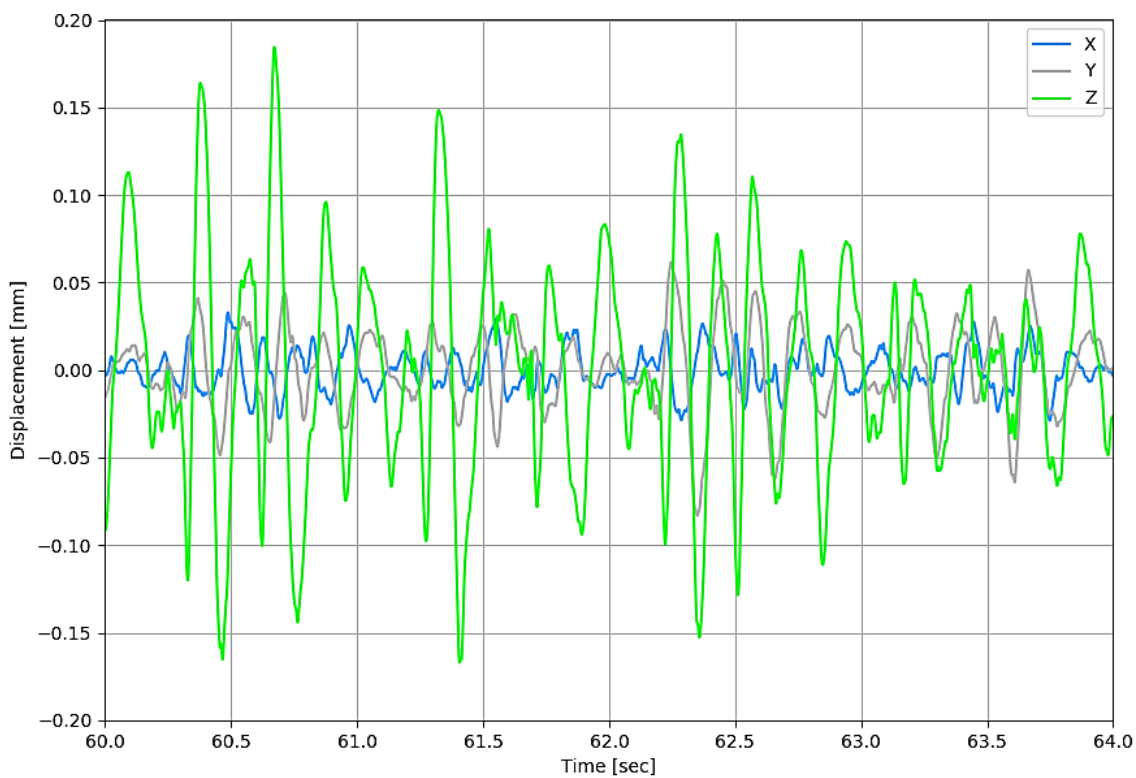
Figure 4-11 and Figure 4-12 illustrate the rotation response about all three Cartesian axes of Kli-Pi 2 and Kli-Pi 3 respectively.

Figure 4-13 and Figure 4-14 illustrate the rotation about the Z-axis and X-axis for all Kli-Pis (laboratory and field test respectively).

The matrix of scatter graphs for Kli-Pi 1 (laboratory test) is illustrated in Figure 4-15 while the matrix of scatter graphs for Kli-Pi 3 (field test) is illustrated in Figure 4-16.



**Figure 4-5: Time-domain deflection: Kli-Pi 1 (500mm, laboratory test, detailed)**



**Figure 4-6: Time-domain deflection: Kli-Pi 3 (250mm, field test, detailed)**

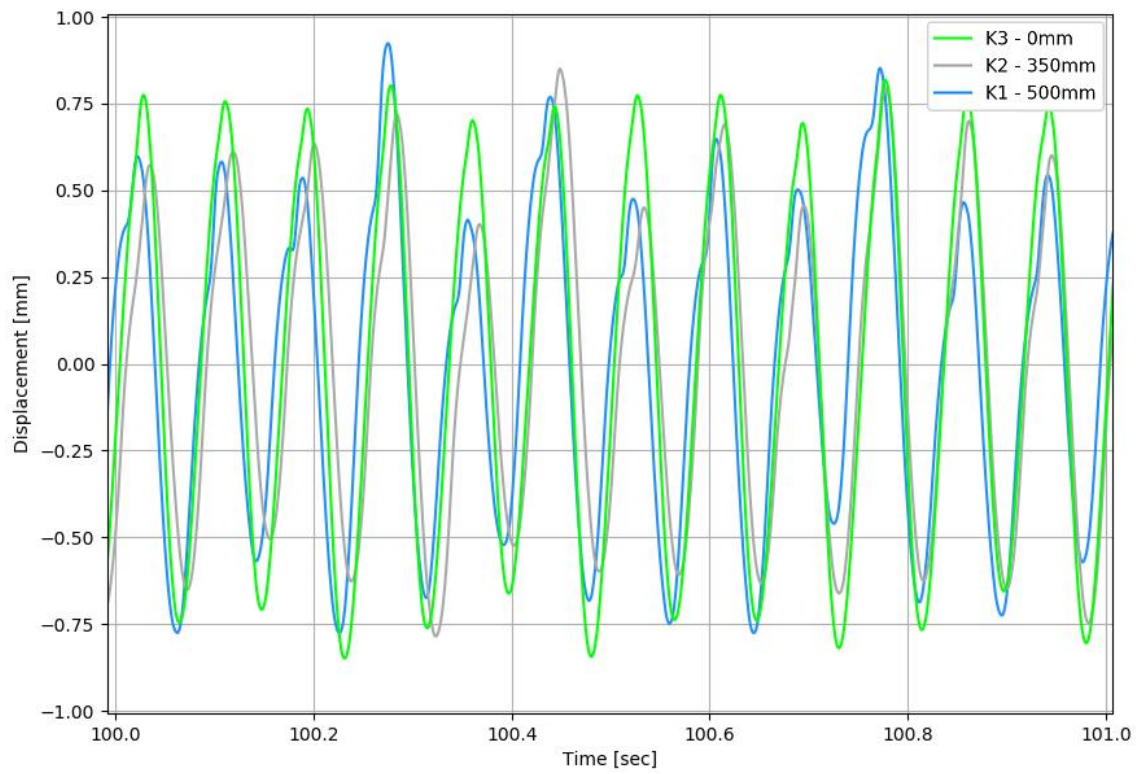


**Figure 4-7: Time-domain deflection: Z-axes of all Kli-Pis (laboratory test, detailed)**

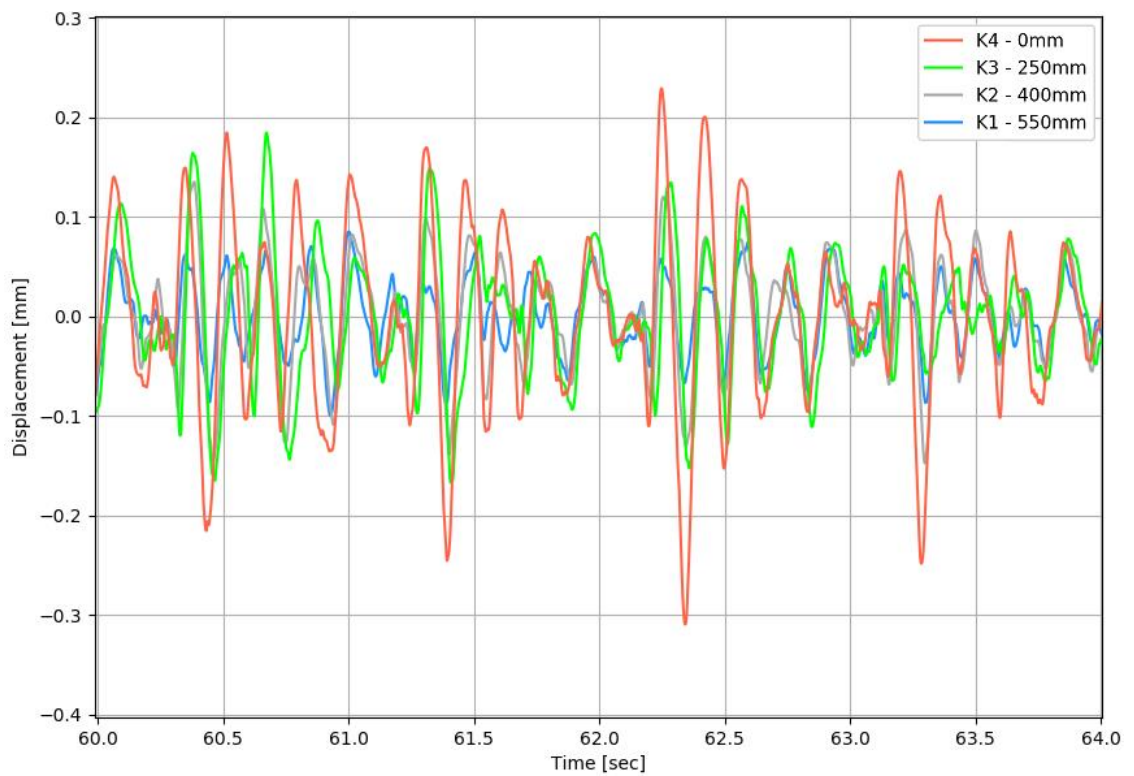


**Figure 4-8: Time-domain deflection: Z-axis of all Kli-Pis (field test, detailed)**

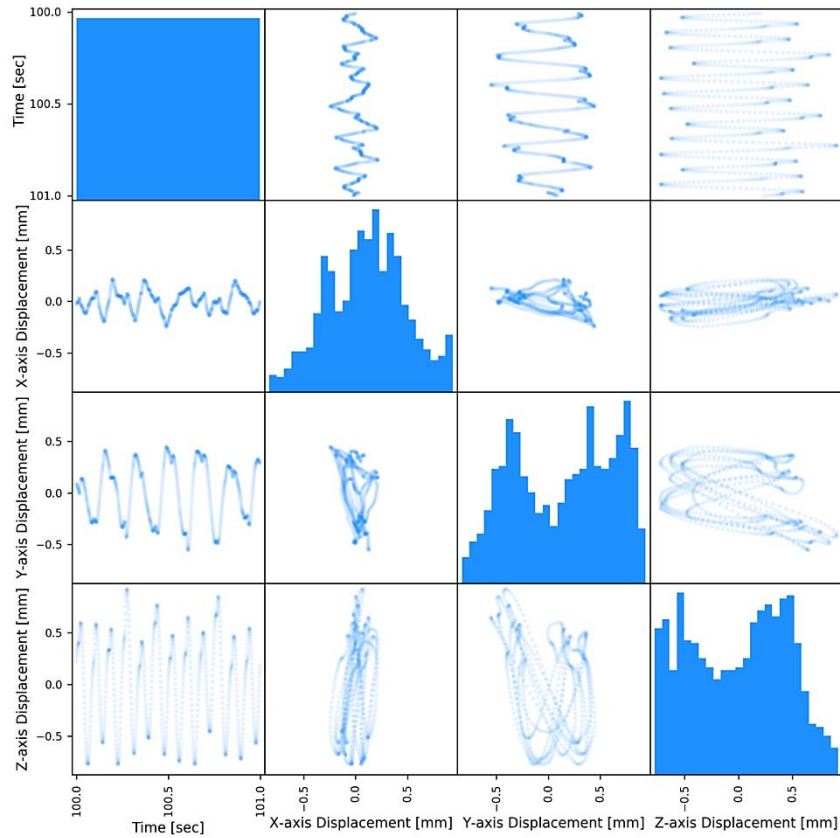


**Figure 4-9: Time-domain displacement matrix: Kli-Pi 1 (500mm, laboratory test, detailed)**

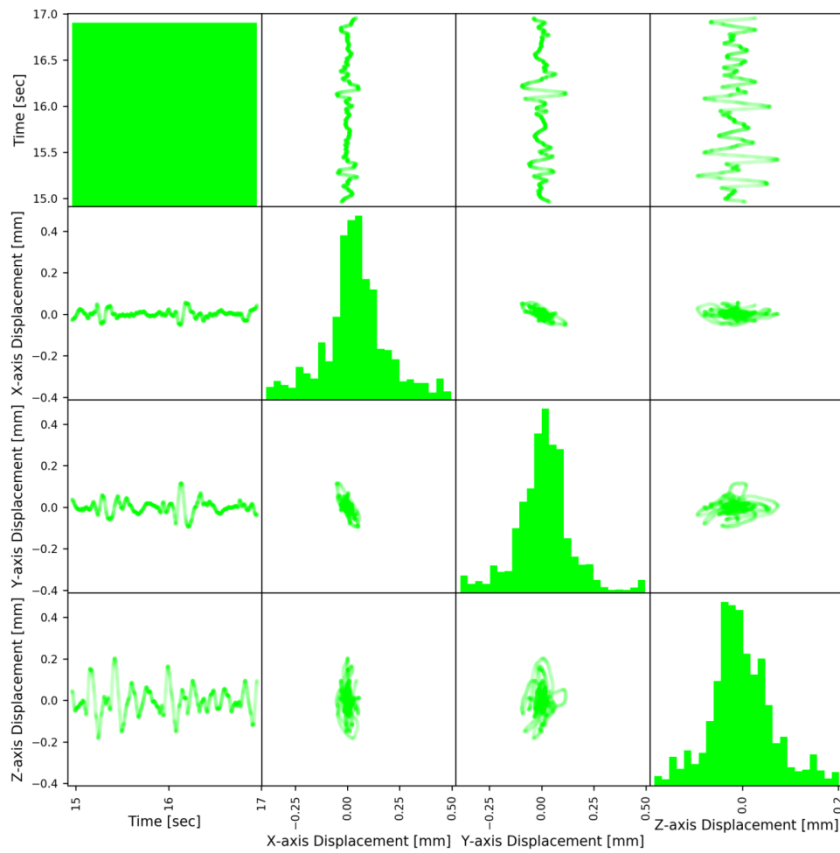


**Figure 4-10: Time-domain displacement matrix: Kli-Pi 3 (250mm, field test, detailed)**

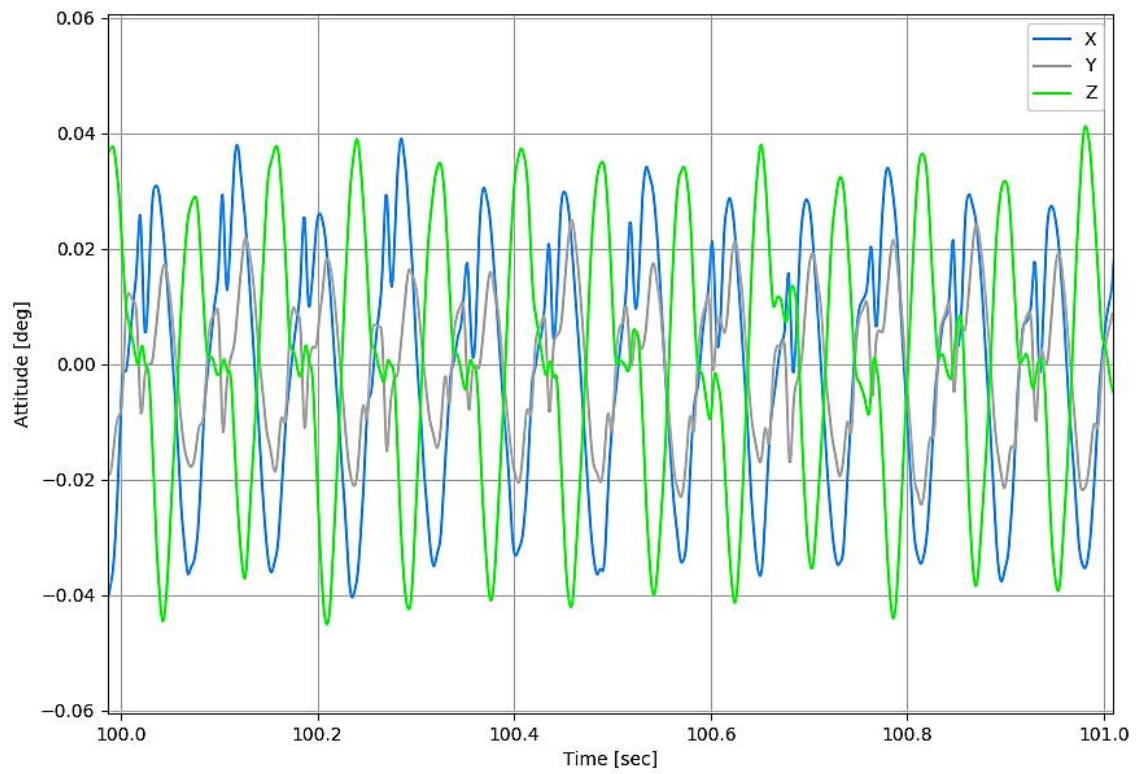


**Figure 4-11: Time-domain rotation: all axes of Kli-Pi 2 (350mm, laboratory test, detailed)**

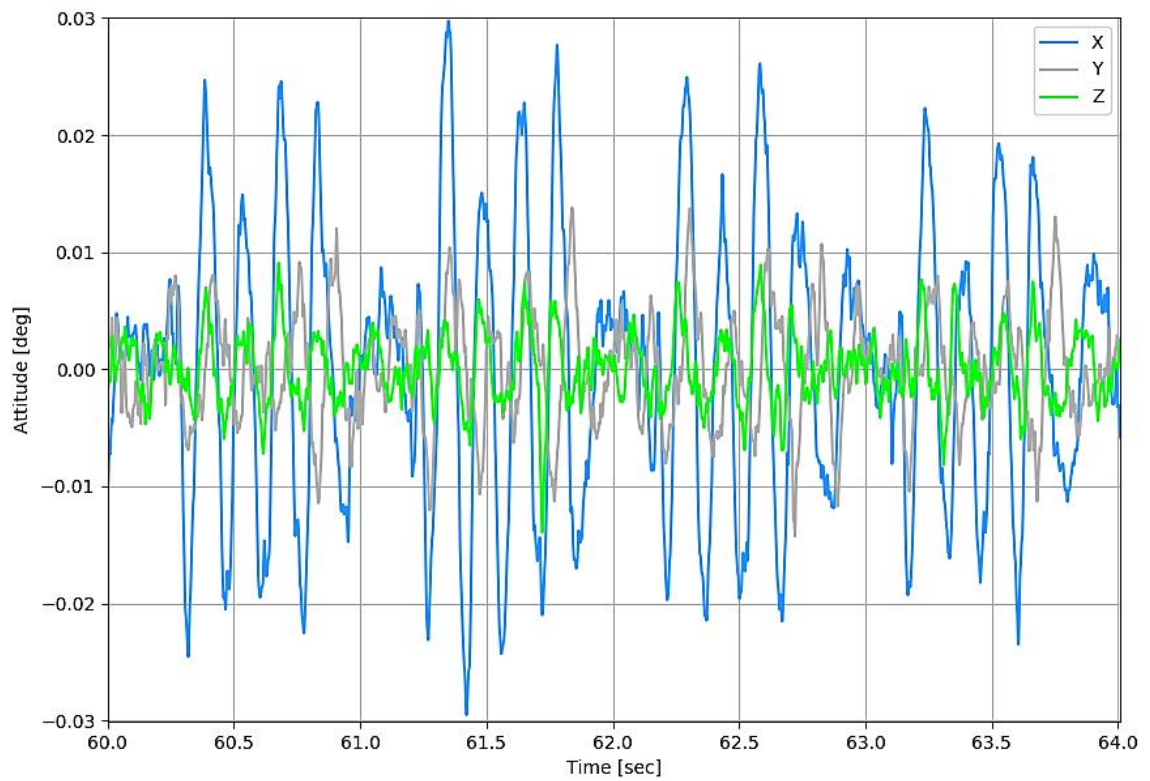


**Figure 4-12: Time-domain rotation: all axes of Kli-Pi 3 (250mm, field test, detailed)**

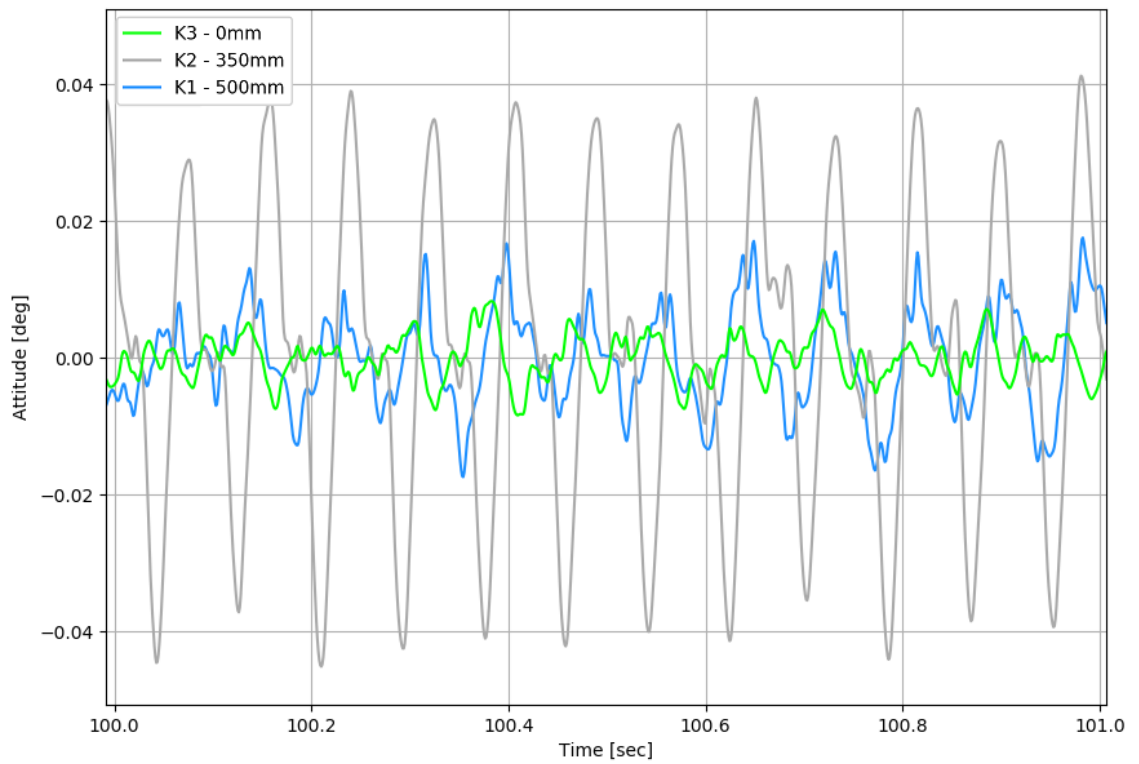


**Figure 4-13: Time-domain rotation: Z-axis of all Kli-Pis (laboratory test, detailed)**

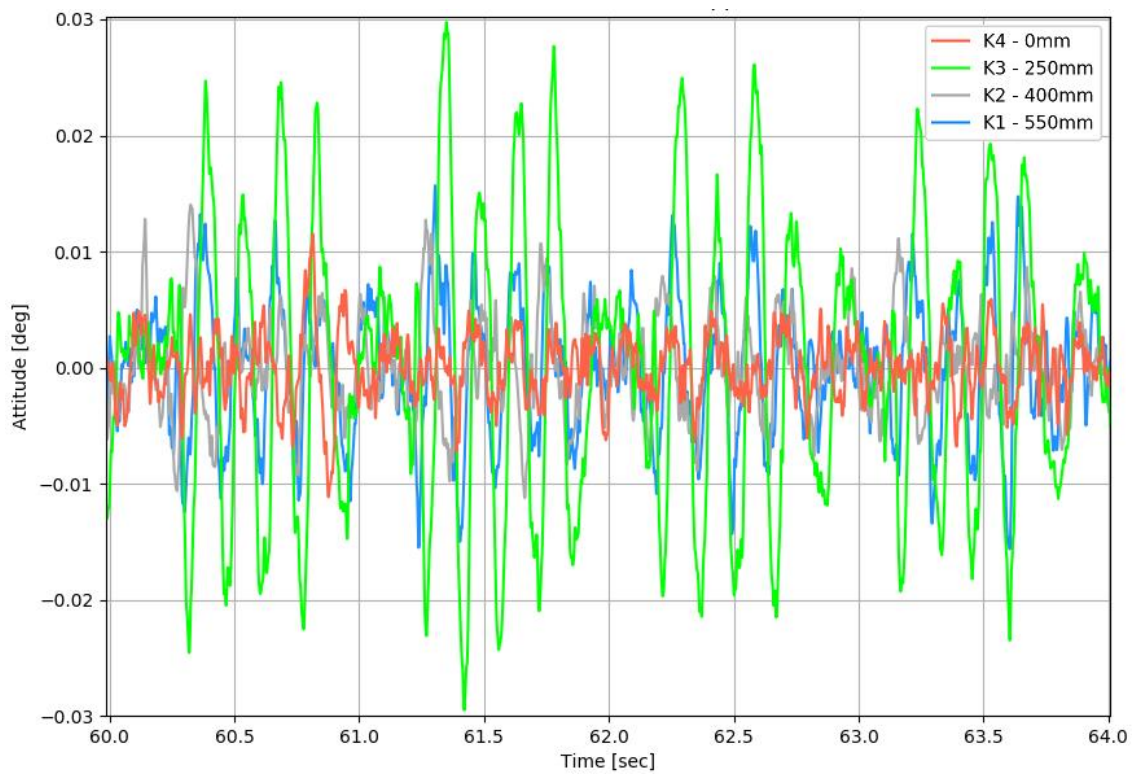


**Figure 4-14: Time-domain rotation: X-axis of all Kli-Pis (field test, detailed)**

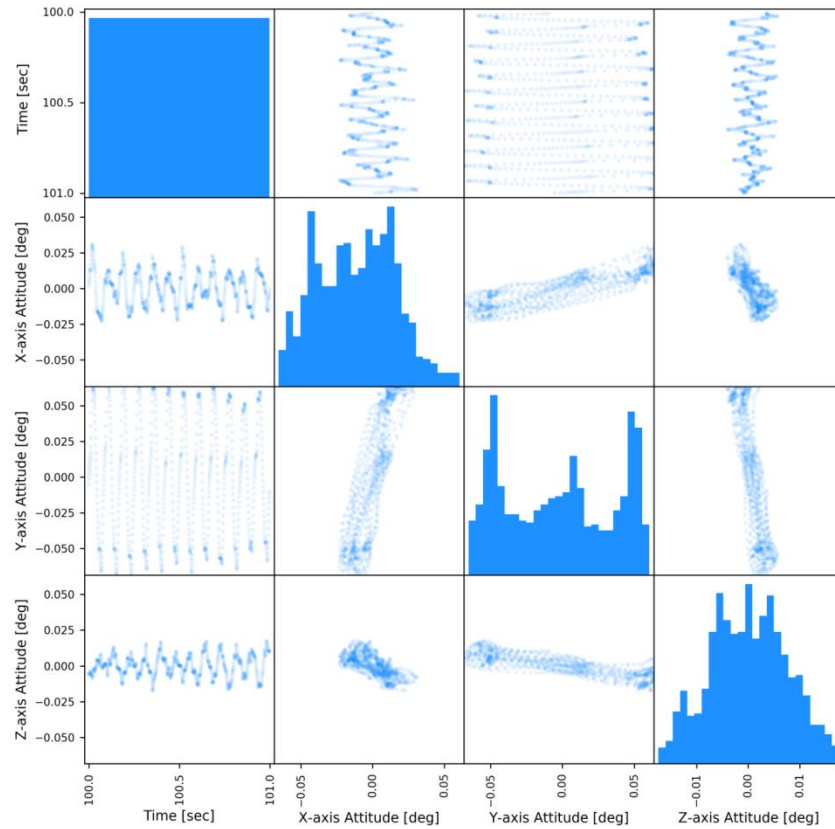


**Figure 4-15: Time-domain rotation matrix: Kli-Pi 1 (500mm, laboratory test, detailed)**

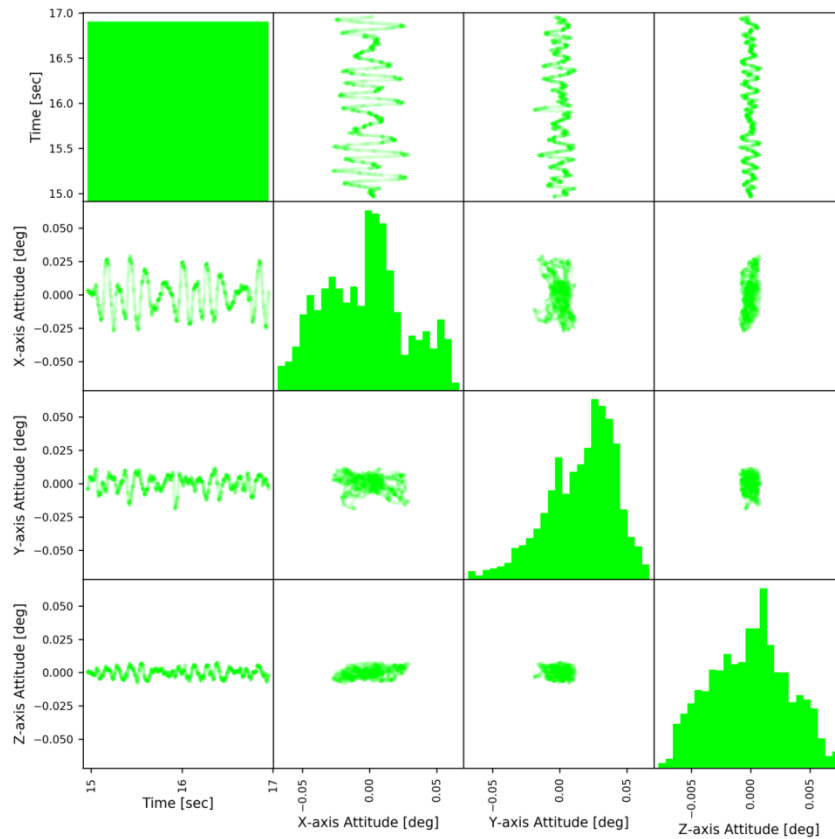


**Figure 4-16: Time-domain rotation matrix: Kli-Pi 3 (250mm, field test, detailed)**

## **5 DISCUSSION OF THE RESULTS**

Based on the literature presented, relating the different mechanisms and effects influencing the interaction and state of order for granular systems, quantitative measurements and statistics for both translations and rotations (time and frequency domains) were formulated. Through the implementation of new instrumentation in the form of Kli-Pi, quantitative results are presented pertaining to the mesoscale behaviour of ballast subjected to quasi-static loading conditions. The discussion of these results is subdivided according to modes of translation and rotation (Chapter 5.1), mechanical work and energy methods (Chapter 5.2), cumulative rotations and displacements (Chapter 5.3) and statistical descriptors of the displacement, rotation and mechanical work (Chapter 5.4).

A Python-centred analysis framework was employed for both data acquisition and processing to automate, to a large extent, the sequential processing steps required. The addition of the SciPy package provides functionality for matrix manipulation, filtering methods, frequency transformations, peak detection and graphing capabilities. Appendix A.2 outlines in detail the processing workflow and its underlying components required to process the data sets into usable information. Following the post-processing phase, new parameterization methods are presented focussing on energy principles and statistical descriptors, each with its own discussion of its application. For brevity, a complete and expanded set of graphs can be found in the appendix for both the laboratory (Appendix A.3) and field experiments (Appendix A.4).

## 5.1 MODES OF TRANSLATION AND ROTATION

For the laboratory test, three Kli-Pis were installed at different depths and subjected to cyclic loading. The final two minutes (7,200 load cycles) of the test, at a frequency of 12 Hz, was investigated due to the decreased potential of shakedown (Liu et al., 2016b) after 12,200 prior loading cycles were applied over a range of frequencies (Table 3-2). This test configuration provided a controlled environment with consistent loading and support characteristics, limiting unknown external variations. A small proportion of the 9 Hz frequency is visible throughout the graphs just prior to the initiation of the 12 Hz phase (Figure 5-1). A summary of the displacement and rotation statistics are provided in Appendix A.5 and Appendix A.6. All the graphs, for a particular type of measurement, use consistent colour schemes (Chapter 3.7.2) for more intuitive visual comparisons.

### 5.1.1 Laboratory Testing

A representative set of measurements was illustrated for Kli-Pi 1 (Figure 4-5) for all three axes. As expected, the translational motion of Kli-Pi is predominantly in the vertical direction (Z-axis), parallel to the axis of loading. On average, a small decrease occurs for the peak-to-peak measurements in the Z-axes with depth when comparing all the Kli-Pis against one another (Figure 4-7). Mean peak-to-peak vertical displacements are 1.5 mm for this particular time period. Small but still significant lateral (Y-axis) and longitudinal (X-axis) displacements were observed, with peak-to-peak amplitudes of 0.8 mm and 0.4 mm respectively. The 2 m/s<sup>2</sup> amplitude for the vertical acceleration is in close agreement with the SmartRock findings of Liu et al. (Figure 2-17).

Over the two minute period, an increase in the peak-to-peak displacements occurred, particularly in the vertical direction (Z-axis). An apparent hysteresis displacement pattern was observed for Kli-Pi 1 that was absent from the response of the sleeper (Kli-Pi 3). The frequency response however remained consistent. An increase in the power spectrum density was observed for the displacement as interlocking between particles developed (Figure 5-1). The lateral frequency spectra produced significantly smaller densities.

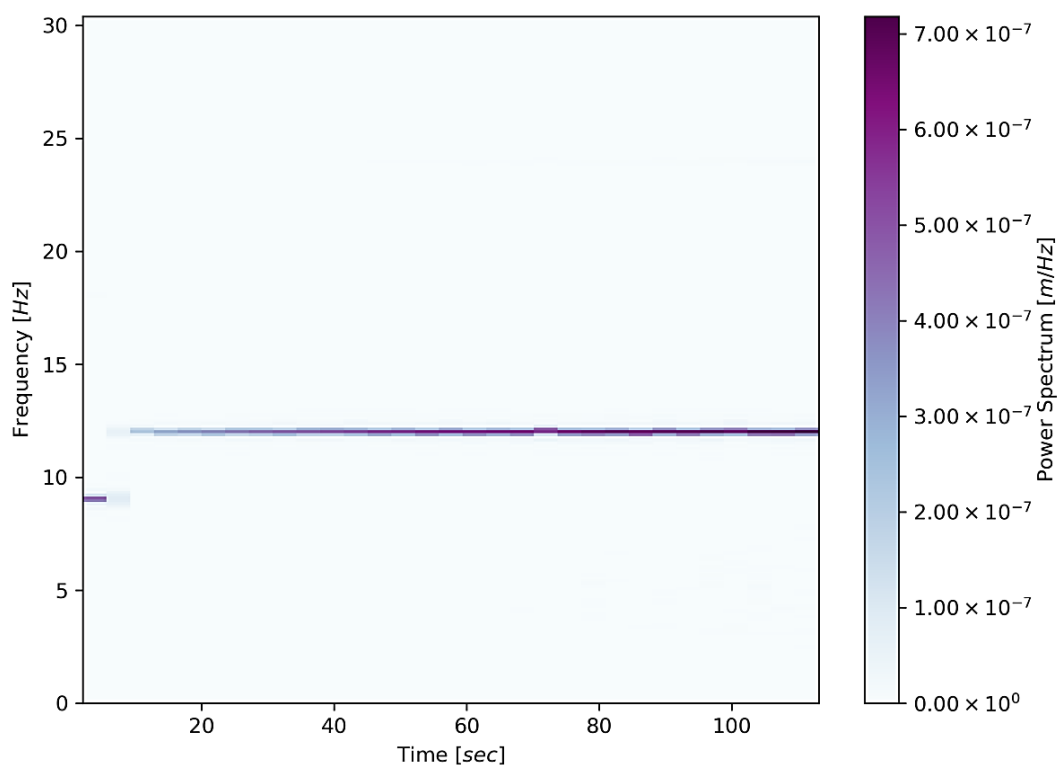


**Figure 5-1: Spectrographic deflection: Z-axis of Kli-Pi 2 (laboratory test)**

Regarding the rotational characteristics, the amplitude was expected to be minimal about the yaw axis (Z-axis) when positioned directly beneath the rail seat, due to the geometry and boundary conditions of the sleeper. This was however contradicted by the measurements, indicating that the dominant rotational axis is in fact about the Z-axis (Figure 4-11), followed closely by rotation about the X-axis. This phenomenon is unique to this instrumented position (Figure 4-13). Similar to the deflection response, the two Kli-Pis in the ballast illustrated a more complex development of the rotational amplitudes. Changes within the ballast matrix were also visible when considering the rotation measurements. The frequency transition from 9 Hz to 12 Hz resulted in a reversal of the preferred axis of rotation for the following 25 s (300 cycles) before reverting back to the original scheme. The peak-to-peak rotation amplitudes near the end of the test remained consistent, with maximum peak-to-peak amplitudes approaching 0.14 degrees. The rotation response appears to be more varied and sensitive to small changes in the skeletal structure or fabric of the surrounding ballast particles, compared to the displacements which approach a more consistent plateau. The preliminary assessment indicates that the peak-to-peak rotation and deflection amplitudes are normally distributed, with varying degrees of skewness.

### 5.1.2 Field Testing

For the field test, four Kli-Pis were installed in the formation subjected to loading from a 100 wagon coal carrying train, propelled by 6 class 10E locomotives. As noted by Gräbe & Clayton (2009), transverse PSR can be expected near the end of the sleeper with the influence extending deeper down into the formation for a higher axle count per bogie. Furthermore, it is known that the most unfavourable combination of stresses can be expected to occur near the mid-depth of the subballast, close to the location of Kli-Pi 1.

Figure 4-6 illustrates the typical deflection response of Kli-Pi 3, positioned directly below the sleeper. The largest influence is about the Z-axis or vertical axis, with peak-to-peak measurements approaching  $300 \mu m$ , with smaller deflections along the lateral directions. Figure 4-8 illustrates the typical, superimposed Z-axis deflection responses for all the Kli-Pis. The general assumption whereby the deflection amplitude reduces with depth does not hold when considering the measurements at the mesoscale or particle level. Significant variation for peak-to-peak amplitudes is observed for all the Kli-Pis. Most apparent is the continuously varying amplitude ratio. For certain axles, the peak-to-peak amplitude of Kli-Pis situated at a greater depth is larger than more shallow measurements. For impact loading events, persistent peaks are observable at both 32 s and 99 s of the deflection response where the peak-to-peak amplitude is more than double. This high energy impact load propagates throughout the structure and granular layers with minimal attenuation. These events are also observable on the FFTs as a narrow, broadband set of frequencies.

The frequency spectra provide additional information relating to the velocity (as discussed by Zhang et al., 2016) and geometry of the train, lateral forces and sleeper-ballast resonance. When considering the entire passage of the train, the majority of the vibrational energy was concentrated along the vertical axis, even at the deepest level of instrumentation, with the locomotives. This dynamic component consisted predominantly of frequencies within the  $125 \text{ Hz} - 150 \text{ Hz}$  range. This band of frequencies is associated with the ballast-sleeper resonance (Figure 2-2). This is also in agreement with the analytical findings of Kouroussis et al. (2015) and Li et al. (2015) in addition to laboratory testing results from Zhai et al. (2004). Similarly, nearly all the lateral displacements were associated with the initial passage of the locomotives, with the longitudinal displacement amplitude up to 50% greater than that of the vertical displacement amplitude (Figure 5-2). This induces a rotating, translational pattern and is indicative of Zhang et al.'s illustrations concerning the theoretical particle movement vectors (Figure 2-10) and magnitudes (Figure 2-11). This influence extended to the subballast where strain ratcheting is known to occur, albeit with a displacement amplitude nearly an order of magnitude smaller.

Characteristic features of train geometry, specifically for the wagons, appeared within the 5 – 10 Hz band of frequencies (Figure 5-2). These frequencies are associated with the passage of the bogies and the car bogie bounce (Figure 2-2). The negative gradient of the discrete lines corresponds to the train slowing down as time progresses. As the confinement of Kli-Pi progressively increases, the geometry dependant frequencies become more concentrated. This again corresponds to the stabilization of peak-to-peak amplitudes associated with the SmartRock experimentation (Liu et al., 2016).

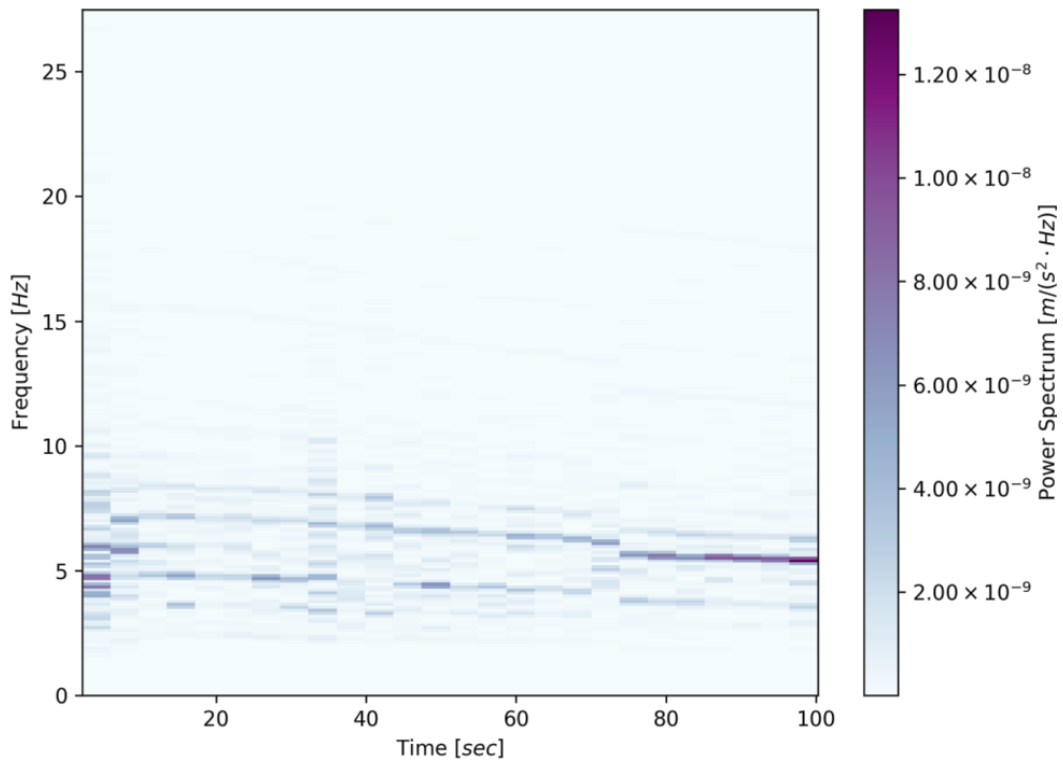


**Figure 5-2: Spectrographic displacement: Z-axis of Kli-Pi 3 (field test)**

Figure 4-12 illustrated the typical rotation response of Kli-Pi 3, situated directly below the sleeper. The dominant axis of rotation about the X-axis is as expected, given that the sleeper will bend about the outer edges owing to the lower second moment of area of the section and support of the underlying ballast. Figure 4-14 compared the X-axis rotation for all four of the Kli-Pis. The largest peak-to-peak rotation measured is attributed to Kli-Pi 3 (0.06 degrees) situated below the sleeper - not the sleeper itself (0.01 degrees). The peak-to-peak rotation magnitude of the Kli-Pis does not reduce linearly with depth. Considering the entire duration of the test, the rotational response appears unaffected by the impact loads observed at 32 s and 99 s. Compared to the displacement graphs, the influence and identification of the

individual axles are significantly simpler (Figure 4-12). This in turn provides the potential for the instrument to be used as an axle counter.

The spectrograms related to the rotational characteristics illustrate a lack of high-frequency spectra. For Kli-Pi 3 in the ballast (Figure 5-3), the geometry-dependent frequencies are identical to that of the displacement spectra (Figure 5-2). Increased variance of the frequency densities were observed with an increase in depth.

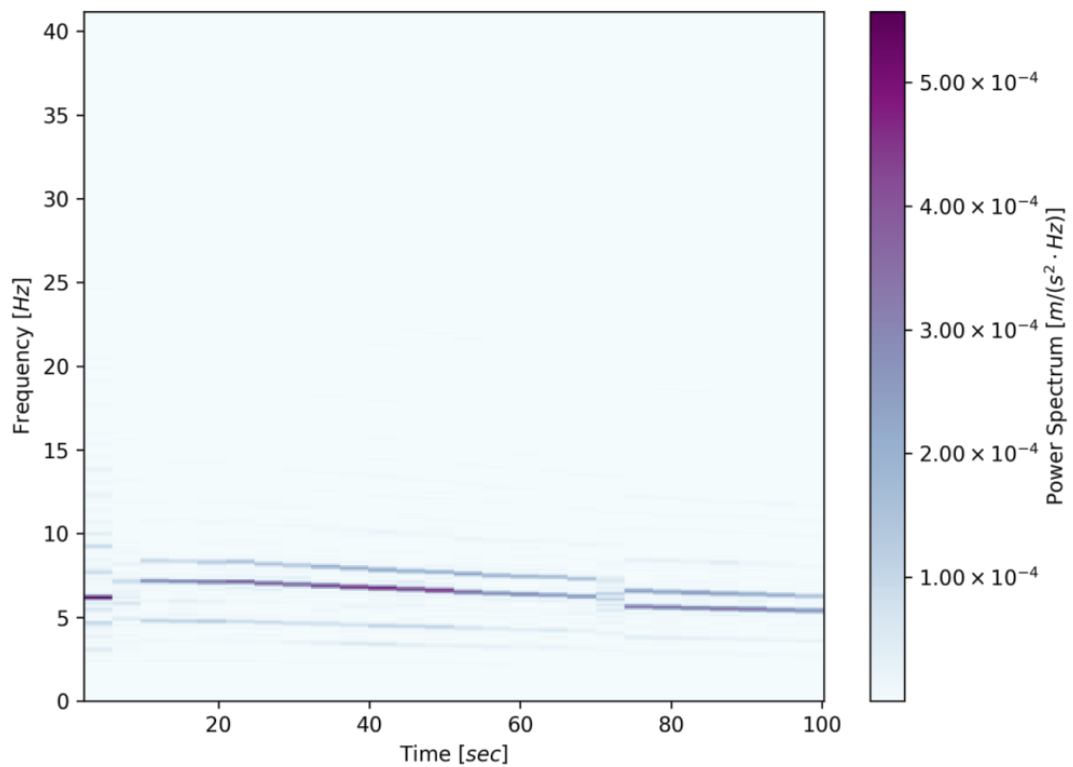


**Figure 5-3: Spectrographic rotation: X-axis of Kli-Pi 3 (field test)**

In summary, the measurements for both the displacement and translation appear more randomized or probabilistic than deterministic, with a number of outlying movement paths occurring during the passage of the train. The distribution of the peak-to-peak measurements, over the entire train passage, is normally distributed with some degree of skewness. The probabilistic nature and wide distribution of the peak-to-peak displacements with a number of outliers is not unique to a particular instrument and is present even for the Kli-Pi fixed to the sleeper.

## 5.2 MECHANICAL WORK AND ENERGY METHODS

From Newton's second law of motion, it can be shown that mechanical work on a rigid body is equal to the change in kinetic energy  $U_K$ , of the linear velocity and rotational motion of the body. Ballast can be considered as a rigid body owing to the small translations and rotations. The rotational energy, that is proportional to the square of the angular velocity, is considered negligibly small. The potential energy  $U_p$ , is associated with the work generated by the potential function (gravitational field). The work generated by this conservative force field is equal to the negative change of the potential energy of the rigid body (Stewart, 2012). The elastic strain energy is difficult to express in three dimensions due to the lack of information relating strain in the lateral directions, probabilistic strain functions and overlapping stress frusta. All energy components associated with friction, heat and audible noise, which is indistinguishable from the sensor noise, are effectively discarded when the data is filtered. It can be assumed that the position of the Kli-Pi instrument within the ballast remains unaltered for the duration of the test. Assuming that the instrument moves along a path  $C$ , given by a function  $\vec{r}(t)$ , through a conservative force field  $\vec{F}$ , the relationship described by Equation 5-1 and Equation 5-2 must hold (over a long period of time) if energy is to be conserved. This in turn provides a means to assess the magnitude of energy associated with a single ballast particle (Equation 5-1 and Equation 5-2).

$$W_k + W_p = 0 \quad (\text{Equation 5-1})$$

$$\int_c \frac{1}{2} m \Delta V^2 d\vec{r} - \int_c m \Delta h_z g d\vec{r} = 0 \quad (\text{Equation 5-2})$$

Where:

$\Delta V$  – Change in body velocity vector

$\Delta h_z$  – Change in body elevation with respect to the potential field

$m$  – Mass of the body (Chapter 3.7.2)

$\nabla \bar{P}$  – Conservative force field

Based on the kinetic and potential energy formulations, the energy or work associated with each Kli-Pi can be calculated. The advantage of the work-based approach is that all three of the translation axes are incorporated in the calculation to provide an improved representation of the particle kinetics. For the laboratory test, the work energy is graphed as a function of time for both the entire (Figure 5-4) and a small section (Figure 5-5) of the test, similar to that of the displacements and rotations (Chapter 5.1). It can be observed that in certain instances, a Kli-Pi at greater depth exhibits greater energy than that of the shallower instruments. It is hypothesized that this could be attributed to the test box storing and releasing elastic energy more efficiently than the granular media some degree, as noticeable lateral deflections were visible during the test. A familiar pattern emerges whereby the peak-to-peak amplitude increases progressively with an increase in the loading cycle count (Figure 5-5). This detailed graph exhibits a similar waveform to that of the deflection response in the Z-axis (Figure 4-7). Just before the conclusion of the test, the peak-to-peak magnitude of the energy approaches  $8\text{ mJ}$  for Kli-Pi 3 and  $6.5\text{ mJ}$  for Kli-Pi 1 and Kli-Pi 2. The same holds true for the field test (Figure 5-7) illustrating a nearly identical response to that of the deflection in the Z-axis (Figure 4-8), albeit with slightly better defined peaks.

Considering the similarities between the deflection response in the Z-axis and the associated energy (Figure 5-6), the kinetic and potential energy can be distinguished to illustrate the respective contribution of each component (for the field test). The kinetic energy (Figure 5-8) will remain positive whilst the potential energy (Figure 5-9) can be either positive or negative (Equation 5-2). For the kinetic energy, the largest source of energy is associated with the locomotives. Impact loading and the shifting of Kli-Pis within the ballast skeletal structure also contribute significantly to the kinetic energy, particularly during the first 6 s, compared to the typical wagon axles. In this instance, the kinetic energy appears to be an improved metric for identifying events where either Kli-Pi or adjoining ballast particles shift relative to one another or instances where potential ballast breakage occurs. For the potential energy, the variations are significantly smaller. For typical operating conditions with passing wagon axles, the potential energy contributes the largest proportion of the total energy. The introduction of this mechanical work parameter quantifies the rearrangement of particles, the magnitude of the quasi-static and impact loads with depth and illustrates the significant amount of energy contributed by the locomotives that account for the lateral and longitudinal movement.

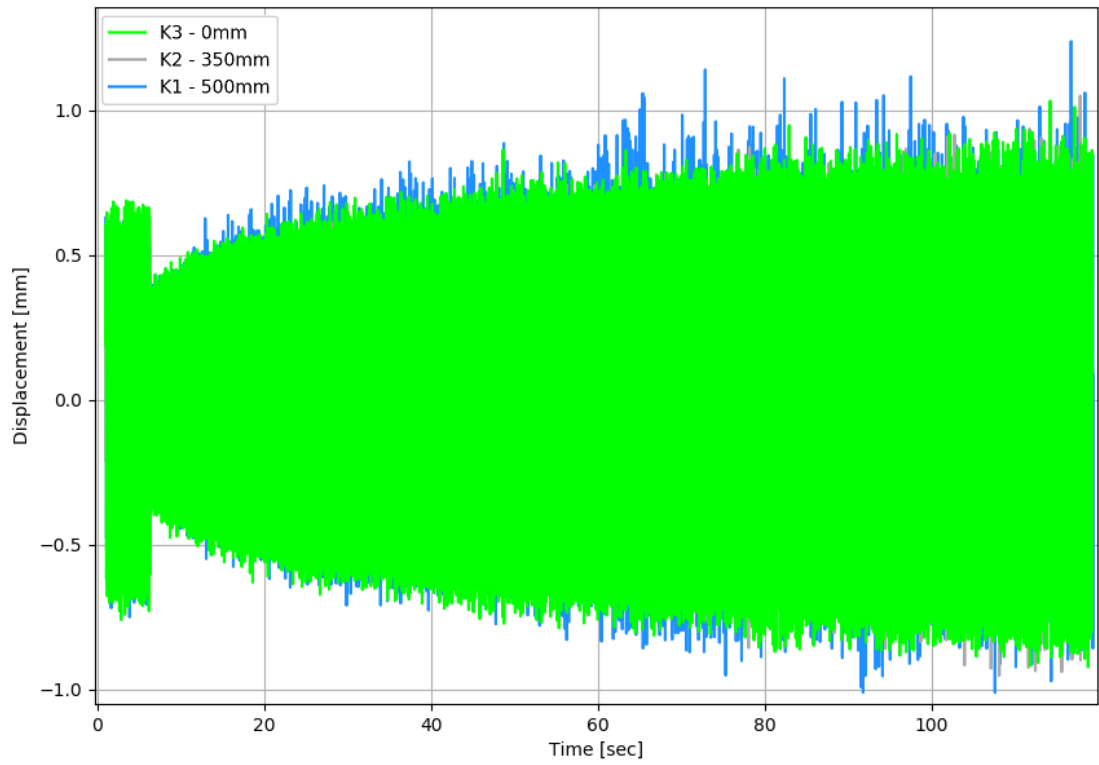


**Figure 5-4: Work energy response of all Kli-Pis (laboratory test)**

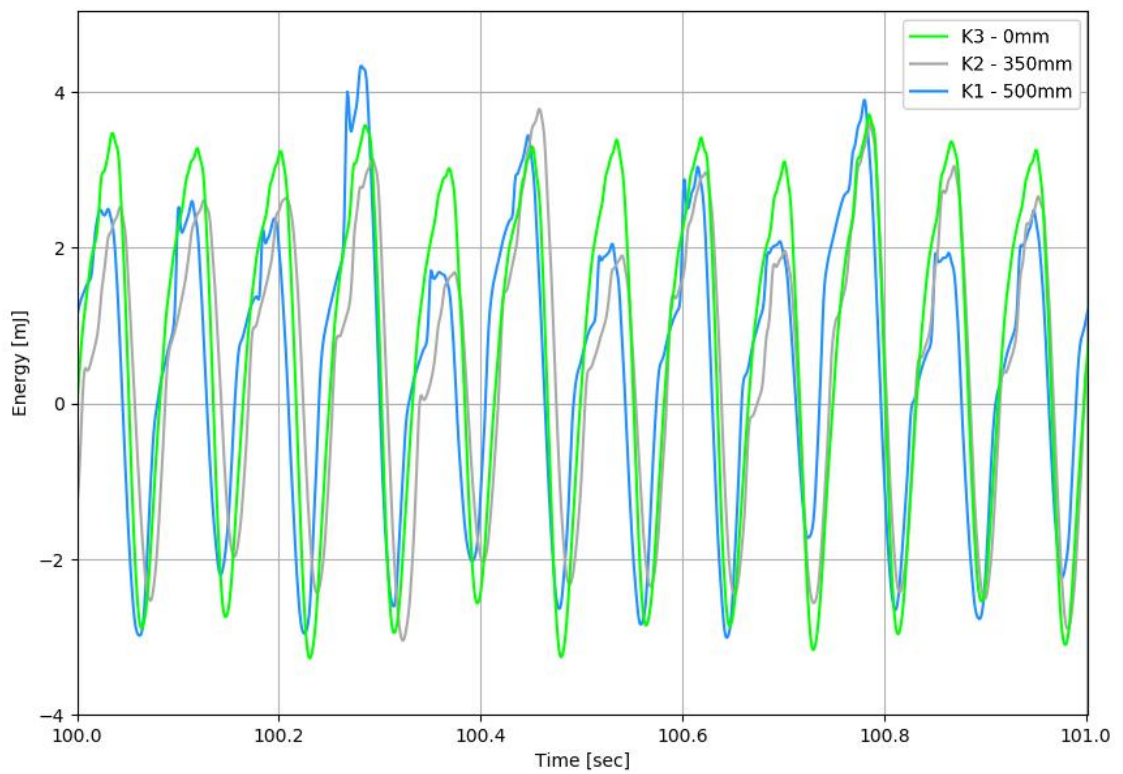


**Figure 5-5: Work energy response of all Kli-Pis (laboratory test, detailed)**

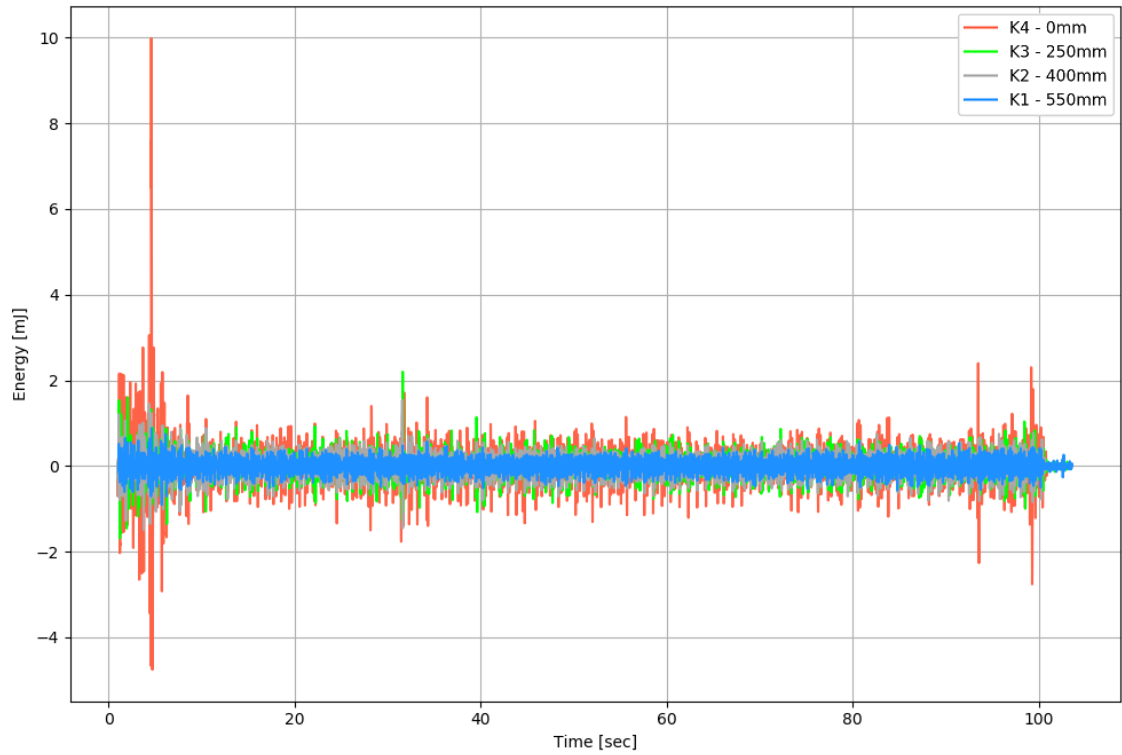


**Figure 5-6: Work response of all Kli-Pis (field test)**

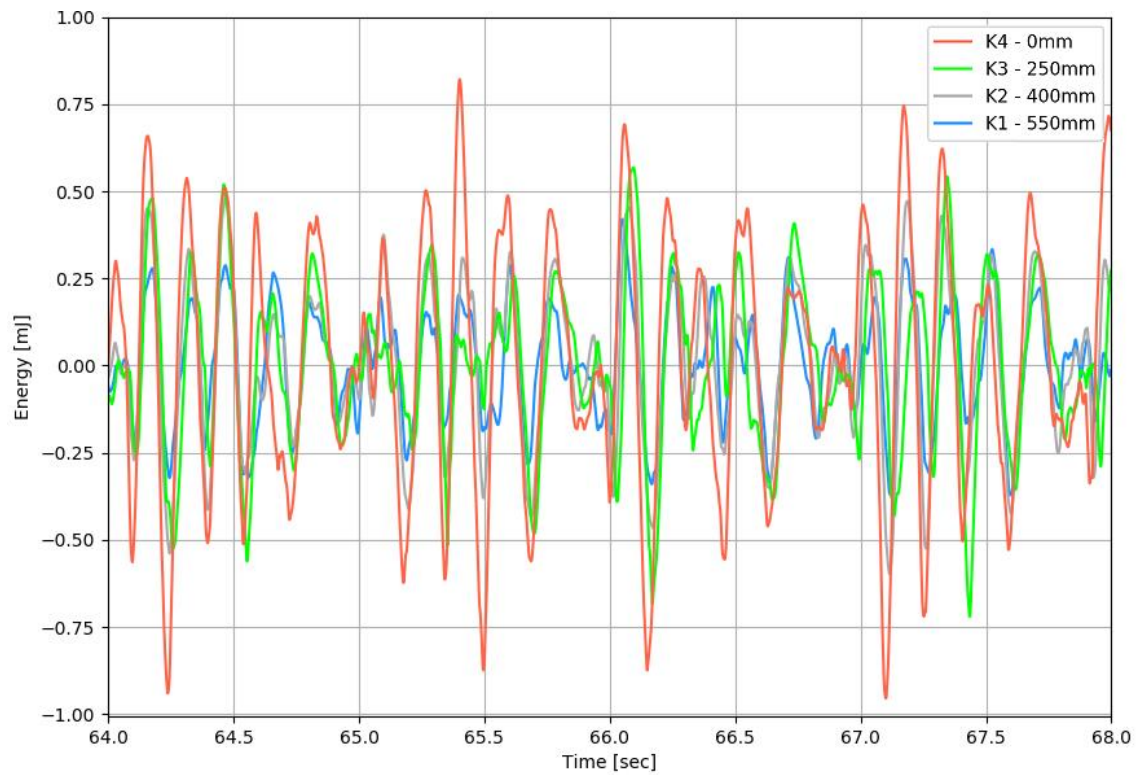


**Figure 5-7: Work response of all Kli-Pis (field test, detailed)**

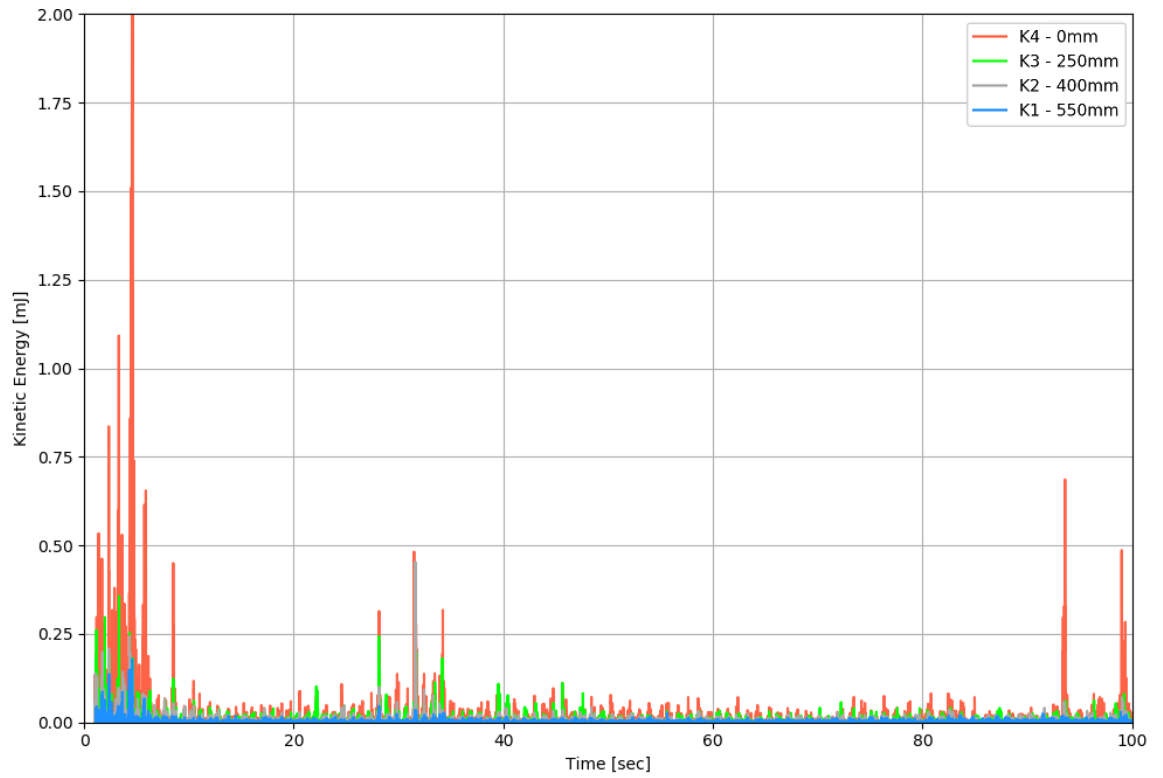


**Figure 5-8: Kinetic energy response of all Kli-Pis (field test)**

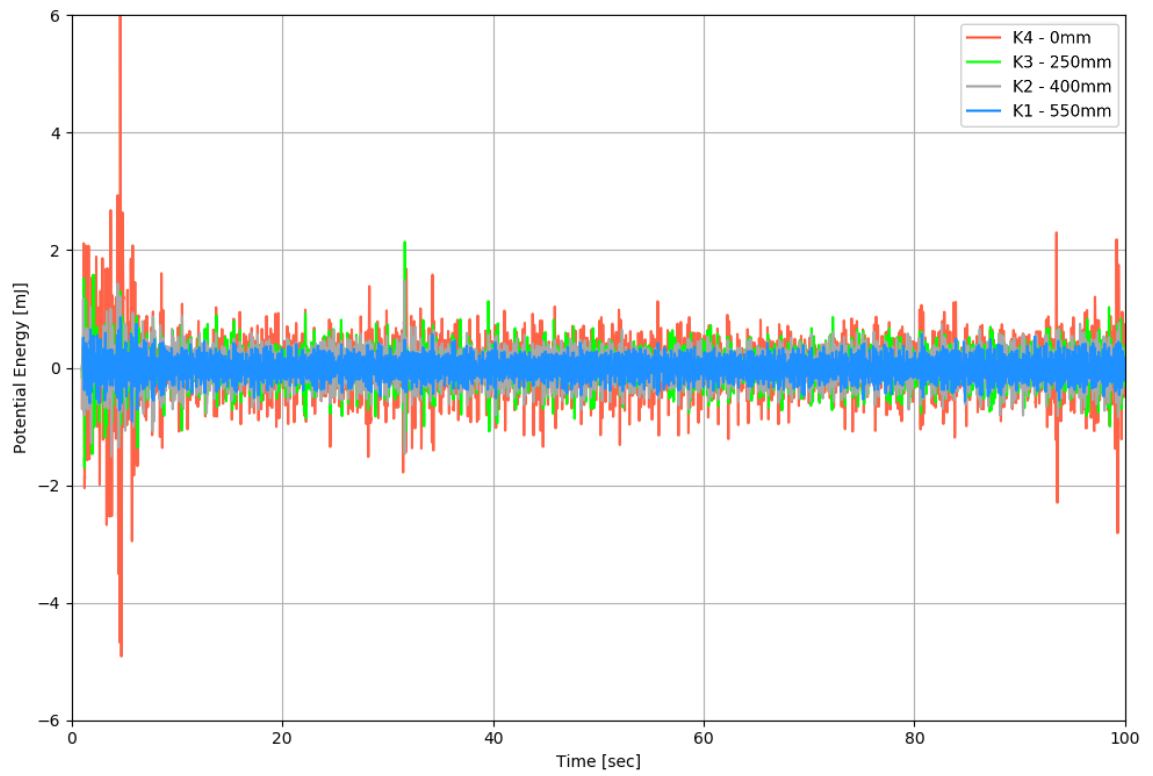


**Figure 5-9: Potential energy response of all Kli-Pis (field test)**

### 5.3 CUMULATIVE DISPLACEMENTS AND ROTATIONS

For both rotations and displacements, the norm of the applicable vector can be integrated over time to provide a better metric of the macroscopic behaviour over a longer span of time, similar to the work principle of Chapter 5.2. This metric will largely be unaffected by short term fluctuations, with the slope of the curve illustrating any changes associated with reorientation or changes in the axle loads. All results have been corrected for noise that artificially increases the slope of the graph (by a constant gradient).

For the laboratory test, the cumulative displacement (Figure 5-10) and rotation (Figure 5-11) is reminiscent of an exponentially increasing curve. This is in agreement with the observation where the peak-to-peak displacements increased over time. For Kli-Pi 1, the cumulative displacement response follows a uniform change in the slope of the curve, whereas the cumulative rotation response contains small perturbations followed by changes in the curve's slope. Considering the depth of installation, the gradient of the cumulative displacement and rotation at the end of the test are nearly equal. At the end of the experiment (120 s), the largest cumulative displacement (Kli-Pi 3) and rotation (Kli-Pi 2) was 4.0 m and 350 degrees respectively. Again, the suspected concentration of elastic energy associated with the test box likely produces the larger gradients, in addition to the boundary conditions providing greater resistance for the ballast to heave laterally over multiple sleeper spans (see Figure 2-10).

The results from the field test provide a vastly different profile compared to that of the laboratory test. Initially, the gradient of the cumulative displacement (Figure 5-10) curve is large, owing to the heavier locomotive axles. The disturbances within the first few seconds likely result from the instrument's shifting position with the confinement increasing rapidly during this initial phase with relatively large contact stresses. Thereafter, up until 34 s, the gradient remains fairly linear. The gradient of the curve increases substantially the shallower the Kli-Pi position. This effect is more prominent than in the laboratory test. For the impact loads at 32 s and 99 s, a sharp increase in the cumulative displacement is observed. This event is visible for all 4 Kli-Pis, decreasing in magnitude with increasing depth as the energy is dissipated. The final cumulative displacements of the curves vary widely, with the sleeper attaining a value (4.8 m) nearly four times that of Kli-Pi 1 (1.3 m) which is positioned within the subballast. For this metric, the cumulative displacement does indeed increase with a reduction in depth if all four of the instruments are considered. The curves of Kli-Pi 2 and 3 appear to diverge from the expected equidistant pattern; however, considering the respective positions of the Kli-Pis, it is likely that the stress value of Kli-Pi 2 and 3 are similar, owing to the overlapping stress frusta of the individual wheel loads.

The rotational response (Figure 5-11) differs significantly from that of the displacements. Kli-Pi 3 exhibits the largest gradient, followed by Kli-Pi 1, 2 and 4. Due to bias (average noise level) removal from the response, the small gradient of Kli-Pi 4 (the sleeper) does appear to reduce in value for certain periods. The large discrepancy between Kli-Pi 2 and 3 is reminiscent of the observation from Chapter 5.2. The proximity of Kli-Pi 3 to the sleeper explains the large influence of the longitudinal PSR on the cumulative rotation calculation. Besides the impact loads not influencing the curves, the transition response from locomotives to lighter wagons is distinctly delayed. Except for the sleeper (Kli-Pi 4), a smooth transition, almost viscoelastic in nature, replaces the sharp change associated with the cumulative displacement. At 50 s a small reduction in the gradient, followed again by an increase at 70 s, can be observed for all the Kli-Pis. This is in the absence of any impact loads (Figure 5-8). Through the introduction of the cumulative displacement and rotation metric, the changes of the granular fabric can indirectly be quantified.

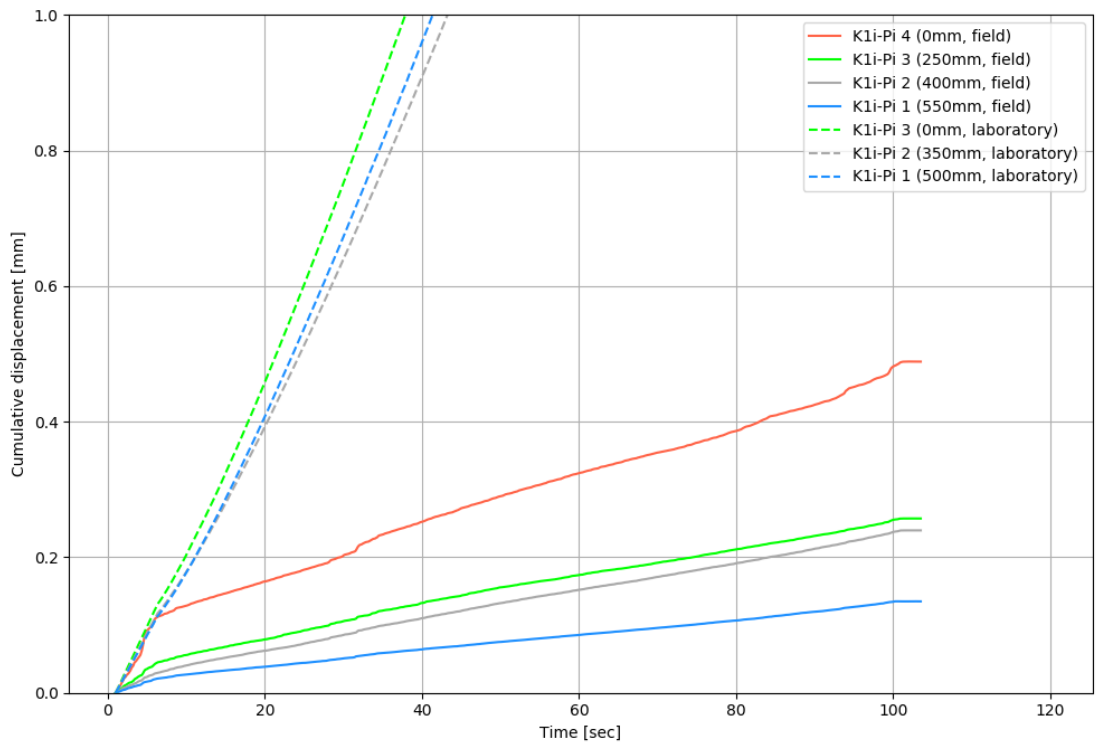


**Figure 5-10: Cumulative displacement of all Kli-Pis (field and laboratory test)**

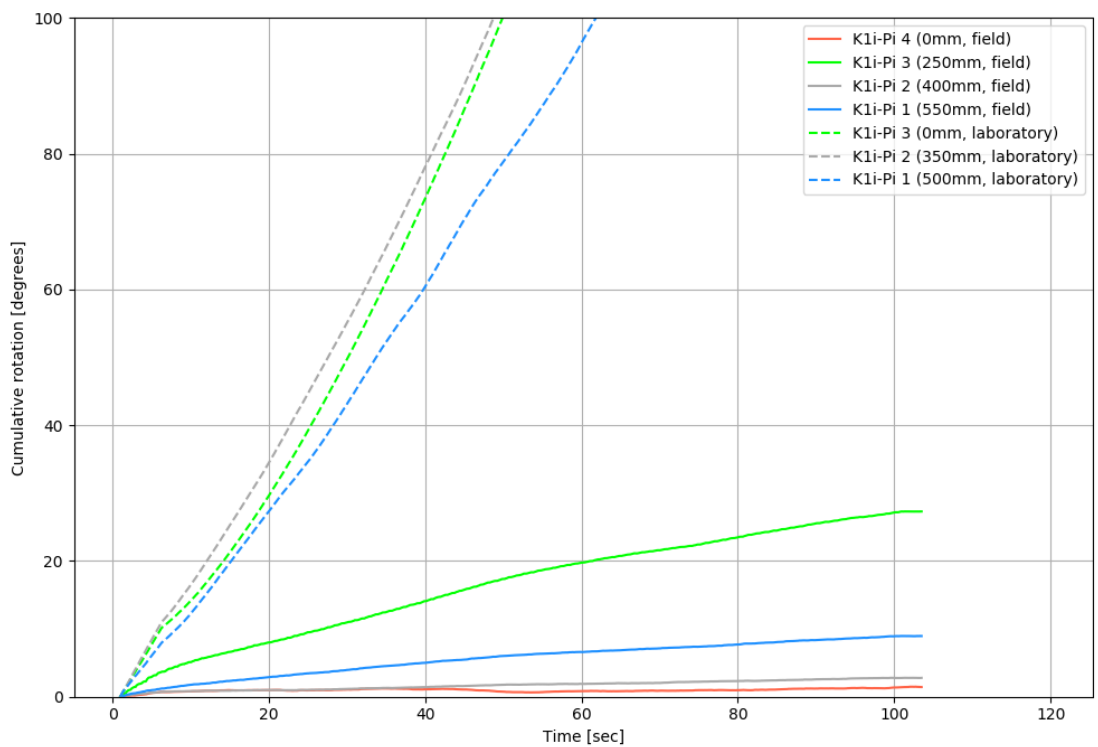


**Figure 5-11: Cumulative rotation of all Kli-Pis (field and laboratory test)**

## 5.4 STATISTICAL DESCRIPTORS

Up to this point, the overarching similarities and differences between modes and characteristics of displacement and rotation responses have been visually illustrated and discussed for two different test configurations. From both the existing literature and the matrix scatter graphs, the probabilistic nature underpinning the particle behaviour is clear (Chapter 2.5.3). Descriptive statistics can be applied to quantitatively summarize and compare the different observations. For any data set, the peak-to-peak amplitudes of the sample are of interest. Unless noted otherwise, the 2,000 largest possible peak-to-peak samples were extracted for each instrument metric (Appendix A.2.5). This value equates to approximately 10 times the number of wagons or 2.5 times the number of axles. This sample size was obtained iteratively to provide a representative sample. For the peak-to-peak displacement, rotation and work, a six parameter descriptive statistic summary is provided. It should be noted that for both the minimum and maximum measurement, percentile values of 1 and 99 are used to avoid outliers. Statistics pertaining to the minimum, mean, maximum, standard deviation, coefficient of variation and skewness of the displacement, rotation and mechanical work are investigated for both the laboratory and field tests. The results presented follow from the preceding discussion of Chapter 5.

### 5.4.1 Displacement

For the laboratory test, the mean displacement (Figure 5-12) is significantly larger than that of the field test, in addition to the dominant axis of displacement concentrated about the Z-axis. The mean displacement of Kli-Pi 2 and 3 are nearly identical, particularly in the Z-axis, which corresponds with the overlapping stress frusta.

For the field test, Kli-Pi 2 and 3 illustrate near identical mean vertical displacement. The net zero displacement stems from the intersection of the load frusta in-between the two successive Kli-Pis. The discontinuous, unbound matrix allows the particles to move to areas of low confinement (crib ballast) or alternatively be suspended in the matrix near the stress discontinuity. This limits any simple approaches pertaining to determining the strain in the different layers using discrete monitoring instrumentation. This provides evidence for the load-carrying “columns” that are periodically altered as noted by Cundall & Strack (1979). Conversely, the laboratory test provided a more uniform response in part due to the simplified load and material characteristics. Table A-1 and Table A-2 summarises the peak-to-peak displacement statistics for the laboratory and field tests respectively.

The coefficient of variance (CoV), for any axis, corresponds with the depth of installation (Figure 5-13). For the laboratory test, the shallower the instrument is positioned, the smaller the CoV parameter. For the field test, the converse is true; the shallower instruments experience a substantially larger CoV. The magnitude of the CoV is significantly larger for the field test which can be attributed to the varying loading conditions and attenuation of different frequencies.

The skewness of the distribution (Figure 5-14) provides information surrounding the “tail” of the data. Positive values of skewness describe a “heavier” tail with larger value. The skewness indirectly relates the coordination number to the shape of the probability density function (Chapter 2.5.3). With an increasing confinement stress, the shape of the PDF shifts from exponential to Gaussian (Kruyt & Rothenburg, 2002) and in turn decreases the skewness of the data. For the laboratory test, the skewness is practically identical for the two Kli-Pis positioned in the ballast. The skewness of the lateral directions (1.3) is significantly larger than those in the vertical direction (0.85). This substantially larger lateral stiffness stems from the use of the rigid laboratory test box.

For the skewness statistic of the field test (Figure 5-14), the composition of locomotive and wagon loads provides a significantly larger skewness ratio than for the laboratory results. For Kli-Pi 3, situated directly beneath the sleeper, the skewness accurately describes the predicted behaviour regarding confinement. Considering all possible degrees of freedom, the ballast is the least confined in the longitudinal or X-axis as the ballast tends to spread out from underneath the sleeper. The X-axis is furthermore the most sensitive to additional friction forces as a result of the positive track gradient. Hence, the skewness is nearly twice as large in the X-axis compared to the other two axes, supporting the findings of Kruyt & Rothenburg (2002). The same phenomena hold true for Kli-Pis 1 and 2 with increasing depth providing increasingly isotropic confinement with an associated decrease in skewness.

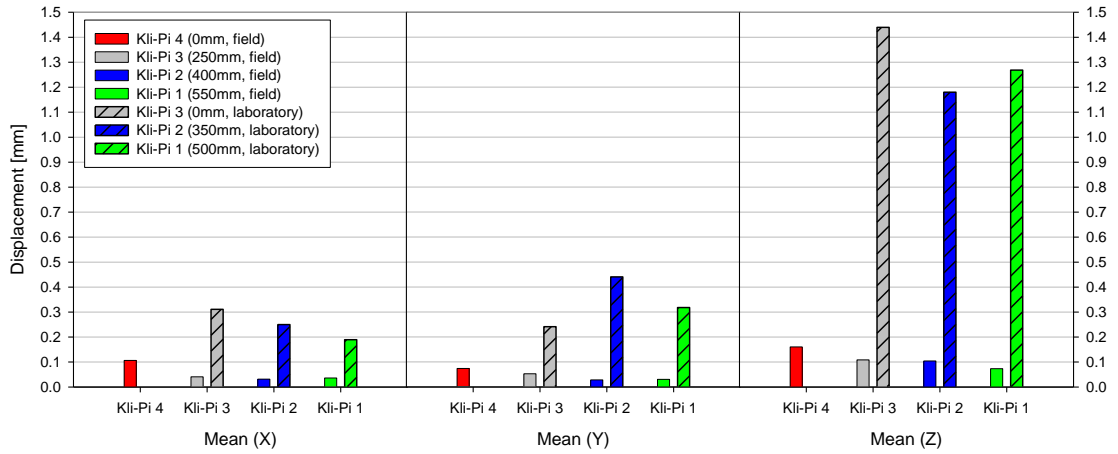


Figure 5-12: Displacement: mean for all axes (field and laboratory test)

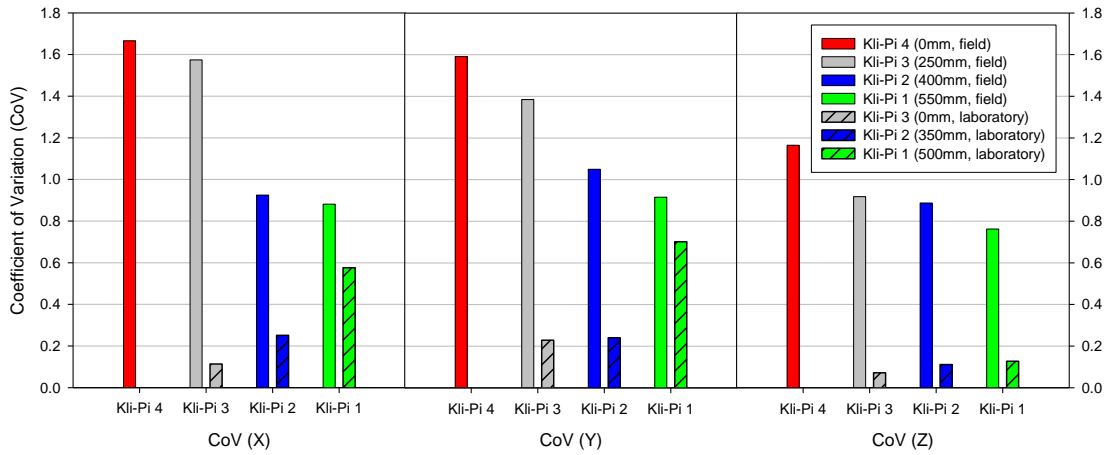


Figure 5-13: Displacement: coefficient of variance for all axes (field and laboratory test)

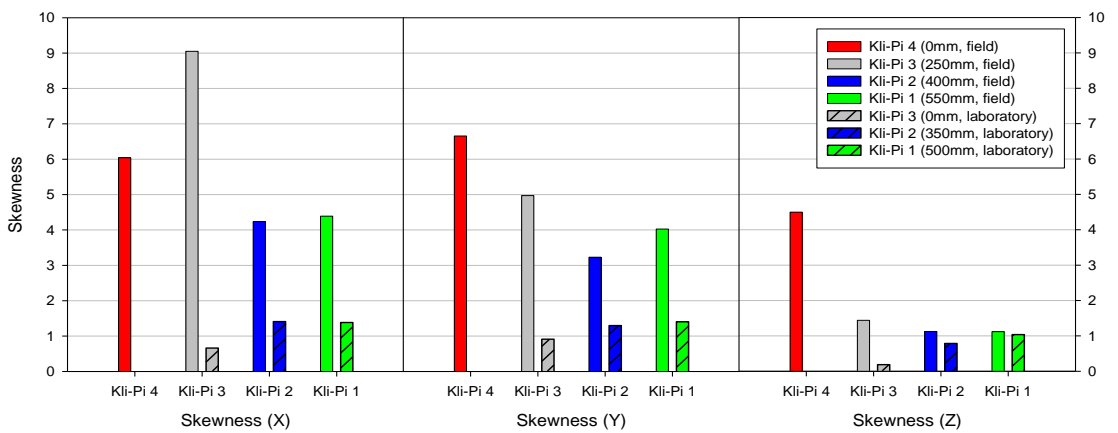


Figure 5-14: Displacement: skewness for all axes (field and laboratory test)

### 5.4.2 Rotation

For ease of interpretation and readability, the rotation amplitude in the graphs is provided in units of arc minutes, where one degree is equal to sixty arc minutes. Table A-3 and Table A-4 summarise the peak-to-peak rotation statistics for the laboratory and field tests respectively. Concerning the mean peak-to-peak rotation for the laboratory test (Figure 5-15), the primary axis of rotation varies depending on the Kli-Pi position with no clear relationship with the depth of installation, except for the X-axis. The magnitude of the rotations is substantially smaller for the field test, but exhibits a higher degree of uniformity among all the Kli-Pis.

For the field test, Kli-Pi 3 positioned beneath the sleeper experiences the largest mean rotation of all the instruments due to its proximity to the sleeper. These observations are in agreement with the findings of Gräbe & Clayton (2009) where transverse PSR can be expected near the end of the sleeper. The second largest rotation is attributed to the Kli-Pi positioned at the subballast interface (Kli-Pi 1) instead of in the middle of the ballast layer (Kli-Pi 2). Secondly, the most unfavourable combination of stresses can be expected to occur near the mid-depth of the subballast, corroborating the rotation measurements of Kli-Pi 1 which was positioned at the subballast interface.

For the laboratory test, the CoV for the rotations (Figure 5-16) tends to increase the shallower the instrument, similar to the CoV for the displacements (Figure 5-13). The small magnitude of the yaw or Z-axis rotation of the sleeper tends to distort the CoV even for a small variance.

For the field test, the influence of the longitudinal principal stress rotation about the X-axis is again visible. Unlike the decreasing CoV for the Y-axis (lateral) and Z-axis (yaw), the variance about the X-axis increases with depth, likely as this axis of rotation follows the shear failure plane in the shoulder ballast. The range of CoV for the field rotation is substantially smaller (0.35 – 0.85) than that of the displacement (0.8 – 1.6).

The skewness of rotation (Figure 5-17) for both the laboratory and field tests is substantially lower than the comparative skewness of the displacement. For the field test, the largest skewness corresponds to the instrument at the greatest depth and confinement (Kli-Pi 1). Kli-Pi 3 situated beneath the sleeper again exhibits lower skewness owing to the reduced confinement, similar to the observation for the displacement. There is no clear correlation between the rotation's skewness statistic and the depth of installation.

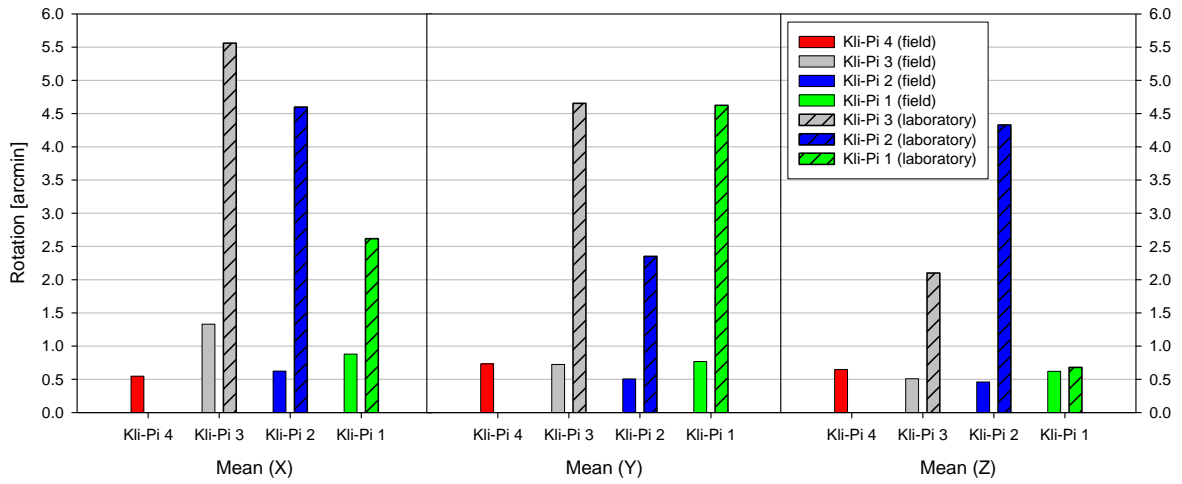


Figure 5-15: Rotation: mean for all axes (field and laboratory test)

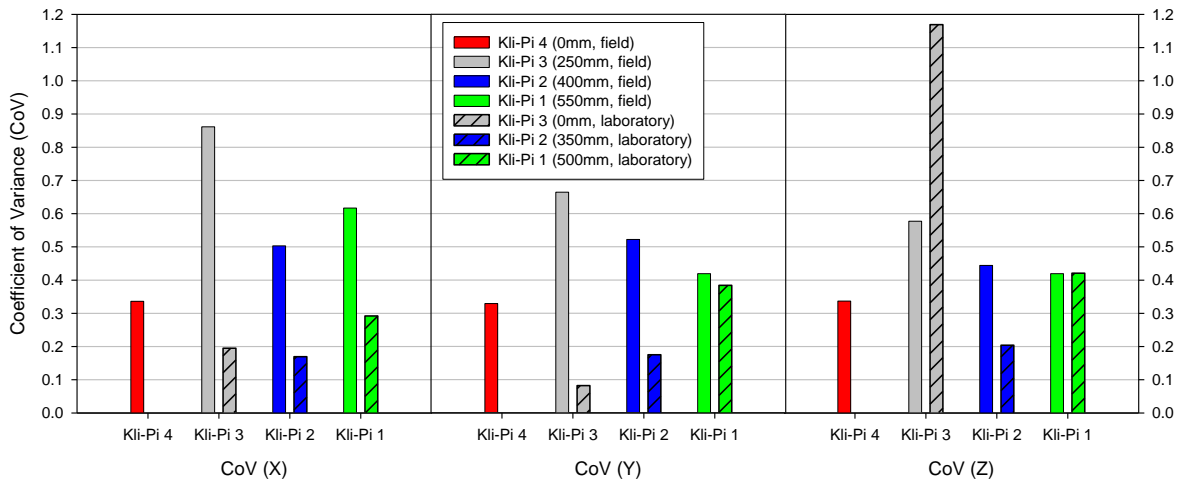


Figure 5-16: Rotation: coefficient of variance for all axes (field and laboratory test)

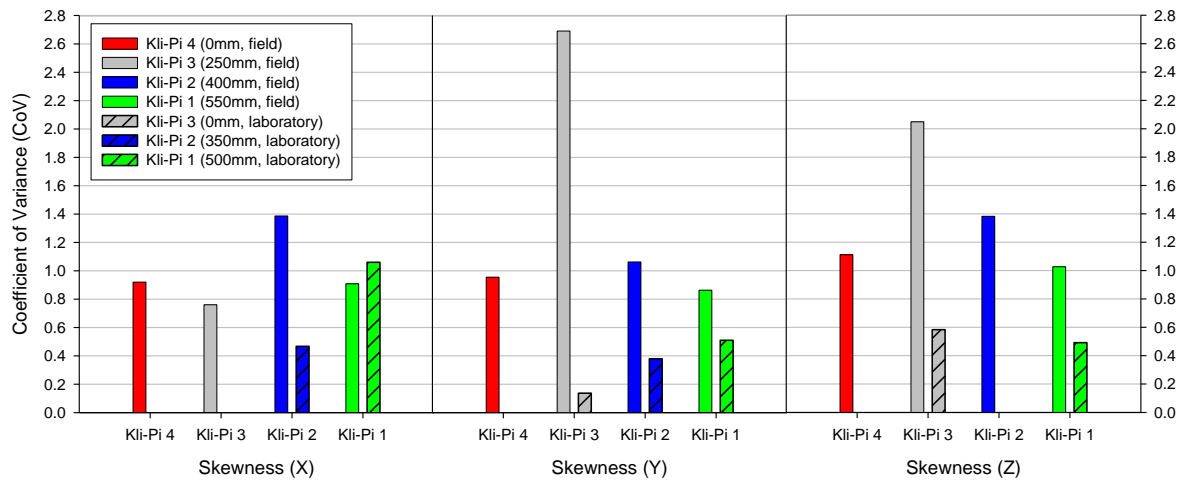


Figure 5-17: Rotation: skewness for all axes (field and laboratory test)

### 5.4.3 Mechanical Work

Finally, the same set of statistics can be applied to the mechanical work. Of all the statistics investigated, the mechanical work provides the most representative results which can be simplified to a quantitative, unambiguous parameter. The work associated with each Kli-Pi in the laboratory test illustrates a great degree of uniformity for the mean, minimum and maximum energy (Figure 5-18). This uniformity is reflected in the small CoV among the Kli-Pis (Figure 5-19).

Comparing the mean energy of the field test to that of the laboratory test (Figure 5-18), the mean amplitude for the field test is approximately an order of magnitude smaller. With the introduction of impact loads, the maximum energy is significantly larger in proportion to the mean and minimum amplitudes. Again, this observation is reflected in the coefficient of variance (Figure 5-19) that is substantially larger than that of the laboratory test. It is noteworthy that the standard deviation, coefficient of variation and skewness statistic of the field test illustrates a *negative* correlation (Figure 5-19) with an increase in depth, exemplifying the fundamental probabilistic dynamics of the ballast.

The Kli-Pis associated with the greatest depth, i.e. in a confined granular state, appear to converge towards a skewness value of 1.1 for both tests. This decrease in skewness corresponds to an increasingly uniform distribution as discussed in Chapter 5.1.1. The large degree of skewness associated with the sleeper could be attributed to the influence of large lateral and longitudinal forces that is rapidly attenuated by the superstructure components. The peak-to-peak statistics for the mechanical work are summarised in Table A-5 and Table A-6 for the laboratory and field tests respectively.

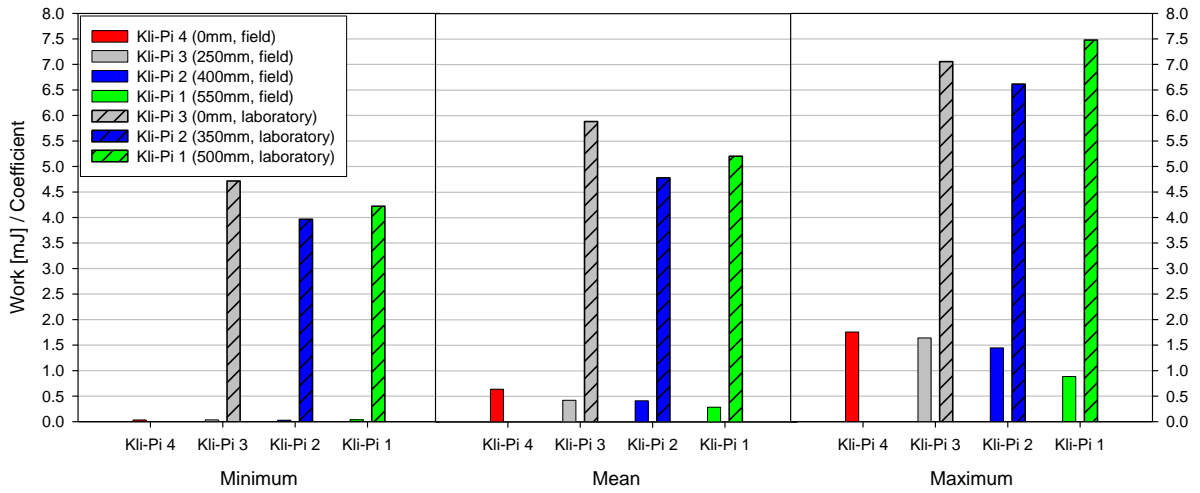


**Figure 5-18: Mechanical work: minimum, mean maximum (field and laboratory test)**

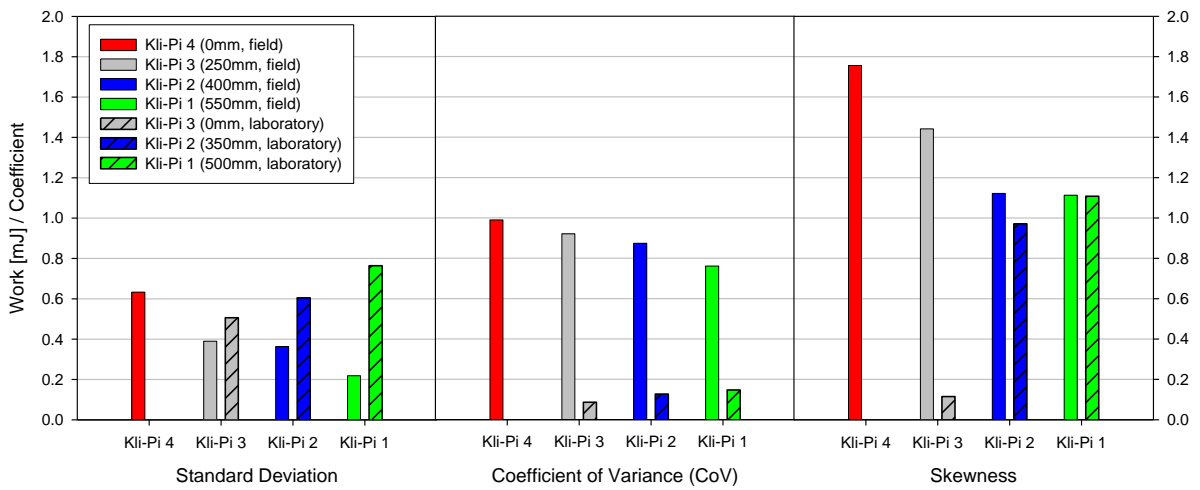


**Figure 5-19: Mechanical work: standard deviation, coefficient of variance (CoV) and skewness (field and laboratory test)**

## **6 CONCLUSIONS AND RECOMMENDATIONS**

In Chapter 1.1, it was noted that the operational performance of ballast appears trivial in its simplicity. The effects of the various mechanisms on the mesoscale performance of the ballast were quantified in significant detail through the development and introduction of new instrumentation, known as Kli-Pi. The recorded particle dynamics was simplified and analysed to provide new performance statistics pertaining to the interaction among the surrounding particle matrix, the quasi-static deformation response and influence of the confining environment with two different test configurations. Cowin & Satake (1979) mentions the importance of these studies to *quantify* the fundamental mechanical behaviour, furthering the understanding of the granular media. The conclusions and recommendations are presented, addressing each of the objectives outlined in Chapter 1.2.

### **6.1 CONCLUSIONS**

#### **6.1.1 Kli-Pi Development and Implementation**

The introduction of Kli-Pi introduced a completely new and novel method to investigate granular materials with greater ease, flexibility and accuracy than has been possible before. With the increasing availability of high-performance consumer-grade electronics, the very definition of instrumentation is continuously evolving toward an environment of low-cost, customizable hardware and increasing ease of implementation for civil engineers. The design and development process of Kli-Pi was dictated by the requirements set out for the intended experimental environments. The calibrated performance of Kli-Pi was found to be comparable to commercial hardware at significantly lower costs, producing accurate, high density data sets for analysis. The information from multiple instruments produced new findings pertaining to ballast dynamics.

### 6.1.2 Mesoscale Behaviour of Discrete Ballast Particles

From the existing literature, extensive discussion surrounds the influence of lateral and longitudinal forces, particle breakage and rearrangement, principal stress rotation and spectral frequencies pertaining to the granular and ballast layers. These topics remain, to a large degree, confined to theoretical discussion and investigation. Considering the limited set of quantitative, experimental data - spanning a period of only two minutes - the information presented provide valuable insight and supportive evidence of existing theories and formulations.

For the field test, longitudinal deflections highlight the large contribution of tractive forces transferred through the rail and sleeper to the ballast and subballast, with amplitudes exceeding that of the deflection in the vertical axis for locomotive axles. This phenomenon of circular displacement patterns corresponds to the numerical results by Zhang et al. (2016). Significant longitudinal movement extends to the subballast interface, where strain ratcheting is known to occur. Furthermore, contrary to traditional deterministic mechanics, the probabilistic nature of the material does not conform to uniform-strain assumptions (Kruyt & Rothenburg, 2002). Probabilistic behaviour governs the particle deflections where instances of alternating positive and negative strain are observed in the vertical direction. This limits any simplistic approaches pertaining to determining the strain in the different layers using discrete monitoring instrumentation. This provides evidence for the load-carrying “columns” that are periodically altered as noted by Cundall & Strack (1979). The laboratory test provided a more uniform response in part due to the simplified load and material characteristics.

The rotation can be considered as a combination of contact stresses and principal stress rotation. The smaller variance of the rotations, compared to that of the displacements, is indicative of a reduced sensitivity toward the mesoscale response instead of a macroscopic response. Chapter 5.4.2 highlighted the respective contributions of the longitudinal PSR from the sleeper ends and the influence on the subballast interface. The rotation statistic appears insensitive towards the depth of installation with the corresponding coefficient of variance markedly smaller than that of the displacements. This in turn provides the potential for the instrument to be used as an accurate, in-situ axle counter. The importance of quantifying the rotation is further highlighted by the viscoelastic response for the cumulative rotation when the heavier locomotives are succeeded by the light wagons, which is notably absent for the cumulative displacement response. Changes in the cumulative displacement and rotation illustrate the changes of the granular fabric, affecting all the Kli-Pis and visible as a change in the gradient of the curve.

The maximization of the available sampling frequency sensor bandwidth provided additional capabilities in investigating the spectral frequencies and energies at different depths of instrumentation. For both the experiments, the largest component of the energy is concentrated along the vertical direction, parallel to the direction of the load. The passage of the locomotives coincided with significant longitudinal and lateral forces from the tractive effort, the influence of which extended to the subballast interface. The high frequency spectra observed is associated with the ballast-sleeper resonance (Figure 2-2). This is in agreement with the analytical findings of Kouroussis et al. (2015), Li et al. (2015) and Zhang et al. (2016) in addition to laboratory testing results from Zhai et al. (2004). The increasing concentration of energy about the specific frequency for both the experiments is indicative of increasing confinement. This corresponds to the stabilization of peak-to-peak amplitudes associated with the SmartRock experimentation (Liu et al., 2016).

### 6.1.3 Energy Principles and Statistical Descriptors

The work energy parameter, accounting for all three spatial dimensions, provides the most representative information. It is an unambiguous parameter for the movement, rearrangement and breakage of particles, the magnitude of the quasi-static and impact loads with depth and illustrates the significant amounts of energy contributed from the locomotives that account for the lateral and longitudinal movement. The distinction between kinetic and potential energy illustrates the influence of high frequency impact events. The laboratory test illustrated minor deviations among the minimum, maximum and mean statistics with near equal maximums for all the Kli-Pis. For the field test, the maximum energy is nearly five times greater than the mean, but shows a decrease in energy for both the statistics with an increase in depth. The influence of the superimposed load frustra on the statistics is also clear. For the statistical descriptors, the observations of Rothenburg & Kruyt (2009) surrounding the probability density function (PDF) for a specific coordinate number (CN), is significant. The Kli-Pis associated with the greatest depth, i.e. in a confined granular state, appear to converge towards a skewness of 1.1 (non-Gaussian PDF), for both the laboratory and field tests. The standard deviation, coefficient of variation and skewness statistics illustrate a *negative* correlation (Figure 5-19) with an increase in depth, exemplifying the fundamental probabilistic behaviour of the ballast.

## 6.2 RECOMMENDATIONS

Based on the results derived from development of Kli-Pi as an instrument, additional quantitative metrics have been developed and illustrated to accurately describe mesoscale ballast dynamics. Audley & Andrews (2013) noted the ideal outcome of describing the relationship between ballast particle dynamics and track stability. Information spanning a long period of time, with the inclusion of typical maintenance activities such as correction of geometry, is desired to establish such a relationship, in combination with existing measurement techniques and instrumentation. The results presented were limited to a short period of time with minimal variation in the environmental conditions and possible load distribution. The effects of ballast particle properties, level of fouling, train speed, moisture ingress and the substructure condition, all contributing to both the macroscopic and mesoscale behaviour, have not been investigated or considered in the results. Different instrumentation locations should also be explored, in particular the centre of the sleeper. The proof-of-concept has however been demonstrated.

Additional statistics present the opportunity to optimise and minimize the amount of data and processing required (e.g. Monte Carlo simulations) to obtain the same value of information. This statistics can function as a calibrated particle model for more powerful DEM simulations such as BlazeDEM (Govender, 2015). These simulations offer significantly faster testing environments for understanding degradation models and the optimization of maintenance models. The theory can be extended to pavement engineering for determining improved soil moduli for highly confined particles. Existing instruments, such as multi-depth deflectometers (MDDs), are expensive and limited in the smallest increments that differential displacement can be measured. Rothenburg & Kruyt (2009) highlight the possibility of using confidence intervals in the calculation of soil properties.

Finally with the development of increasingly sophisticated sensors and hardware, smaller instruments that can continually operate in the environment spanning longer periods of time will become available. As noted in Chapter 5.3, energy losses associated with noise and friction is theoretically quantifiable when the sensor accuracy improves to a suitable degree. Long distance communications technologies (e.g. LoRa communications) and reduction in costs will allow for the proliferation of smart devices to continuously monitor both the track and traffic levels remotely and in real-time. These smart devices can in turn provide a continuous stream of information to an intelligent system with predictive analytics to create a true “smart” railway network with real-time monitoring applications.

## 7 REFERENCES

- Aikawa, A. 2009. Techniques to Measure Effects of Passing Trains on Dynamic Pressure Applied to Sleeper Bottoms and Dynamic Behaviour of Ballast Stones. *Quarterly Report of Railway Technical Research Institute*, Volume 50, No. 2, pp 102-109.
- Audley, M. & Andrews, J.D. 2013. The Effects of Tamping on Railway Track Geometry Degradation. *Proceedings of the Institution of Mechanical Engineers, Part F: Journal of Rail and Rapid Transit*, Volume 227, Issue 4, pp 376-391.
- Bennett, R., Hayes-Gill, B., Crowe, J.A., Armitage, R., Rodgers, D. & Hendroff, A. 1999. Wireless Monitoring of Highways. *Smart Structures and Materials 1999: Smart Systems for Bridges, Structures and Highways*, Volume 3671, pp 173-182.
- Billauer, E. 2010. Peak Detection in Python. Online: <https://gist.github.com/endolith/250860>. Accessed 15 February 2018.
- Bergstrom, J.S., Quinn, D.J., Chow, S. & Govindarajan S.M. 2013. Non-Linear Viscoplastic Material Modelling of the Degradation Response of PLA. *Proceedings of the ASME 2013 Conference on Frontiers in Medical Devices: Application of Computer Modelling and Simulation*.
- Bohr, N. 1928. Das Quantenpostulat und die neuere Entwicklung der Atomistik (The Quantum Postulate and the Recent Development of Atomism). *Die Naturwissenschaften (Natural Sciences)*, Volume 16, pp 245–257.
- Broekman, A. 2017a. Kli-Pi Calibration Procedure Comparison Using a Lathe. Available at: <https://youtu.be/mX1rKXyPEjQ> (Accessed: 12 January 2018)
- Broekman, A. 2017b. 3D MakerBot Printing at UP's Makerspace. Available at: <https://youtu.be/v0HNIINEXvpA> (Accessed: 19 January 2018)
- Broekman, A. & Gräbe, P.J. 2018. Development and Calibration of a Wireless, Inertial Measurement Unit (Kli-Pi) for Railway and Transportation Applications. *37<sup>th</sup> Annual South African Transportation Conference (SATC2018)*, pp 521 - 531.

Brown, C.B. 1978. The Use of Maximum Entropy in the Characterization of Granular Media. *Proceedings of the US-Japan Seminar on Continuum Mechanics and Statistical Approaches in the Mechanics of Granular Media*, pp 98-108.

Burden, R.L., Faires, D.J. & Burden, A.M. 2016. Numerical Analysis. 10th Edition, Cengage Learning, pp 108.

Busch, P. 2008. The Time-Energy Uncertainty Relation. *Time in Quantum Mechanic*, pp 69-98.

Çelebi, M. 2006. Real-Time Seismic Monitoring of the New Cape Girardeau Bridge and Preliminary Analyses of Recorded Data: An Overview. *Earthquake Spectra*, Volume 22, No. 3, pp 609-630.

Cerna, M & Harvey, A.F. 2000. National Instruments Application Note 041: The Fundamentals of FFT-Based Signal Analysis and Measurement. Online: <http://www.iaa.ncku.edu.tw/~jjmiao/download/FFTAnalysis.pdf> (Accessed 16 February 2018)

Cowin, S.C. & Satake, M. 1979. Continuum Mechanical and Statistical Approaches in the Mechanics of Granular Materials. *Journal of Rheology*, Volume 23, No. 2, pp 243-256.

Cundall, P.A. & Strack, O.D.L. 1979. A Discrete Numerical Model for Granular Assemblies. *Géotechnique*, Volume 29, No. 1, pp 47-65.

Evans, T.M. & Brown, C.B. 2014. Microstates and Macrostructures for Granular Assemblies. *Geo-Congress 2014 Technical papers: Geo-characterization and Modelling for Sustainability*, pp 2858-2866.

Fong, W.T., Ong, S.K. & Nee, A.Y.C. 2008. Methods for in-field User Calibration of an Inertial Measurement Unit without External Equipment. *Journal of Measurement Science and Technology*, Volume 19, No. 8.

Gebre-Egziabher, D. 2004. Design and Performance Analysis of a Low-cost Aided Dead Reckoning Navigator. PhD Thesis, Stanford University, California, United States of America.

Govender, N. 2015. Blaze-DEM: A GPU Based Large Scale 3D Discrete Element Particle Transport Framework. PhD Thesis, University of Pretoria, Pretoria, South Africa.

Gräbe, P.J. & Clayton C.R.I. 2009. Effects of Principal Stress Rotation on Permanent Deformation in Rail Track Foundations. *Journal of Geotechnical and Geoenvironmental Engineering*, Volume 135, Issue 4, pp 555-565.

Graizer, V.M. 2010. Strong Motion Recordings and Residual Displacements: What Are We Actually Recording in Strong Motion Seismology? *Seismological Research Letters*, Volume 81, Issue 4, pp 635-639.

Huang, H., Tutumluer, E. 2011. Discrete Element Modelling for Fouled Railroad Ballast. *Construction and Building Materials*, Volume 25, No. 8, pp 3306-3312.

Indraratna, B., Ngo, N.T. & Rujikiatkamjorn, C. 2011. Behaviour of Geogrid-Reinforced Ballast under Various Levels of Fouling. *Geotextiles and Geomembranes*, Volume 29, Issue 3, pp 313-322.

Intel. 2016. Intel Edison Compute Module: Hardware Guide. [Online] [www.intel.com](http://www.intel.com). Available at: [https://www.intel.com/content/dam/support/us/en/documents/edison/sb/edison-module\\_HG\\_331189.pdf](https://www.intel.com/content/dam/support/us/en/documents/edison/sb/edison-module_HG_331189.pdf) (Accessed 14 January 2017)

Jacobsz, S, Kearsley, E, & Kock, J. 2014. The Geotechnical Centrifuge Facility at the University of Pretoria. *Proceedings of the 8th International Conference on Physical Modelling in Geotechnics*, 14-17 January, Perth, Australia, pp 169-174.

Jideani, T.C.U. 2018. The Development of Suitable Cyclic Loading and Boundary Conditions for Ballast Box Tests. Master of Engineering Dissertation, University of Pretoria, South Africa, pp 66.

Jekeli, C. 2001. Inertial Navigation Systems with Geodetic Applications. Walter de Gruyter, New York / Berlin, Chapter 4.2, pp 114-116.

Jia, Y.B. 2016. Computer Science 477/577 Notes. Iowa State University.

Kempe, V. 2011. Inertial MEMS: Principles and Practice. 1<sup>st</sup> Edition, Cambridge University Press.

Klar, A., Levenberg, E., Tur, M. & Zadok, A. 2016. Sensing for Smart Infrastructure: Prospective Engineering Applications. *Proceedings of the International Conference on Smart Infrastructure and Construction*, 27-29 June, ICE Publishing, United Kingdom, pp 289-295.

- Kitamura, R. 1980. Analysis of Deformation Mechanism of Particulate Material Based on the Probability Theory. PhD Dissertation, Kyoto University, Japan, pp 17.
- Kobayashi, H., Mark, B.L. & Turin, W. 2012. Probability, Random Processes and Statistical Analysis. Cambridge University Press, New York, United States of America, pp 348-352.
- Kouroussis, G., Caucheteur, C., Kinet, D., Alexandrou, G., Verlinden, O. & Moeyaert, V. 2015. Review of Trackside Monitoring Solutions: From Strain Gauges to Optical Fibre Sensors. *Sensors*, Volume 15, Issue 8, pp 20115-20139.
- Kouroussis, G., Connolly, D.P. & Verlinden O. 2014. Railway-induced Ground Vibrations – A Review of Vehicle Effects. *International Journal of Rail Transportation*, Volume 2, Issue 2, pp 69-110.
- Kruyt, N.P. & Rothenburg, L. 2002. Probability Density Functions of Contact Forces for Cohesionless Frictional Granular Materials. *International Journal of Solids and Structures*, Volume 39, pp 571-583.
- Kuipers, J.B. 2000. Quaternions and Rotation Sequences. *Proceedings of the International Conference on Geometry, Integrability and Quantization*, pp 127-143.
- Lamas-Lopez, F., Cui, Y.J., Costa Aguiar, S. & Calon, N. 2017. Assessment of Integration Methods for Displacement Determination using Field Accelerometer and Geophone Data. *Journal of Zhejiang University*, Volume 18, Issue 7, pp 553-566.
- Lekarp, F., Isacsson, U. & Dawson A. 2000. State of the Art. II: Permanent Strain Response of Unbound Aggregates. *Journal of Transportation Engineering*, Volume 126, No. 1, pp 76-83.
- Lemkin, M. & Boser, B.E. 1999. A Three-Axis Micromachined Accelerometer with a CMOS Position-Sense Interface and Digital Offset-Trim Electronics. *IEEE Journal of Solid-State Circuits*, Volume 34, No. 4.
- Li, D., Hyslip, J., Sussmann, T. & Chrismer, S. 2015a. *Railway Geotechnics*. CRC Press, pp 52-63.
- Li, D., Hyslip, J., Sussmann, T. & Chrismer, S. 2015b. *Railway Geotechnics*. CRC Press, pp 93-100.

- Lim, W.L. 2004. Mechanics of Railway Ballast Behaviour. PhD Thesis, University of Nottingham, Nottingham.
- Liu, S., Haung, H. & Qiu, T. 2015. Laboratory Development and Testing of “SmartRock” for Railroad Ballast using Discrete Element Modelling. *Proceedings of the 2015 Joint Rail Conference*, San Jose, California, United States of America.
- Liu, S., Huang, H., Qiu, T. & Gao, L. 2016a. Comparison of Laboratory Testing Using SmartRock and Discrete Element Modelling of Ballast Particle Movement. *Journal of Materials in Civil Engineering*, Volume 29, No 3, pp 1-7.
- Liu, S., Huang, H., Qiu, T. & Gao, Y. 2016b. Study on the Ballast Particle Movement at Different Locations beneath Crosstie using “SmartRock”. *Proceedings of the 2016 Joint Rail Conference*, Columbia, South Carolina, United States of America.
- Liu, S., Haung, H., Qiu, T. & Kwon, J. 2016c. Effect of Geogrid on Railroad Ballast Particle Movement. *Transportation Geotechnics*, Volume 9, pp 110-122.
- Liu, S., Haung, H., Qiu, T., Shen, S. 2018. Sensing Mechanism and Real-Time Computing for Granular Materials. *Journal of Computing in Civil Engineering*, Volume 32, Issue 4.
- Lobo-Guerrero, S. & Vallejo, L.E. 2006. Discrete Element Method Analysis of Railroad Ballast Degradation during Cyclic Loading. *Granular Matter* (8)3, pp 195-204.
- Lynch, J.P. & Loh, K. 2006. A Summary Review of Wireless Sensors and Sensor Networks for Structural Health Monitoring. *The Shock and Vibration Digest*, Volume 38, pp 91-128.
- Makse, H.A., Johnson, D.L. & Schwartz, L.M. 2000. Packing of Compressible Granular Materials. *Physical Review Letters*, Volume 84, Issue 18, pp 4160-4163.
- Milne, D., Le Pen, L., Watson, G., Thompson, D., Powrie, W., Hayward, M. & Morley, S. 2016a. Measuring Ballast Acceleration at Track Level. *Third International Conference on Railway Technology: Research, Development and Maintenance*.
- Milne, D., Le Pen L., Watson, G., Thompson, D., Powrie, W., Hayward, M. & Morley, S. 2016b. Proving MEMS Technologies for Smarter Railway Infrastructure. *3<sup>rd</sup> International Conference on Transportation Geotechnics*, Volume 143, pp 1077-1084.

Mvelase, G.M., Anochie-Boateng, J.K. & Gräbe, P.J. 2012. Application of Laser Based Technology to Quantify Shape Properties of Railway Ballast. *31<sup>st</sup> Annual Southern African Transport Conference (SATC)*, pp 243-254.

Nathanson, H.C & Wickstrom, R.A. 1965. A Resonant-Gate Silicon Surface Transistor with High-Q Bandpass Properties. *Applied Physics Letters*, Volume 7, Issue 4, pp 84.

Nathanson, H.C & Wickstrom, R.A. 1968. Microelectronic Frequency Selective Apparatus with Vibratory Member and Means Responsive Thereto. US Patent No. 3413573.

Nejikovsky, B. & Keller, E. 2000. Wireless Communications Based System to Monitor Performance of Rail Vehicles. *Proceedings of the IEEE/ASME Joint Railroad Conference*, Newark, NJ, United States of America, pp 111–124.

Rothenburg, L & Kruyt, N.P. 2009. Micromechanical Definition of an Entropy for Quasi-Static Deformation of Granular Materials. *Journal of the Mechanics and Physics of Solids*, Volume 57, pp 634-655.

Rucker, W. 1982. Dynamic Interaction of Railroad-Bed with the Subsoil. *Soil Dynamics & Earthquake Engineering Conference*, pp 435-448.

Selig, E.T. & Waters, J.M. 1994. Track Geo-technology and Substructure Management. 1st ed. London, United Kingdom: Tomas Telford Ltd.

Shannon, C.E. 1948. A Mathematical Theory of Communication. *The Bell System Technical Journal*, Volume 27, No. 3, pp 379-423.

Shi, B., Murakami, Y. & Wu., Z. 1998. Orientation of Aggregates of Fine- Grained Soil: Quantification and Application. *Engineering Geology*, Volume 50, Issues 1-2, pp 59-70.

Skog, I. & Händel, P. 2006. Calibration of a MEMS Inertial Measurement Unit. *Proceedings of the XVII IMEKO World Congress Metrology for a Sustainable Development*.

Smith, C. 2017. Equal distribution of benefits needed - WEF expert. [Online] [www.fin24.com](http://www.fin24.com). Available at: <http://www.fin24.com/Economy/equal-distribution-of-benefits-needed-wef-expert-20170904> [Accessed 9 December 2017].

Transnet Freight Rail (TFR). 1998. S406: Specification for the Supply of Stone Contents. Johannesburg: TFR.

Stewart, J. 2012. Calculus, Early Transcendentals. 7<sup>th</sup> Edition, Cengage Learning, United States of America, pp 1082.

STMicroelectronics. 2013a. H3LIS331DL MEMS Motion Sensor: Low-Power High-G 3-Axis Digital Accelerometer. [Online] [www.st.com](http://www.st.com). Available at: <https://cdn.sparkfun.com/assets/c/6/5/8/d/en.DM00053090.pdf> [Accessed 31 December 2017]

STMicroelectronics . 2013b. iNEMO Inertial Module: 3D Accelerometer, 3D Gyroscope, 3D magnetometer. [Online] [www.st.com](http://www.st.com). Available at: <https://www.mouser.com/ds/2/389/lsm9ds0-955023.pdf> [Accessed 14 January 2017]

Straser, E. G. & Kiremidjian, A.S. 1998. A Modular, Wireless Damage Monitoring System for Structures. Technical Report 128, John A. Blume Earthquake Engineering Center, Stanford University.

Tait, P.G. 1886. Quaternions. Encyclopaedia Britannica, 9<sup>th</sup> Edition, Volume 20, pp 160-164.

Titterton, D. & Weston, J. 2004. Strapdown Inertial Navigation Technology. The American Institute of Aeronautics and Astronautics, 2<sup>nd</sup> Edition.

Tutumluer, E., Huang, H., Hashash, Y. & Ghaboussi, J. 2006. Aggregate Shape Effects on Ballast Tamping and Railroad Track Lateral Stability. *Proceedings of the AREMA Annual Conference*, pp 17-20.

U.S. Department of Transportation. 2010. 2010 Status of the National Highways, Bridges, and Transit: Conditions and Performance. Report to Congress.

Wilke, D.N., Govender, N., Pizette, P. & Abriak, N.E. 2016. Computing with Non-Convex Polyhedra on the GPU. *Proceedings of the 7<sup>th</sup> International Conference on Discrete Element Methods*, pp 1371-1377.

Woodman, O.J. An Introduction to Inertial Navigation. 2007. *Technical Report*, No. 696, University of Cambridge Computer Laboratory.

Yoctopuce. 2015. The Intel Edison and Yoctopuce. [Online] Available at: <http://www.yoctopuce.com/EN/article/the-intel-edison-and-yoctopuce> [Accessed 14 January 2018]

Zaiss, C. 2012. IMU Design for High Vibration Environments with Special Consideration for Vibration Rectification. Dissertation, Master of Science, Department of Mechanical and Manufacturing Engineering, Calgary, Alberta.

Zhang, X., Zhao, C. & Zhai, W. 2016. Dynamic Behaviour Analysis of High-Speed Railway Ballast under Moving Vehicle Loads using Discrete Element Method. *International Journal of Geomechanics*, Volume 17, No. 7.

Zhai, W.M., Wang, K.Y. & Lin, J.H. 2004. Modelling and Experiment or Railway Ballast Vibrations. *Journal of Sound and Vibration*, Volume 270, pp 673-683.

## A APPENDIX

The appendix provides additional details where it is deemed applicable, especially development relating to Kli-Pi. Numerous small changes and design considerations were required that had a measurable impact on the progress of the development; software configurations, distro (Ubilinux) specific additions changes and interaction with software and design details that are easily overlooked. Each chapter in the appendix is divided into the respective sections as reflected in the layout of the primary chapter headings in the document.

### A.1 IMU Calibration Derivation and Procedure

#### A.1.1 Tri-axis Accelerometer

For a given tri-axis accelerometer, the non-orthogonal sensor frame will not be aligned with the body (or platform) frame coordinate system (Figure A-1).

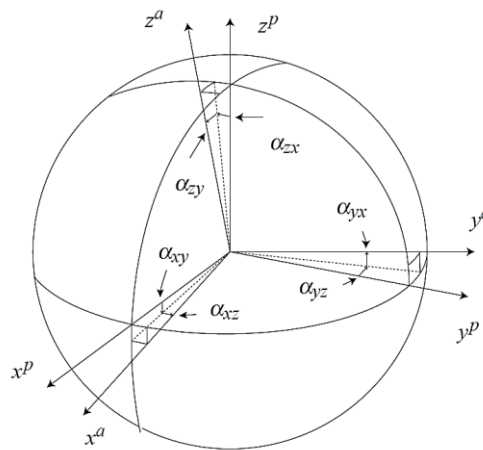


**Figure A-1: Misalignment between non-orthogonal sensors axes and the platform frame (Skog & Händel, 2006)**

To simplify the transformation matrix between the sensor and platform, it can be stated that the  $x$ -axis of the sensor and platform are aligned with one another, simplifying the representation to Equation 7-1.

$$s^p = M_a s^a = \begin{bmatrix} 1 & -\alpha_{yz} & \alpha_{zy} \\ 0 & 1 & -\alpha_{zx} \\ 0 & 0 & 1 \end{bmatrix} s^a \quad (\text{Equation 7-1})$$

Where:

$s^p$  – Specific force in platform coordinates

$s^a$  – Specific force in sensor coordinates

$M_a$  – Accelerometer misalignment matrix

Similarly, the scale factor matrix  $S_a$ , and bias vector  $b_a$ , for the accelerometer can be defined (Equation 7-2).

$$S_a = \begin{bmatrix} S_{xx} & S_{xy} & S_{xz} \\ S_{yx} & S_{yy} & S_{yz} \\ S_{zx} & S_{zy} & S_{zz} \end{bmatrix}, b_a = \begin{bmatrix} b_{x_a} \\ b_{y_a} \\ b_{z_a} \end{bmatrix} \quad (\text{Equation 7-2})$$

For an ideal accelerometer the scale factor matrix reduces to an identity matrix. Thus the relationship between the measured acceleration vector for the platform frame,  $a_{p,k}$  and the true acceleration vector,  $a_{s,k}$  is defined (Equation 7-3).

$$a_{p,k} = M_a S_a (a_{s,k} - b_a) \quad (\text{Equation 7-3})$$

Considering the effect of cross axis sensitivity and sensor misalignment to be the same, and ignoring the product of off-diagonal terms of both  $M_a$  and  $S_a$ , the diagonally dominant error matrix,  $E_a$  is defined (Equation 7-4).

$$E_a \approx \begin{bmatrix} S_{xx} & S_{xy} - S_{yy}\alpha_{yz} & S_{xz} + S_{zz}\alpha_{zy} \\ S_{yx} & S_{yy} & S_{yz} - S_{zz}\alpha_{zx} \\ S_{zx} & S_{zy} & S_{zz} \end{bmatrix} = \begin{bmatrix} e_{00} & e_{01} & e_{02} \\ e_{10} & e_{11} & e_{12} \\ e_{20} & e_{21} & e_{22} \end{bmatrix} \quad (\text{Equation 7-4})$$

The error model for the accelerometer can now be rewritten (Equation 7-5).

$$a_{p,k} = E_a (a_{s,k} - b_a) \quad (\text{Equation 7-5})$$

The error parameters of the cost function are defined by vector  $\theta_a$  (Equation 7-6).

$$\theta_a = [e_{00} \ e_{01} \ e_{02} \ e_{10} \ e_{11} \ e_{12} \ e_{20} \ e_{21} \ e_{22} \ b_x \ b_y \ b_z] \quad (\text{Equation 7-6})$$

Equation 7-7 defines a function  $h$  that relates the measured acceleration vector for the platform frame,  $a_{P,k}$  and the true acceleration vector  $a_{S,k}$ .

$$h(a_{S,k}, \theta_a) = E_a(a_{S,k} - b_a) = a_{P,k} \quad (\text{Equation 7-7})$$

For an ideal tri-axis accelerometer, the following statement must hold as stated by Skog & Händel: “*the magnitude of the static acceleration measured must equal that of the gravity vector*”. Assuming that the uncalibrated gravitational acceleration  $G$  is constant, the cost function can be defined to measure the amount of deviation from unity for  $N$  sets of measurement (Equation 7-8).

$$A_a(\theta_a) = \sum_{n=0}^{N-1} (1 - \|h(a_{S,k}, \theta_a)_n\|^2)^2 \quad (\text{Equation 7-8})$$

### A.1.2 Tri-axis Gyroscope

Before commencement of the gyroscope calibration, it is required that the complimentary IMU accelerometer has already been calibrated according to the procedure detailed in Appendix A.1.1. Fong et al. (2008) expands upon the notion of calibrating the IMU gyroscope without precision instruments. Due to the random drift errors that are present, all bias values are first subtracted from the dataset. The same methodology is followed for the gyroscope as with the accelerometer to define the sensor axes misalignment, scale factors and cross-axis sensitivities. The angular velocity vector  $\omega$  is expressed in radians per second. The misalignment correction matrix  $M_g$  is specified in full, where there is no predefined alignment, unlike Skog & Handel’s model. The scale factor matrix  $S_g$  is identical to that of the accelerometer. Thus the relationship between the measured angular vector for the platform frame,  $\omega_{P,k}$  and the true angular vector,  $\omega_{S,k}$  is defined (Equation 7-9).

$$\omega_{P,k} = M_g S_g(\omega_{S,k}) \quad (\text{Equation 7-9})$$

Where:

$$S_g = \begin{bmatrix} S_{xx} & S_{xy} & S_{xz} \\ S_{yx} & S_{yy} & S_{yz} \\ S_{zx} & S_{zy} & S_{zz} \end{bmatrix}$$

$$M_g = \begin{bmatrix} 1 & -\alpha_{yz} & \alpha_{zy} \\ \alpha_{xz} & 1 & -\alpha_{zx} \\ -\alpha_{xy} & \alpha_{yx} & 1 \end{bmatrix}$$

Cross-axis sensitivities are not distinguished in a separate step or matrix, instead simplifying to Equation 7-10:

$$\omega_{P,k} = E_g(\omega_{S,k}) \quad (\text{Equation 7-10})$$

Where:

$$E_g \approx \begin{bmatrix} S_{xx} & S_{xy} - S_{yy}\alpha_{yz} & S_{xz} + S_{zz}\alpha_{zy} \\ S_{yx} + S_{xx}\alpha_{xz} & S_{yy} & S_{yz} - S_{zz}\alpha_{zx} \\ S_{zx} - S_{xx}\alpha_{xy} & S_{zy} + S_{yy}\alpha_{yx} & S_{zz} \end{bmatrix} = \begin{bmatrix} e_{00} & e_{01} & e_{02} \\ e_{10} & e_{11} & e_{12} \\ e_{20} & e_{21} & e_{22} \end{bmatrix}$$

A cost function is defined by  $\Gamma$  that integrates a sequence of angular velocities  $\omega_{P,k}$ , from  $k = 0$  to  $k = N$ , starting from the initial gravity vector  $u_0$  which is defined by the IMU's calibrated accelerometer. The gravity vector  $u_g$  at step  $N$  is defined by the uncalibrated gyroscope (Equation 7-11).

$$u_g = \Gamma(\omega_{P,k}, u_0) \quad (\text{Equation 7-11})$$

Any orientation integration algorithm can define  $\Gamma$ , integrating the angular velocity vectors  $\omega_{P,k}$ , to establish the updated orientation vector. The orientation is represented using quaternion operations with a second-order numerical integration algorithm (Appendix A.2.1). The quaternion  $q_k$ , can be related to the quaternion from the previous step  $q_{k-1}$  (Equation 7-12).

$$q_k = \left[ \cos\left(0.5|\delta\beta|I + \frac{1}{|\delta\beta|}\sin(0.5|\delta\beta|)B\right) \right] q_{k-1} \quad (\text{Equation 7-12})$$

Where:

$$\delta\beta = \omega_{P,k}$$

$$\Delta t = \begin{pmatrix} \delta\beta_x \\ \delta\beta_y \\ \delta\beta_z \end{pmatrix}$$

$$|\delta\beta| = \sqrt{\delta\beta_x^2 + \delta\beta_y^2 + \delta\beta_z^2}$$

$$B = \begin{pmatrix} 0 & \delta\beta_x & \delta\beta_y & \delta\beta_z \\ -\delta\beta_x & 0 & \delta\beta_z & -\delta\beta_y \\ -\delta\beta_y & -\delta\beta_z & 0 & \delta\beta_x \\ -\delta\beta_z & -\delta\beta_y & -\delta\beta_x & 0 \end{pmatrix}$$

$$I = \begin{pmatrix} 1 & 0 & 0 & 0 \\ 0 & 1 & 0 & 0 \\ 0 & 0 & 1 & 0 \\ 0 & 0 & 0 & 1 \end{pmatrix}$$

$\Delta t$  – Time interval between measurements

The quaternions are calculated for the sequence from  $k = 0$  to  $k = N$  until the final orientation is represented by  $q_n = (a, b, c, d)^T$ , for which the rotation matrix  $R$  (Jekeli, 2001) is defined by Equation 7-13:

$$R = \begin{pmatrix} a^2 + b^2 - c^2 - d^2 & 2(bc + ad) & 2(bd - ac) \\ 2(bc - ad) & a^2 - b^2 + c^2 - d^2 & 2(cd + ab) \\ 2(bd + ac) & 2(cd - ab) & a^2 - b^2 - c^2 + d^2 \end{pmatrix} \quad (\text{Equation 7-13})$$

The estimated gravity vector  $u_g$ , is obtained from the transformation of the starting gravity vector  $u_0$  (Equation 7-14).

$$u_g = Ru_0 \quad (\text{Equation 7-14})$$

The error parameters for the cost function are defined by the vector  $\theta_g$  (Equation 7-15).

$$\theta_g = [e_{00} \ e_{01} \ e_{02} \ e_{10} \ e_{11} \ e_{12} \ e_{20} \ e_{21} \ e_{22}] \quad (\text{Equation 7-15})$$

For an ideal tri-axis gyroscope, the following statement must hold as formulated by Fong et al.: *“the magnitude of the static acceleration measured must equal that of the gravity vector computed using the IMU orientation integration algorithm, which in turn uses the gyroscopes”*. This property holds whenever the IMU is static after an arbitrary motion. Assuming that the uncalibrated gravitational acceleration  $G$  is constant, the cost function is defined to measure the amount of deviation from unity for  $N$  sets of measurement. The cost function measures the norm of the difference between the estimated gravity vector  $u_g$ , and the calibrated gravity vector using the static accelerometer  $u_a$  (Equation 7-16).

$$A_g(\theta_g) = \sum_{n=0}^{N-1} \left\| (u_a - u_g)_n \right\|^2 \quad (\text{Equation 7-16})$$

### A.1.3 Calibration Procedure

The authors recommend that more sets of data are gathered than the number of unknown variables, to avoid inadequate systems in the function space that reduce the probability of finding the optimal solution vector. It was found that a minimum angular difference of  $10^\circ$  between static states produced satisfactory results. Rotations should not be reversed as this cancels out any error terms, leading to diverging vector terms. A simple hinged platform was assembled from recycled material (Figure A-2). The IMU unit is fixed on the steel plate with Prestik (also referred to as Blu Tack). For each of the axes of the body frame, the IMU is rotated a full  $\sim 210^\circ$  about the hinge. For each successive rotation, the unit is first rotated  $\sim 45^\circ$  about the vertical axis. After 8 rotations the IMU is in the same orientation as the first measurement of the set; each major axis is successively rotated for additional measurements to acquire a total of 24 data sets. The solver of choice is a downhill simplex method that is provided by the SciPy (Scientific Python) Python module. This allows specification of the starting vector, the number of iterations to be executed and the suitable stop criterion. The starting vector of the uncalibrated IMU is that of an ideal IMU (Equation 7-17).

$$\begin{bmatrix} \theta_a \\ \theta_g \end{bmatrix} = \begin{bmatrix} 1 & 0 & 0 & 0 & 1 & 0 & 0 & 0 & 1 & 0 & 0 & 0 \\ 1 & 0 & 0 & 0 & 1 & 0 & 0 & 0 & 1 & - & - & - \end{bmatrix} \quad (\text{Equation 7-17})$$



**Figure A-2: Calibration tool assembly with a rotating platform about the hinge**

As an example, the first IMU prototype was calibrated with the following vectors obtained after the optimization process:

$$E_{a1} = \begin{bmatrix} 1.0075 & 0.0048 & -0.0007 \\ 0.0063 & 1.0238 & -0.0018 \\ 0.0007 & 0.0034 & 1.0115 \end{bmatrix}$$

$$b_{a1} = \begin{bmatrix} -0.0257 \\ -0.0142 \\ -0.0466 \end{bmatrix}$$

$$E_{g1} = \begin{bmatrix} 1.1176 & 0.0313 & -0.0032 \\ -0.0163 & 1.1312 & -0.0141 \\ -0.0040 & -0.0032 & 1.1414 \end{bmatrix}$$

The scale factors of the accelerometer closely match a value of unity. The bias vector was observable before calibration took place and is the largest source of error for small accelerations. The gyroscope scale factors are approximately 13% above unity, meaning that the angular vector reported from the sensor frame is smaller than the true angular vector. For both the sensors, the cross axis sensitivities and non-orthogonality account for minimal deviation from the true measurement. For all four IMU prototypes, similar calibration factors were obtained, indicating that all the sensors likely formed part of the same manufacturing batch.

## A.2 Software Analysis and Implementation

A summary of the analysis workflow using Python is summarised. This workflow can be subdivided according to calibration and orientation methods, filtering consideration, approximation and integration methods, frequency domain transformations and peak identification.

### A.2.1 Calibration and Orientation Methods

After the calibration procedure (Chapter 3.6), the set of calibration factors are applied to the data sets using matrix multiplication, which are represented in the sensor coordinate frame. Every set of recorded data is bound to have stationary portions of data - these inactive states can be removed to minimize the amount of data that requires processing. By calculating the average variance for each accelerometer axis, the static positions of data can be automatically calculated and removed. These static portions of data are used to calculate the orientation of the sensor frame relative to the global frame, ultimately aligning the arbitrary sensor frame to the global frame.

Any orientation or reorientation scheme is traditionally expressed using three Euler angles. These angles describe the orientation of a body (sensor) relative to a fixed (global) coordinate system. Euler rotations can however reach a state of singularity, otherwise referred to as gimbal locking, whereby the pitch ( $\theta$ ) assumes a value of  $\pm 90^\circ$  (Gebre-Egziabher, 2004). The alignment of two of the three axes leads to the loss of one DoF. Quaternion representations of orientations circumnavigate this problem and simplify transformations in the Euclidian space using successive matrix multiplication operations. It can be considered an improvement upon Cartesian geometry by representing the isotropic Euclidian space with a 4-dimensional vector, comprised of three imaginary components and one real component (Tait, 1886).

Thus, for any given acceleration, velocity and displacement vector recorded by the IMU with respect to the sensor coordinate frame, the transformation operation for all the measurements can be expressed in the global frame. The quaternion (Equation 7-18) can be represented as either the sum of real and imaginary numbers or as a vector defining the element in  $\mathbb{R}^4$  (Kuipers, 2000):

$$q = q_0 + iq_1 + jq_2 + kq_3 = (q_0, q_1, q_2, q_3) \quad (\text{Equation 7-18})$$

Equation 7-19 expresses the relationship among the imaginary components:

$$i^2 = j^2 = k^2 = ijk = -1 \quad (\text{Equation 7-19})$$

The relationship between the quaternion and its inverse is given by Equation 7-20.

$$q^{-1}q = qq^{-1} = 1 \quad (\text{Equation 7-20})$$

The initial pitch and roll rotation are obtained from the static portion of the data of the tri-axis accelerometer, with the yaw component assumed to be zero (Chapter 3.7.3). The rotation vector in Euclidian geometry ( $\mathbb{R}^3$ ) can be expressed as a pure quaternion ( $\mathbb{R}^4$ ) whose real component is equal to zero (Figure A-3). Any unit quaternion  $q$ , can be expressed with Equation 7-21.

$$q = q_0 + \bar{q} = \cos \theta + \bar{u} \sin \theta; \bar{u} = \frac{\bar{q}}{|\bar{q}|}, \tan \theta = \frac{|\bar{q}|}{q_0} \quad (\text{Equation 7-21})$$

Kuipers (2000) states the theorem of the quaternion operator for the transformation of  $\bar{v} \rightarrow q$  can be expressed using Equation 7-22.

$$L_{q^{-1}}(\bar{v}) = q^* \bar{v} q = w = (q_0^2 - |\bar{q}|^2) \bar{v} + 2(\bar{q} \cdot \bar{v}) \bar{q} + 2q_0(\bar{q} \times \bar{v}) \quad (\text{Equation 7-22})$$

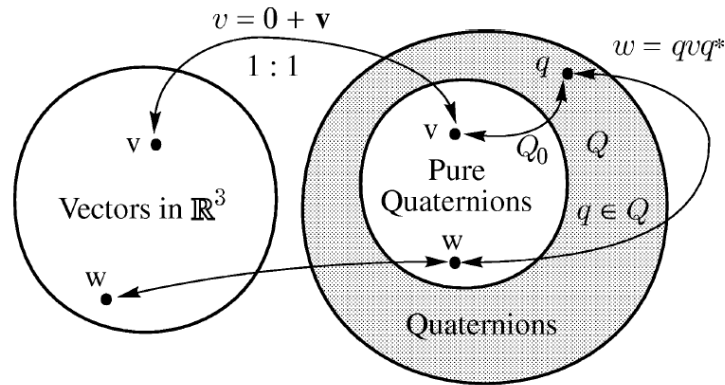


**Figure A-3: Relationship between vectors in Euclidian geometry and quaternions  
(Kuipers, 2000)**

This operation is the equivalent of rotating of an arbitrary coordinate frame through an angle of  $2\theta$ , about  $\bar{q}$ , with respect to vector  $\bar{v}$ . A similar methodology can be followed to perform the reverse operation that is  $q \rightarrow \bar{v}$ . This transformation provides the quaternion rotation necessary to align the sensor to the global frame. This starting orientation need only be applied to the first data sample at time  $t_{N=0}$  for accurate gyroscopic readings. For arbitrary small rotations this transformation is applied to the entire data set. The gyroscopic readings, expressed as angular velocity, relate the change in attitude of the IMU between successive measuring points. Given the small rotations associated with the particle embedded in the soil strata, a less accurate but faster integration method that is discussed in Appendix A.1.2 is implemented. It can be proven (Jia, 2016) that for a given angular velocity vector  $\dot{\omega}$  recorded by the gyroscope at time step  $n$ , the relationship between two successive quaternions separated over a time period  $\Delta t$  can be expressed using Euler's method of numerical integration (Equation 7-23):

$$q_{n+1} = q_k + \frac{1}{2} \Delta t \dot{\omega} q_k \quad (\text{Equation 7-23})$$

### A.2.2 Filtering Considerations

Lamas-Lopez et al. (2017) concluded that more than 95% of the measured displacement is constituted from frequencies below 25 Hz – 85% for wavelengths longer than the bogie distance and 10% for wavelengths between axle and bogie distances. Moreover, taking into account accelerometer measurements that require double integration together with the Nyquist criterion, a minimum sampling frequency of 250 Hz is required if representative displacements are to be recorded. Eliminating samples with frequencies above half the sampling frequencies prevents erroneous representations of the spectra. Moreover, the type of signal processing has a strong influence when considering integration of geophone and accelerometer data. Studies of strong-motion movement associated with earthquakes concluded that the estimation of permanent displacements presents complexities, even with highly accurate instrumentation, due to low-frequency responses of the displacement (Graizer, 2010). For each integration step, Lamas-Lopez et al. implemented a high-pass filter to eliminate the baseline readings, followed by a low-pass filter ( $f_c = 1.5 \text{ Hz}$ ). The frequency value was chosen based upon the operating velocity of the train, together with the baseline defects present after integration of the signal. This method does however exclude frequency responses below the selected cut-off value. The choice of a Butterworth filter is based upon its simplicity when compared to an elliptical or Chebyshev filter, requiring only the cut-off frequency and the filter order. The choice of a higher order filter defines a sharper transition that eliminates frequencies between 0 Hz and the low value cut-off frequency (1.5 Hz).

Based on the work of Lamas-Lopez et al. (2017), Milne et al. (2016b) and Chapter 3, a Butterworth filter of order 3 with a frequency band of 4 – 200 Hz was implemented for both the accelerometer and gyroscope data (Chapter 3.6.1) that provided the required accuracy over the operational frequency range of the IMU (Figure 3-10). For each integration operation, e.g. integrating acceleration to velocity, the lower cut-off frequency is divided by two.

### A.2.3 Approximation and Integration Methods

To compare orientation and displacement information, the angular velocity and linear acceleration require single and double integration respectively. Whenever a higher order integration method such the Simpson method is implemented, the integrated function will only consists of half the number of samples compared to that of the original function. This creates complexities in processing different sets of data, each corresponding to a different sampling rate and time-axis array. This can be avoided if the number of samples is artificially increased prior to an integration operation. This operation is referred to as “super sampling”. For increased accuracy, a modified, 2<sup>nd</sup> order, Lagrange interpolation polynomial is implemented to approximate the recorded, discrete function. The general form of the interpolation polynomial (Burden et al., 2016) is given by Equation 7-24.

$$L_{n,k}(x) = \prod_{\substack{i=0 \\ i \neq k}}^n \frac{(x-x_i)}{(x_k-x_i)} \quad (\text{Equation 7-24})$$

Given the fixed sampling rate and interpolation scheme, the Lagrange interpolation polynomial can be simplified to a general expression to provide the interpolated function value. Equation 7-25 expresses the interpolated function value  $f(x_{int})$ , situated between points  $x_{i-1}$  and  $x_i$ , with the addition of point  $x_{i+1}$  for increased accuracy:

$$f(x_{int}) = 0.375x_{i-1} + 0.75x_i - 0.125x_{i+1} \quad (\text{Equation 7-25})$$

Once the super sampled data array is calculated using the function above, Simpson’s method is employed to numerically integrate the data set. The same function is used to super sample the corresponding time axis. If there are an uneven number of samples, the last entry of the array is discarded. After integration the new array will have two less the number of samples of the original array due to the integration procedure. Once all integration operations have been completed, the arrays are truncated to ensure all remaining operations are based on samples of a fixed length.

#### A.2.4 Frequency Domain Transformation

The Fast Fourier Transform (FFT), derived from Discrete Fourier Transform (DFT), produce the average frequency content of a signal over the entire time period that the signal was acquired (Cerna & Harvey, 2000). FFT-based signal analysis can be extended to include the Power Spectrum and Cross Power Spectrum. The resolution and frequency range of a spectrum plot is dependent on both the number of points acquired over the sampling window and sampling rate. Both a sufficient sampling frequency, together with an adequate number of samples, is required in order to obtain a sufficient spectral resolution. The frequency resolution  $\Delta f$ , can be expressed as a function of both the number of samples  $N$ , and the length  $\Delta t$ , over which the window was sampled (Equation 7-26).

$$\Delta f = \frac{1}{N\Delta t} \quad (\text{Equation 7-26})$$

Where a FFT analysis of a sample provides information on the spectrum of frequencies of the sampling window, a spectrograph visually represents these spectra as a function of time. The relative amplitude of each frequency spectra is illustrated by the intensity of the colour scale, providing a third dimension of information on a single graph. For example, Kouroussis et al. (2014) assessed the transfer of energy through different track materials by a train using a power spectrum density of the recorded data. The power spectrum provides the mean squared amplitude at each frequency interval (Cerna & Harvey, 2000). Each component in the frequency domain can be assessed based on the track structure response. Furthermore, it is known that the dynamic effects on the track materials are attenuated according to the distance from the source (Kouroussis et al., 2015). The power spectrum density method normalizes the amplitude spectrum to that which would be measured by a 1 Hz-wide, square filter centred at a particular frequency line. For a signal measured in units of Voltage, the units of measurement would be  $V/\sqrt{Hz}$  for the amplitude spectral density. A reciprocal relationship does however exist for the degree of accuracy to which the frequency and temporal dimensions can be calculated for a spectrogram that stem from the Fourier analysis' uncertainty relations (Busch, 2008). This wave analogy corresponds to the time-energy uncertainty relation proposed by Bohr (1928). The analogous formulation relates the position and momentum of a particle, to which a limit exists for the accuracy or certainty between the two conjugate variables (Equation 7-27).

$$\Delta t \Delta E \geq h \leftrightarrow \Delta x \Delta p \geq h \quad (\text{Equation 7-27})$$

The implication of this constraint is the clarity with which spectrographic information can be expressed. The spectrogram functions provided with Python can be configured to set both the desired length of the data sample (or sampling window) and the number of samples for the FFT over the length of the data set. A suitable combination of these variables was found through iterative optimization to best represent the inherent characteristic of the data sets. For the purposes of the research objectives, a higher degree of accuracy of the frequency spectra is desired to resolve geometry dependant dynamic excitation, rather than the time dimension. Even though the time domain is of a lower resolution, it remains clear enough to distinguish locomotives from wagons and periodic characteristics from abrupt movement incidents within the layers. A formal definition of the power spectral density function is explained in depth by Kobayashi (2012). For FFT analysis, the magnitude of the power spectrum density is defined as the algebraic length of the vector array (composed of both real and imaginary components).

### **A.2.5 Peak Identification**

One of the most suitable methods to quantify and compare measurements for cyclic responses is calculating the peak-to-peak differences. This is equally suited for both linear and rotational modes of movement. Billauer (2010) employs a method to find the highest point surrounded by two lower points. This avoids the need for either filtering the signal or applying the zero-derivate method. The software, originally programmed for MATLAB, has since been ported to Python providing an automated means to quantify the peak-to-peak measurements. The threshold value is chosen as a fraction of the mean value for a particular data set such that the number of peaks is equal to or greater than ten times the axle count.

### A.3 Laboratory Testing Graphs

A hyperlinked summary of the graphs that follow:

Figure A-4: Time-domain deflection: X-axis of all Kli-Pis (laboratory test, detailed)

Figure A-5: Time-domain deflection: Y-axis of all Kli-Pis (laboratory test, detailed)

Figure A-6: Time-domain deflection: Z-axis of all Kli-Pis (laboratory test)

Figure A-7: Time-domain deflection: Y-axis of all Kli-Pis (laboratory test)

Figure A-8: Time-domain deflection: all axes of Kli-Pi 3 (0mm, laboratory test)

Figure A-9: Spectrographic acceleration: Z-axis of Kli-Pi 2 (350mm, laboratory test)

Figure A-10: Spectrographic deflection: Z-axis of Kli-Pi 2 (350mm, laboratory test)

Figure A-11: Spectrographic deflection: X-axis of Kli-Pi 2 (350mm, laboratory test)

Figure A-12: Spectrographic deflection: Y-axis of Kli-Pi 2 (350mm, laboratory test)

Figure A-13: Time-domain rotation: all axes of Kli-Pi 1 (500mm, laboratory test)

Figure A-14: Time-domain rotation: all axes of Kli-Pi 2 (350mm, laboratory test)

Figure A-15: Time-domain rotation: all axes of Kli-Pi 3 (0mm, laboratory test)

Figure A-16: Time-domain rotation: all axes of Kli-Pi 1 (500mm, laboratory test)

Figure A-17: Time-domain rotation: all axes of Kli-Pi 3 (0mm, laboratory test)

Figure A-18: Time-domain displacement matrix: Kli-Pi 1 (500mm, laboratory test)

Figure A-19: Time-domain displacement matrix: Kli-Pi 1 (500mm, laboratory test, detailed)

Figure A-20: Time-domain displacement matrix: Kli-Pi 2 (350mm, laboratory test)

Figure A-21: Time-domain displacement matrix: Kli-Pi 2 (350mm, laboratory test, detailed)

Figure A-22: Time-domain displacement matrix: Kli-Pi 3 (0mm, laboratory test)

Figure A-23: Time-domain displacement matrix: Kli-Pi 3 (0mm, laboratory test, detailed)

Figure A-24: Time-domain rotation matrix: Kli-Pi 1 (500mm, laboratory test)

Figure A-25: Time-domain rotation matrix: Kli-Pi 1 (500mm, laboratory test, detailed)

Figure A-26: Time-domain rotation matrix: Kli-Pi 2 (350mm, laboratory test)

Figure A-27: Time-domain rotation matrix: Kli-Pi 2 (350mm, laboratory test, detailed)

Figure A-28: Time-domain rotation matrix: Kli-Pi 3 (0mm, laboratory test)

Figure A-29: Time-domain rotation matrix: Kli-Pi 3 (0mm, laboratory test, detailed)

Figure A-30: Time-domain displacement: all Kli-Pis (laboratory test, 60 degrees)

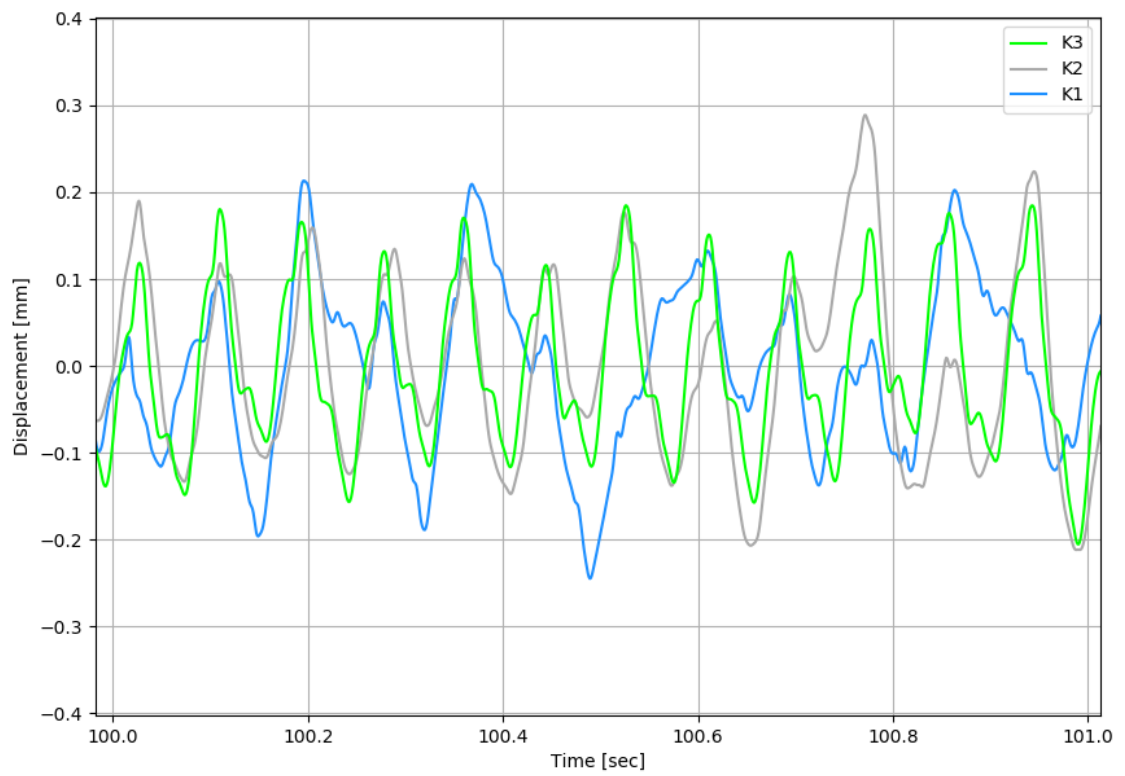
Figure A-31: Time-domain displacement: all Kli-Pis (laboratory test, 120 degrees)

Figure A-32: Time-domain displacement: all Kli-Pis (laboratory test, 210 degrees)

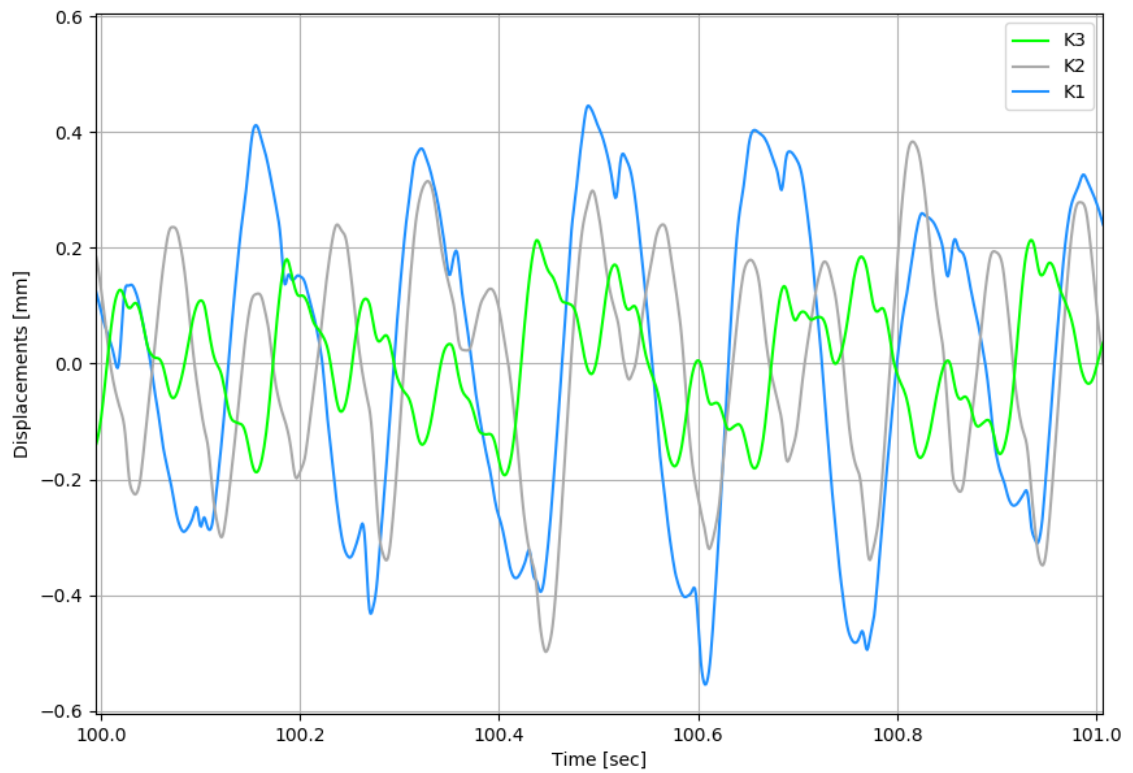
Figure A-33: Time-domain rotation: all Kli-Pis (laboratory test, 60 degrees)

Figure A-34: Time-domain rotation: all Kli-Pis (laboratory test, 120 degrees)

Figure A-35: Time-domain rotation: all Kli-Pis (laboratory test, 210 degrees)



**Figure A-4: Time-domain deflection: X-axis of all Kli-Pis (laboratory test, detailed)**



**Figure A-5: Time-domain deflection: Y-axis of all Kli-Pis (laboratory test, detailed)**

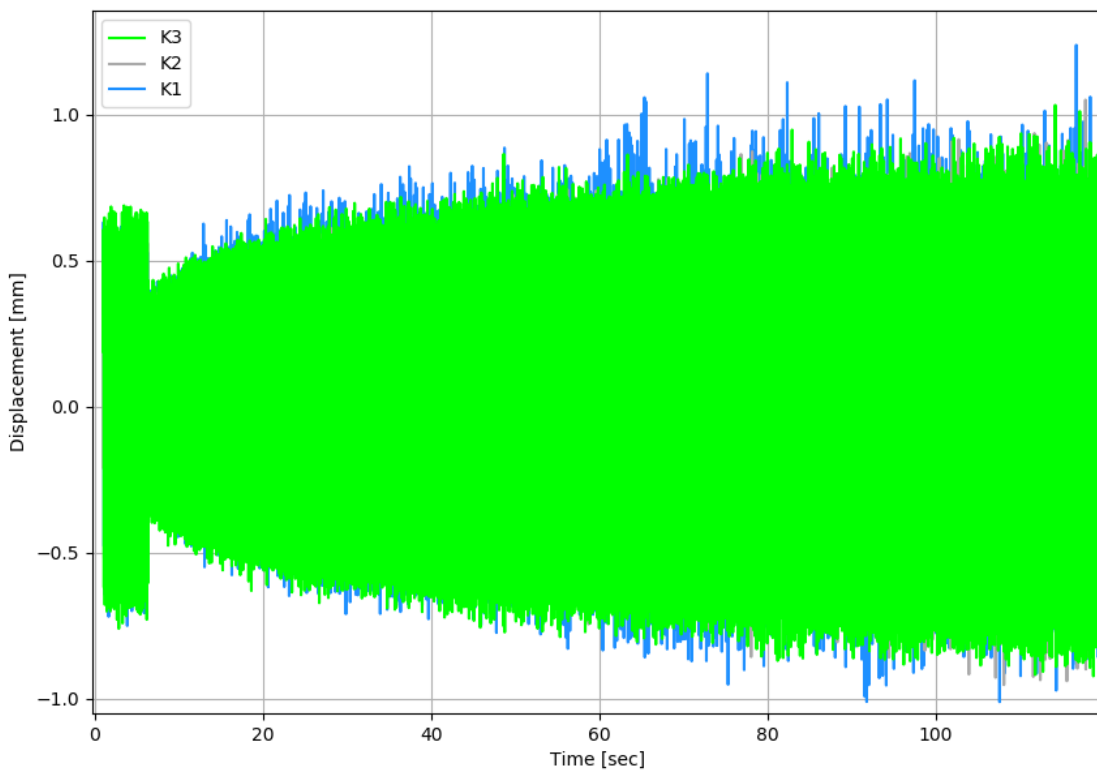


**Figure A-6: Time-domain deflection: Z-axis of all Kli-Pis (laboratory test)**

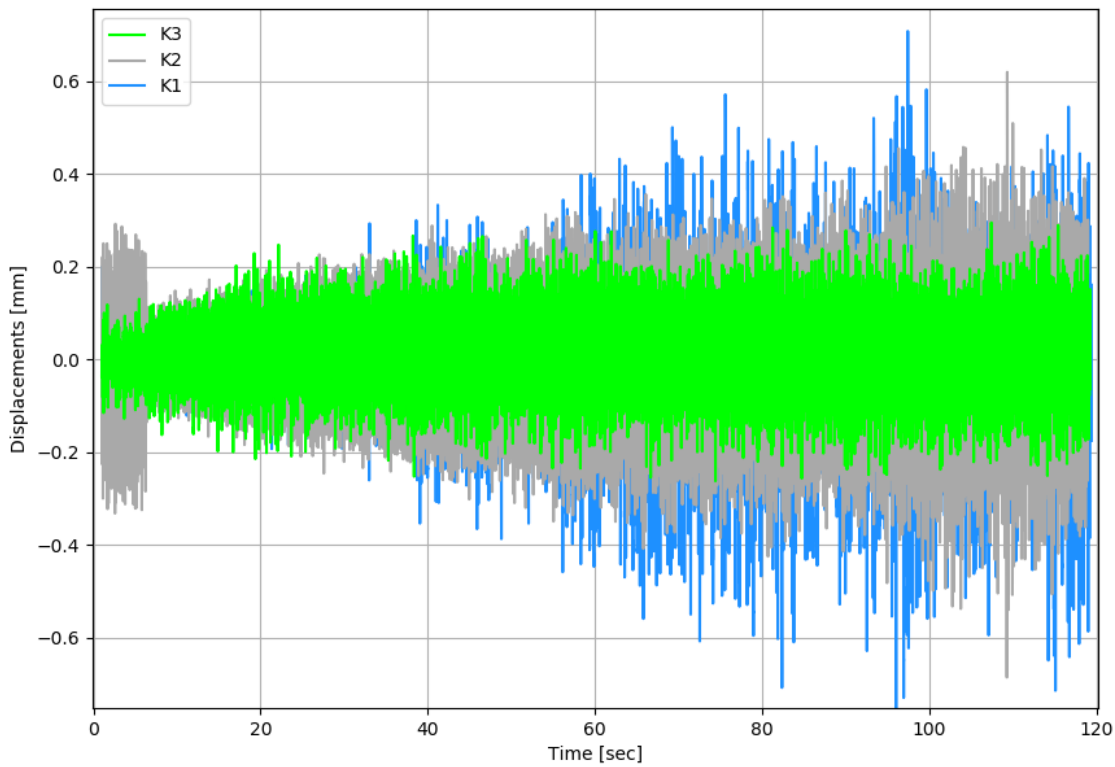


**Figure A-7: Time-domain deflection: Y-axis of all Kli-Pis (laboratory test)**

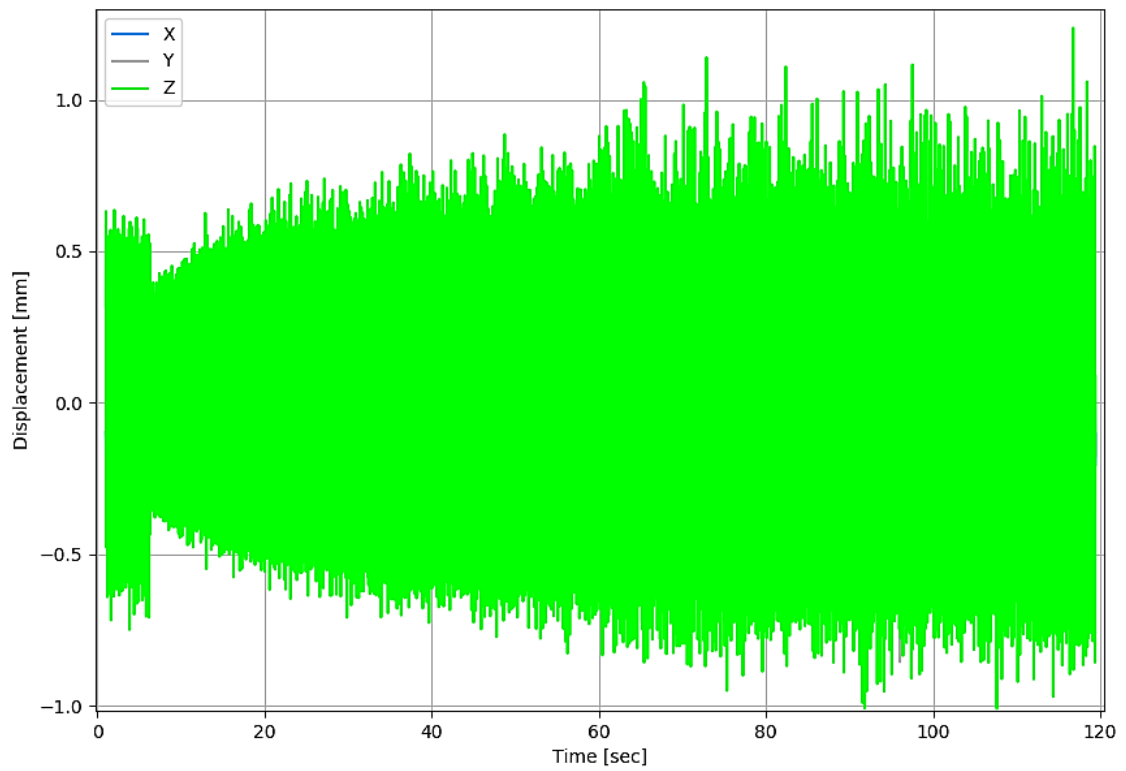


**Figure A-8: Time-domain deflection: all axes of Kli-Pi 3 (0mm, laboratory test)**

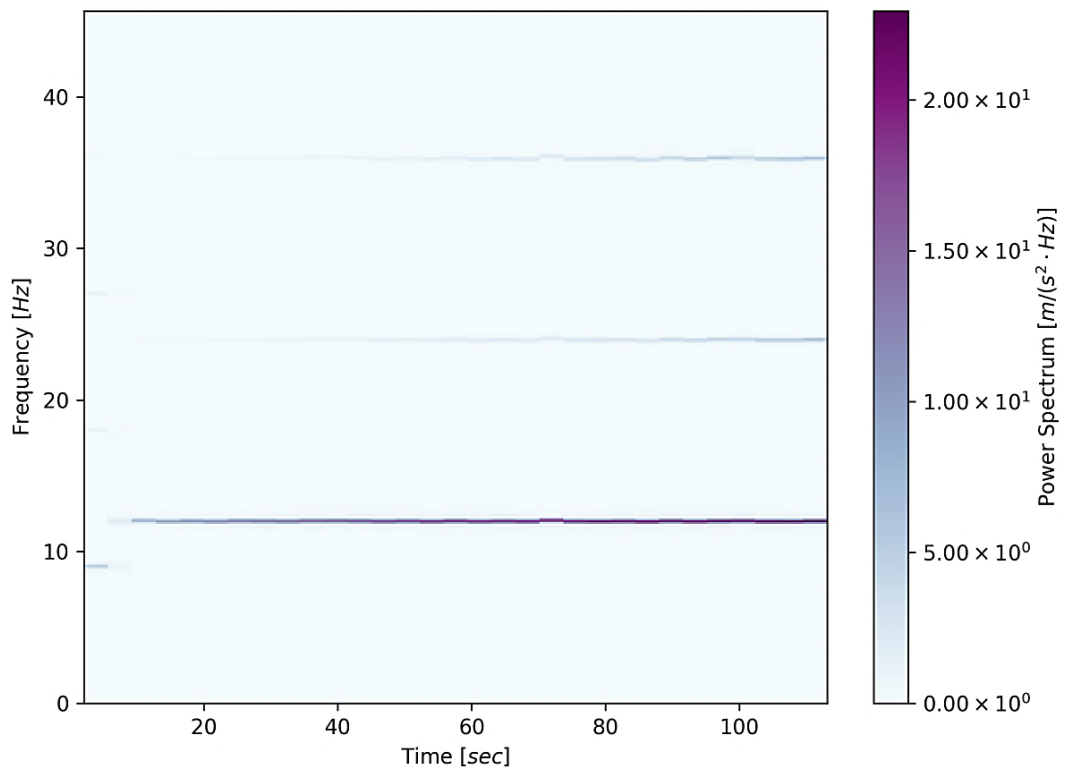


**Figure A-9: Spectrographic acceleration: Z-axis of Kli-Pi 2 (350mm, laboratory test)**

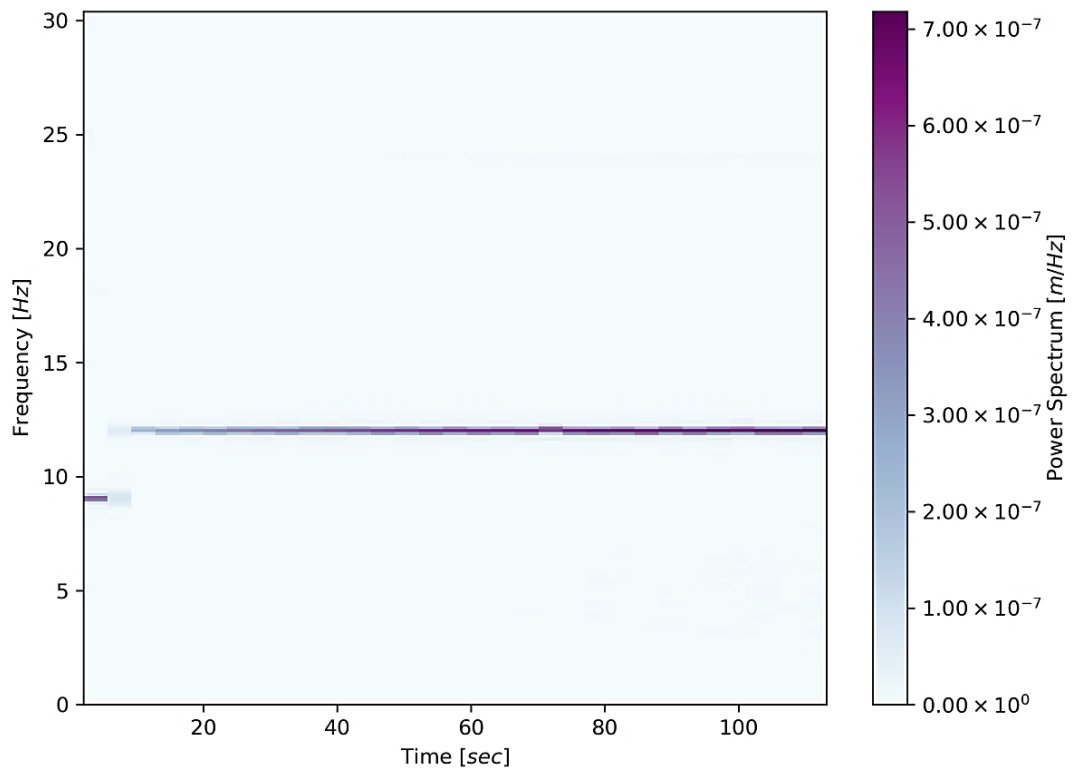


**Figure A-10: Spectrographic deflection: Z-axis of Kli-Pi 2 (350mm, laboratory test)**

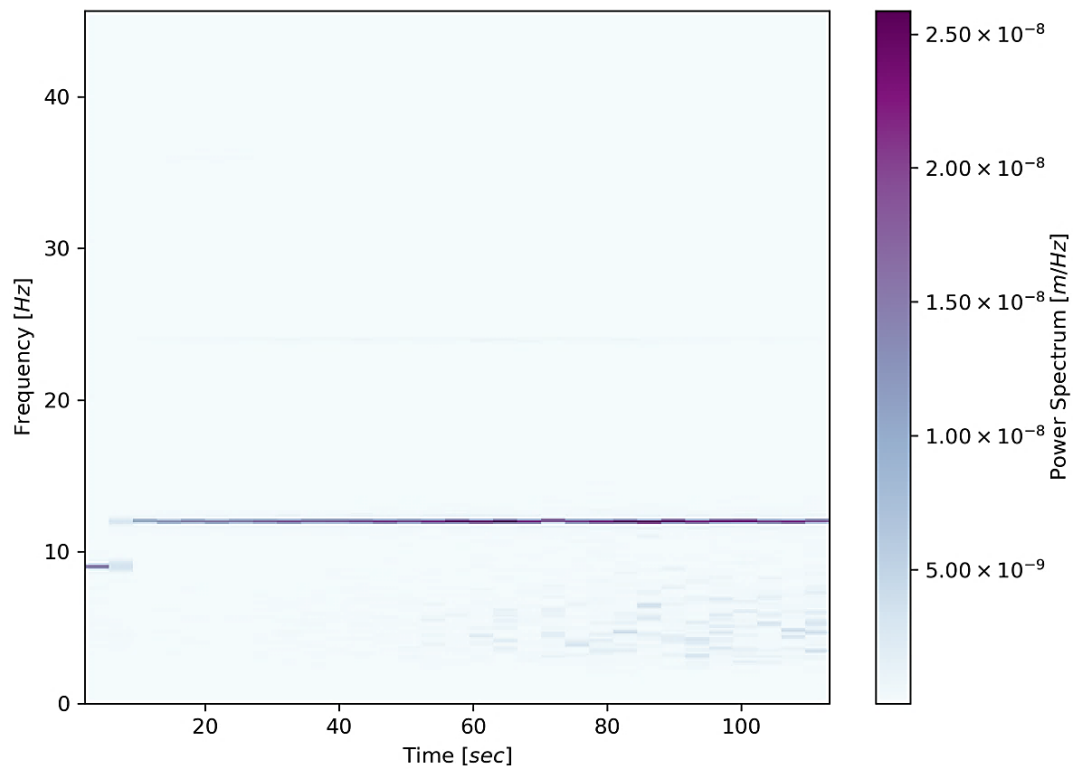


**Figure A-11: Spectrographic deflection: X-axis of Kli-Pi 2 (350mm, laboratory test)**

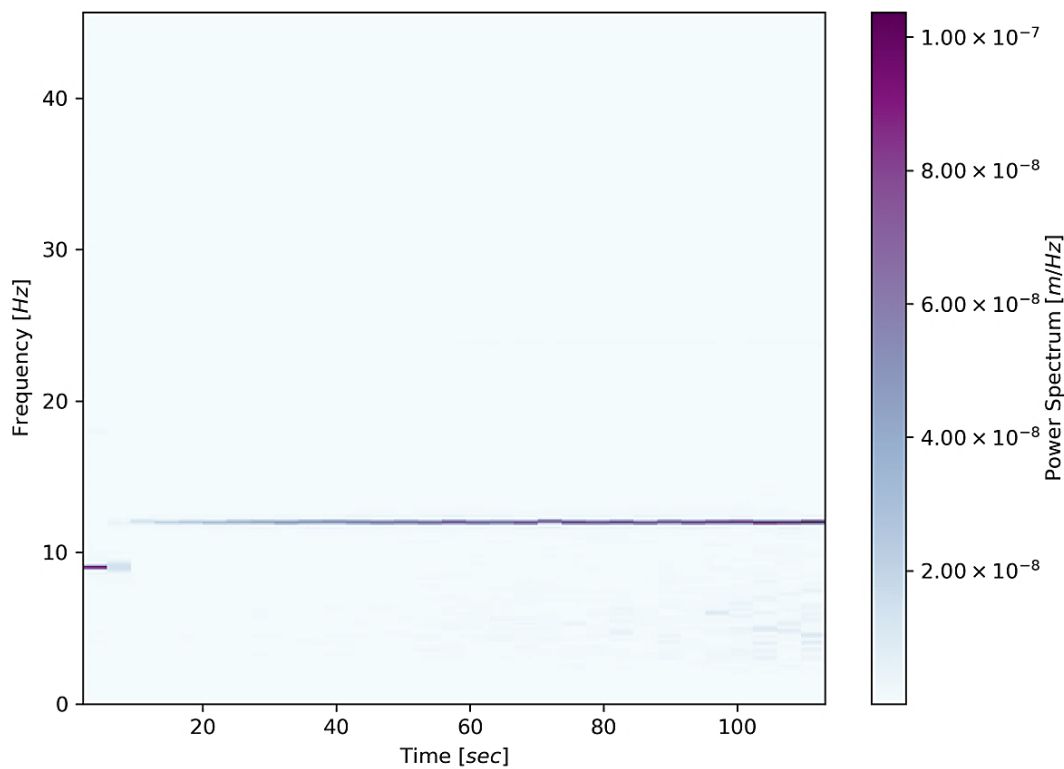


Figure A-12: Spectrographic deflection: Y-axis of Kli-Pi 2 (350mm, laboratory test)

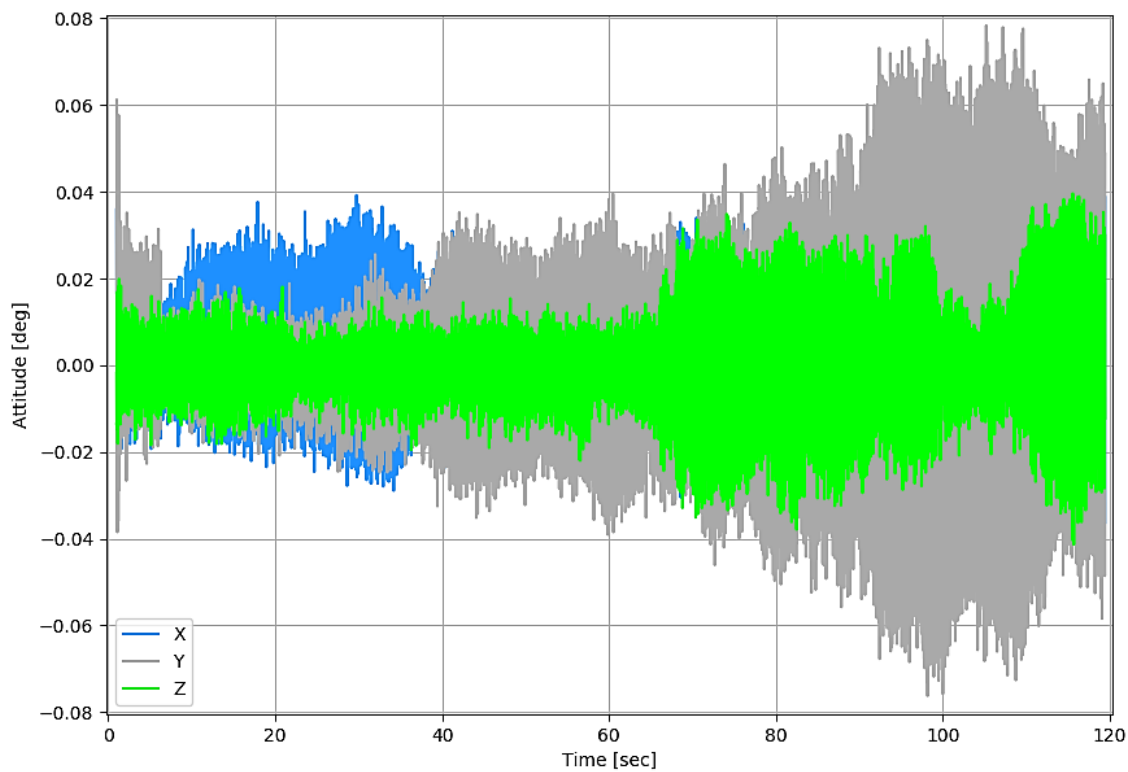
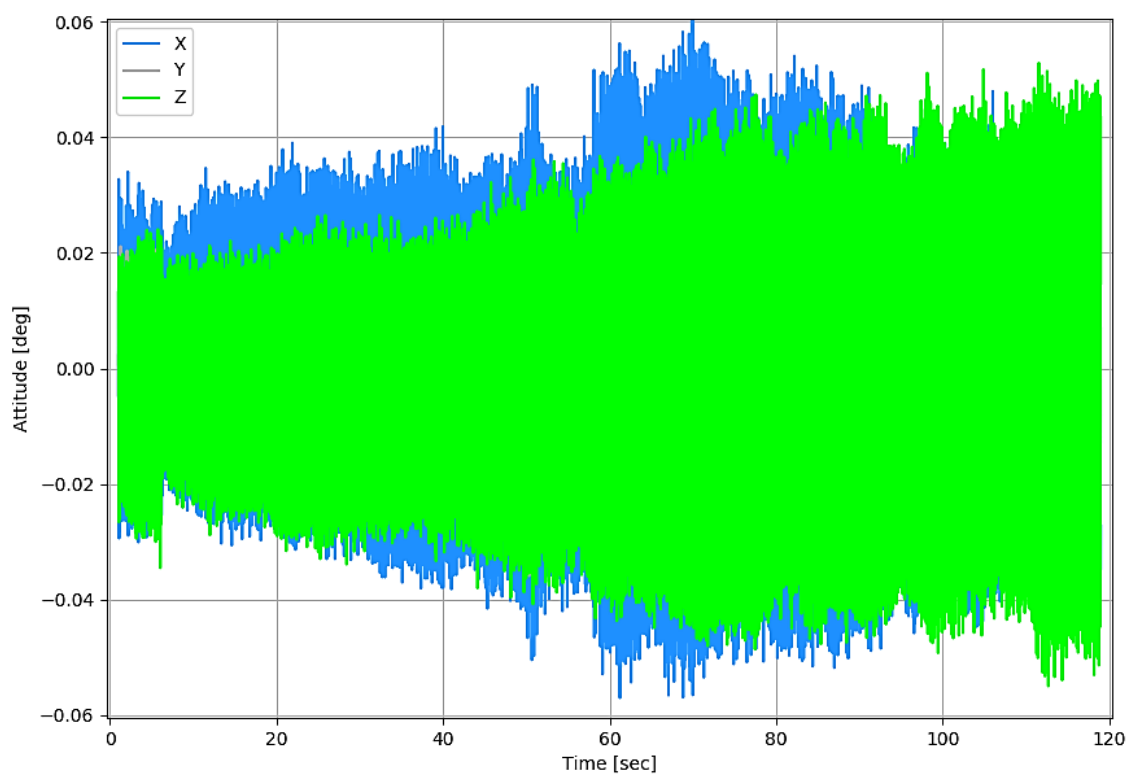
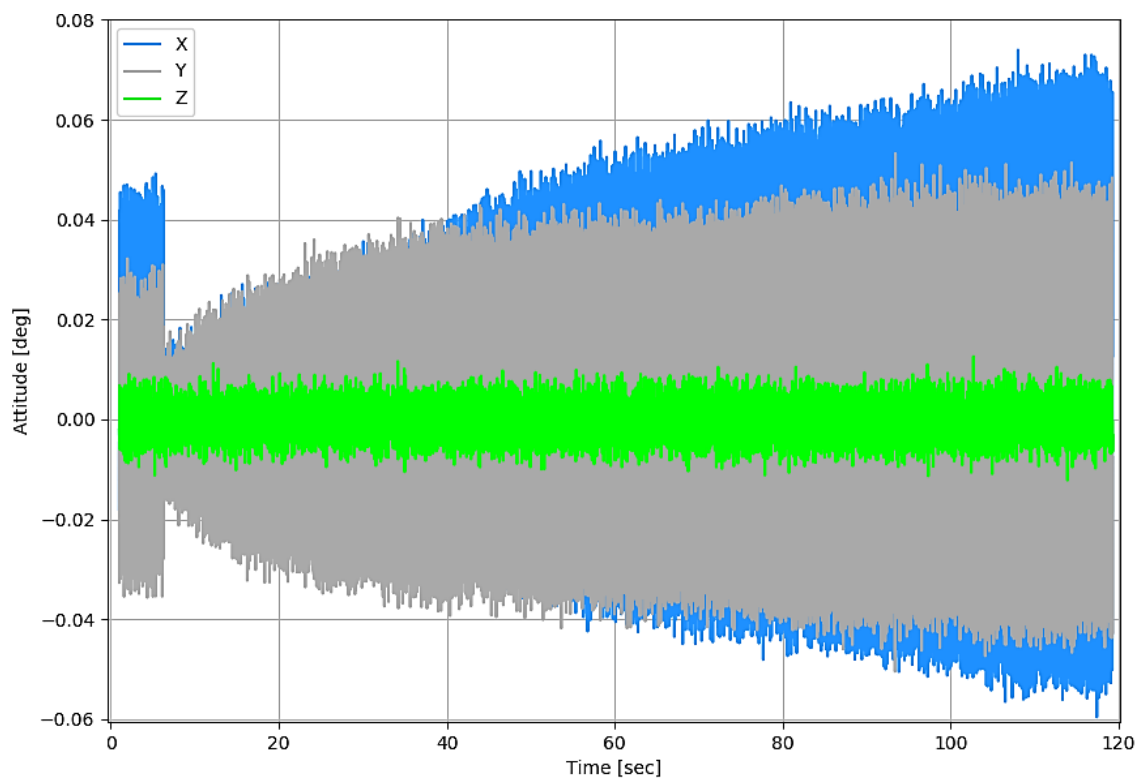


Figure A-13: Time-domain rotation: all axes of Kli-Pi 1 (500mm, laboratory test)



**Figure A-14: Time-domain rotation: all axes of Kli-Pi 2 (350mm, laboratory test)**



**Figure A-15: Time-domain rotation: all axes of Kli-Pi 3 (0mm, laboratory test)**

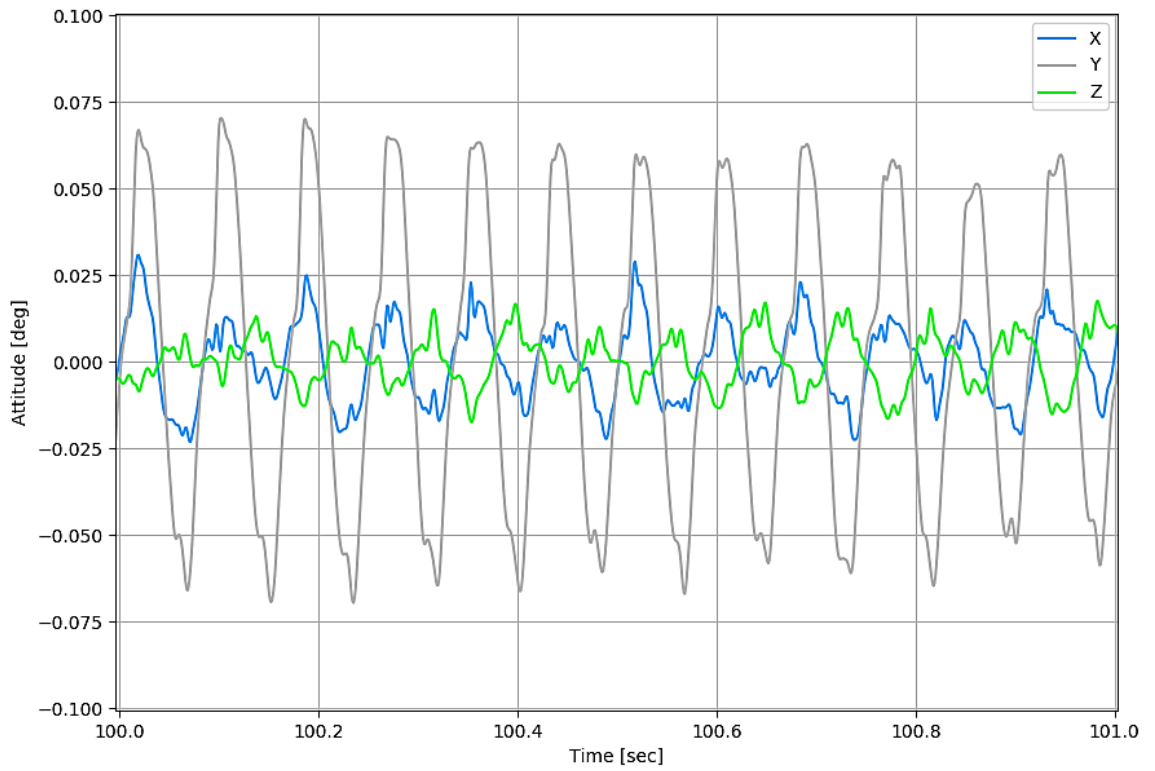


**Figure A-16: Time-domain rotation: all axes of Kli-Pi 1 (500mm, laboratory test)**

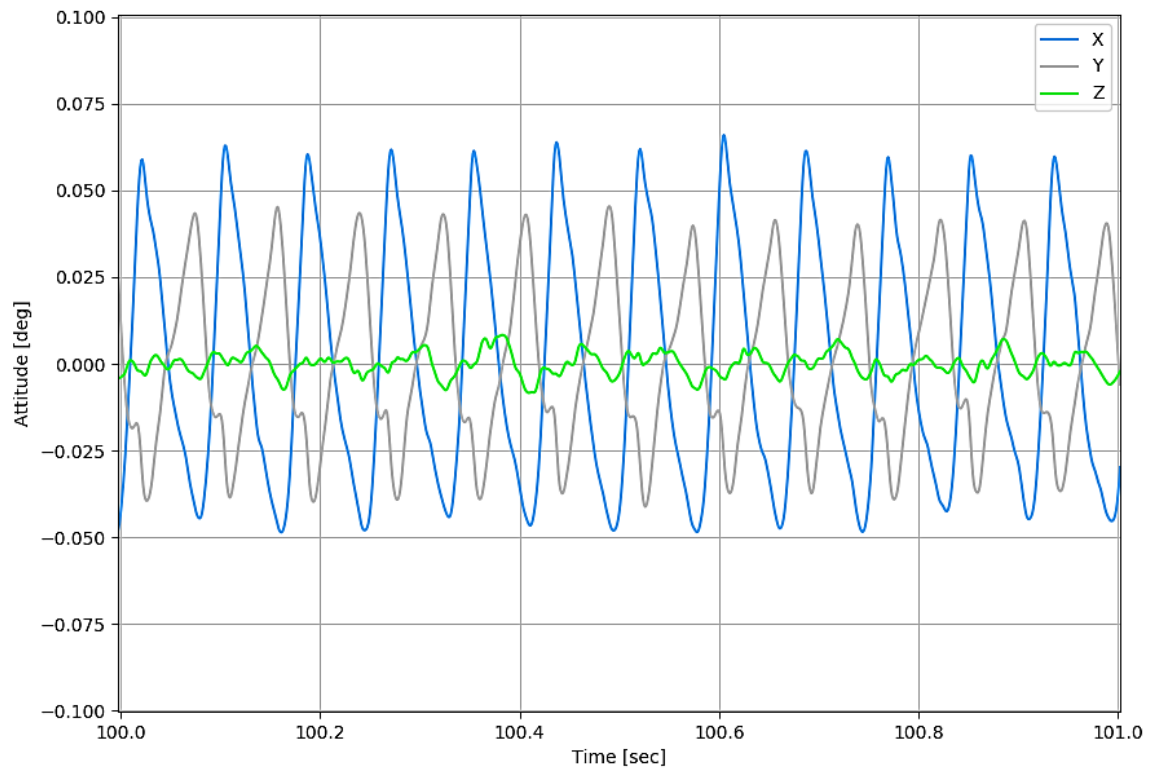


**Figure A-17: Time-domain rotation: all axes of Kli-Pi 3 (0mm, laboratory test)**

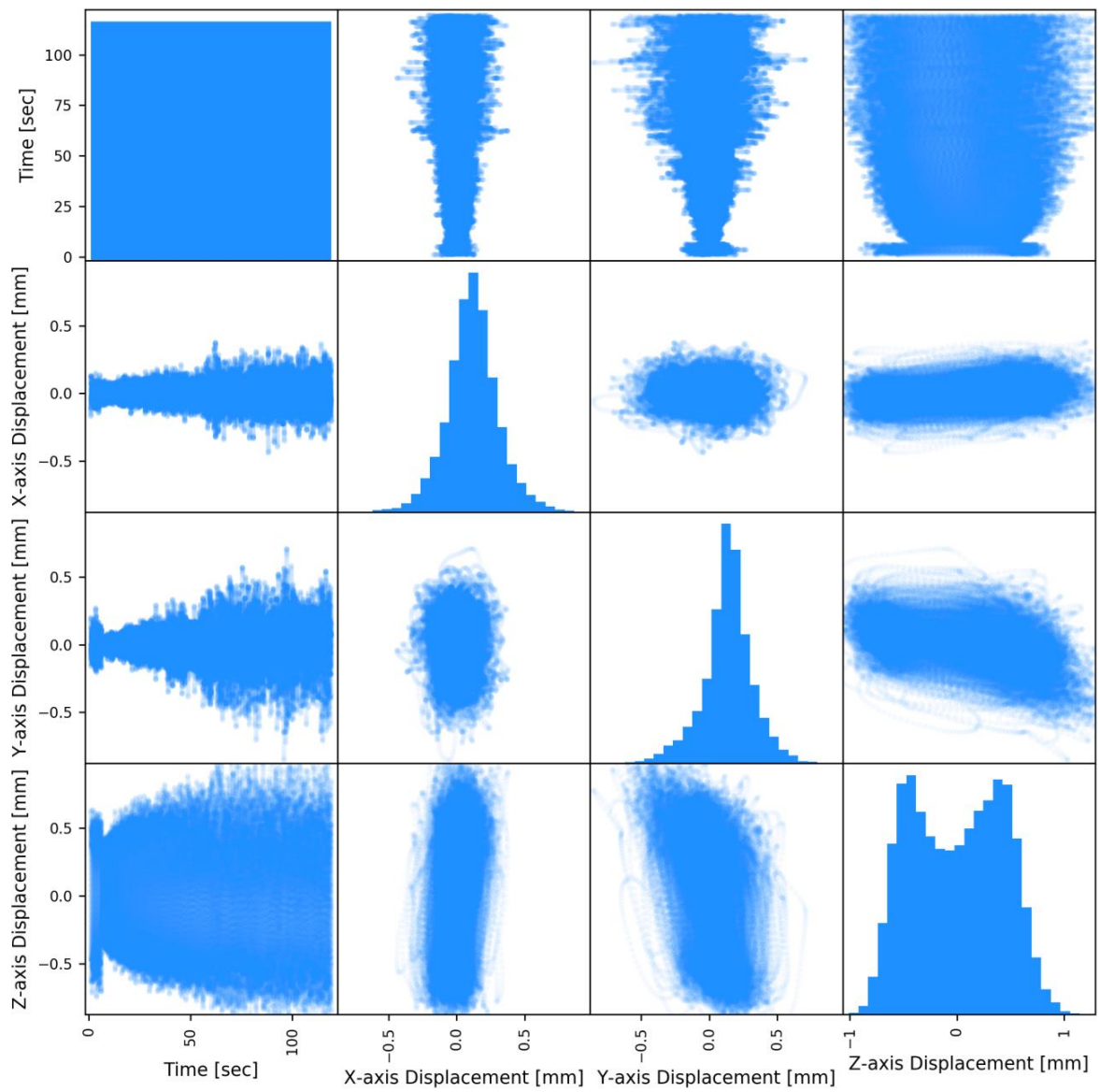


**Figure A-18: Time-domain displacement matrix: Kli-Pi 1 (500mm, laboratory test)**

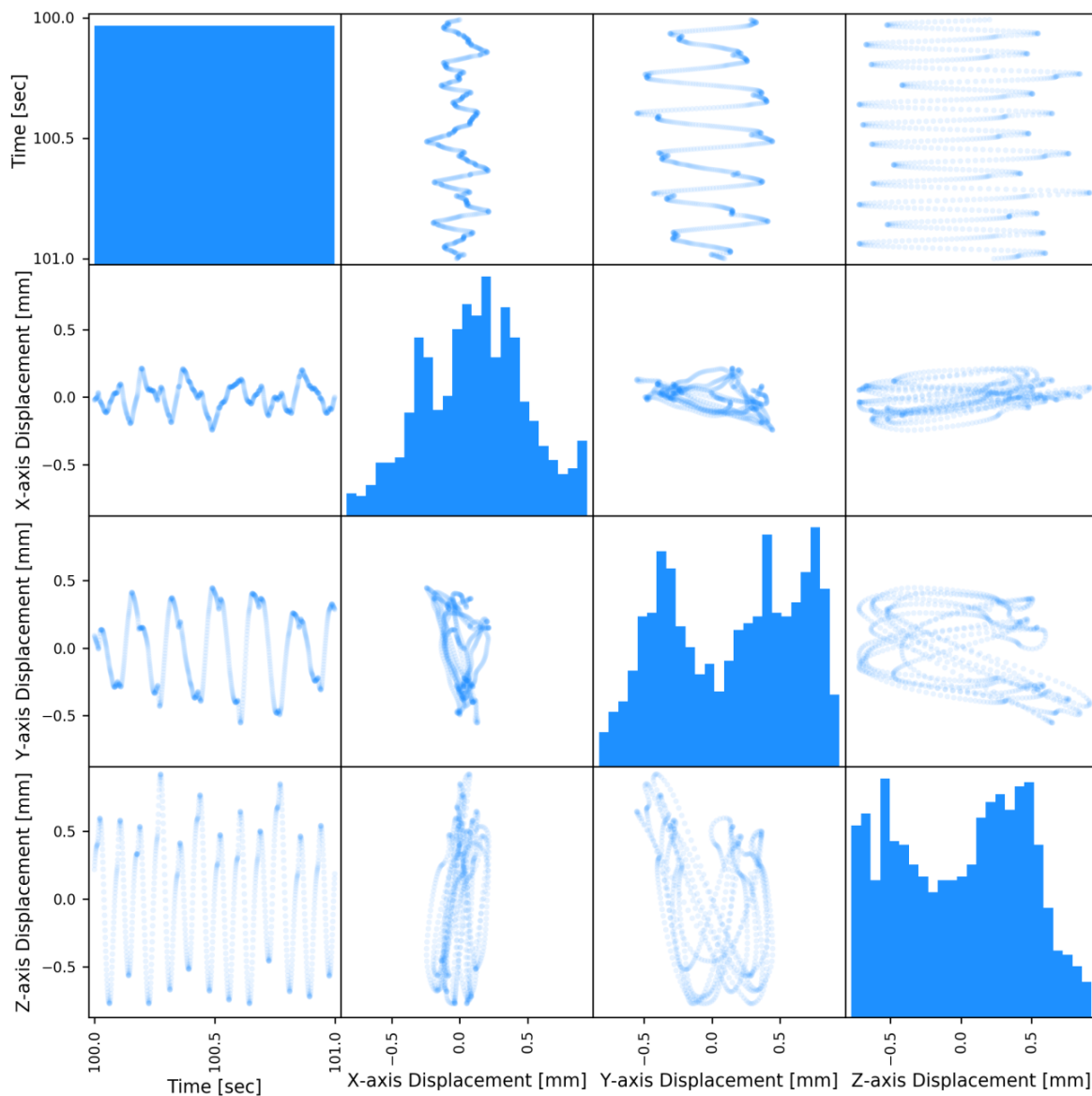


**Figure A-19: Time-domain displacement matrix: Kli-Pi 1 (500mm, laboratory test, detailed)**

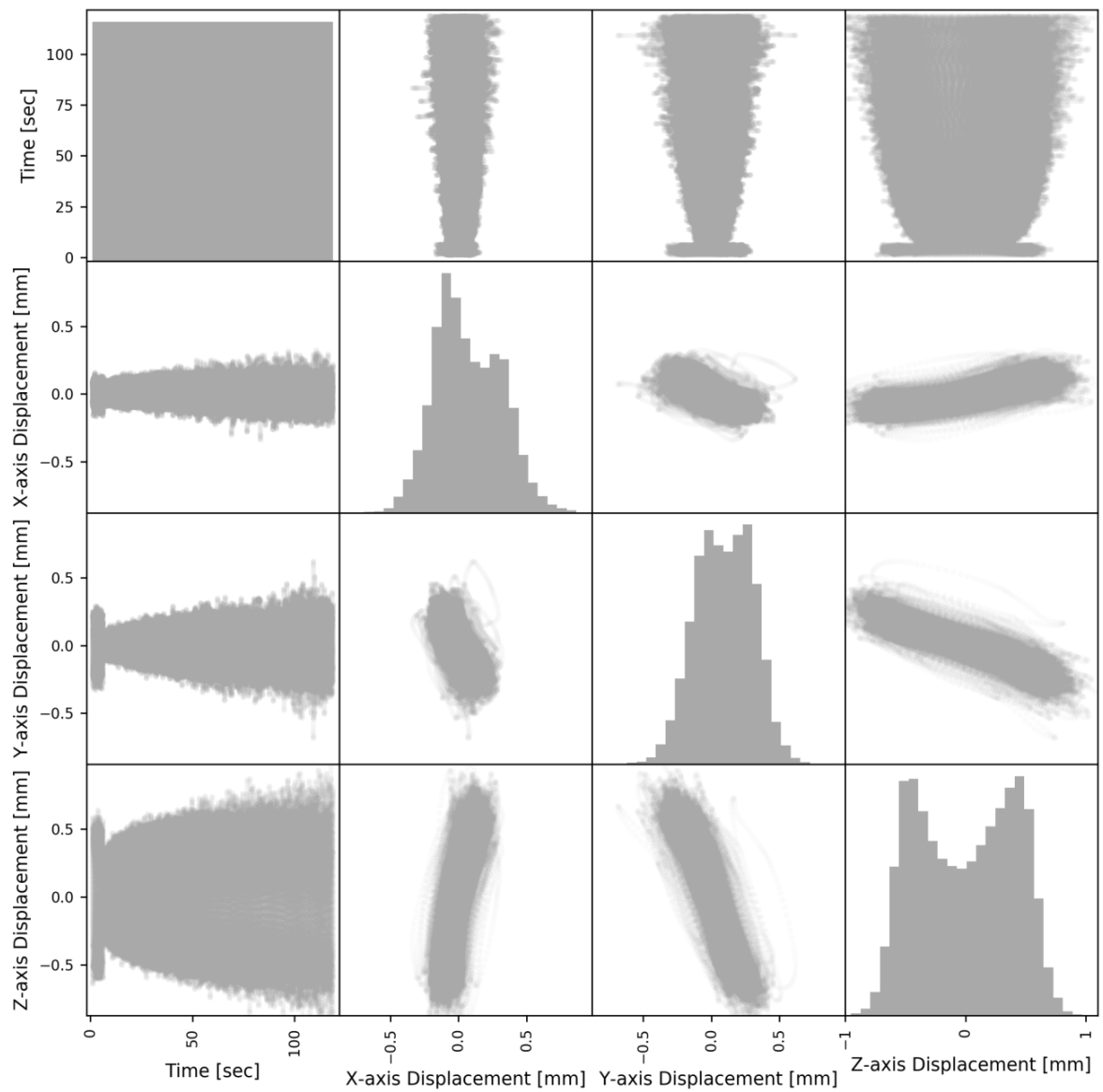


**Figure A-20: Time-domain displacement matrix: Kli-Pi 2 (350mm, laboratory test)**

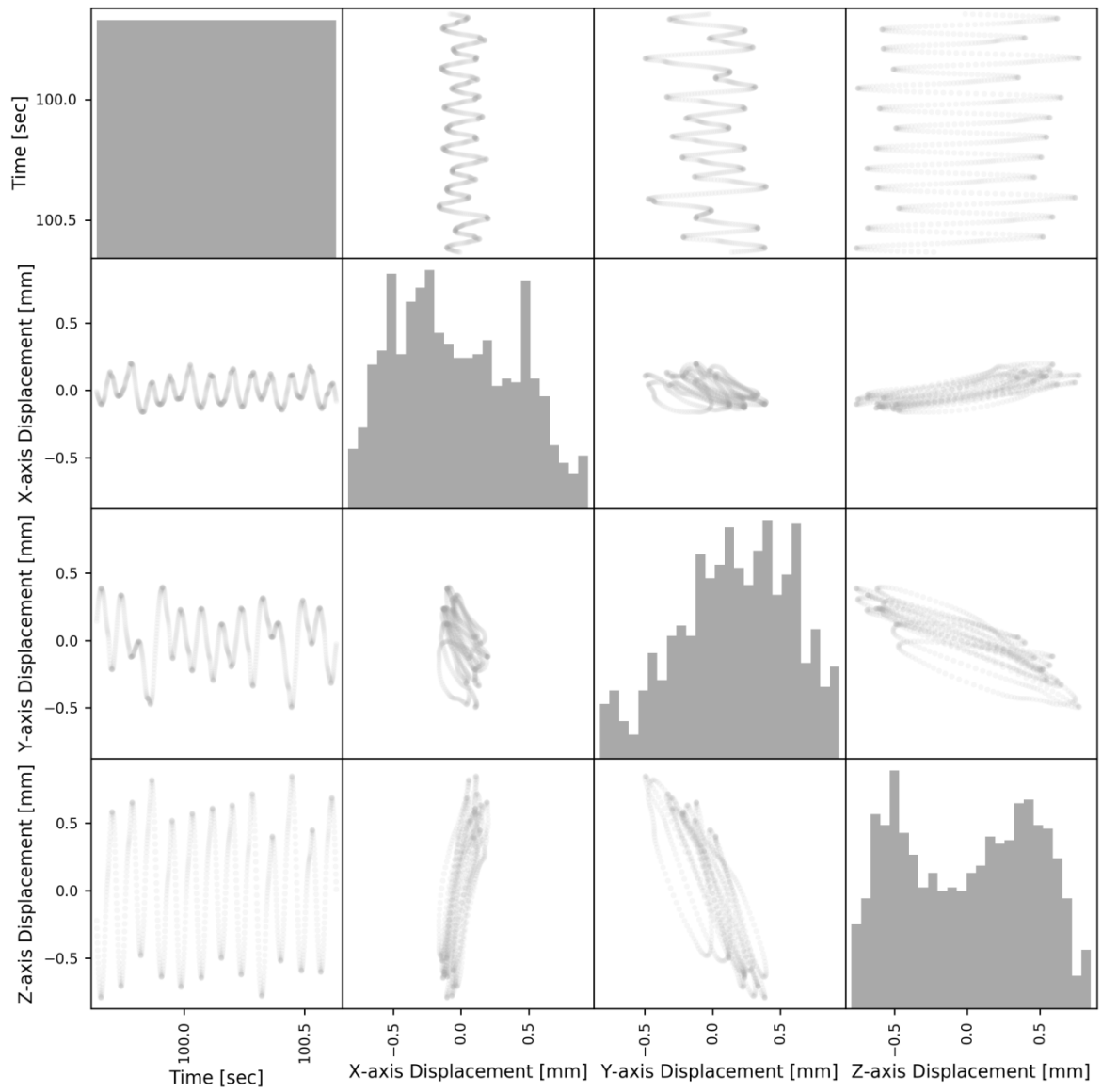


**Figure A-21: Time-domain displacement matrix: Kli-Pi 2 (350mm, laboratory test, detailed)**

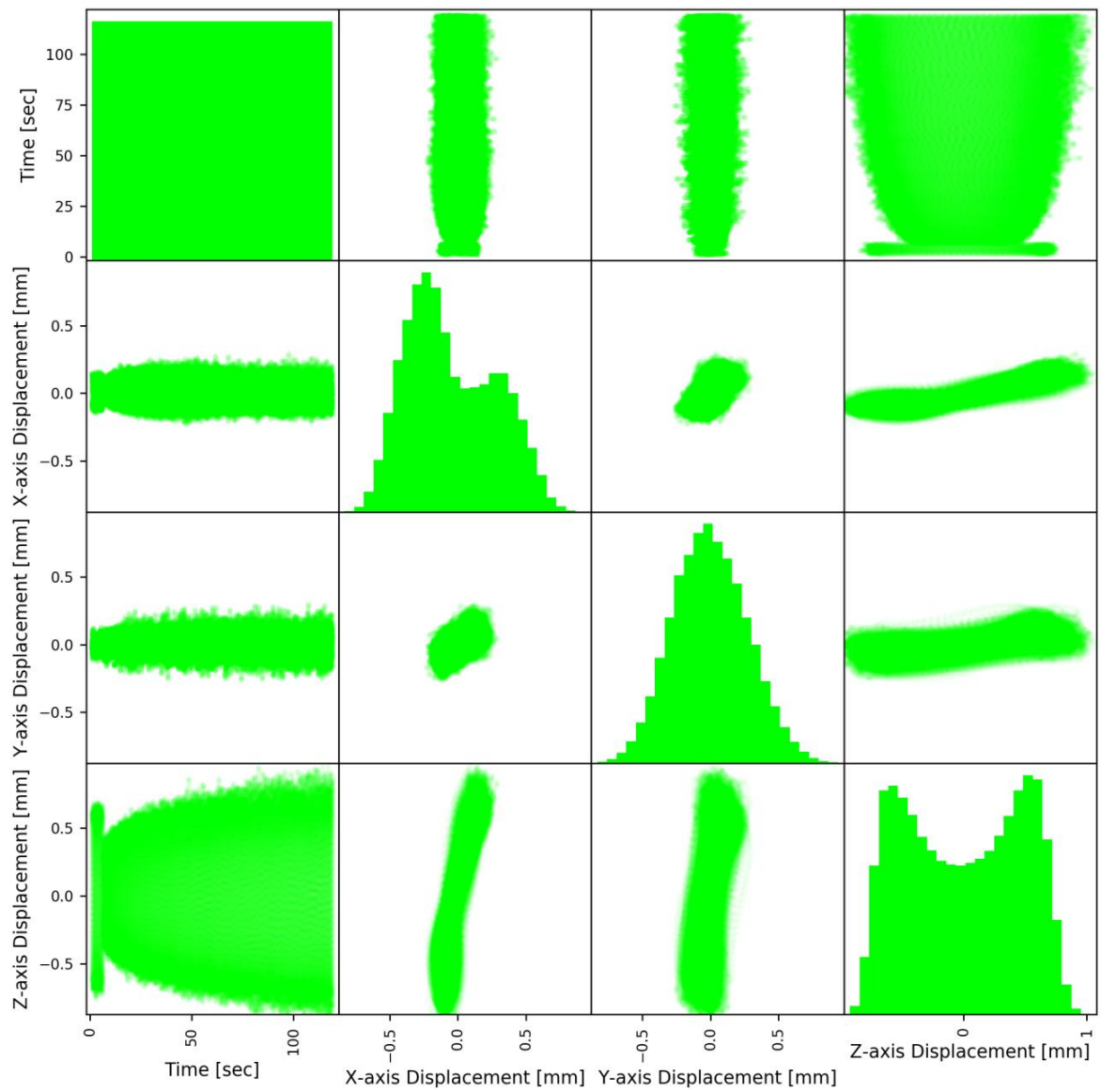


**Figure A-22: Time-domain displacement matrix: Kli-Pi 3 (0mm, laboratory test)**

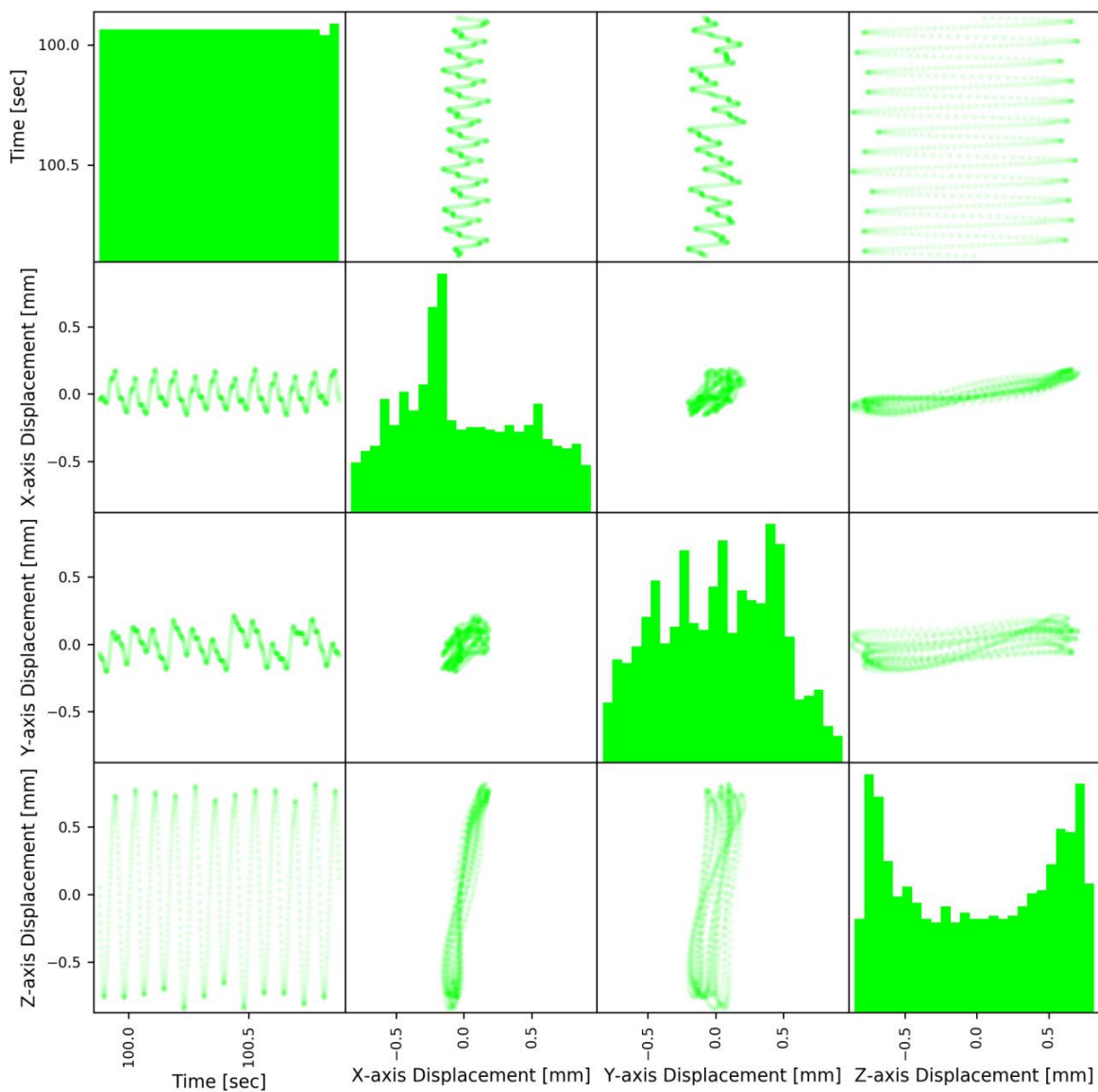


**Figure A-23: Time-domain displacement matrix: Kli-Pi 3 (0mm, laboratory test, detailed)**

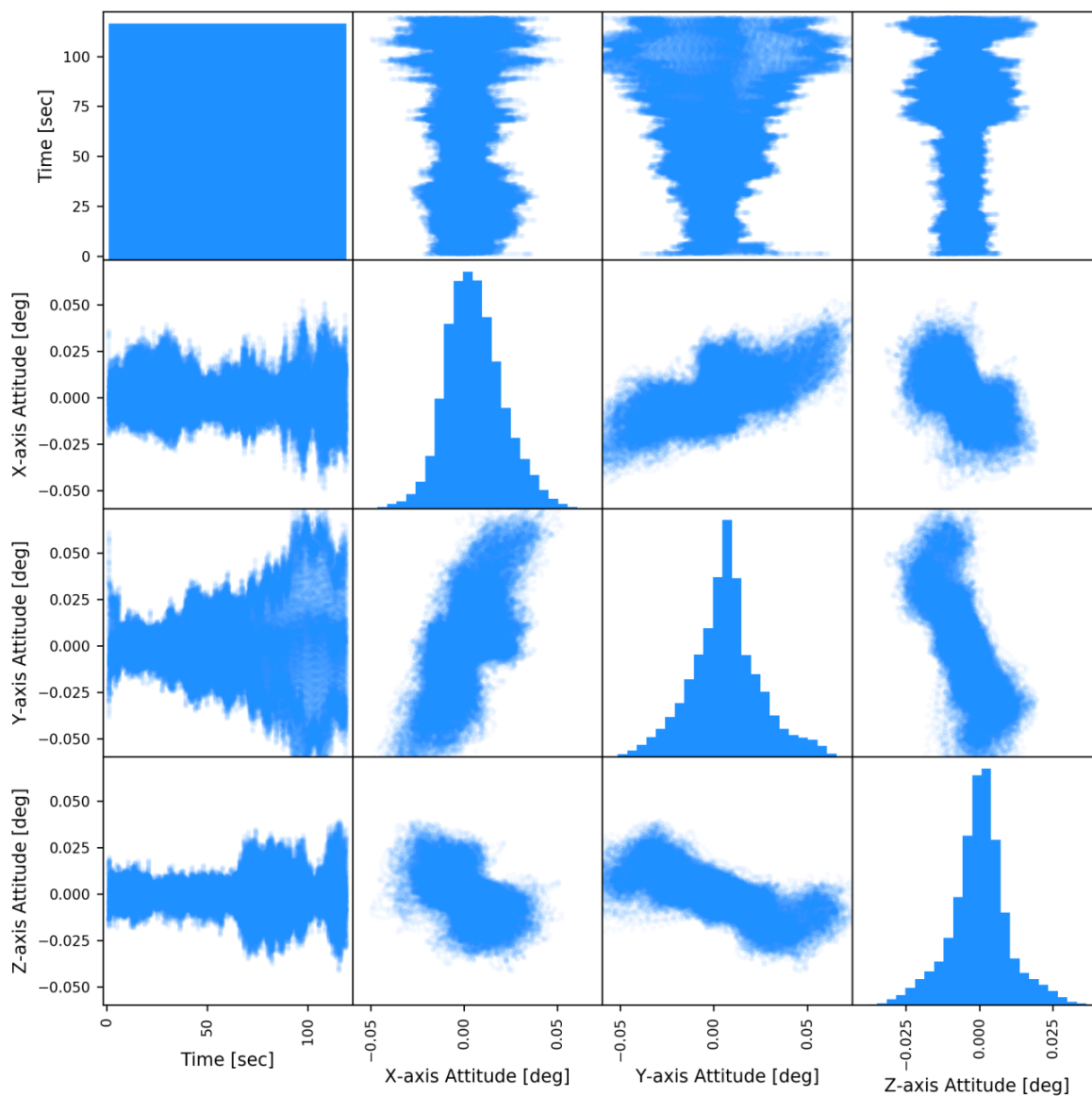


**Figure A-24: Time-domain rotation matrix: Kli-Pi 1 (500mm, laboratory test)**

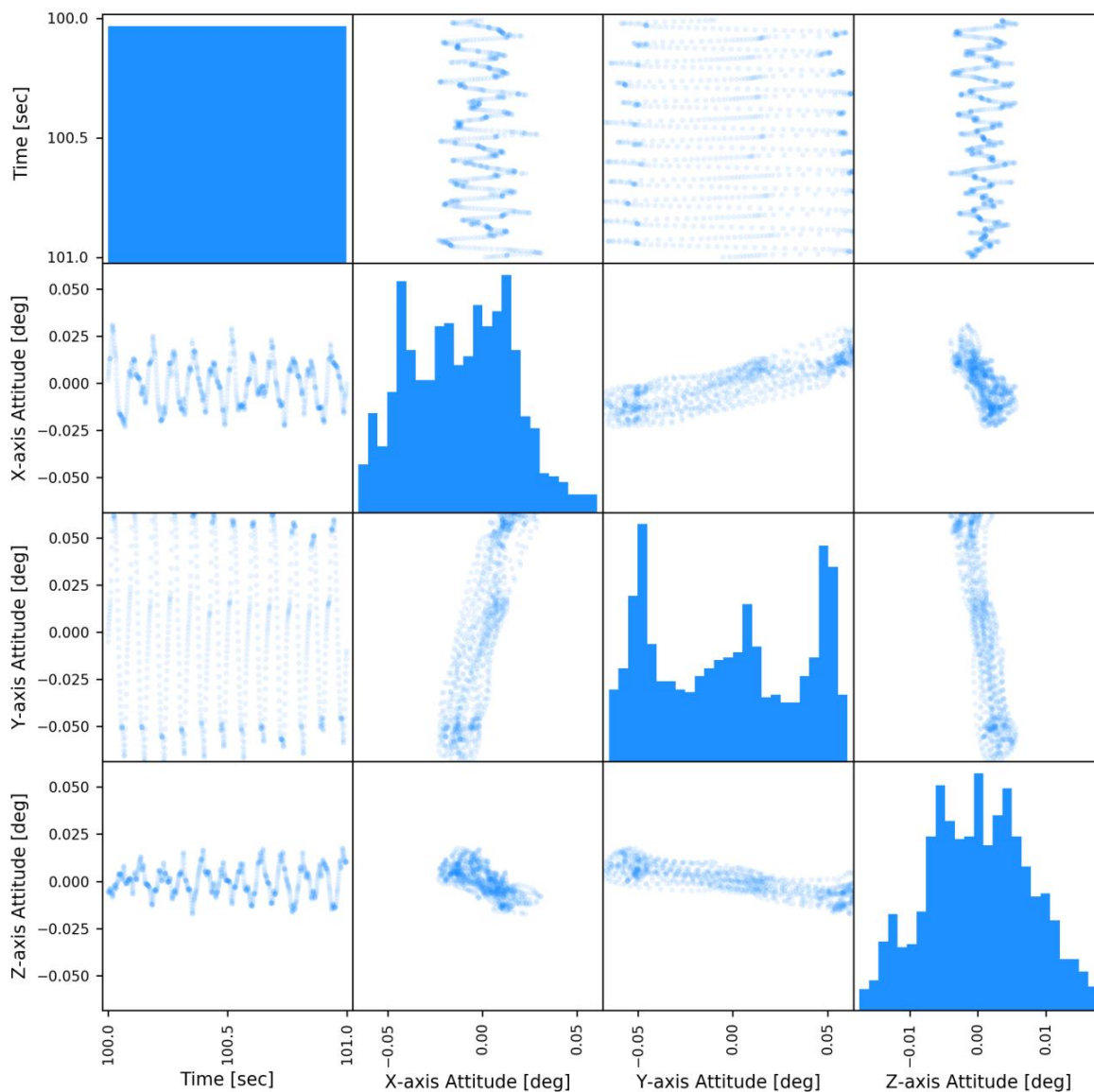


**Figure A-25: Time-domain rotation matrix: Kli-Pi 1 (500mm, laboratory test, detailed)**

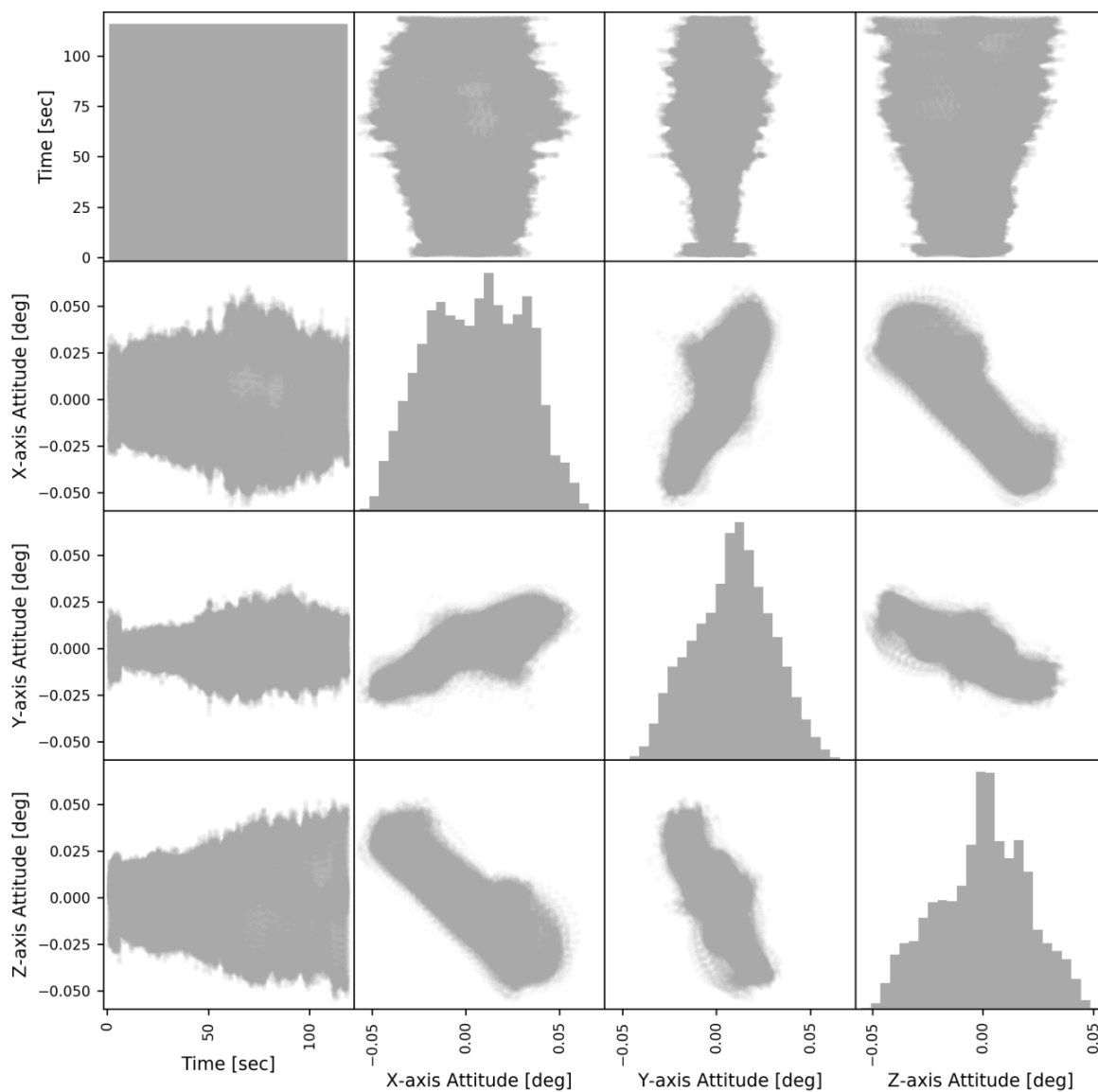


**Figure A-26: Time-domain rotation matrix: Kli-Pi 2 (350mm, laboratory test)**

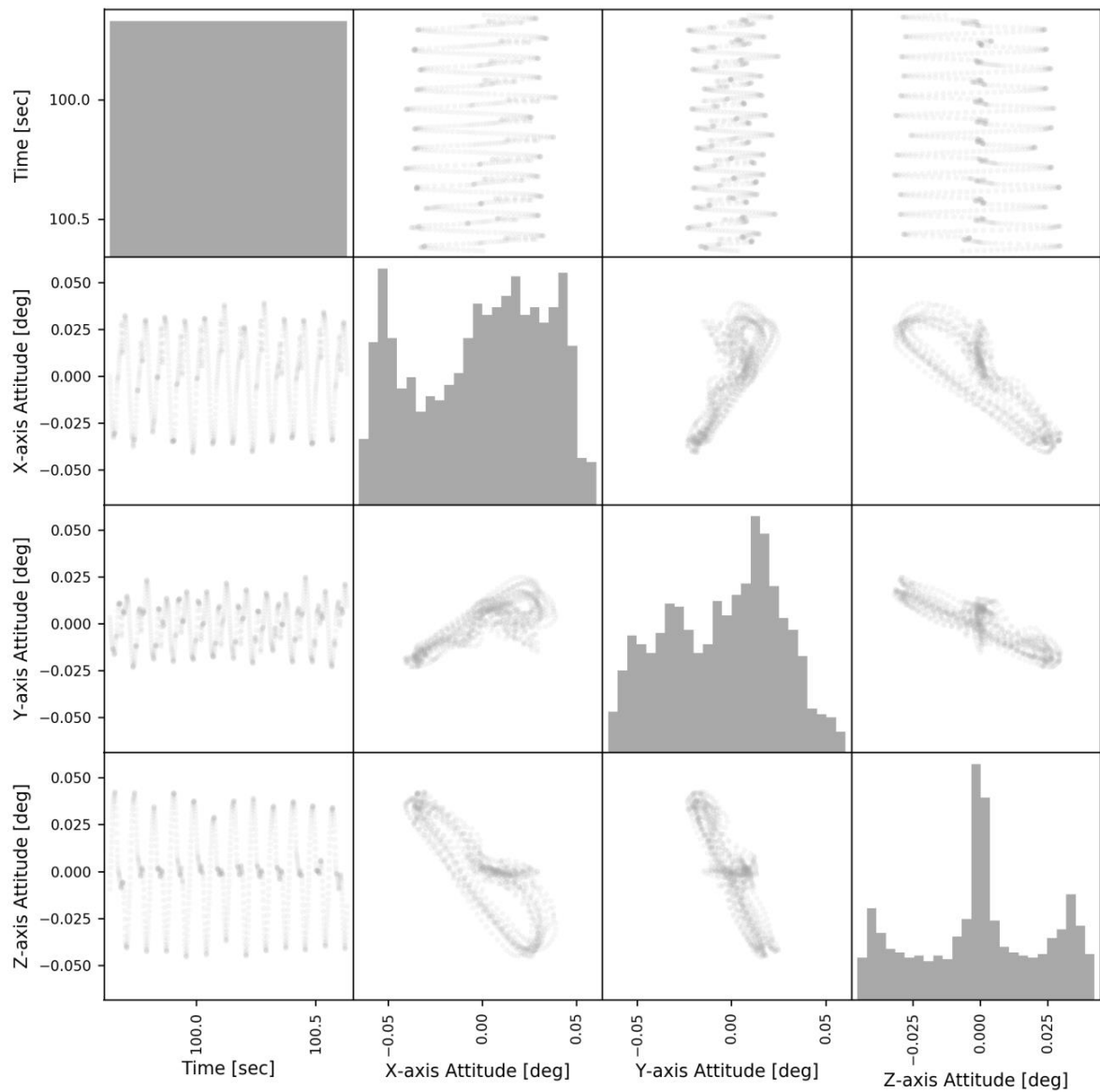


**Figure A-27: Time-domain rotation matrix: Kli-Pi 2 (350mm, laboratory test, detailed)**

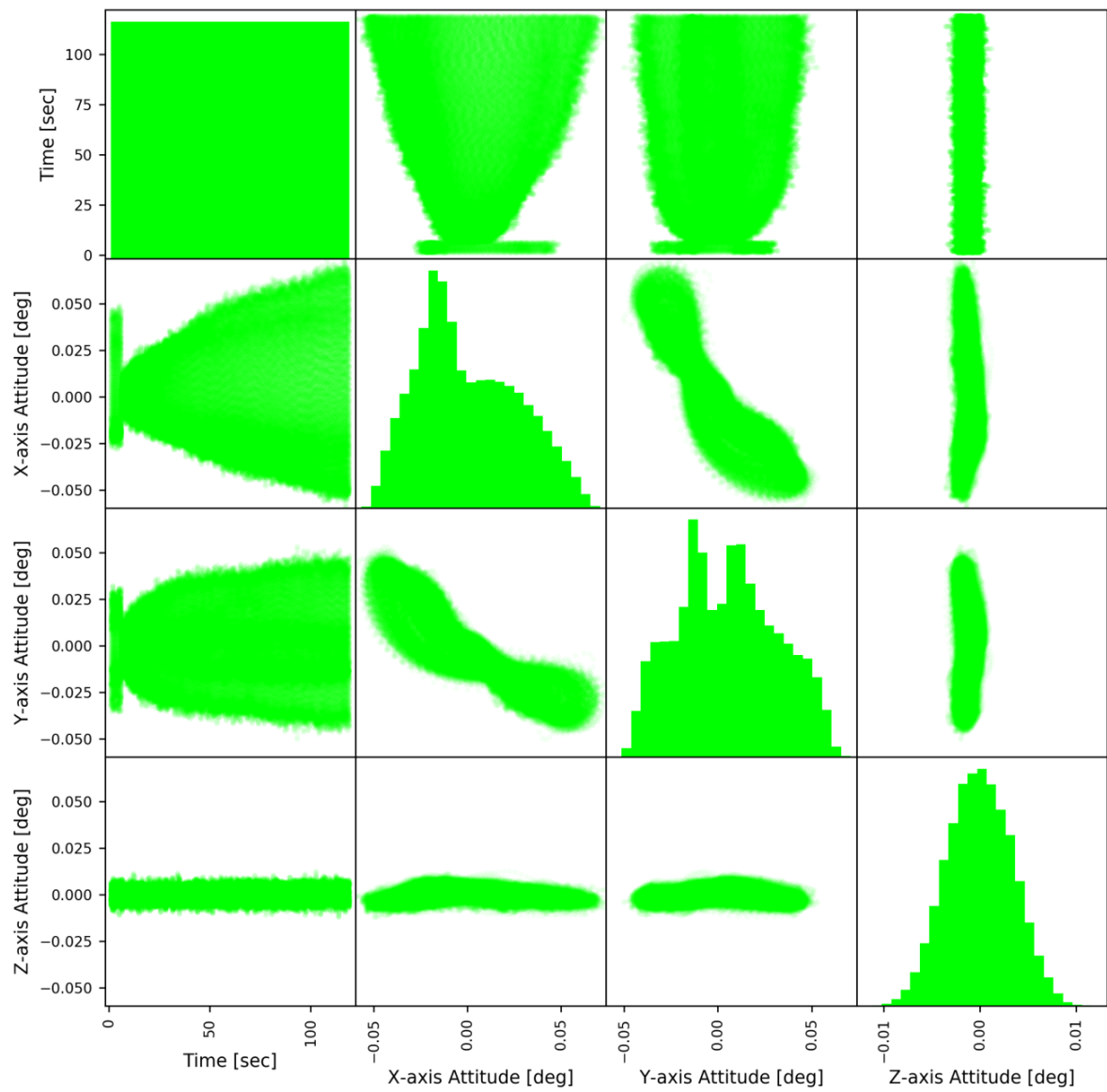


**Figure A-28: Time-domain rotation matrix: Kli-Pi 3 (0mm, laboratory test)**

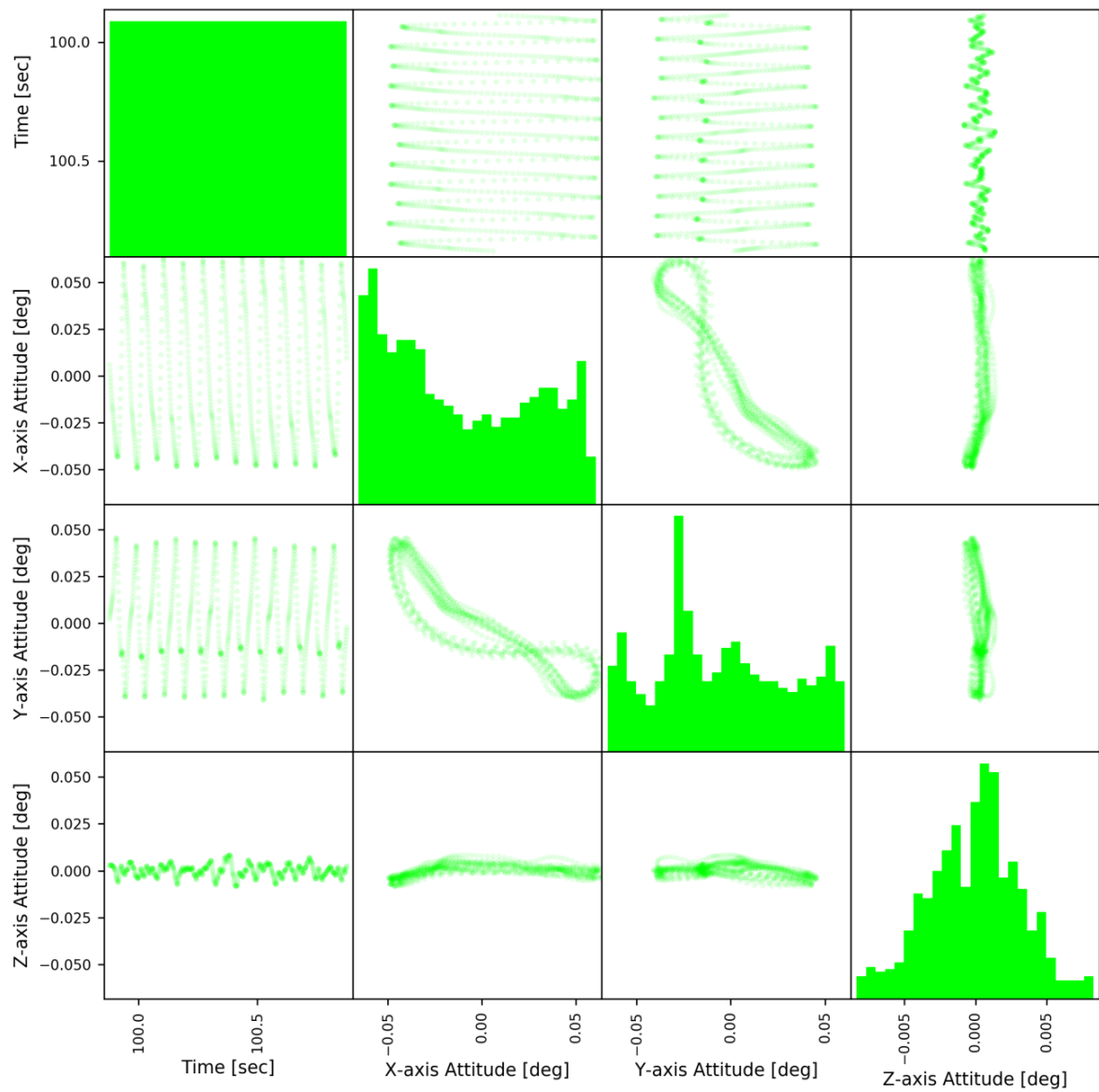


**Figure A-29: Time-domain rotation matrix: Kli-Pi 3 (0mm, laboratory test, detailed)**

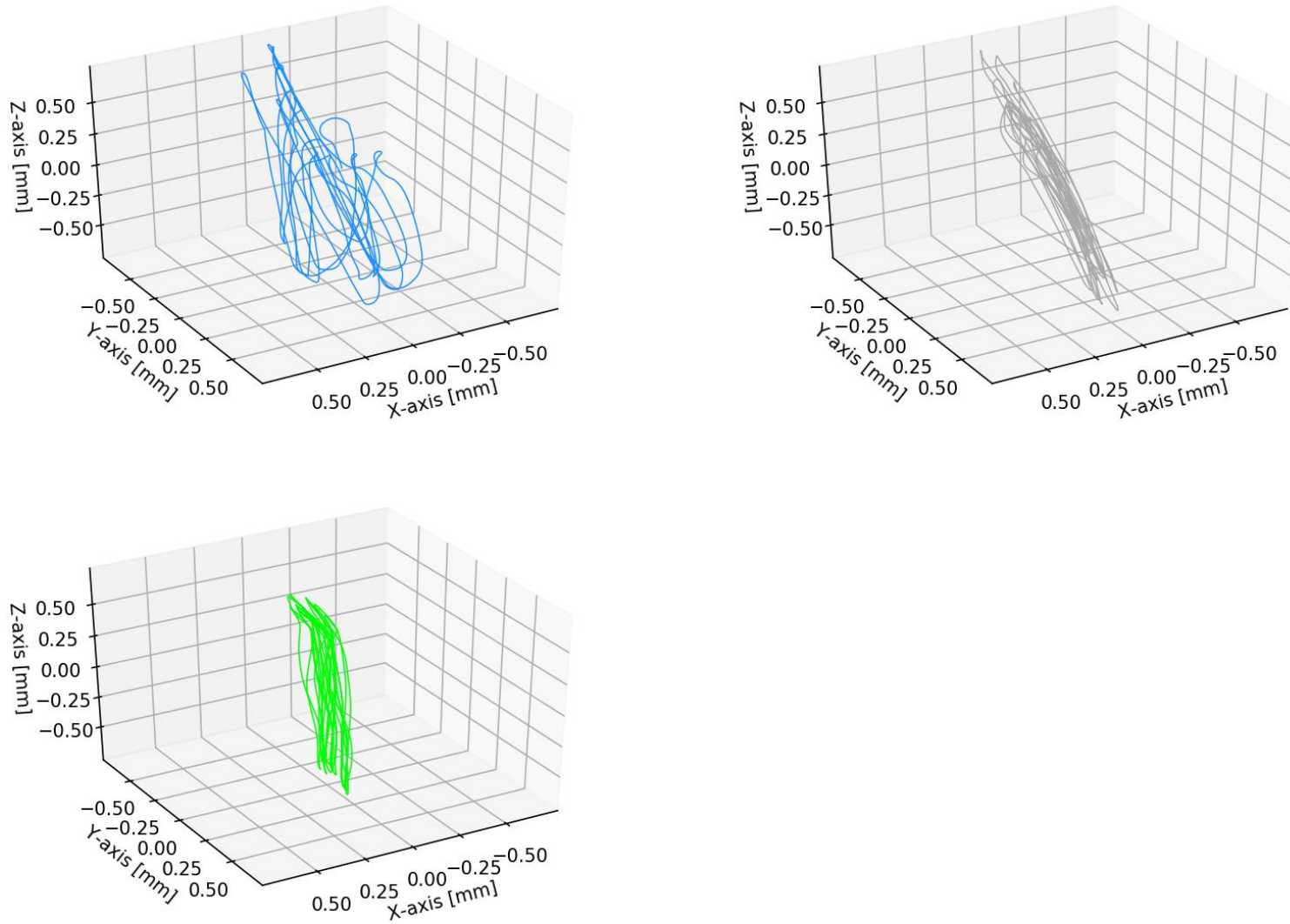


**Figure A-30: Time-domain displacement: all Kli-Pis (laboratory test, 60 degrees)**

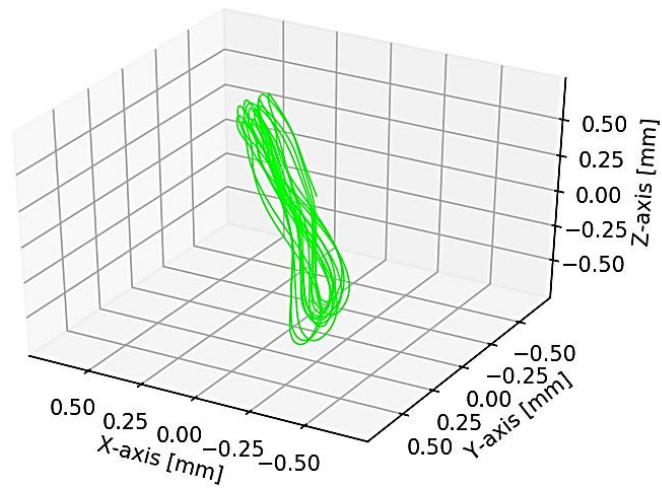
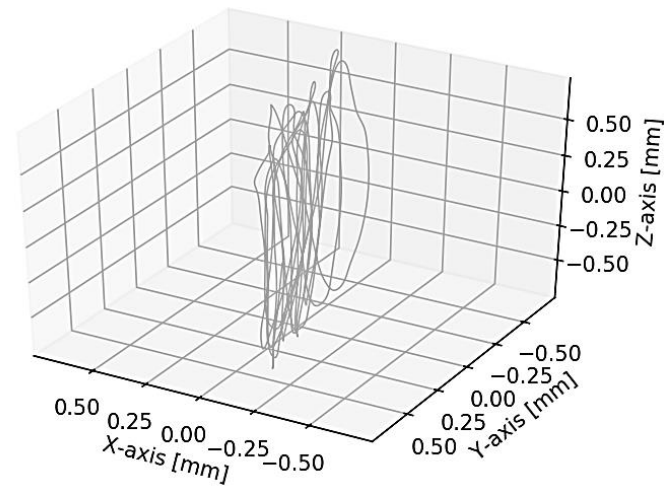
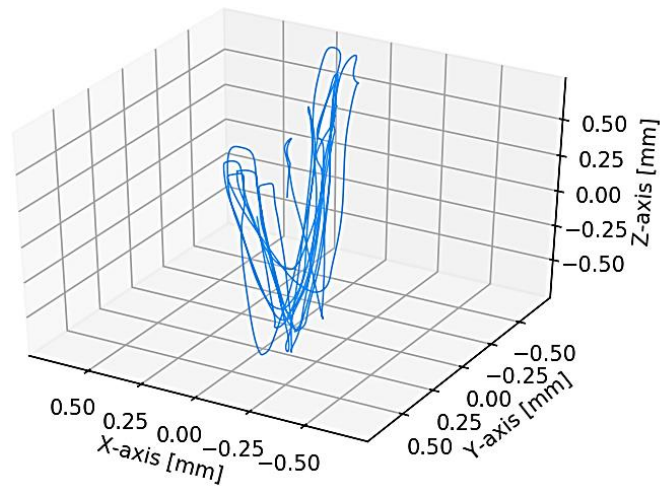


**Figure A-31: Time-domain displacement: all Kli-Pis (laboratory test, 120 degrees)**

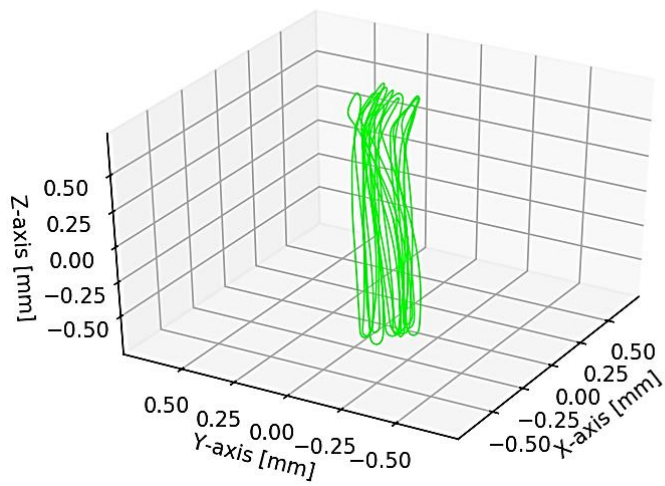
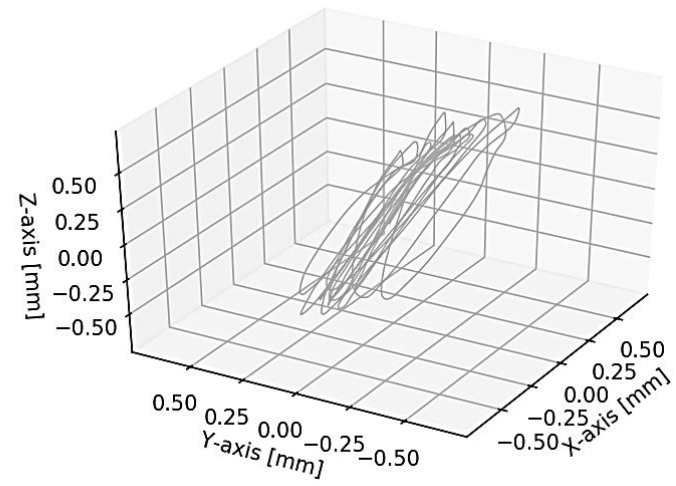
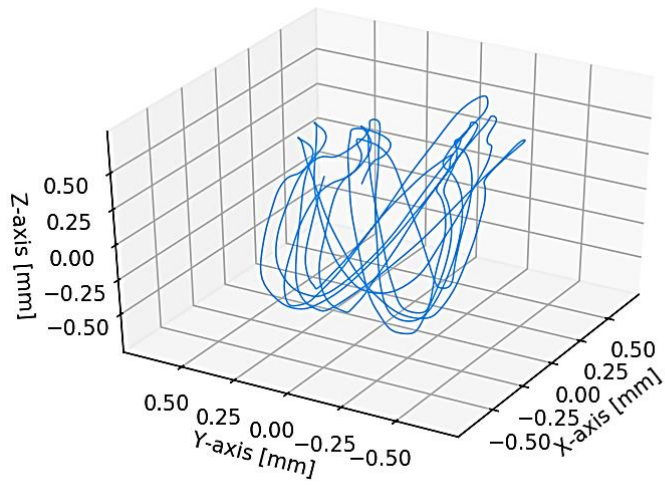


**Figure A-32: Time-domain displacement: all Kli-Pis (laboratory test, 210 degrees)**

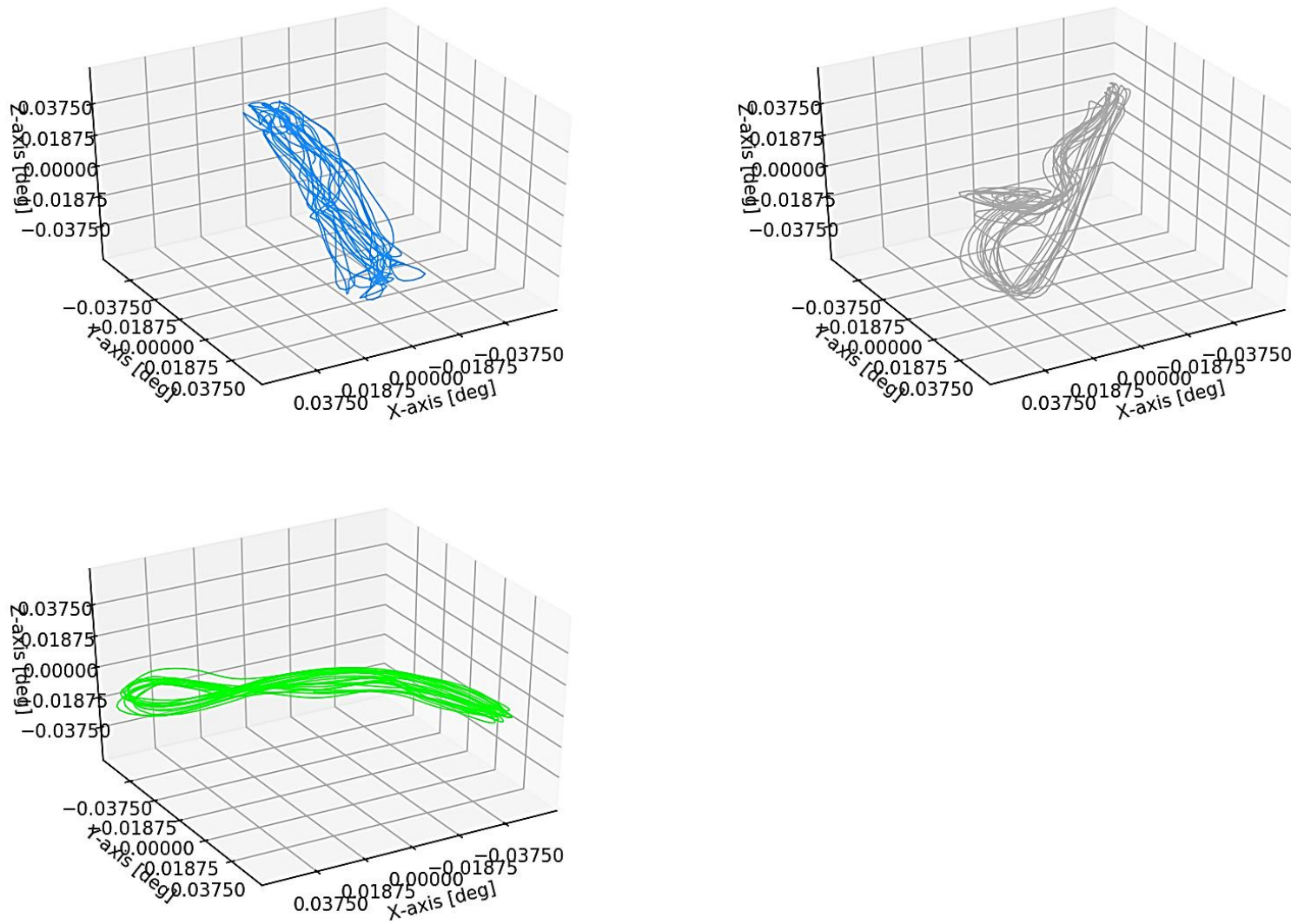
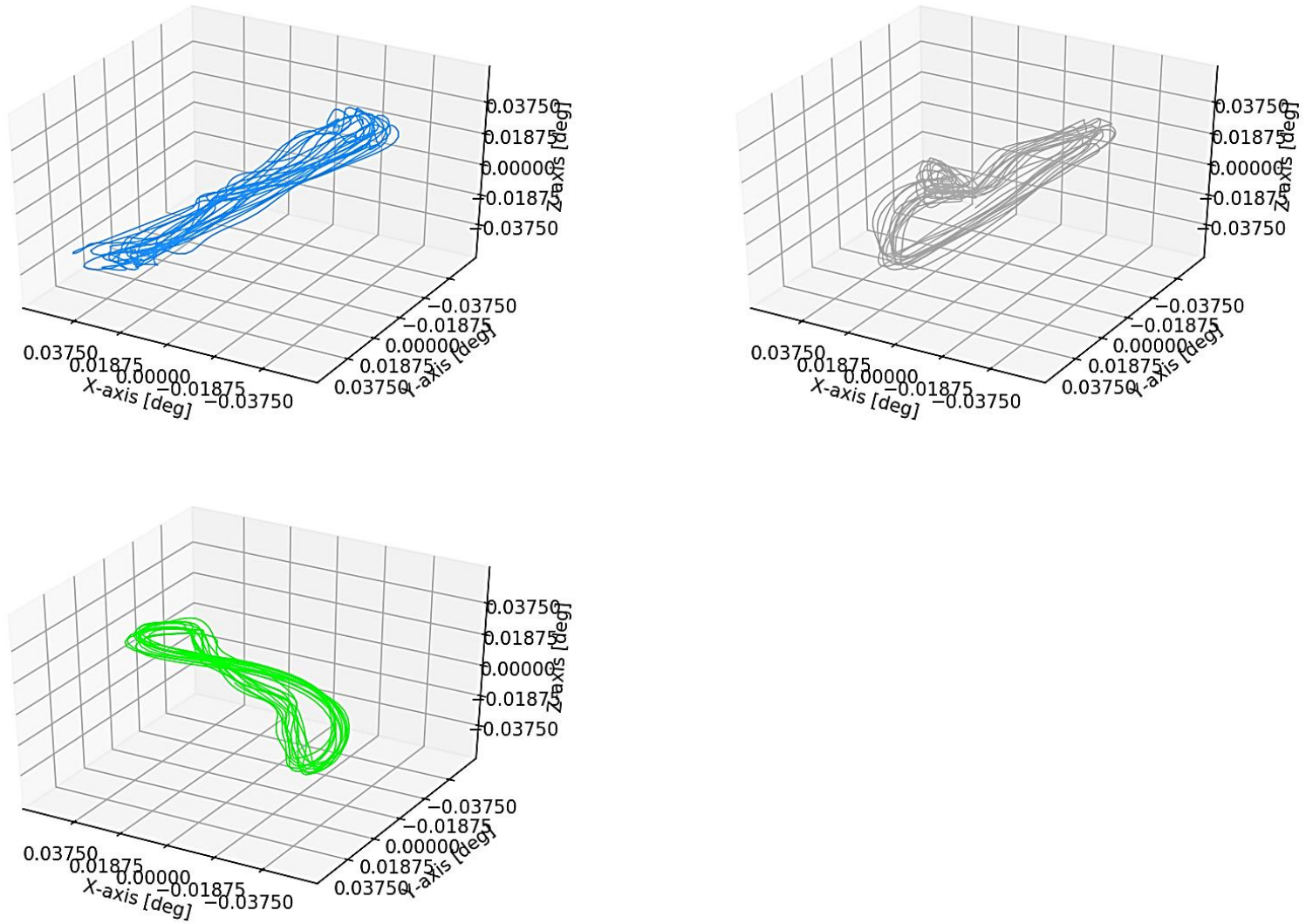
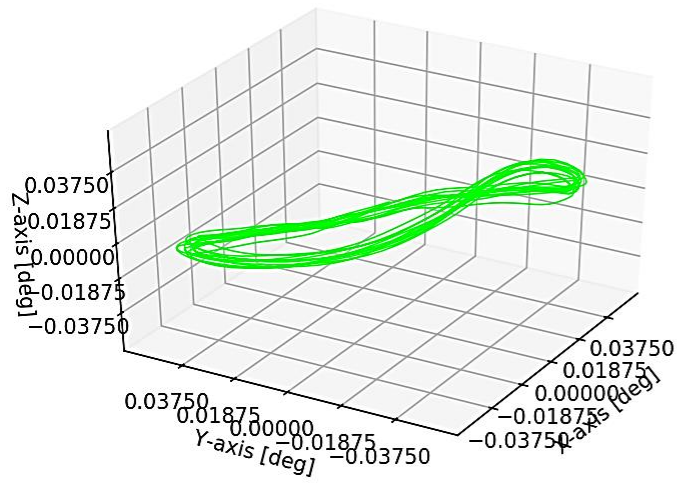
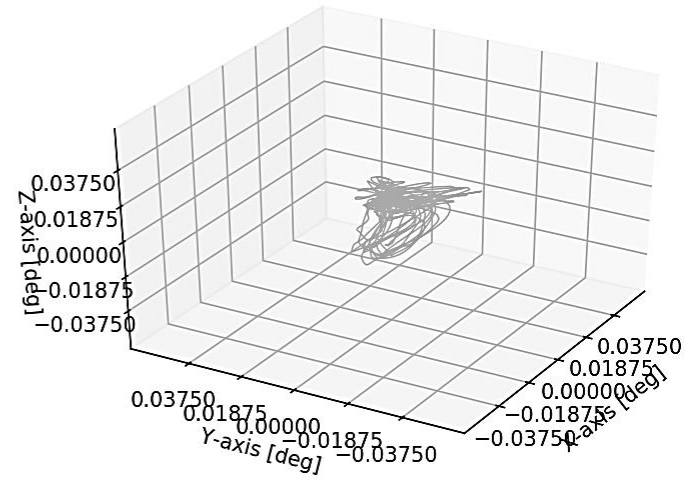
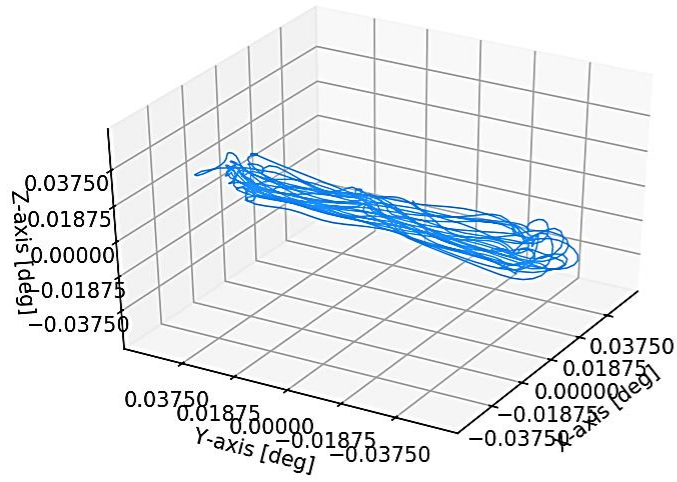


Figure A-33: Time-domain rotation: all Kli-Pis (laboratory test, 60 degrees)



**Figure A-34: Time-domain rotation: all Kli-Pis (laboratory test, 120 degrees)**



**Figure A-35: Time-domain rotation: all Kli-Pis (laboratory test, 210 degrees)**

## A.4 Field Testing Graphs

A hyperlinked summary of the graphs that follow:

Figure A-36: Time-domain deflection: X-axis of all Kli-Pis (field test, detailed)

Figure A-37: Time-domain deflection: Y-axis of all Kli-Pis (field test, detailed)

Figure A-38: Time-domain deflection: X-axis of all Kli-Pis (field test)

Figure A-39: Time-domain deflection: Y-axis of all Kli-Pis (field test)

Figure A-40: Time-domain rotation: X-axis of all Kli-Pis (field test)

Figure A-41: Time-domain rotation: Y-axis of all Kli-Pis (field test)

Figure A-42: Time-domain deflection: Z-axis of all Kli-Pis (field test, impact load)

Figure A-43: Time-domain rotation: X-axis of all Kli-Pis (field test, impact load)

Figure A-44: Spectrographic acceleration: Z-axis of Kli-Pi 1 (550mm, field test)

Figure A-45: Spectrographic acceleration: Z-axis of Kli-Pi 1 (550mm, field test, detailed)

Figure A-46: Spectrographic displacement: Z-axis of Kli-Pi 1 (550mm, field test, detailed)

Figure A-47: Spectrographic displacement: X-axis of Kli-Pi 3 (250mm, field test, detailed)

Figure A-48: Spectrographic displacement: Y-axis of Kli-Pi 3 (250mm, field test, detailed)

Figure A-49: Spectrographic displacement: Z-axis of Kli-Pi 3 (250mm, field test, detailed)

Figure A-50: Spectrographic displacement: X-axis of Kli-Pi 1 (550mm, field test, detailed)

Figure A-51: Spectrographic acceleration: Z-axis of Kli-Pi 3 (250mm, field test)

Figure A-52: Spectrographic acceleration: Z-axis of Kli-Pi 4 (0mm, field test)

Figure A-53: Spectrographic rotation: X-axis of Kli-Pi 4 (0mm, field test, detailed)

Figure A-54: Spectrographic rotation: X-axis of Kli-Pi 1 (550mm, field test, detailed)

Figure A-55: Spectrographic rotation: Y-axis of Kli-Pi 1 (550mm, field test, detailed)

Figure A-56: Spectrographic rotation: Z-axis of Kli-Pi 1 (550mm, field test, detailed)

Figure A-57: Spectrographic rotation: X-axis of Kli-Pi 3 (250mm, field test, detailed)

Figure A-58: Time-domain displacement matrix: Kli-Pi 1 (550mm, field test)

Figure A-59: Time-domain displacement matrix: Kli-Pi 1 (550mm, field test, detailed)

Figure A-60: Time-domain displacement matrix: Kli-Pi 2 (400mm, field test)

Figure A-61: Time-domain displacement matrix: Kli-Pi 2 (400mm, field test, detailed)

Figure A-62: Time-domain displacement matrix: Kli-Pi 3 (250mm, field test)

Figure A-63: Time-domain displacement matrix: Kli-Pi 3 (250mm, field test, detailed)

Figure A-64: Time-domain displacement matrix: Kli-Pi 4 (0mm, field test)

Figure A-65: Time-domain displacement matrix: Kli-Pi 4 (0mm, field test, detailed)

Figure A-66: Time-domain rotation matrix: Kli-Pi 1 (550mm, field test)

Figure A-67: Time-domain rotation matrix: Kli-Pi 1 (550mm, field test, detailed)

Figure A-68: Time-domain rotation matrix: Kli-Pi 2 (400mm, field test)

Figure A-69: Time-domain rotation matrix: Kli-Pi 2 (400mm, field test, detailed)

Figure A-70: Time-domain rotation matrix: Kli-Pi 3 (250mm, field test)

Figure A-71: Time-domain rotation matrix: Kli-Pi 3 (250mm, field test, detailed)

Figure A-72: Time-domain rotation matrix: Kli-Pi 4 (0mm, field test)

Figure A-73: Time-domain rotation matrix: Kli-Pi 4 (0mm, field test, detailed)

Figure A-74: Time-domain displacement: all Kli-Pis (field test, 60 degrees)

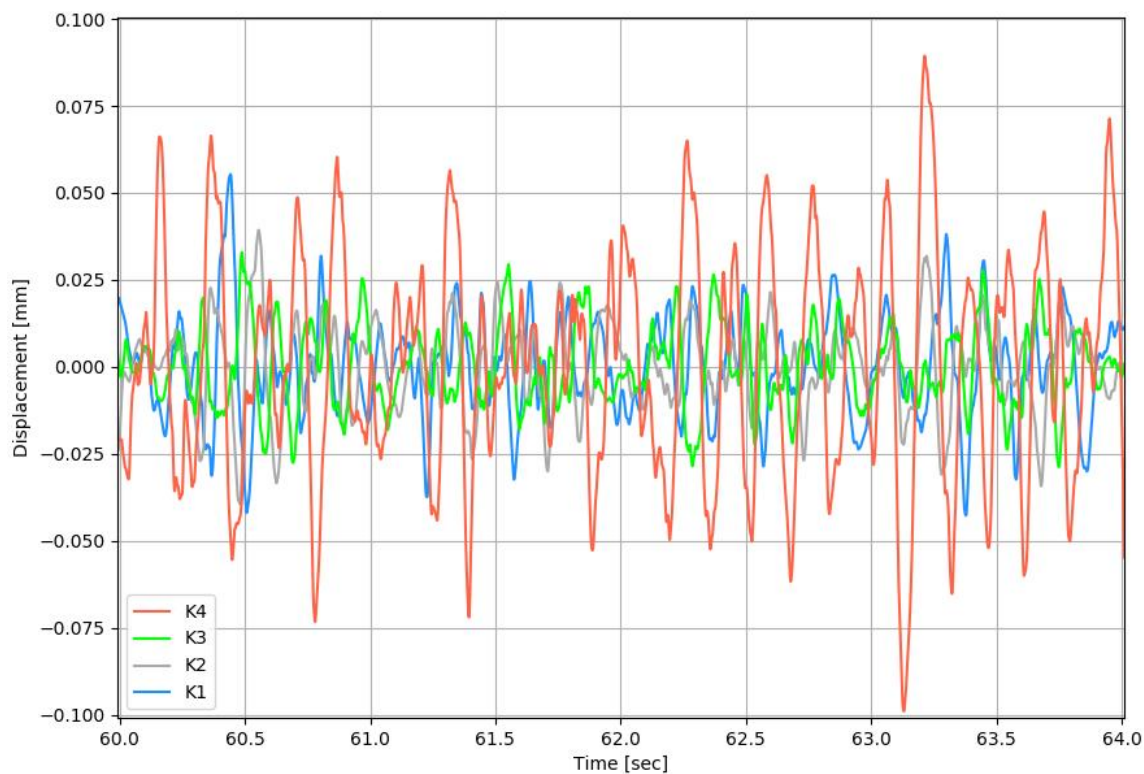
Figure A-75: Time-domain displacement: all Kli-Pis (field test, 120 degrees)

Figure A-76: Time-domain displacement: all Kli-Pis (field test, 210 degrees)

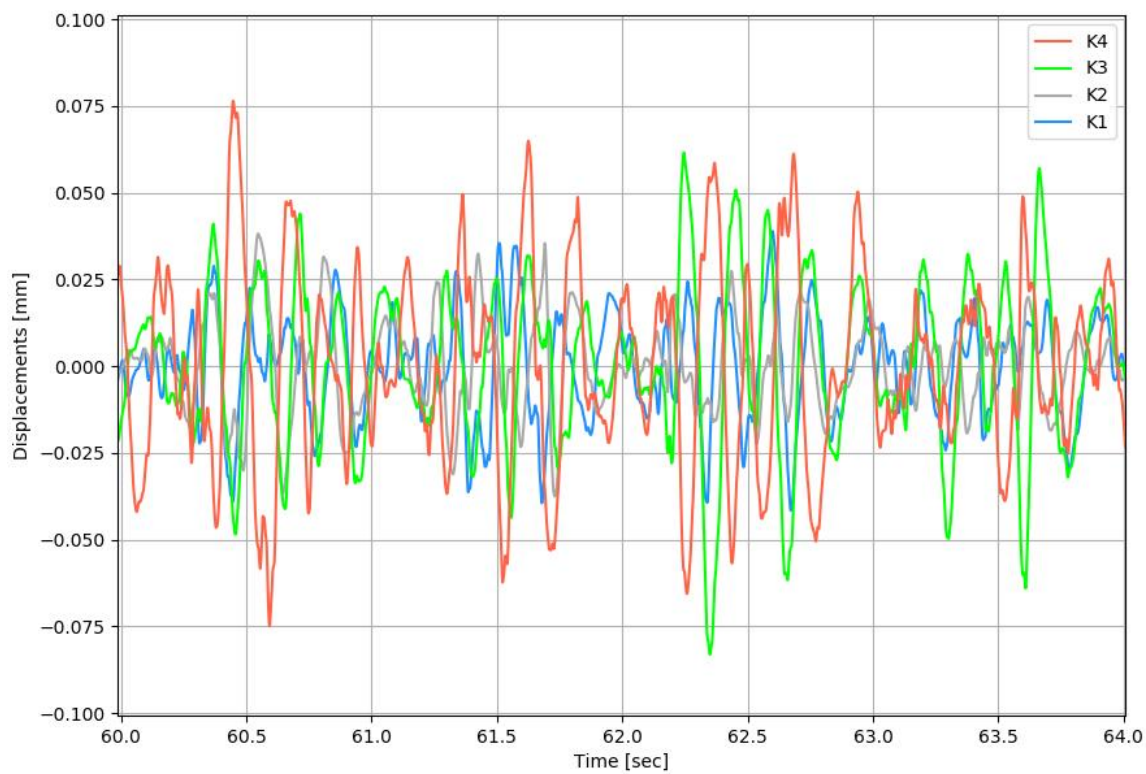
Figure A-77: Time-domain rotation: all Kli-Pis (field test, 60 degrees)

Figure A-78: Time-domain rotation: all Kli-Pis (field test, 120 degrees)

Figure A-79: Time-domain rotation: all Kli-Pis (field test, 210 degrees)



**Figure A-36: Time-domain deflection: X-axis of all Kli-Pis (field test, detailed)**



**Figure A-37: Time-domain deflection: Y-axis of all Kli-Pis (field test, detailed)**

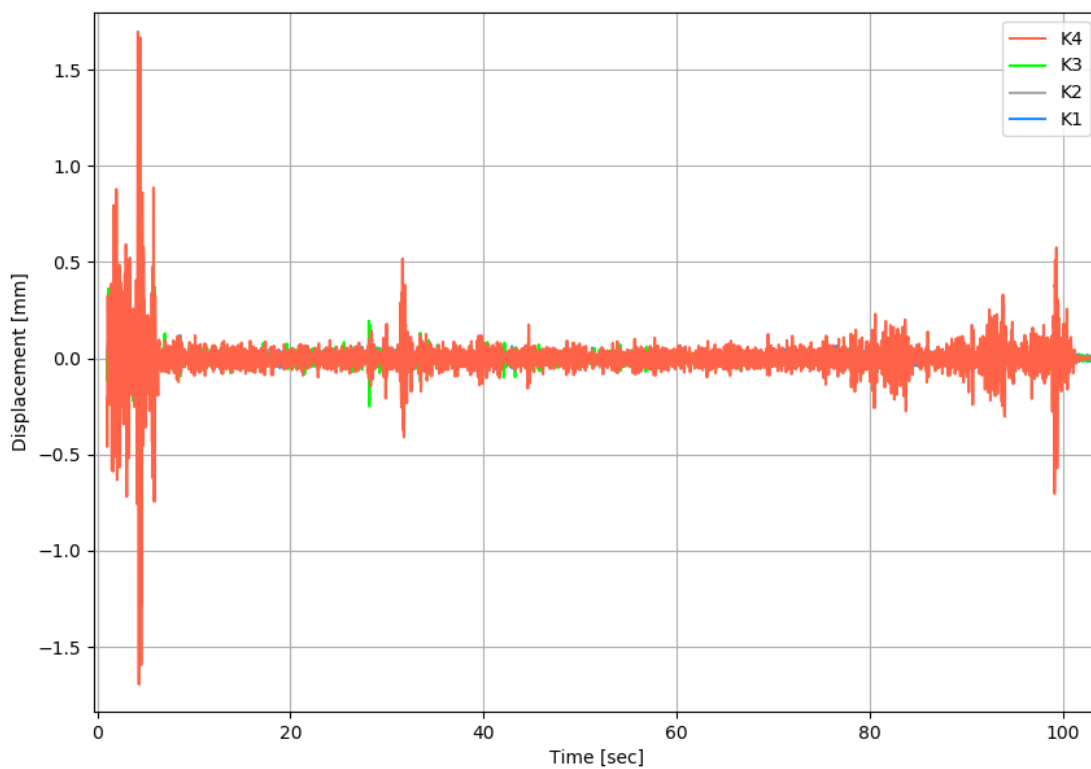


**Figure A-38: Time-domain deflection: X-axis of all Kli-Pis (field test)**

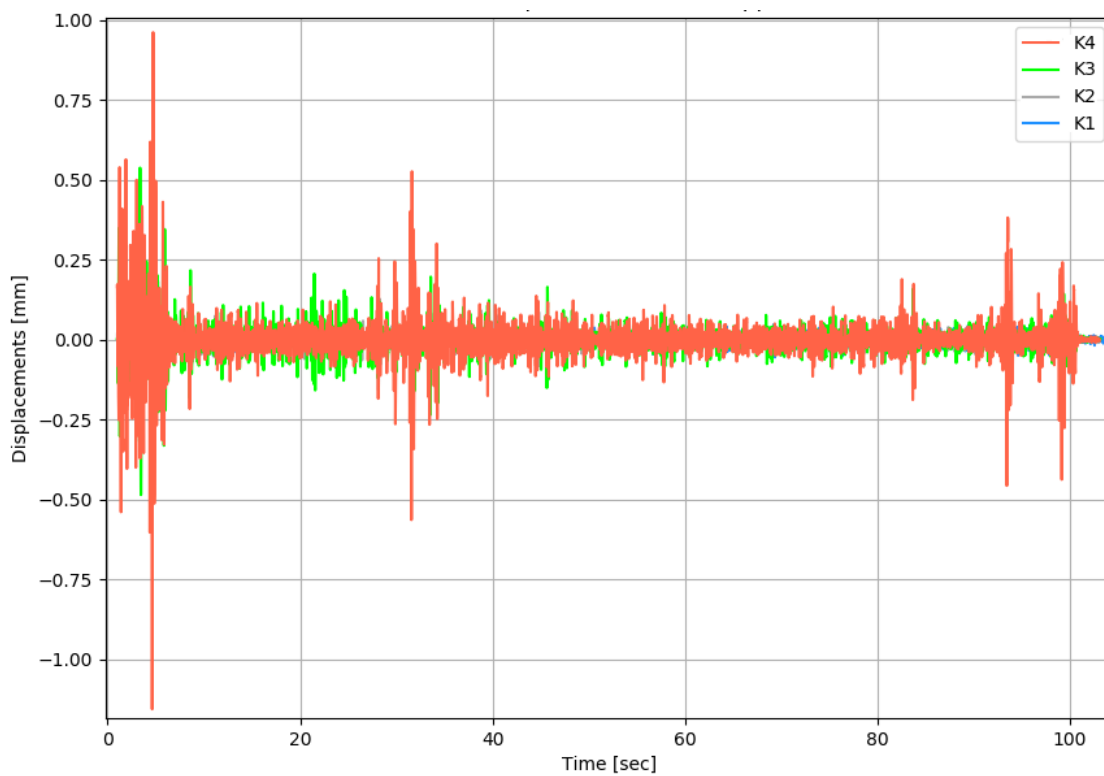


**Figure A-39: Time-domain deflection: Y-axis of all Kli-Pis (field test)**

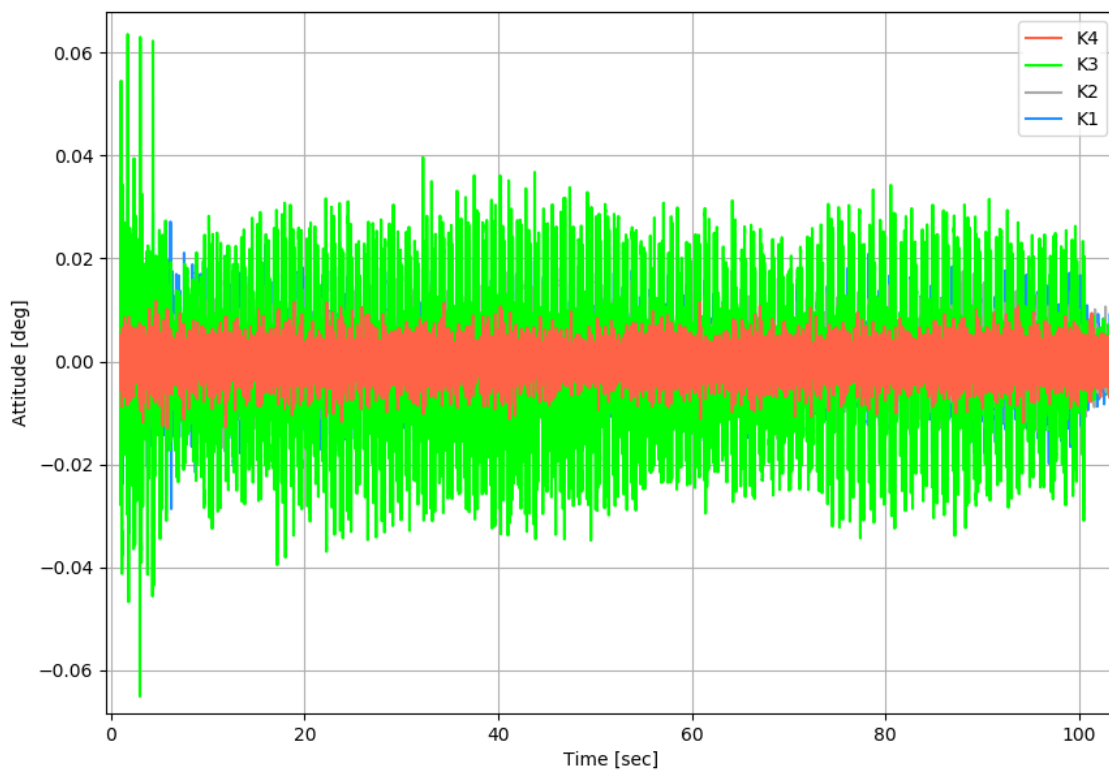


**Figure A-40: Time-domain rotation: X-axis of all Kli-Pis (field test)**

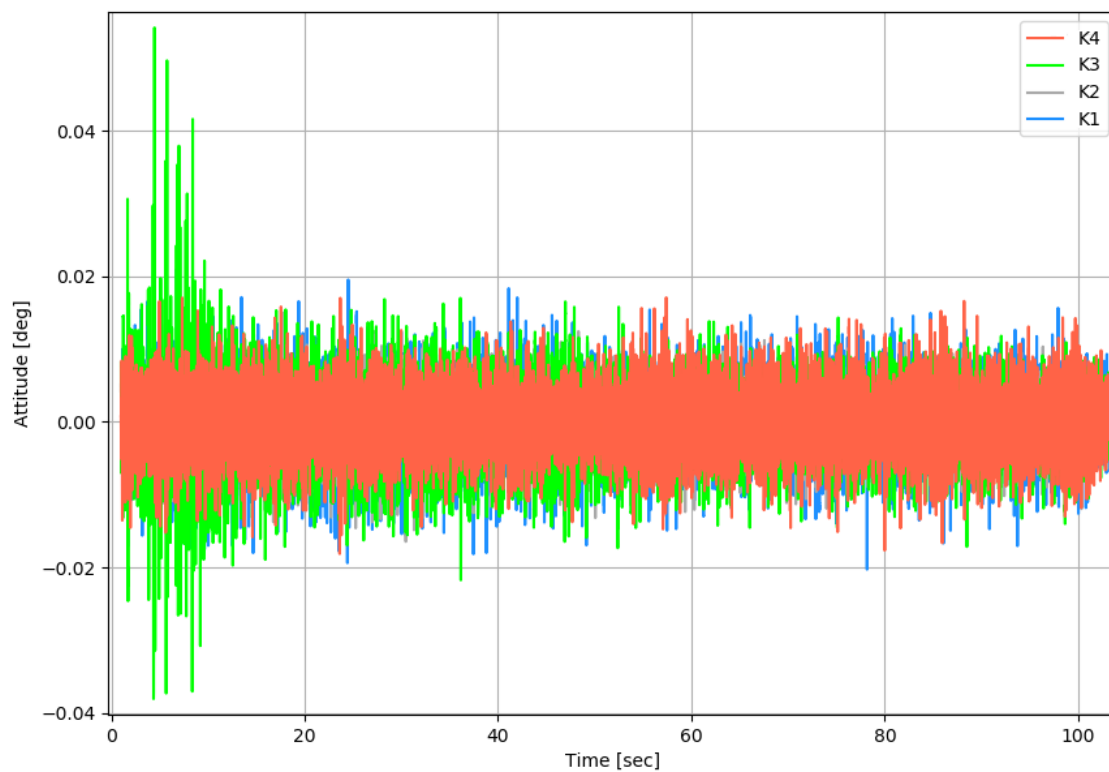


**Figure A-41: Time-domain rotation: Y-axis of all Kli-Pis (field test)**

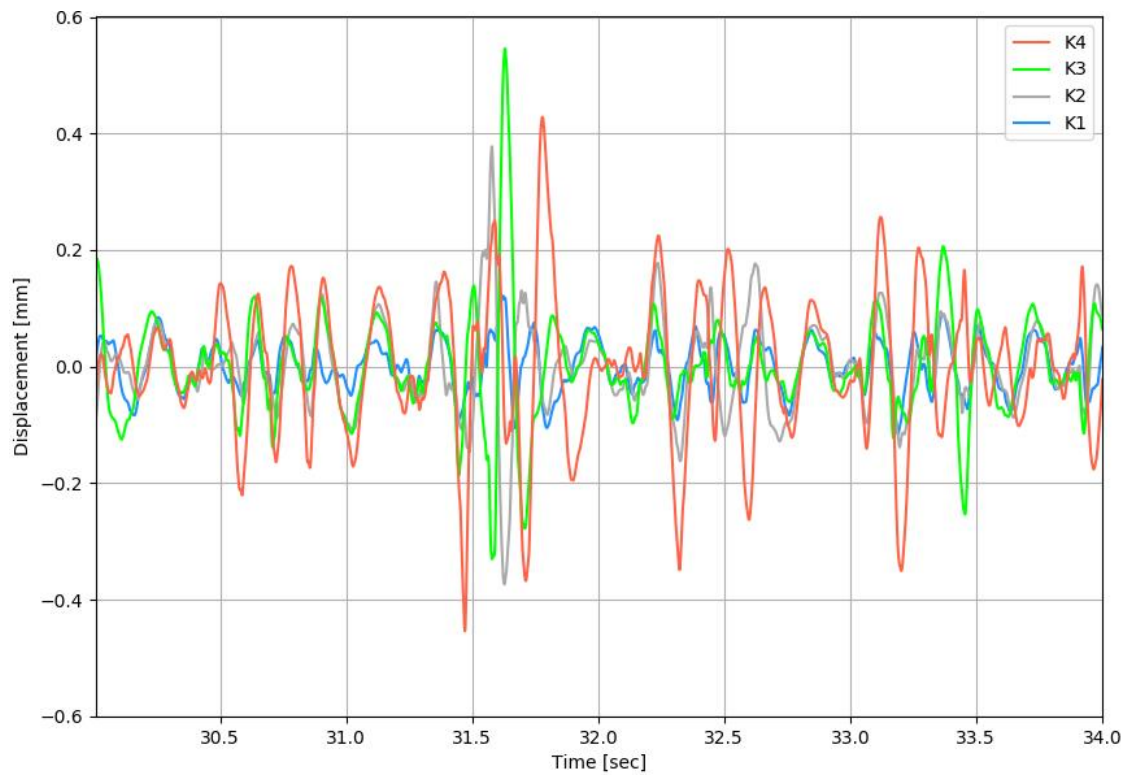


**Figure A-42: Time-domain deflection: Z-axis of all Kli-Pis (field test, impact load)**

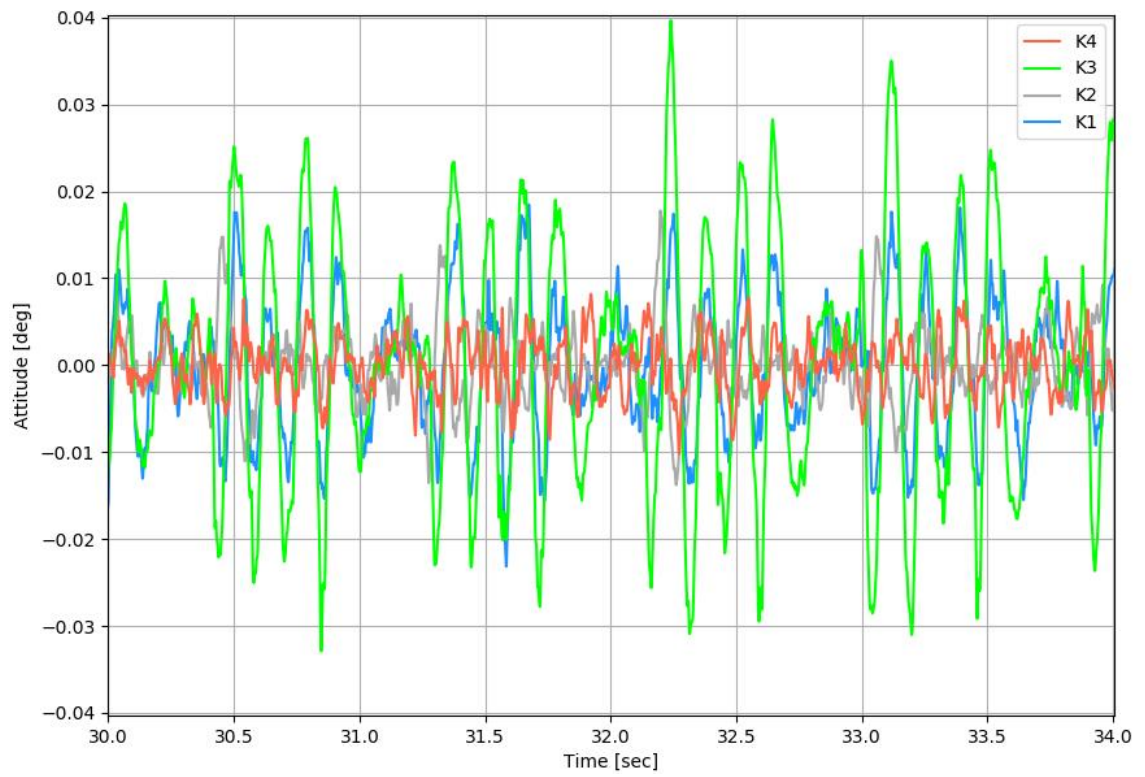


**Figure A-43: Time-domain rotation: X-axis of all Kli-Pis (field test, impact load)**

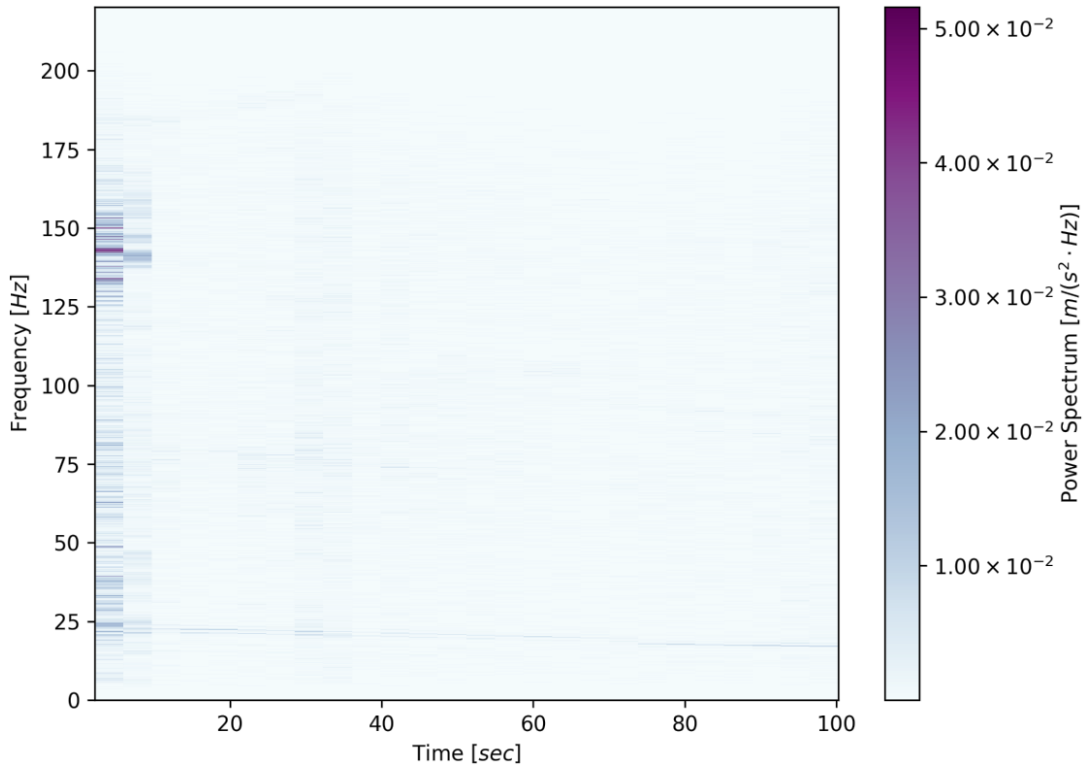


**Figure A-44: Spectrographic acceleration: Z-axis of Kli-Pi 1 (550mm, field test)**

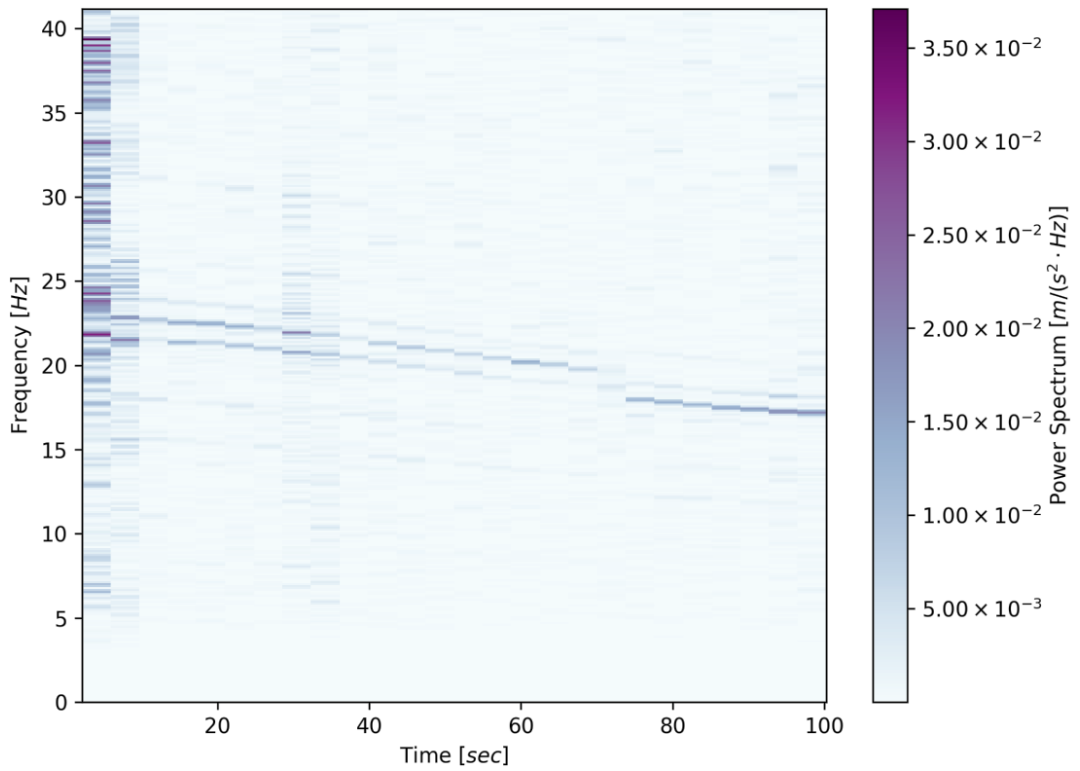


**Figure A-45: Spectrographic acceleration: Z-axis of Kli-Pi 1 (550mm, field test, detailed)**

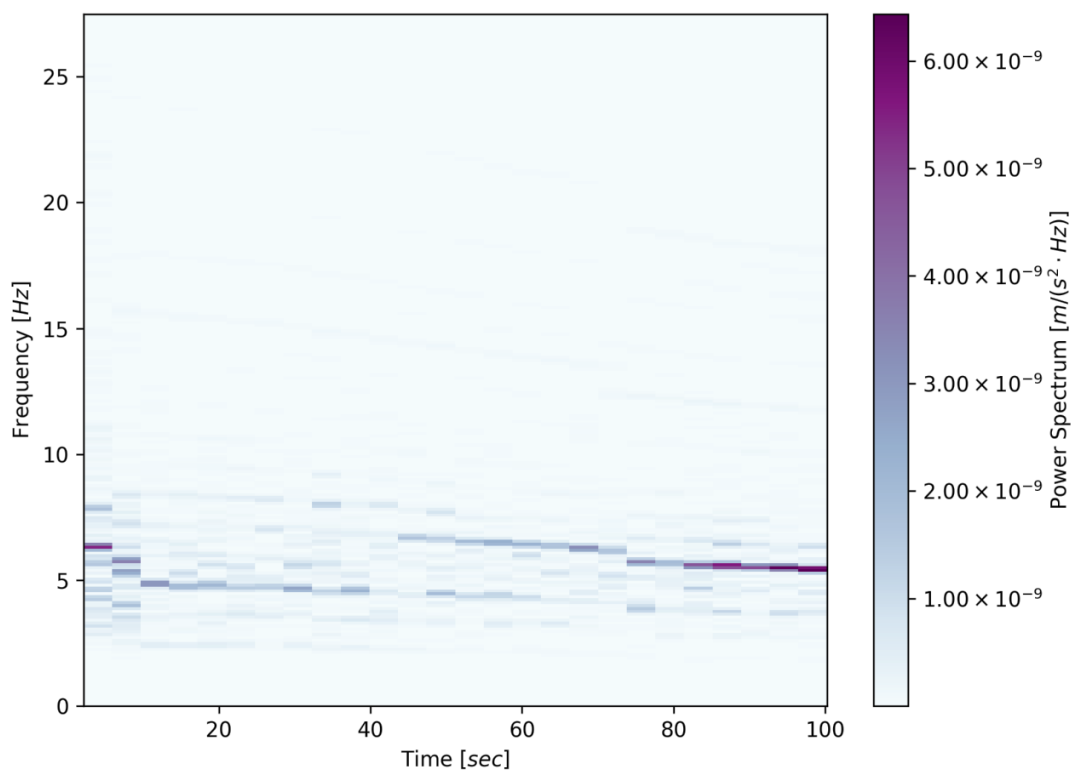


**Figure A-46: Spectrographic displacement: Z-axis of Kli-Pi 1 (550mm, field test, detailed)**

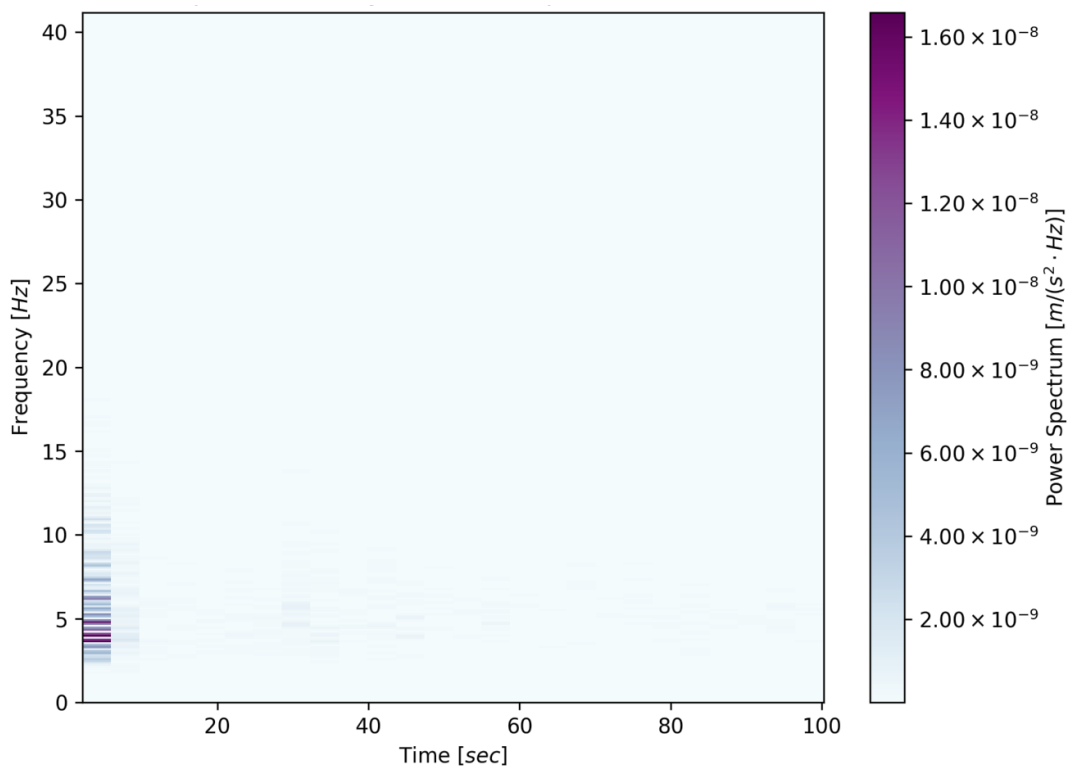


**Figure A-47: Spectrographic displacement: X-axis of Kli-Pi 3 (250mm, field test, detailed)**

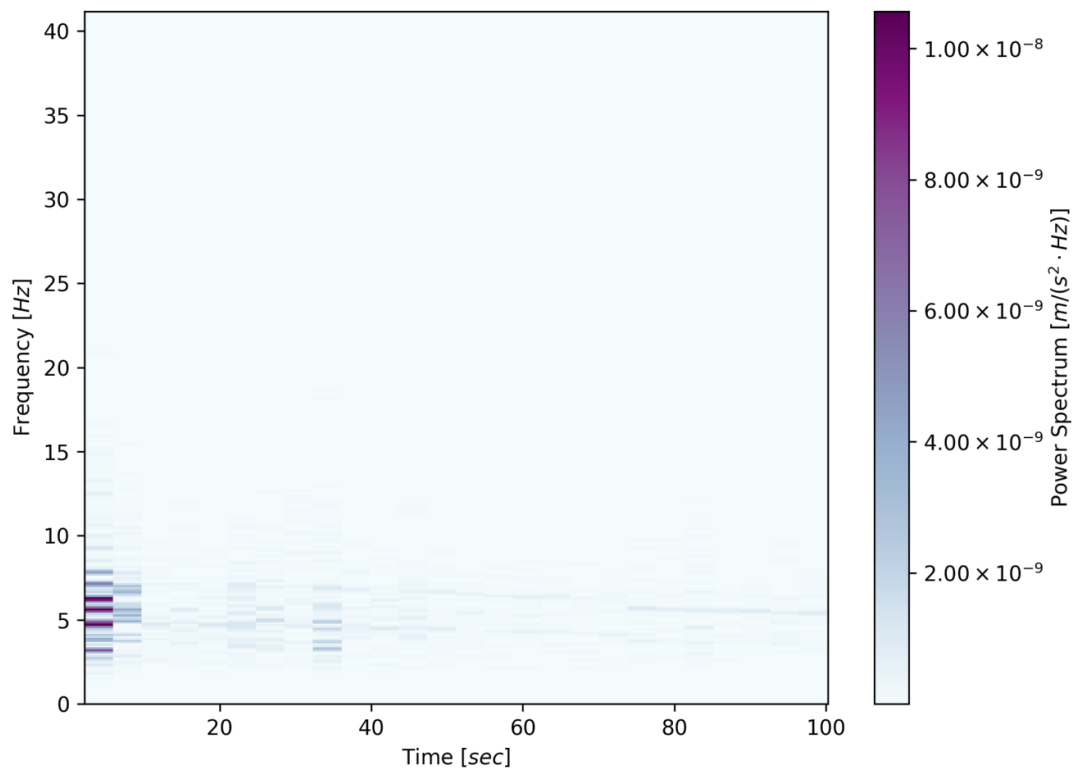


**Figure A-48: Spectrographic displacement: Y-axis of Kli-Pi 3 (250mm, field test, detailed)**

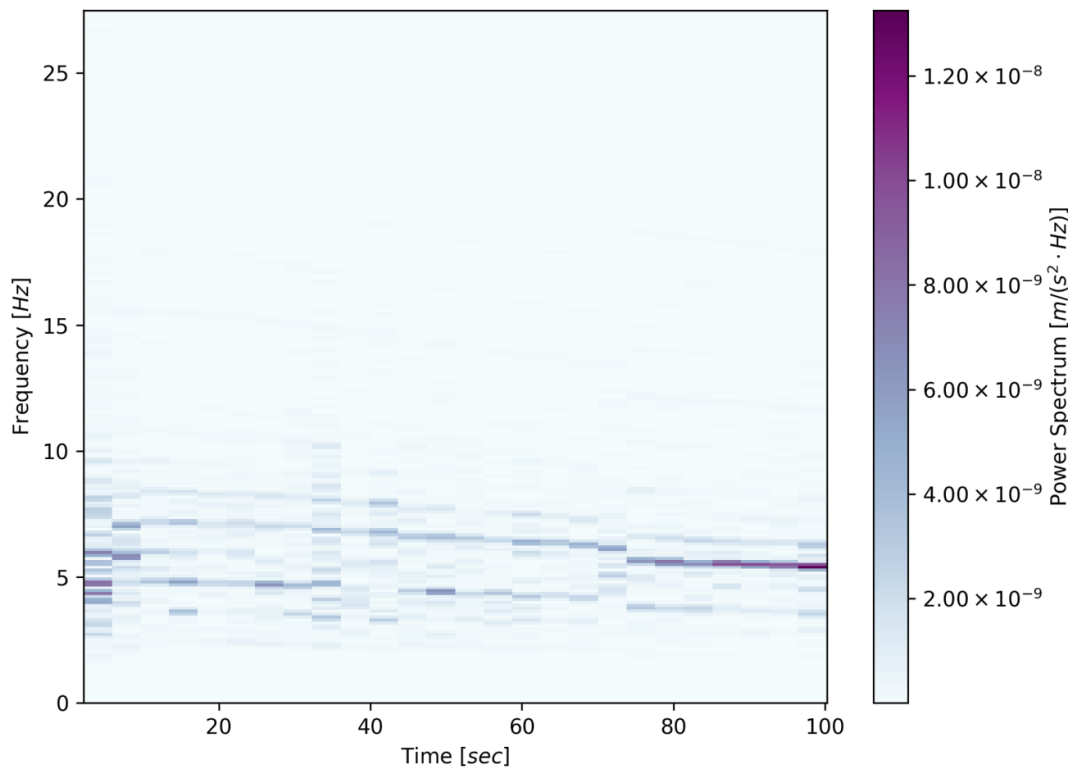


**Figure A-49: Spectrographic displacement: Z-axis of Kli-Pi 3 (250mm, field test, detailed)**

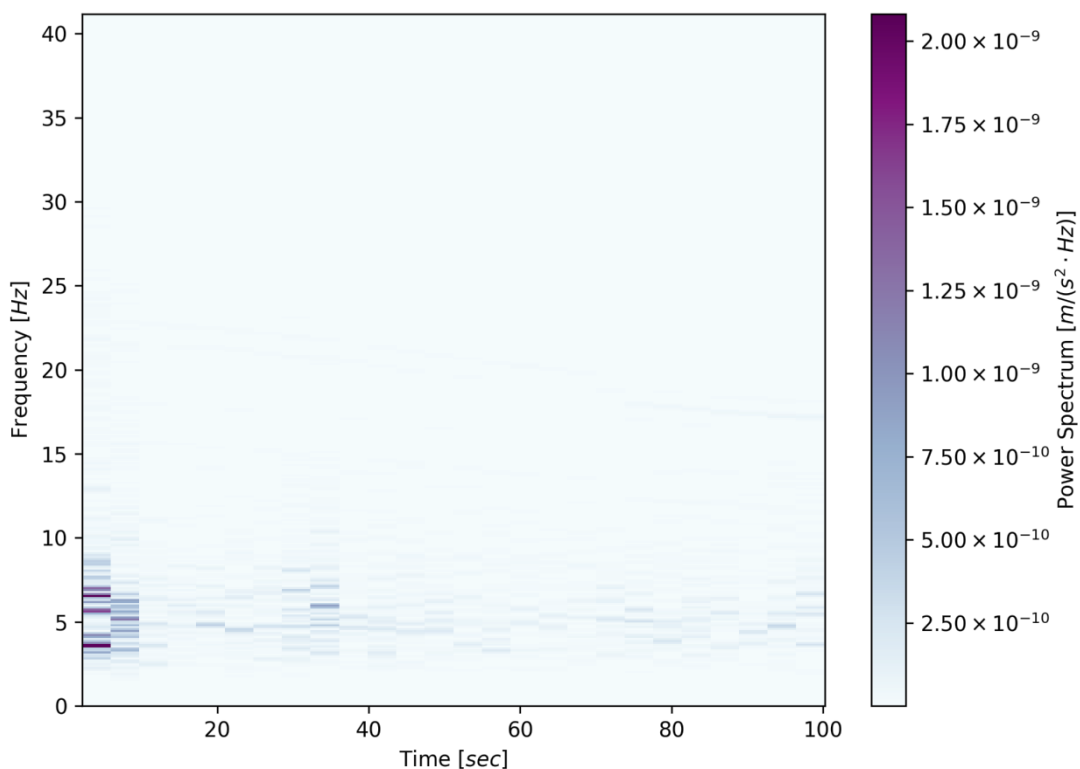


**Figure A-50: Spectrographic displacement: X-axis of Kli-Pi 1 (550mm, field test, detailed)**

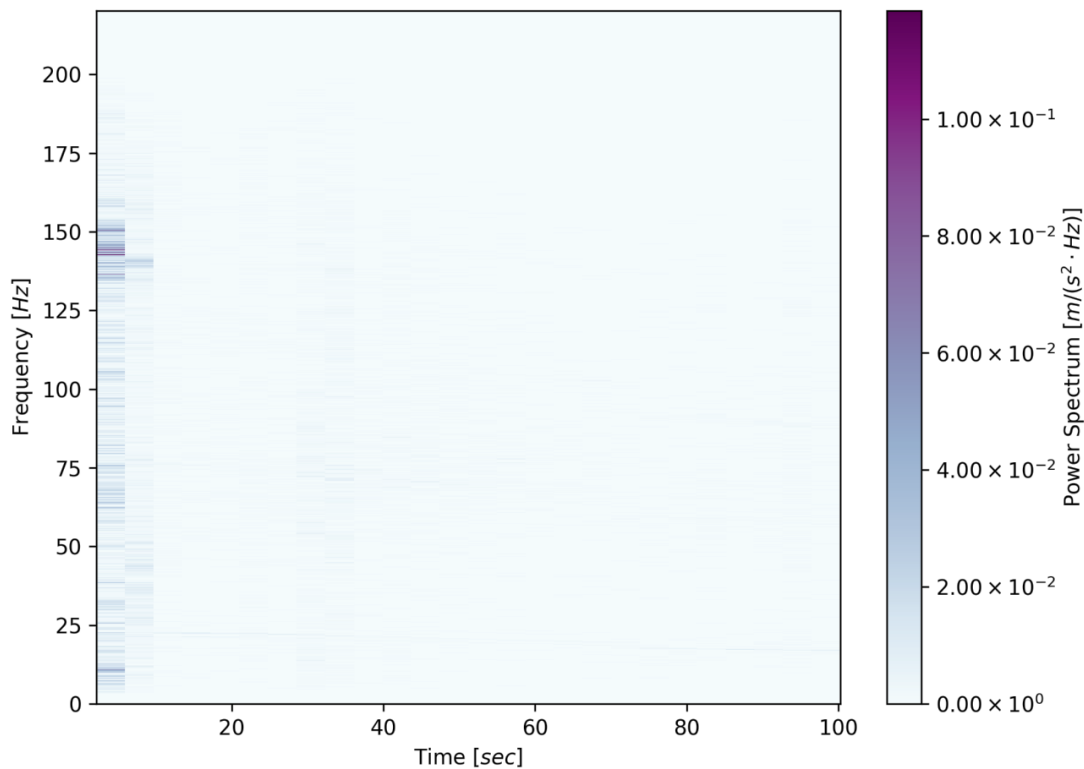


**Figure A-51: Spectrographic acceleration: Z-axis of Kli-Pi 3 (250mm, field test)**

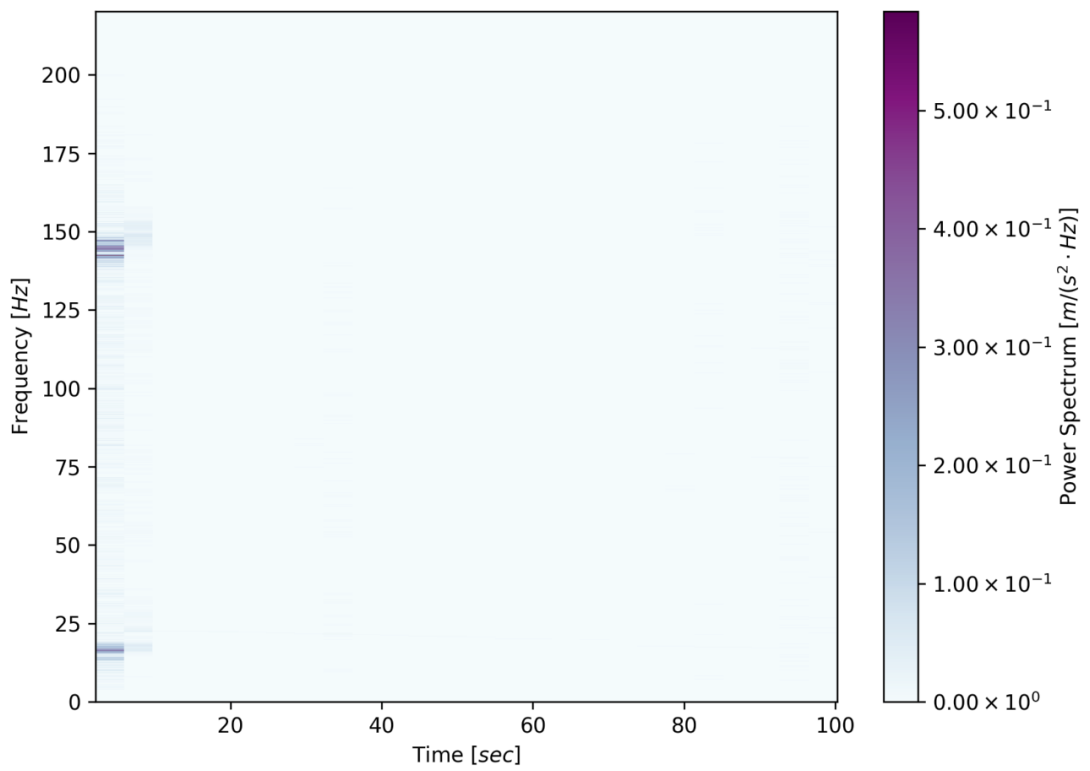


**Figure A-52: Spectrographic acceleration: Z-axis of Kli-Pi 4 (0mm, field test)**

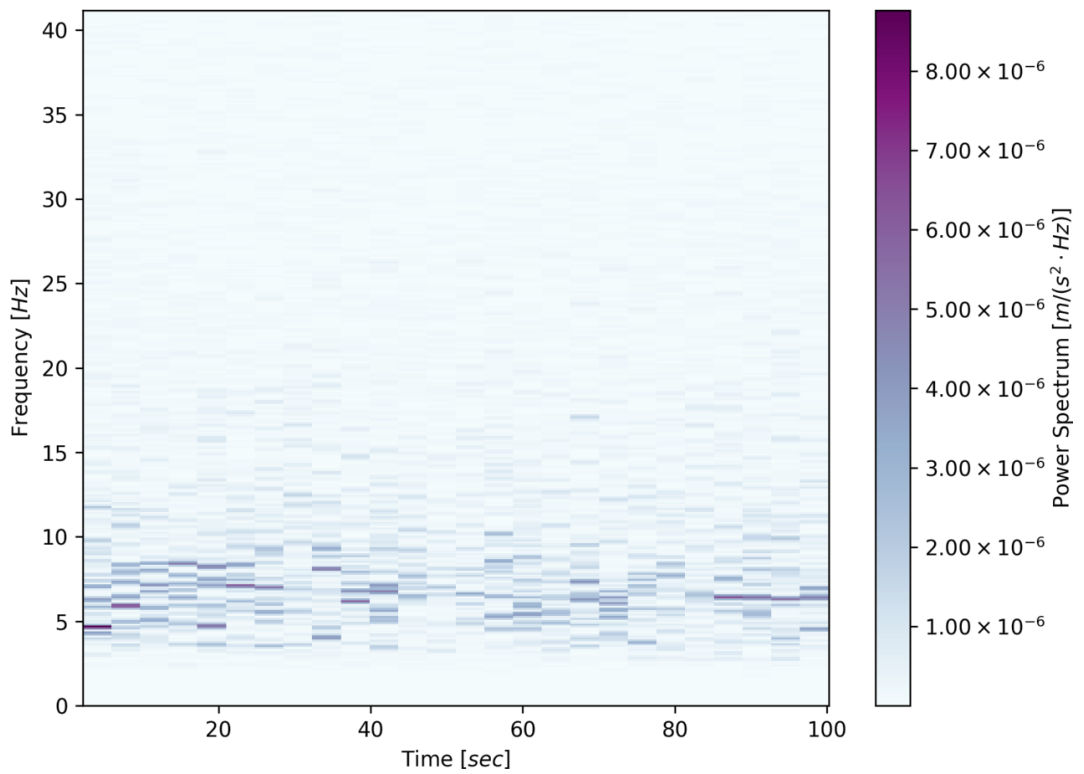


**Figure A-53: Spectrographic rotation: X-axis of Kli-Pi 4 (0mm, field test, detailed)**

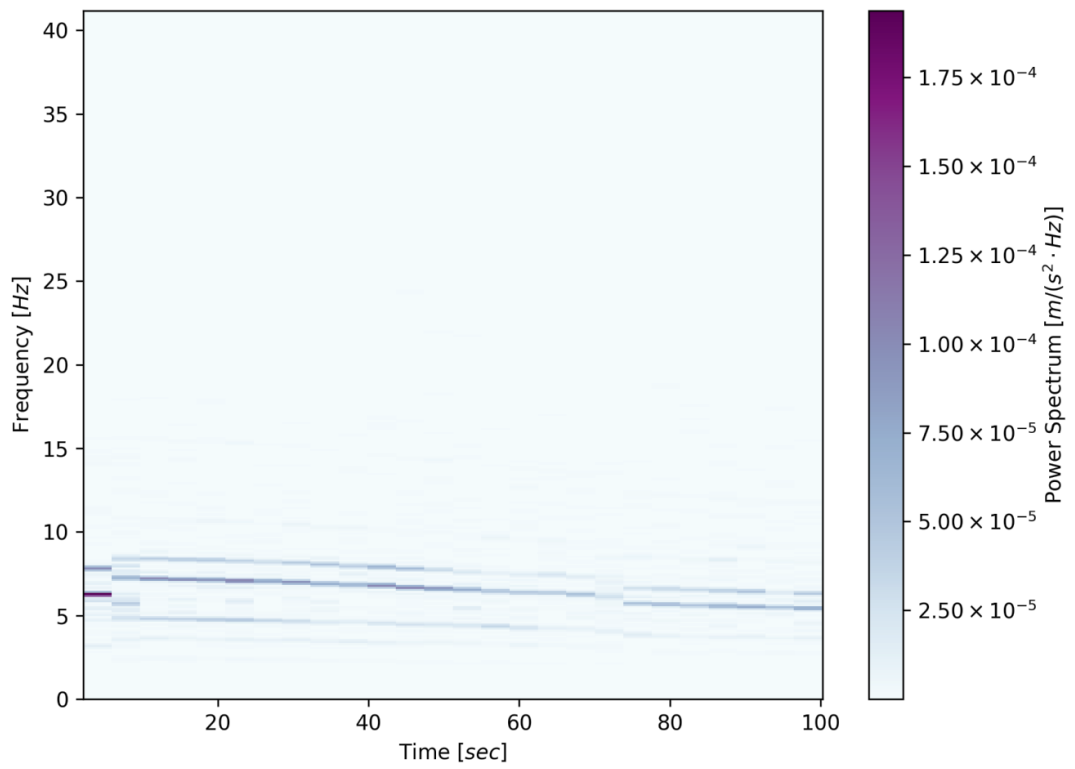


**Figure A-54: Spectrographic rotation: X-axis of Kli-Pi 1 (550mm, field test, detailed)**

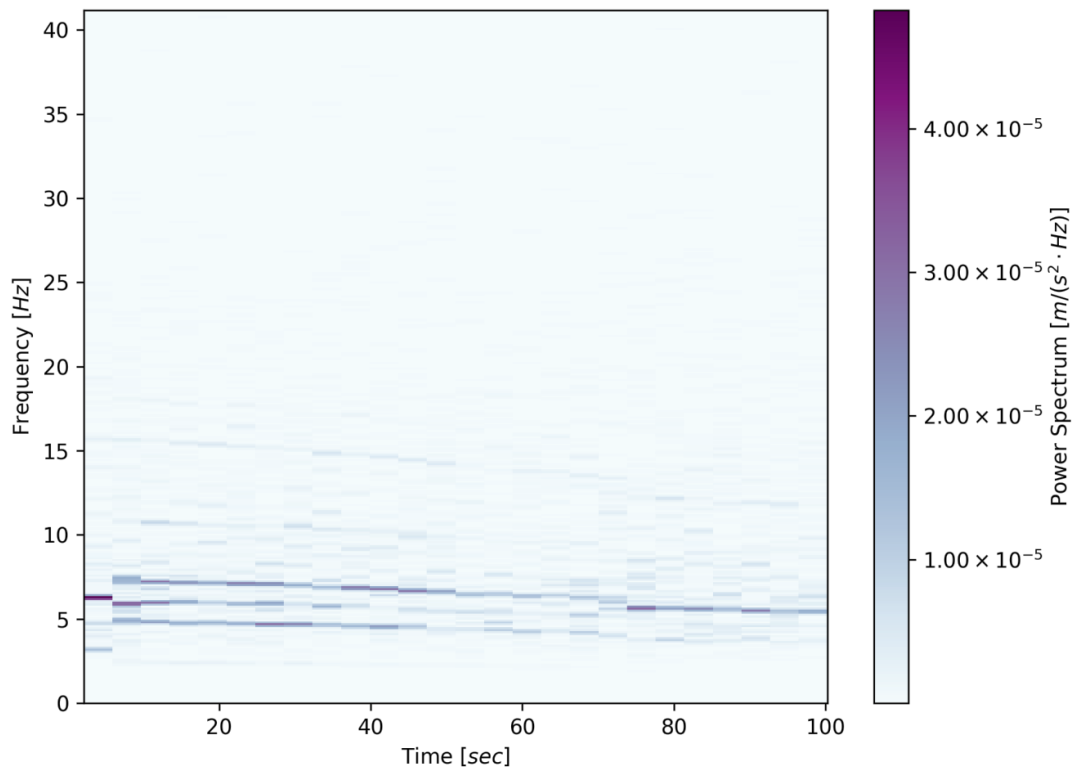


**Figure A-55: Spectrographic rotation: Y-axis of Kli-Pi 1 (550mm, field test, detailed)**

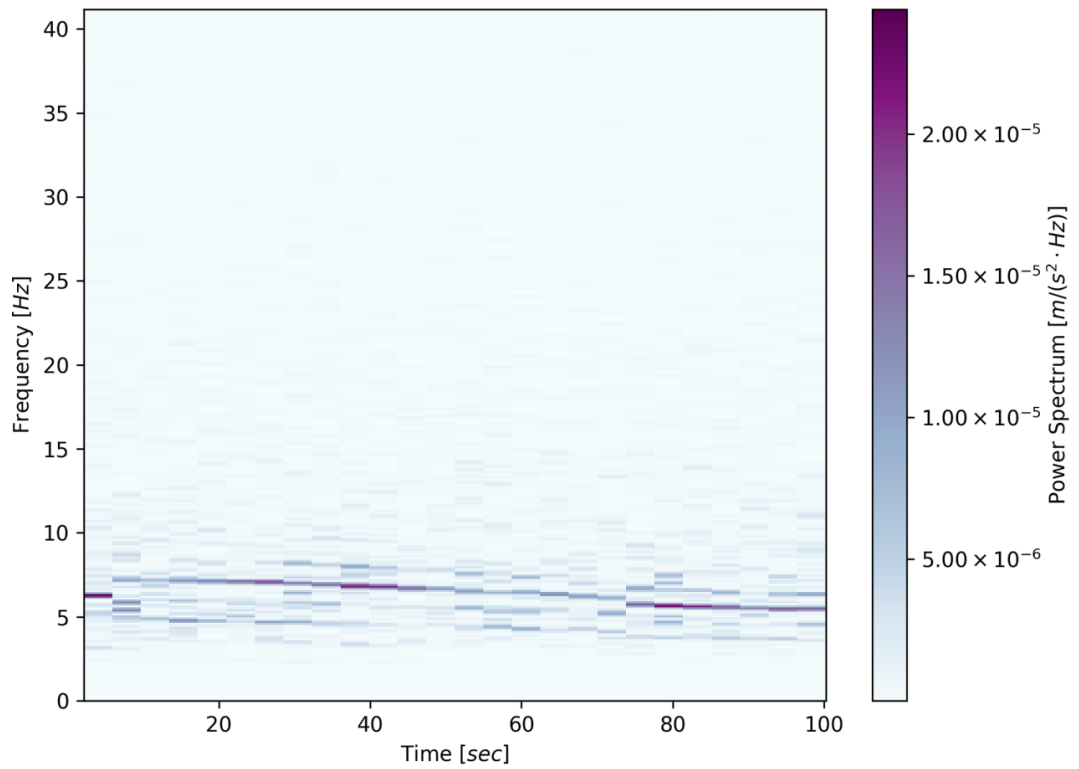


**Figure A-56: Spectrographic rotation: Z-axis of Kli-Pi 1 (550mm, field test, detailed)**

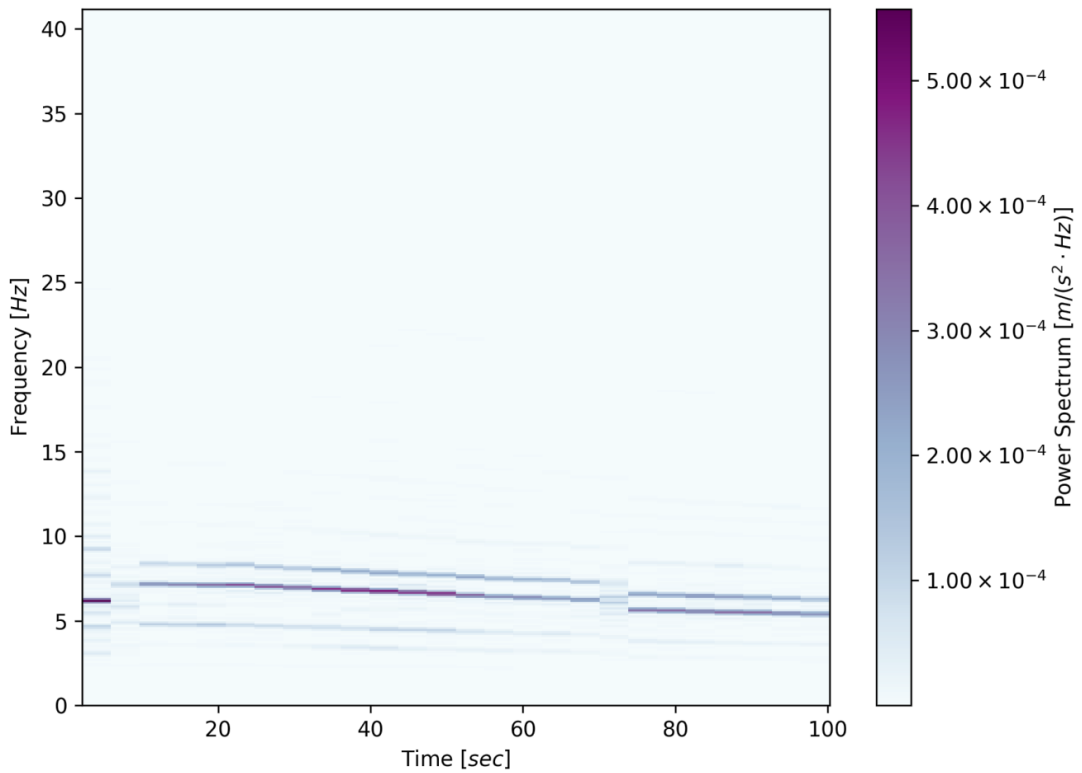


**Figure A-57: Spectrographic rotation: X-axis of Kli-Pi 3 (250mm, field test, detailed)**

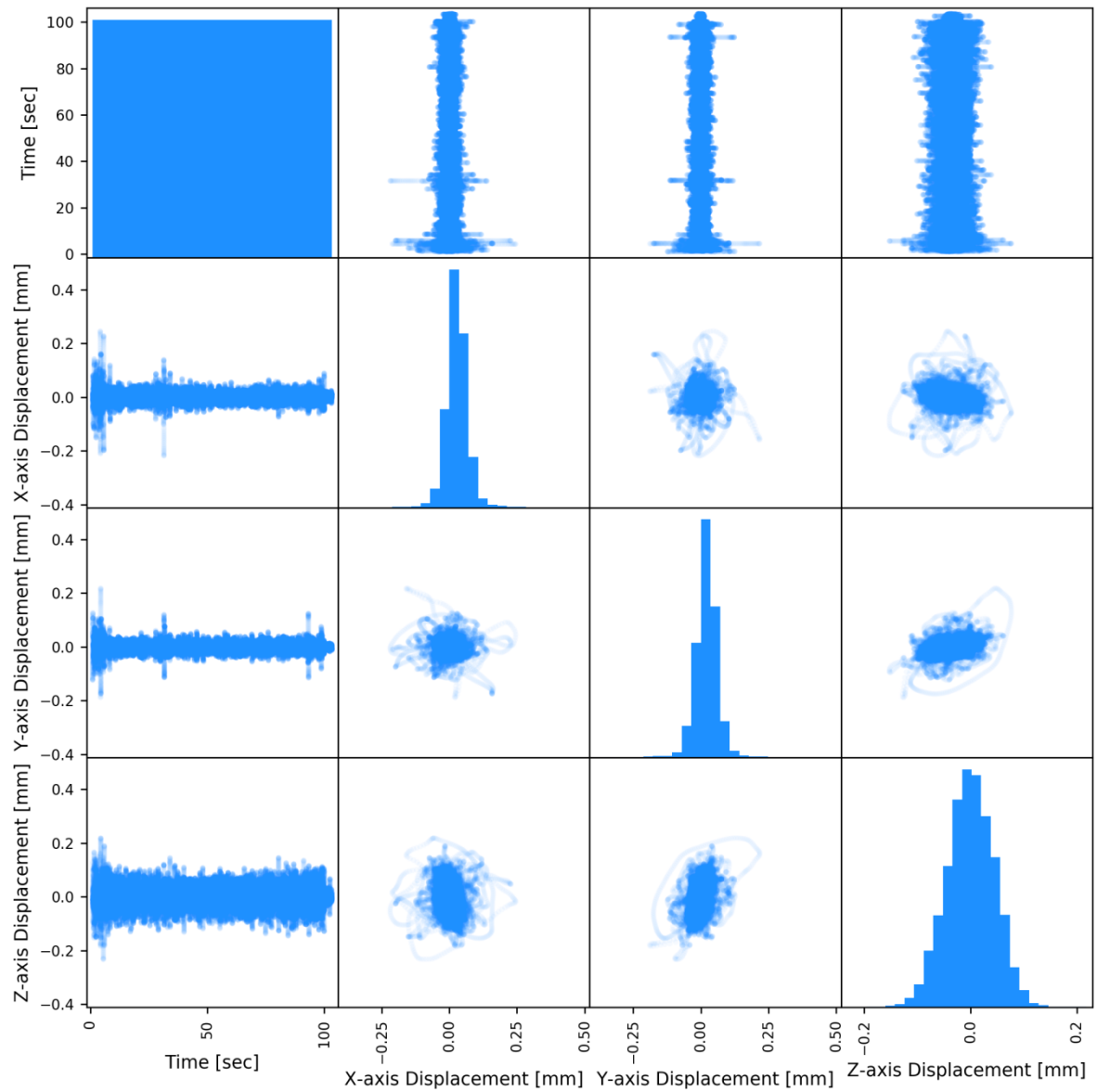


**Figure A-58: Time-domain displacement matrix: Kli-Pi 1 (550mm, field test)**

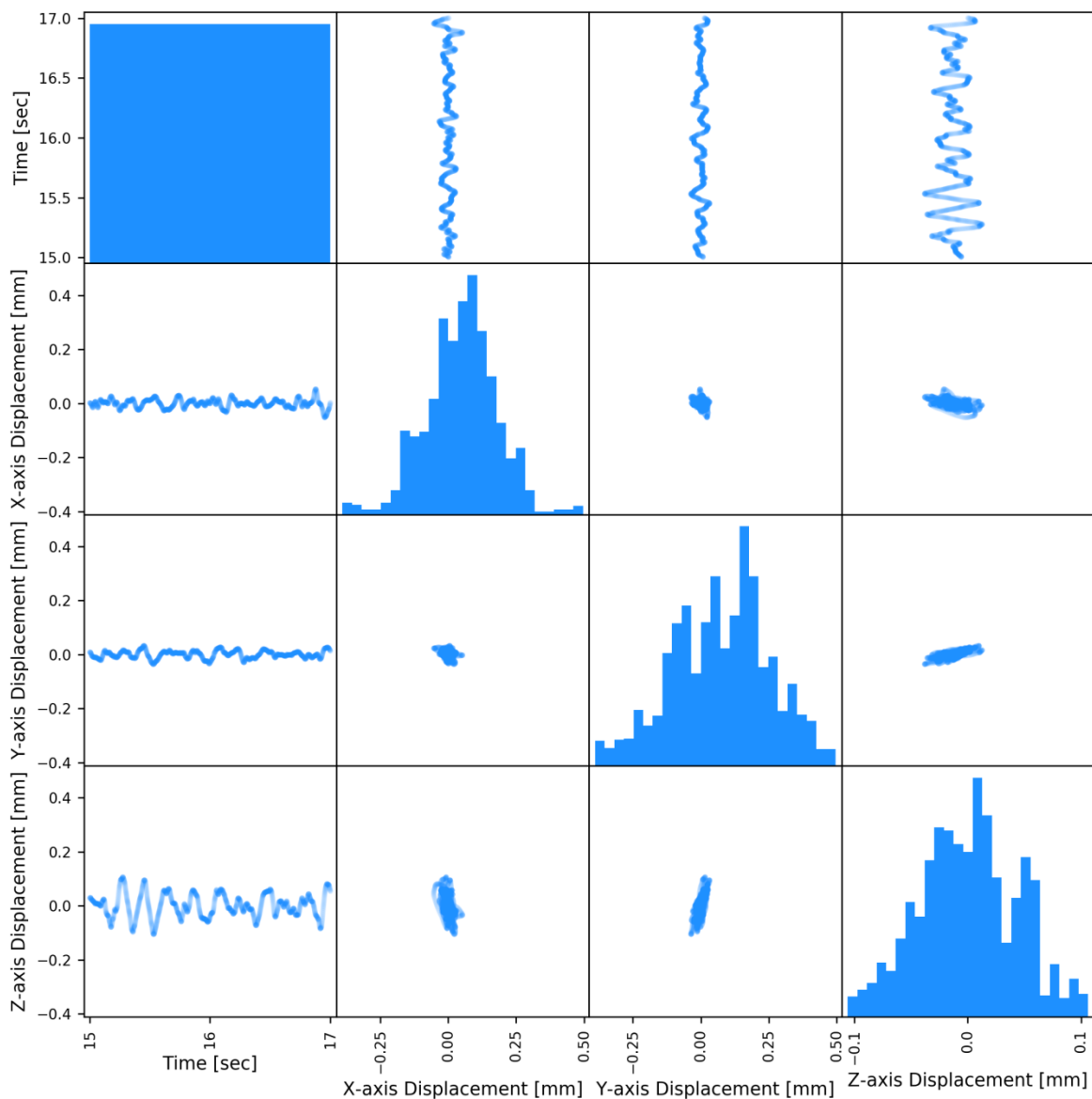


**Figure A-59: Time-domain displacement matrix: Kli-Pi 1 (550mm, field test, detailed)**

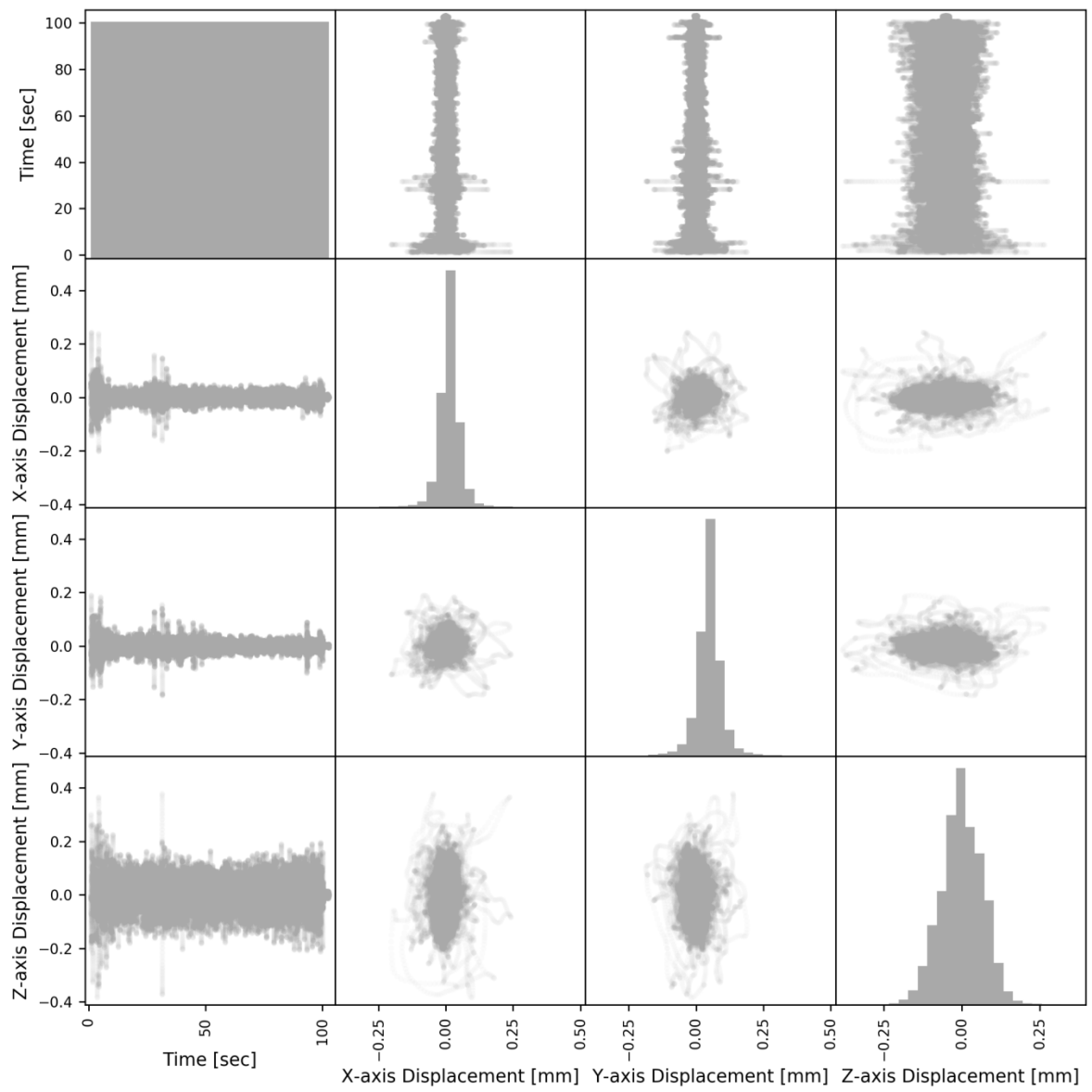


**Figure A-60: Time-domain displacement matrix: Kli-Pi 2 (400mm, field test)**

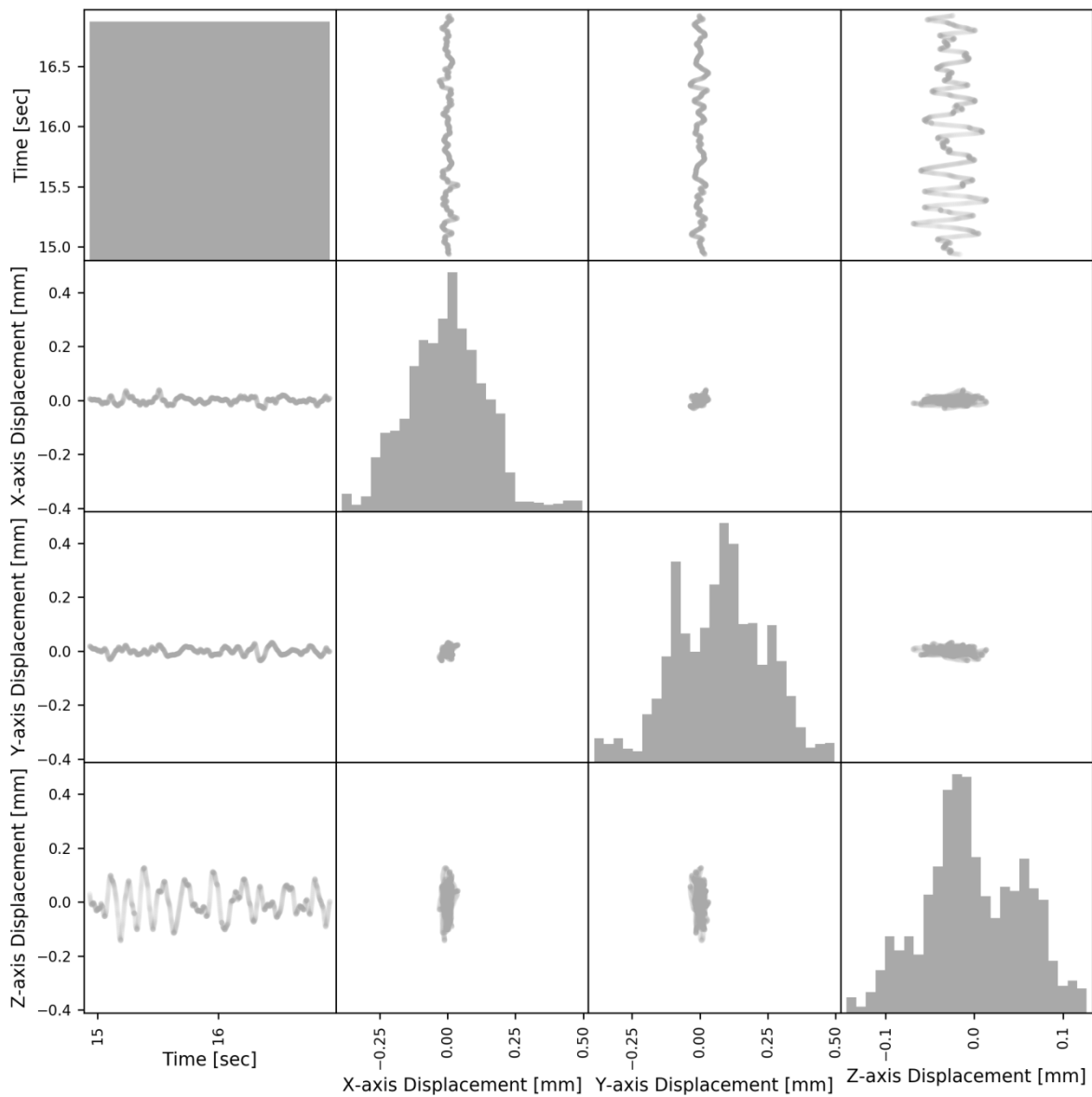


**Figure A-61: Time-domain displacement matrix: Kli-Pi 2 (400mm, field test, detailed)**

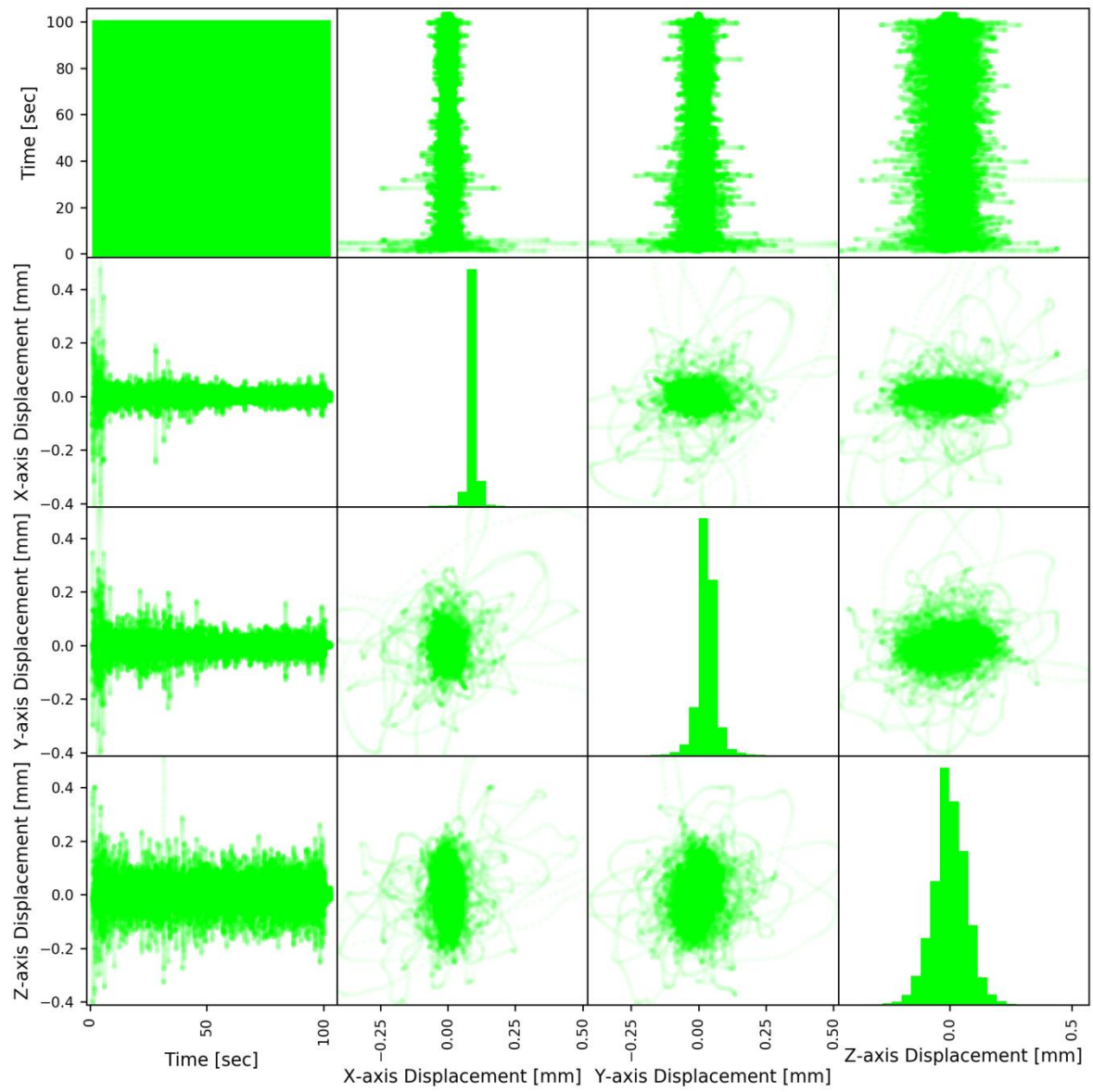


**Figure A-62: Time-domain displacement matrix: Kli-Pi 3 (250mm, field test)**

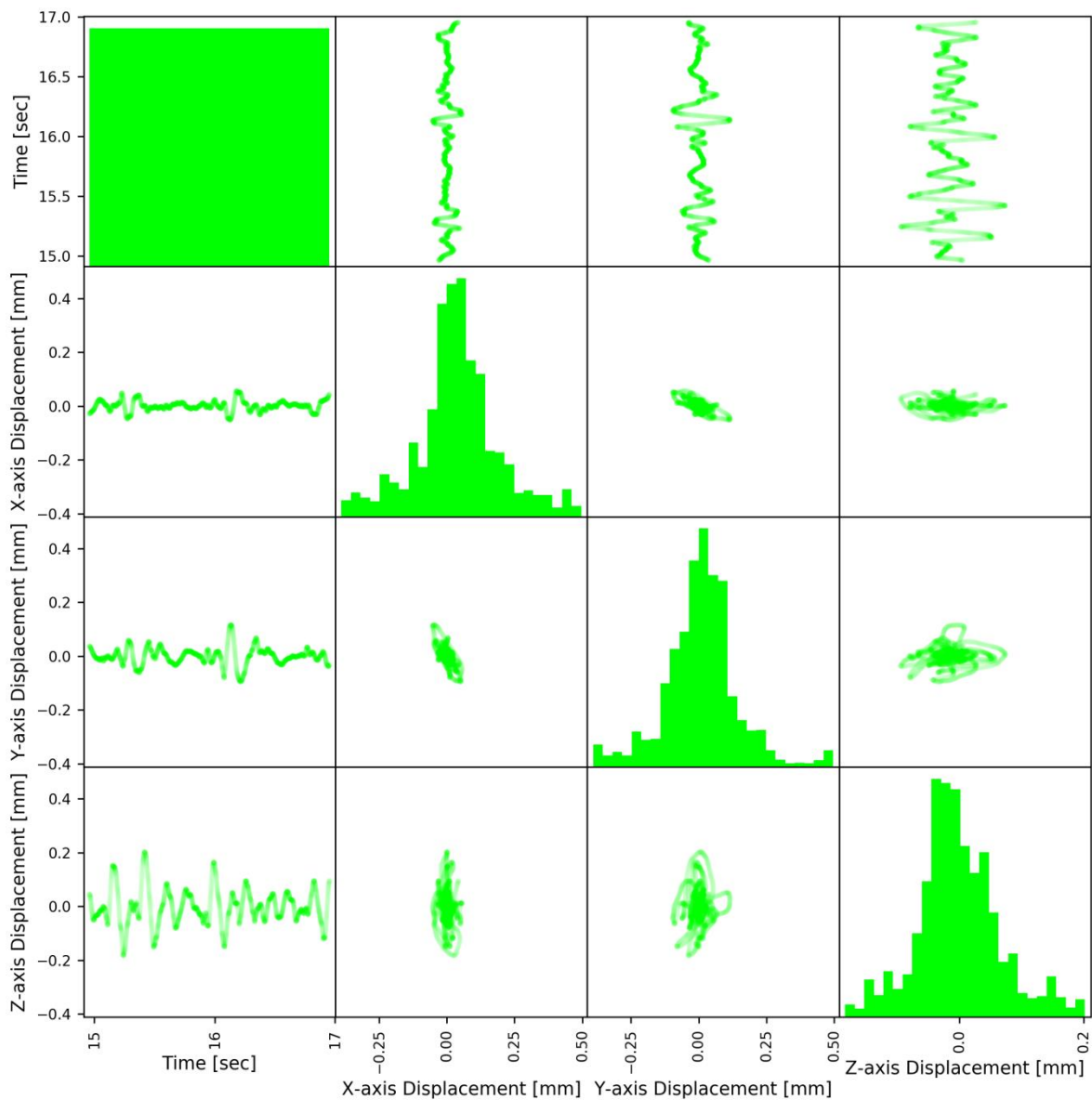


**Figure A-63: Time-domain displacement matrix: Kli-Pi 3 (250mm, field test, detailed)**

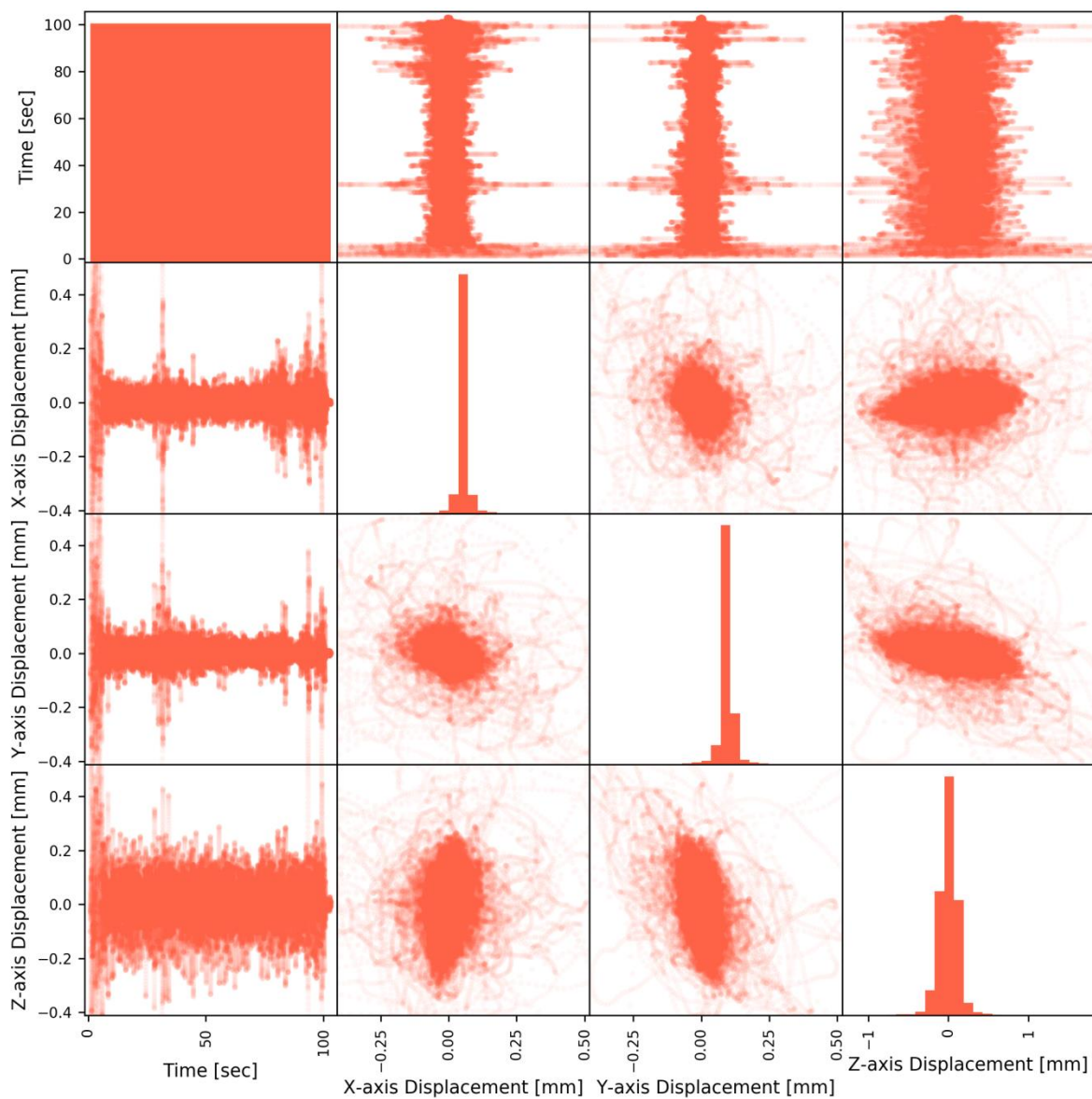


**Figure A-64: Time-domain displacement matrix: Kli-Pi 4 (0mm, field test)**

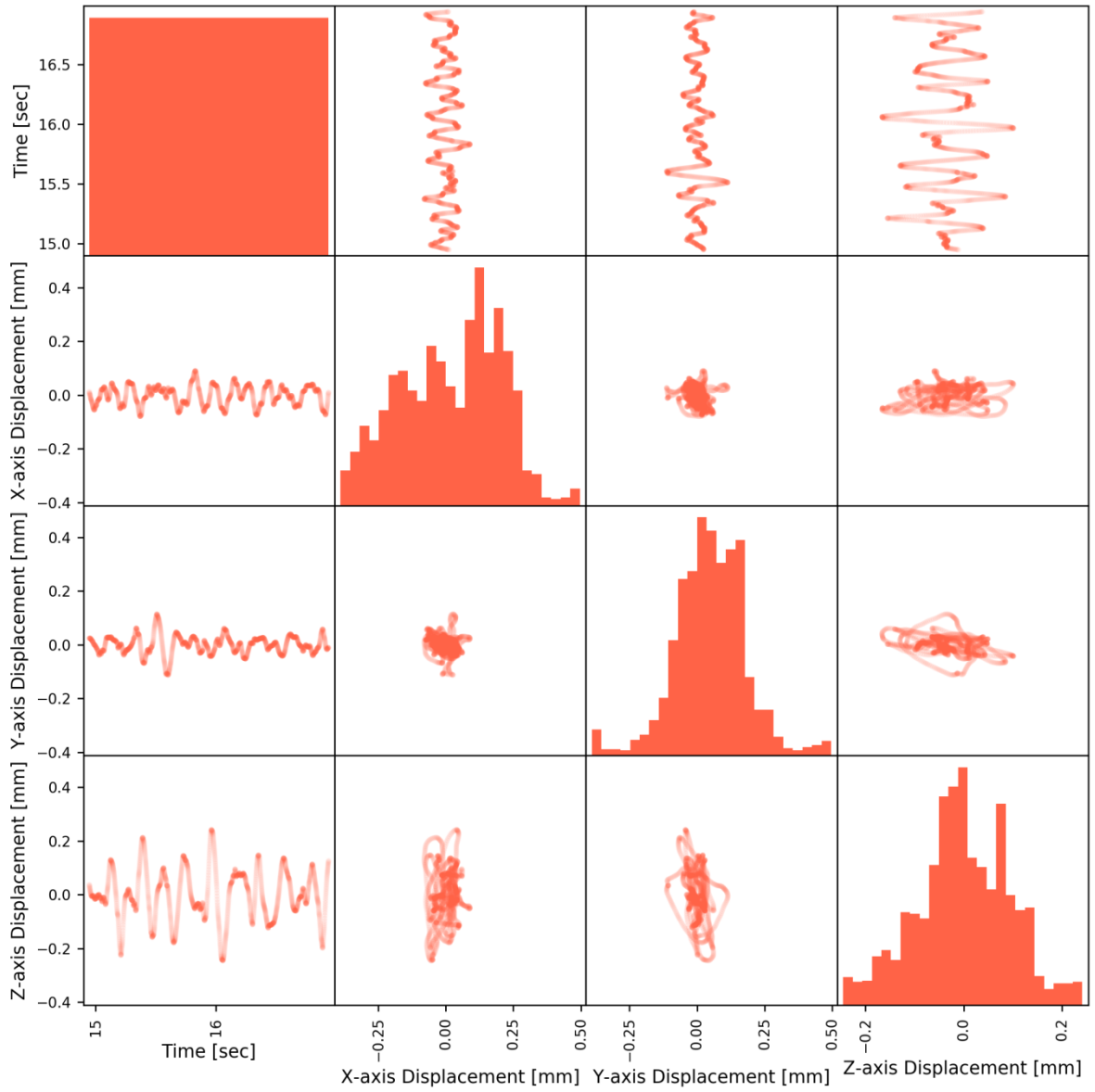


**Figure A-65: Time-domain displacement matrix: Kli-Pi 4 (0mm, field test, detailed)**

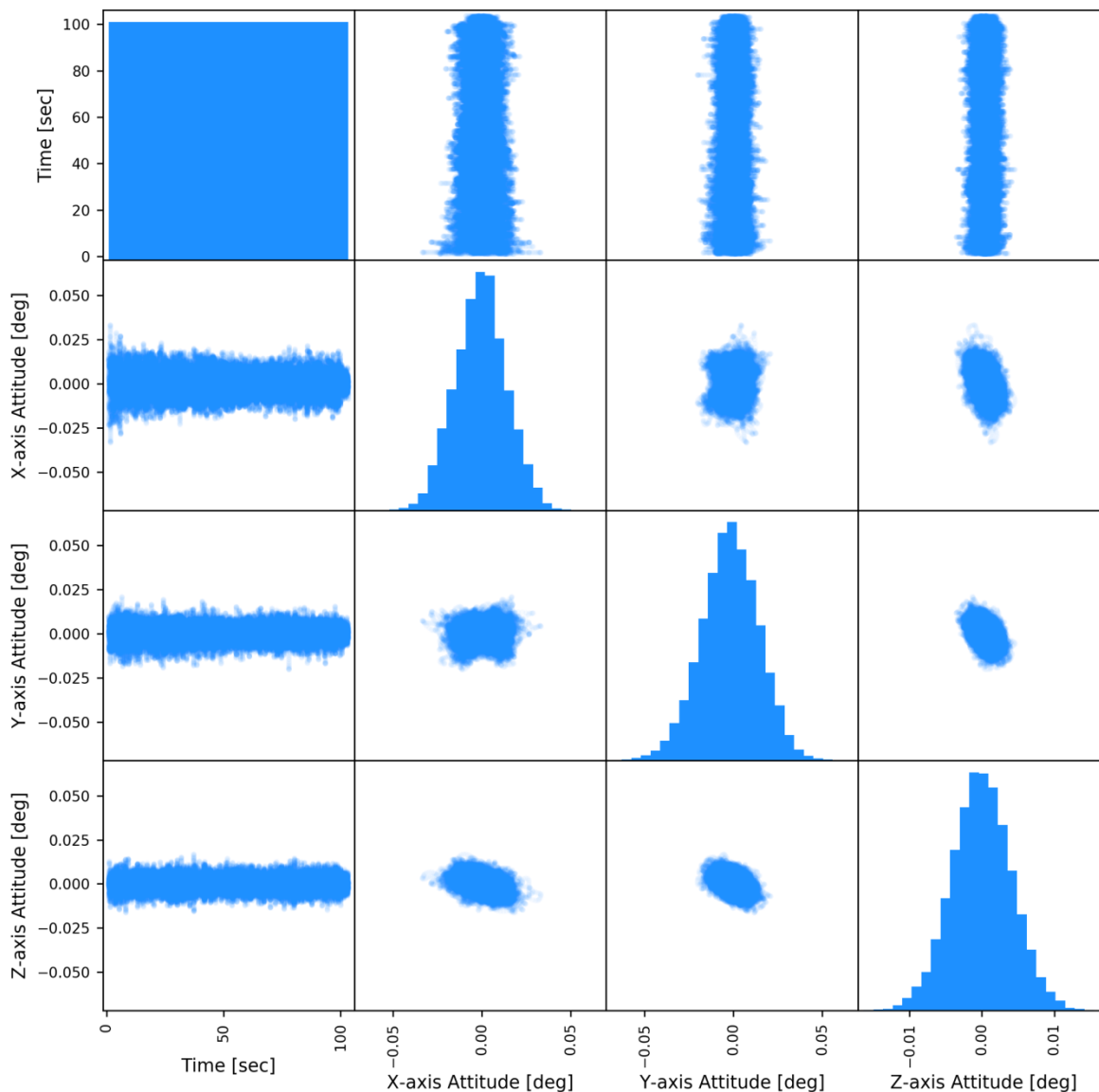


**Figure A-66: Time-domain rotation matrix: Kli-Pi 1 (550mm, field test)**

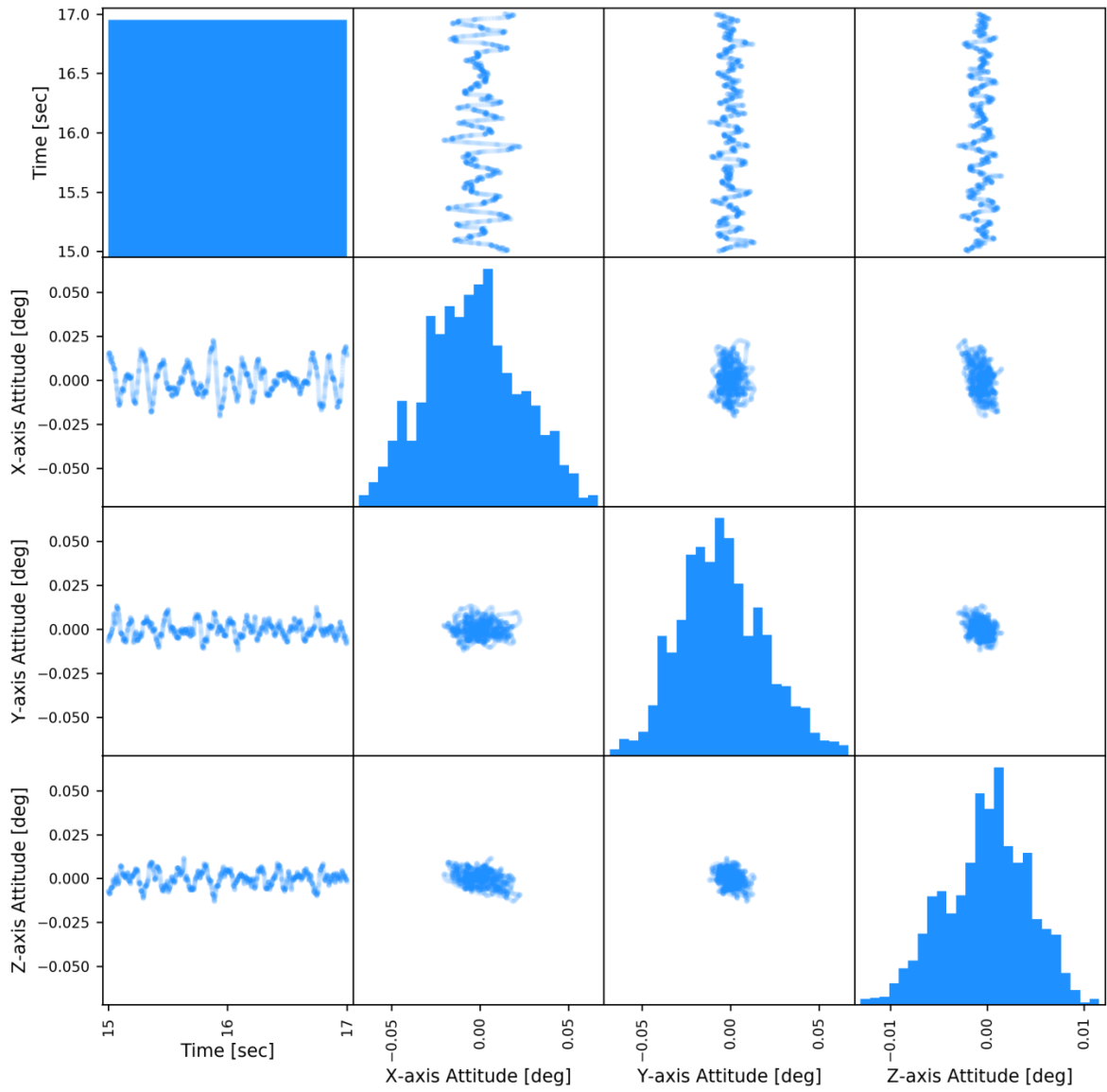


**Figure A-67: Time-domain rotation matrix: Kli-Pi 1 (550mm, field test, detailed)**

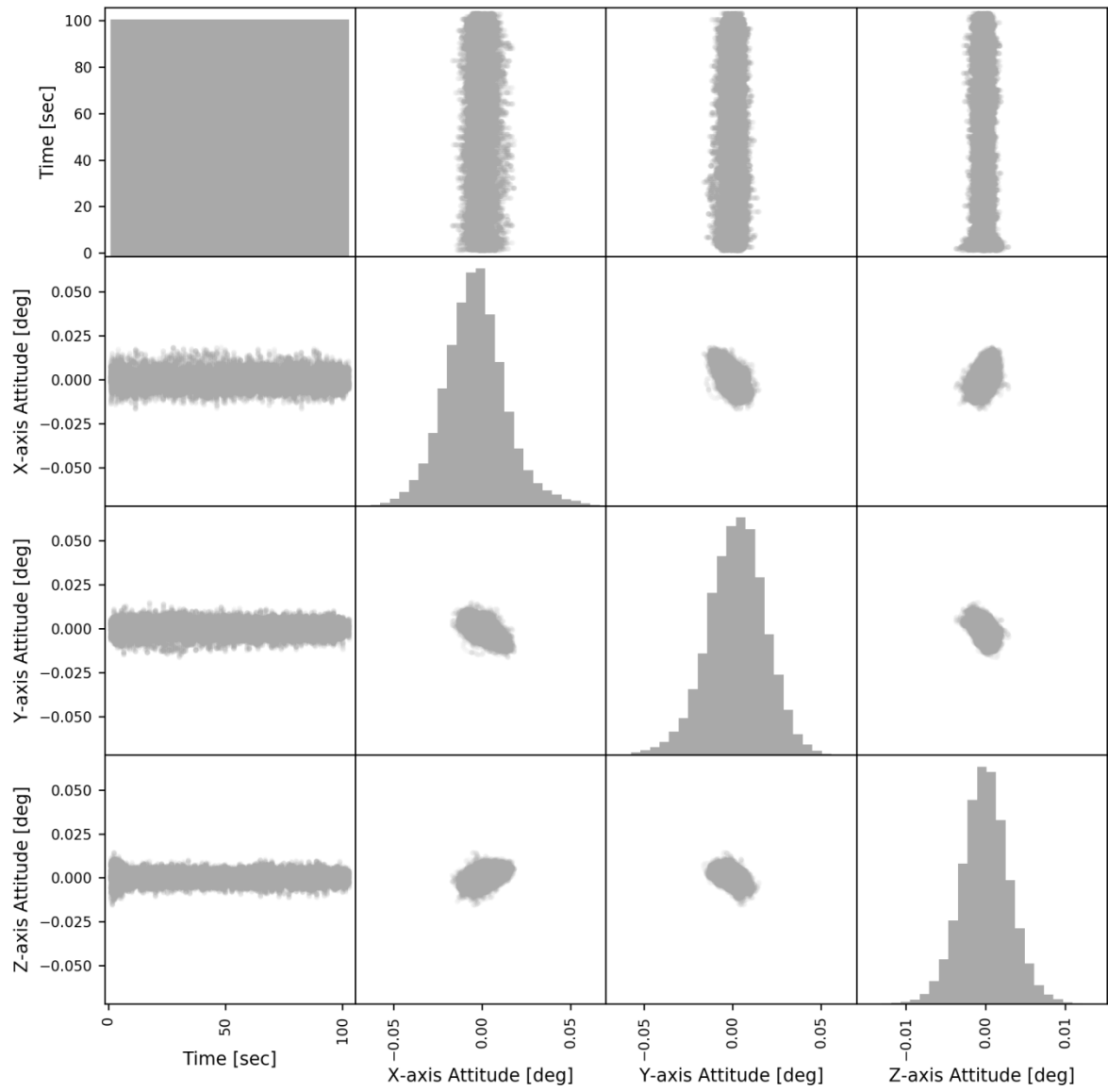


**Figure A-68: Time-domain rotation matrix: Kli-Pi 2 (400mm, field test)**

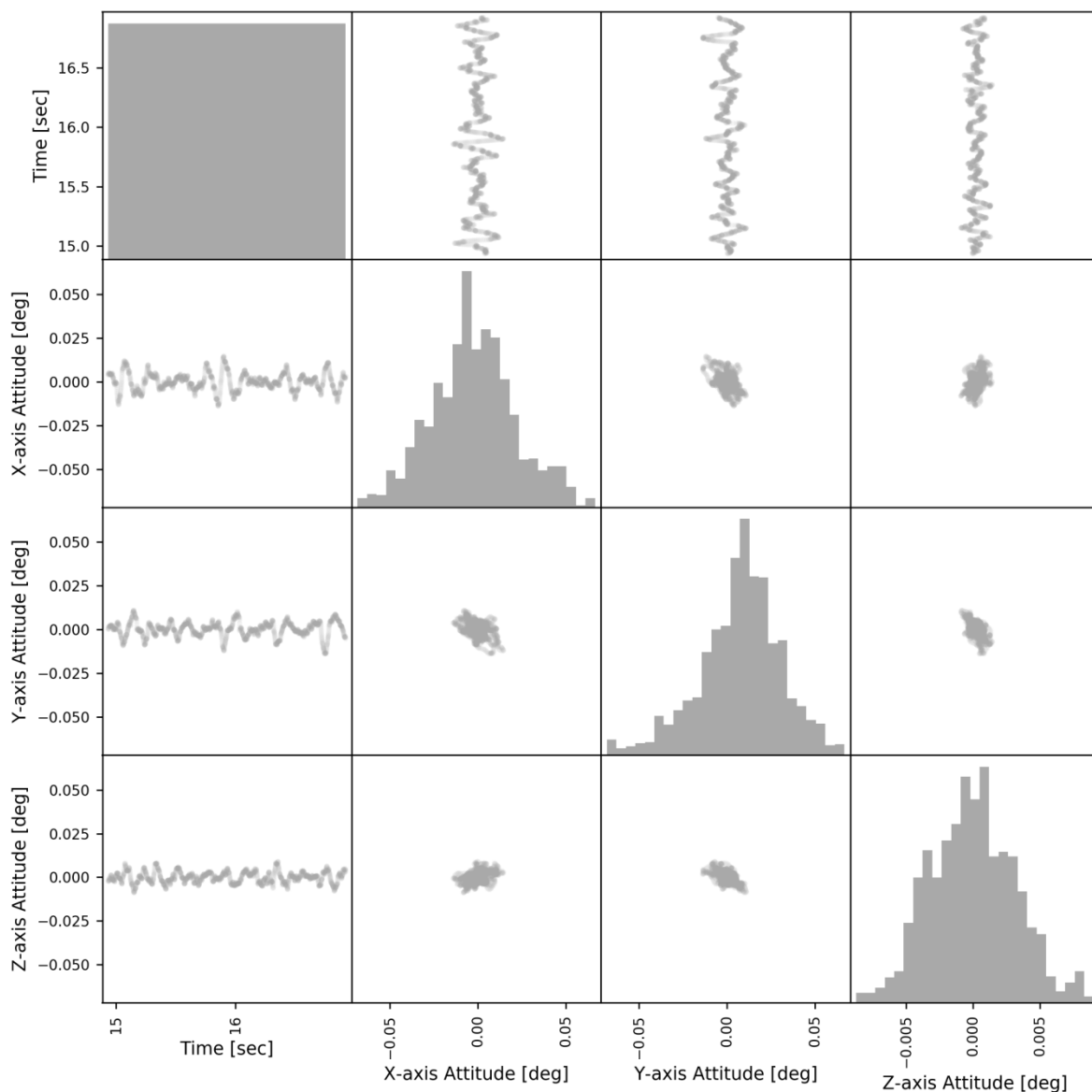


**Figure A-69: Time-domain rotation matrix: Kli-Pi 2 (400mm, field test, detailed)**

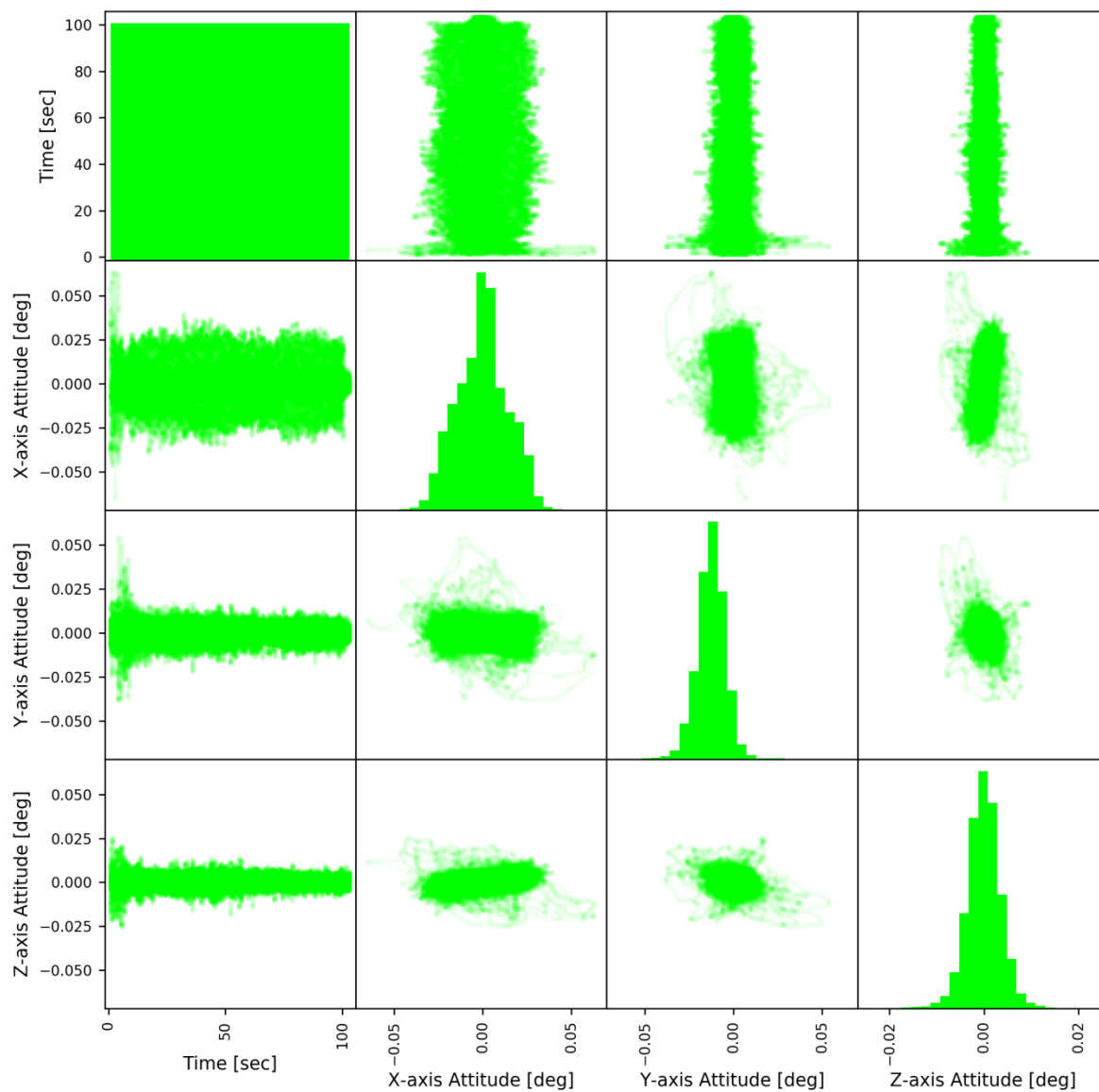


**Figure A-70: Time-domain rotation matrix: Kli-Pi 3 (250mm, field test)**

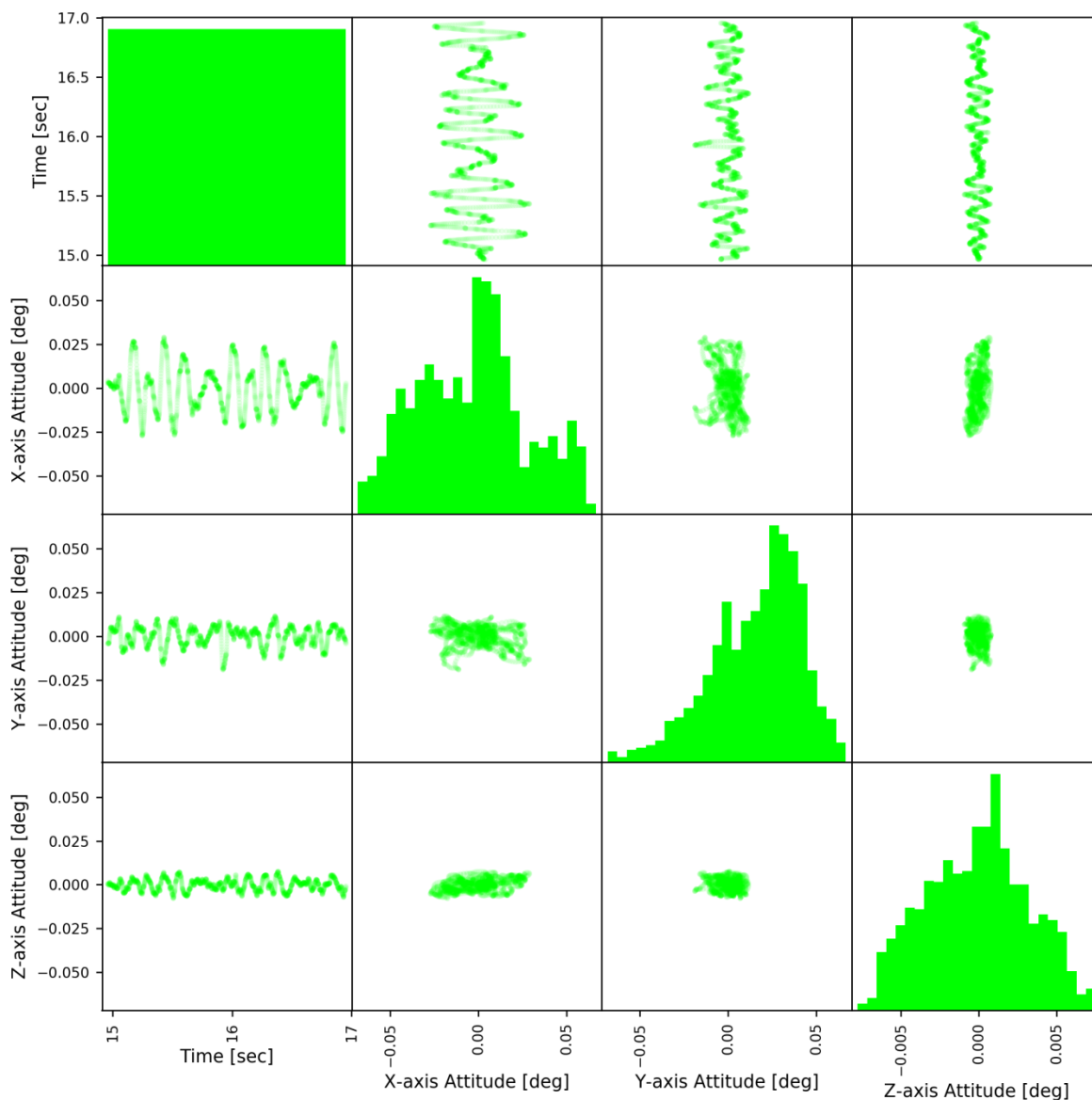
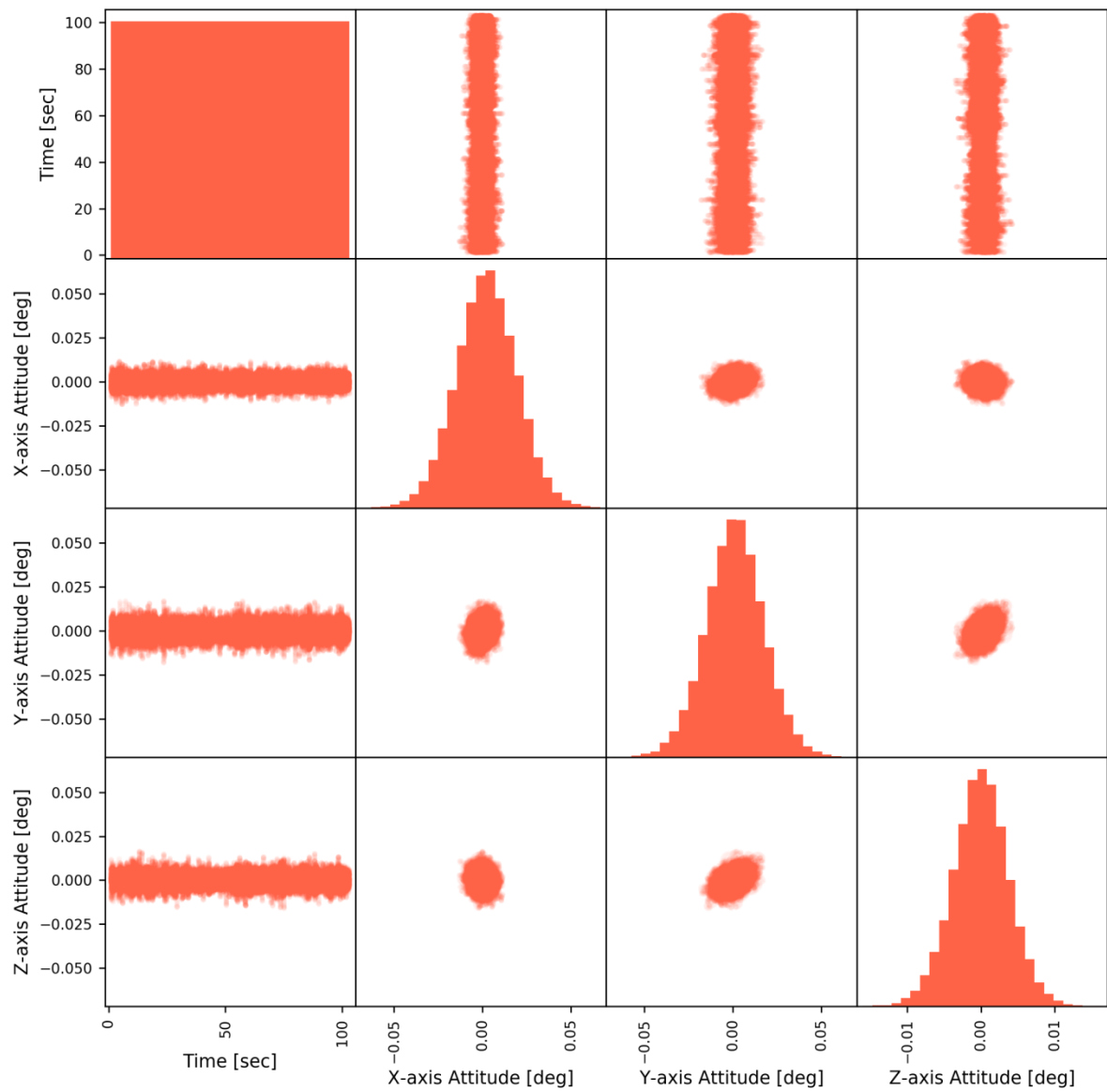
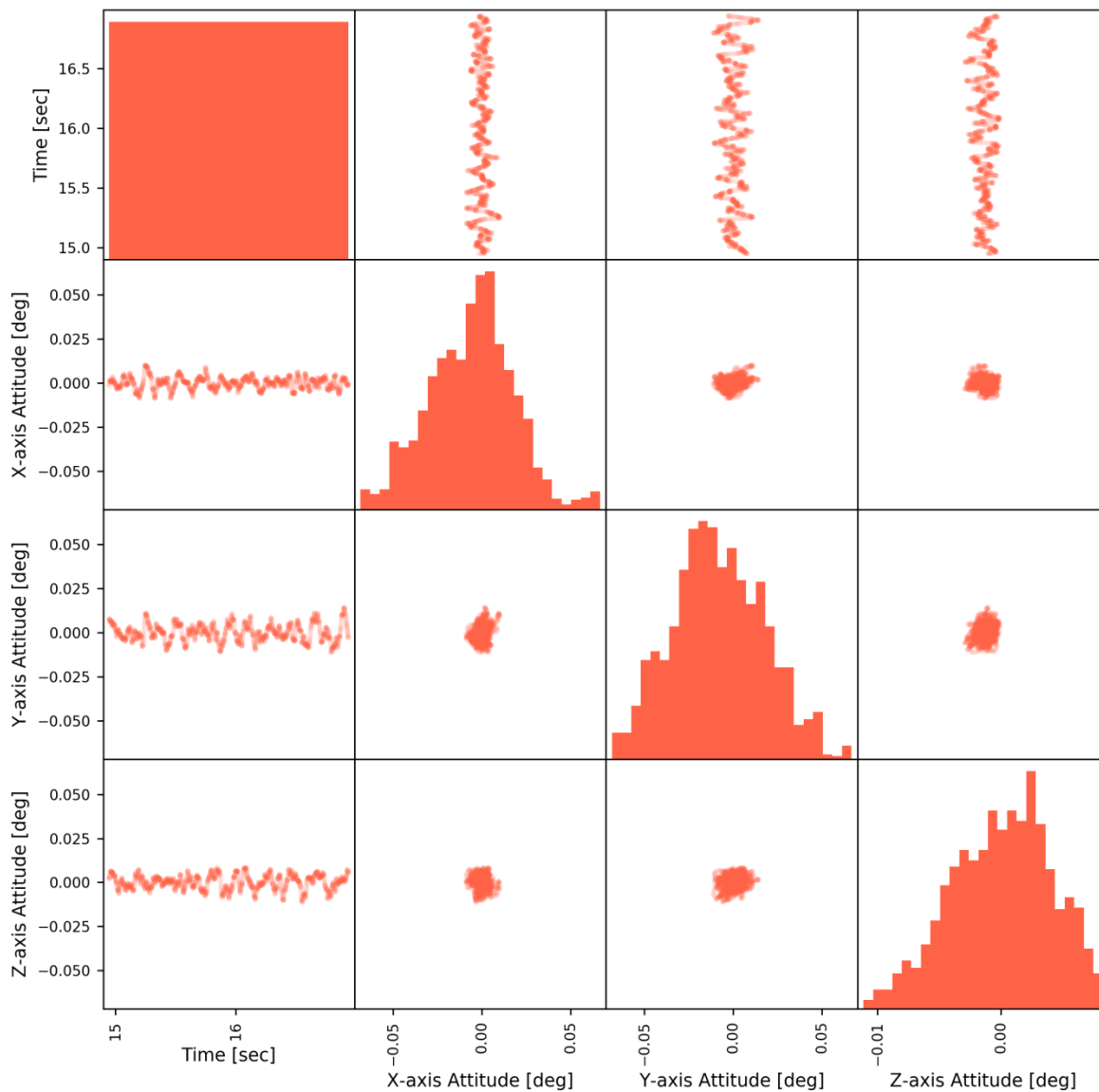


Figure A-71: Time-domain rotation matrix: Kli-Pi 3 (250mm, field test, detailed)



**Figure A-72: Time-domain rotation matrix: Kli-Pi 4 (0mm, field test)**



**Figure A-73: Time-domain rotation matrix: Kli-Pi 4 (0mm, field test, detailed)**

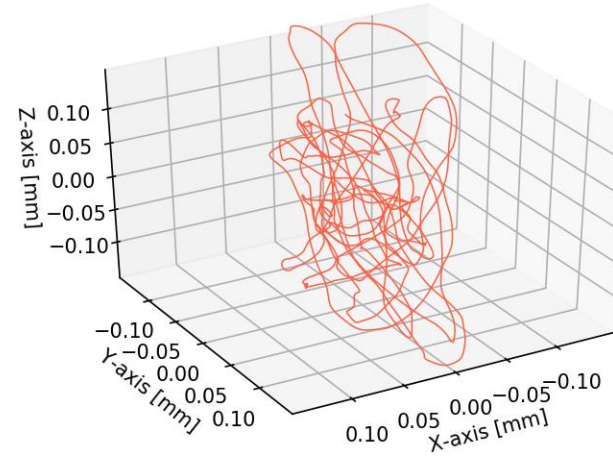
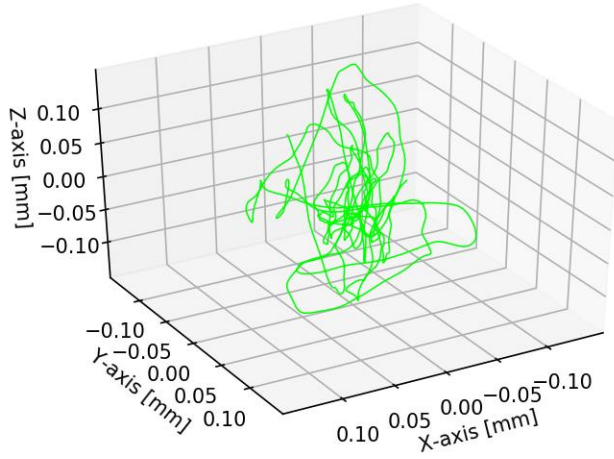
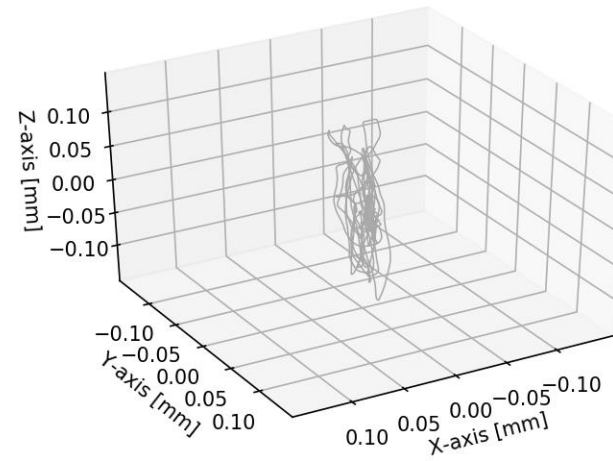
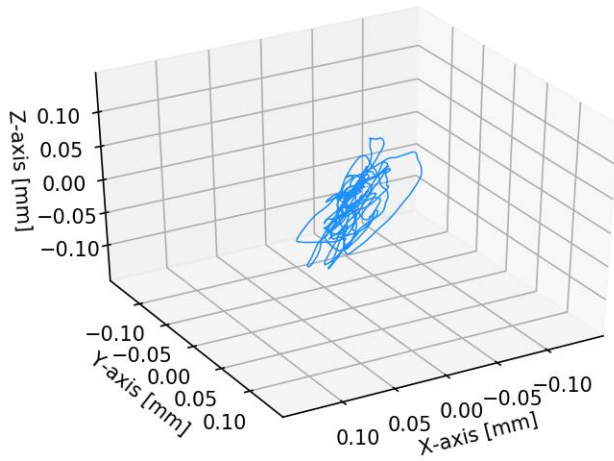


**Figure A-74: Time-domain displacement: all Kli-Pis (field test, 60 degrees)**

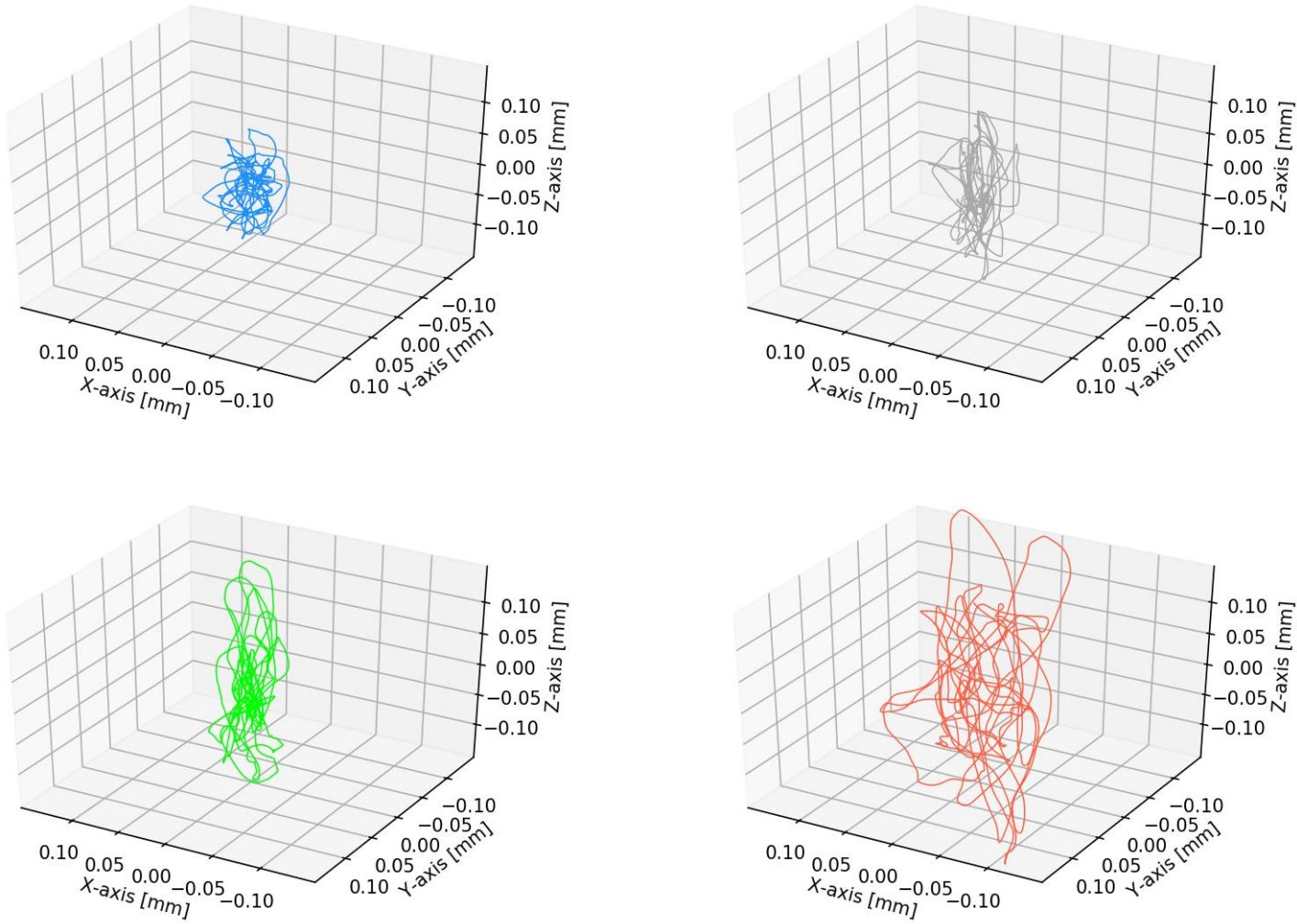


**Figure A-75: Time-domain displacement: all Kli-Pis (field test, 120 degrees)**

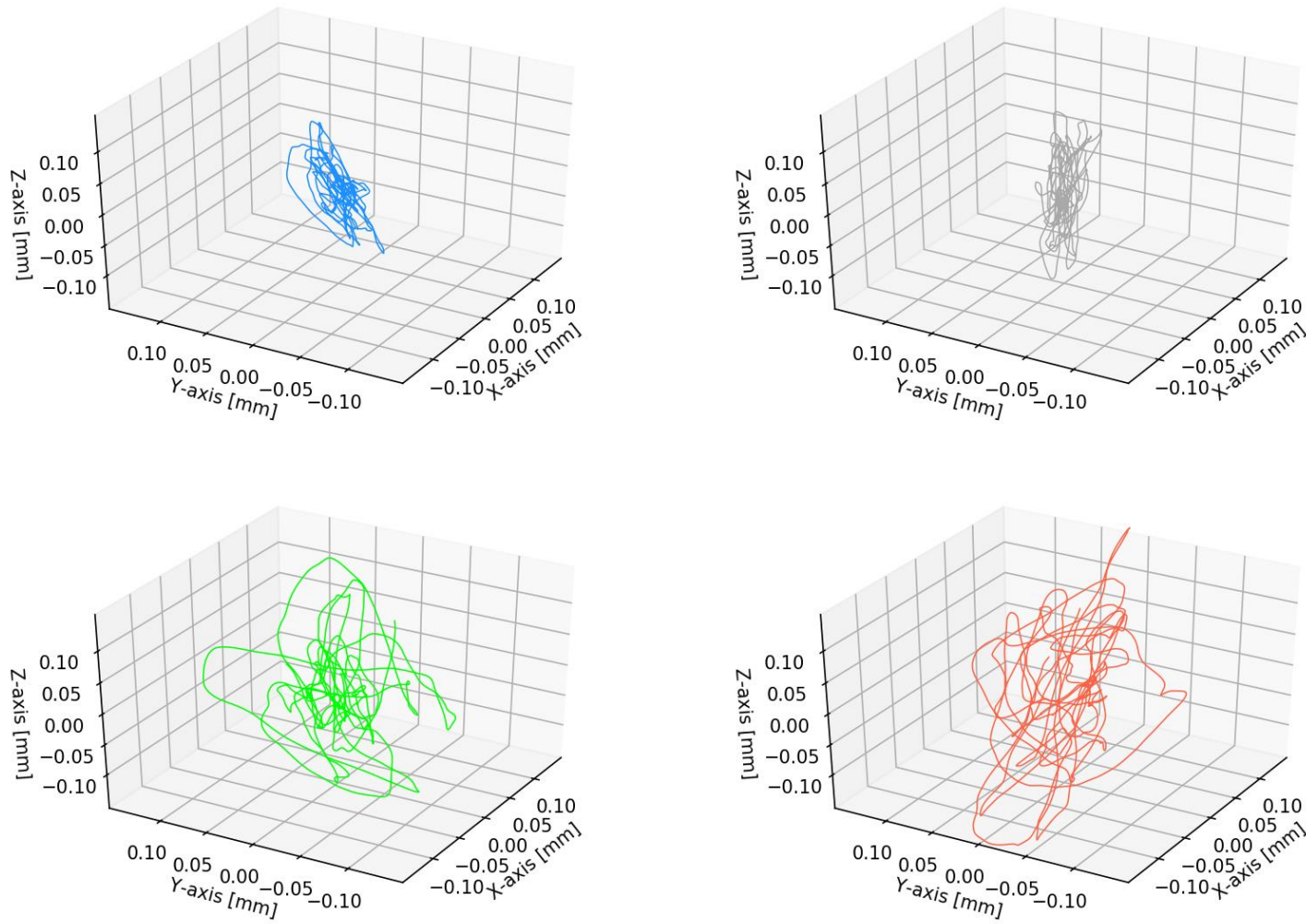


**Figure A-76: Time-domain displacement: all Kli-Pis (field test, 210 degrees)**

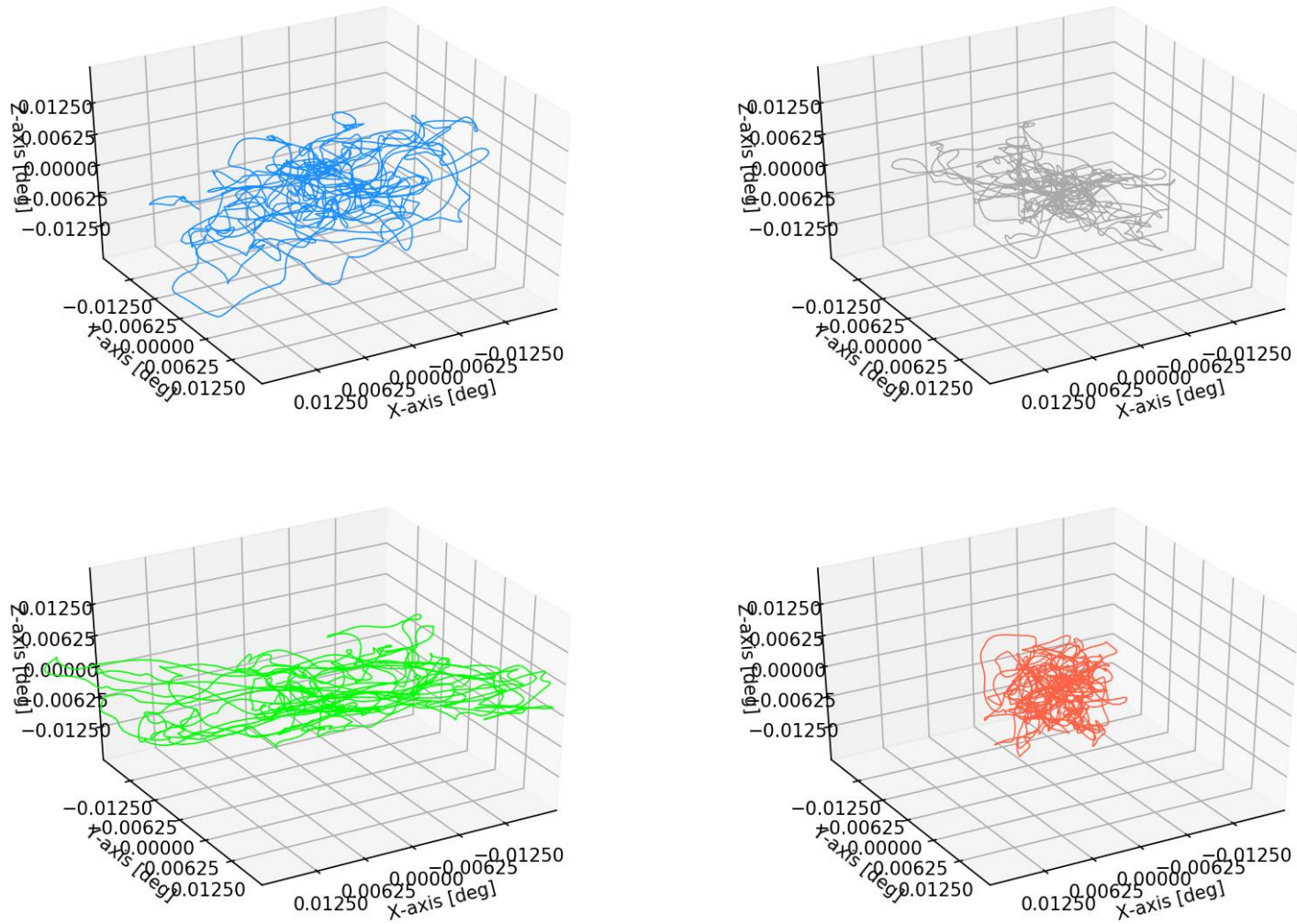


**Figure A-77: Time-domain rotation: all Kli-Pis (field test, 60 degrees)**

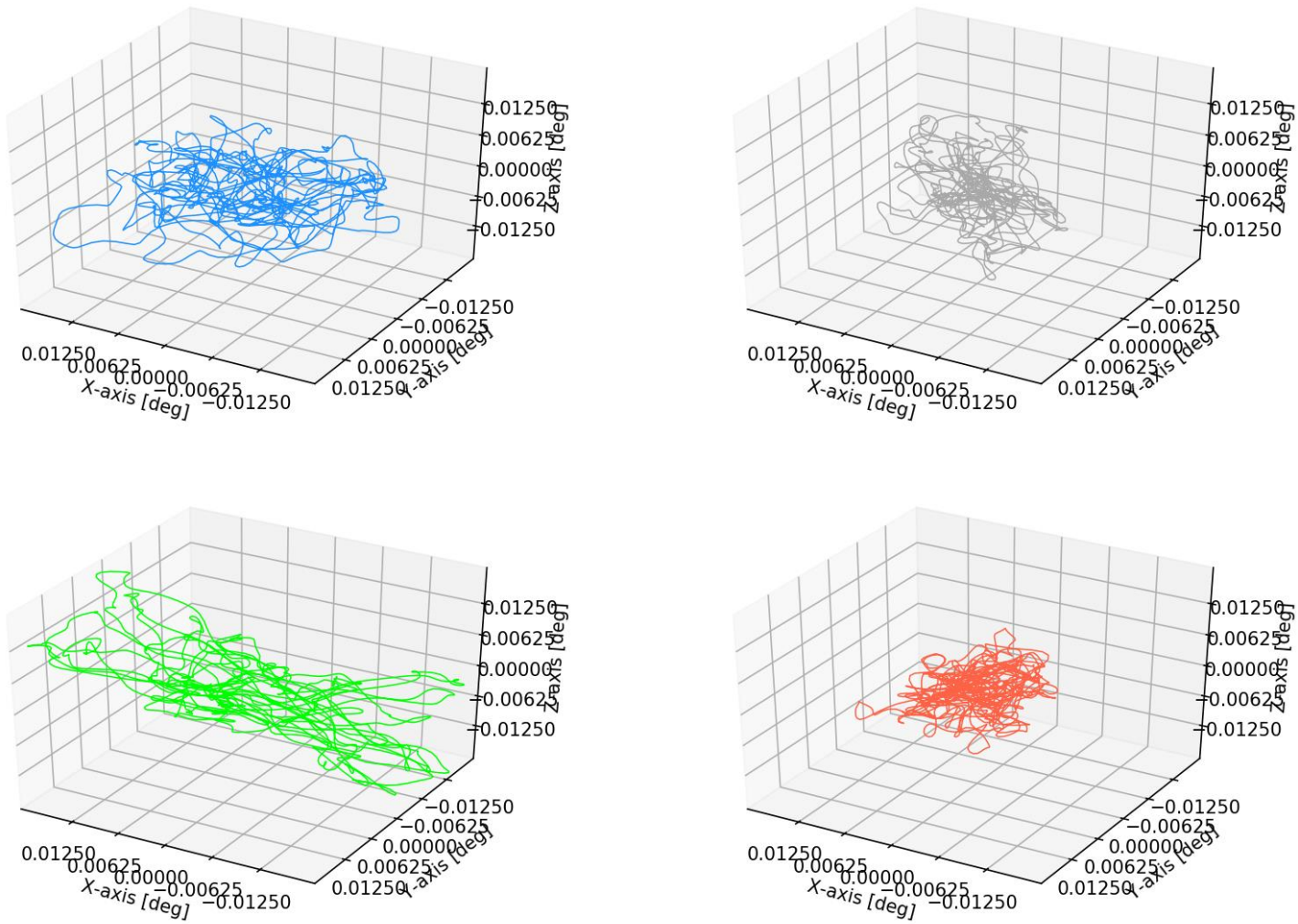


**Figure A-78: Time-domain rotation: all Kli-Pis (field test, 120 degrees)**

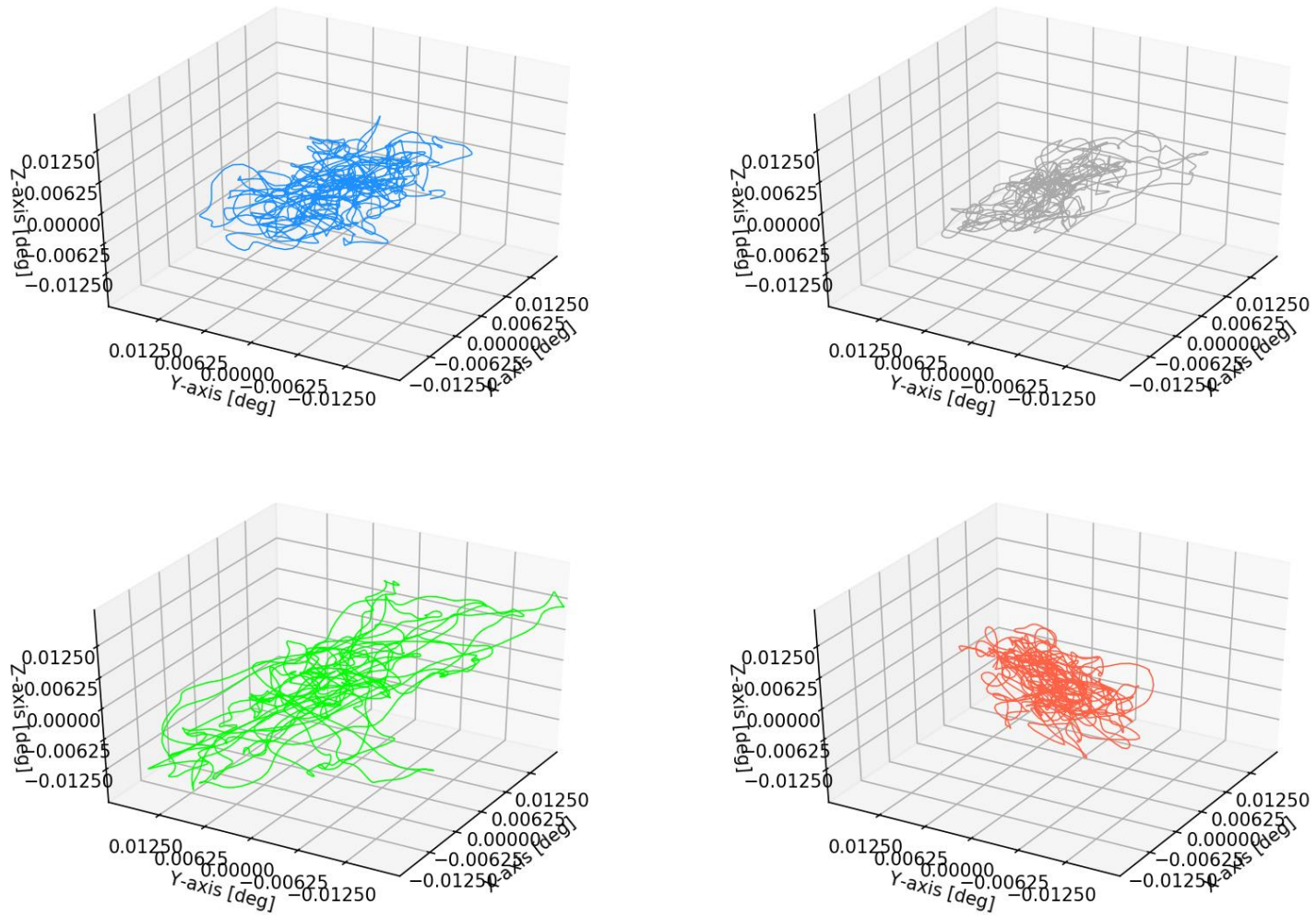


**Figure A-79: Time-domain rotation: all Kli-Pis (field test, 210 degrees)**

## A.5 Summary of Displacement Statistics

**Table A-1: Peak-to-Peak displacement comparison for the laboratory test (all Kli-Pis)**

Parameter	Kli-Pi 1 (500mm)			Kli-Pi 2 (350mm)			Kli-Pi 3 (0mm)		
	X	Y	Z	X	Y	Z	X	Y	Z
Mean [mm]	0.189	0.318	1.269	0.245	0.441	1.180	0.311	0.241	1.440
Minimum [mm]	0.061	0.079	1.014	0.170	0.285	0.956	0.249	0.150	1.247
Maximum [mm]	0.536	0.988	1.753	0.460	0.778	1.549	0.414	0.407	1.671
Std Dev [mm]	0.109	0.223	0.162	0.063	0.106	0.132	0.035	0.055	0.104
CoV	0.576	0.702	0.127	0.251	0.241	0.112	0.114	0.229	0.072
Skewness	1.386	1.404	1.038	1.410	1.298	0.785	0.661	0.914	0.189

**Table A-2: Peak-to-Peak displacement comparison for the field test (all Kli-Pis)**

Parameter	Kli-Pi 1 (550mm)			Kli-Pi 2 (400mm)			Kli-Pi 3 (250mm)			Kli-Pi 4 (0mm)		
	X	Y	Z	X	Y	Z	X	Y	Z	X	Y	Z
Mean [mm]	0.036	0.030	0.074	0.031	0.028	0.104	0.041	0.053	0.109	0.106	0.074	0.161
Minimum [mm]	0.008	0.006	0.009	0.007	0.004	0.007	0.007	0.004	0.009	0.013	0.008	0.005
Maximum [mm]	0.162	0.137	0.229	0.155	0.150	0.363	0.292	0.355	0.419	1.027	0.563	0.685
Std Dev [mm]	0.032	0.028	0.056	0.291	0.298	0.925	0.064	0.073	0.100	0.177	0.117	0.187
CoV	0.881	0.916	0.762	0.925	1.050	0.887	1.574	1.385	0.918	1.666	1.591	1.165
Skewness	4.390	4.028	1.119	4.238	3.230	1.124	9.049	4.972	1.440	6.042	6.656	4.498

## A.6 Summary of Rotation Statistics

**Table A-3: Peak-to-Peak rotation comparison for the laboratory test (all Kli-Pis)**

Parameter	Kli-Pi 1 (500mm)			Kli-Pi 2 (350mm)			Kli-Pi 3 (0mm)		
	X	Y	Z	X	Y	Z	X	Y	Z
Mean [arcmin]	2.618	4.625	2.100	4.599	2.351	4.329	5.560	4.655	0.681
Minimum [arcmin]	1.592	2.336	0.997	3.519	1.684	2.920	3.451	3.967	0.457
Maximum [arcmin]	4.817	8.355	4.140	6.311	3.293	5.805	7.342	5.473	1.020
Std Dev [arcmin]	0.765	1.776	0.884	0.780	0.412	0.884	1.084	0.383	0.796
CoV	0.292	0.384	0.421	0.170	0.175	0.204	0.195	0.082	1.169
Skewness	1.060	0.510	0.492	0.467	0.380	-0.269	-0.254	0.137	0.584

**Table A-4: Peak-to-Peak rotation comparison for the field test (all Kli-Pis)**

Parameter	Kli-Pi 1 (550mm)			Kli-Pi 2 (400mm)			Kli-Pi 3 (250mm)			Kli-Pi 4 (0mm)		
	X	Y	Z	X	Y	Z	X	Y	Z	X	Y	Z
Mean [arcmin]	0.879	0.768	0.620	0.625	0.506	0.460	1.330	0.724	0.508	0.548	0.733	0.647
Minimum [arcmin]	0.261	0.332	0.283	0.265	0.185	0.203	0.180	0.239	0.192	0.285	0.390	0.345
Maximum [arcmin]	2.277	1.652	1.358	1.635	1.262	1.100	3.732	2.651	1.583	1.097	1.425	1.344
Std Dev [arcmin]	0.542	0.322	0.260	0.314	0.264	0.204	1.145	0.481	0.293	0.184	0.241	0.218
CoV	0.617	0.419	0.419	0.503	0.522	0.444	0.861	0.664	0.577	0.336	0.329	0.337
Skewness	0.909	0.864	1.027	1.387	1.062	1.383	0.760	2.691	2.049	0.921	0.955	1.112

## A.7 Summary of Work Statistics

**Table A-5: Peak-to-Peak work comparison for the laboratory test (all Kli-Pis)**

<b>Parameter</b>	<b>Kli-Pi 1 (500mm)</b>	<b>Kli-Pi 2 (350mm)</b>	<b>Kli-Pi 3 (0mm)</b>
<b>Mean [mJ]</b>	5.207	4.782	5.885
<b>Minimum [mJ]</b>	4.222	3.966	4.717
<b>Maximum [mJ]</b>	7.478	6.645	7.055
<b>Std Dev [mJ]</b>	0.764	0.605	0.506
<b>CoV</b>	0.147	0.127	0.086
<b>Skewness</b>	0.115	0.971	1.108

**Table A-6: Peak-to-Peak work comparison for the field test (all Kli-Pis)**

<b>Parameter</b>	<b>Kli-Pi 1 (550mm)</b>	<b>Kli-Pi 2 (400mm)</b>	<b>Kli-Pi 3 (250mm)</b>	<b>Kli-Pi 4 (0mm)</b>
<b>Mean [mJ]</b>	0.287	0.415	0.424	0.639
<b>Minimum [mJ]</b>	0.037	0.028	0.034	0.032
<b>Maximum [mJ]</b>	0.885	1.445	1.641	2.699
<b>Std Dev [mJ]</b>	0.219	0.363	0.390	0.633
<b>CoV</b>	0.761	0.874	0.921	0.990
<b>Skewness</b>	1.756	1.442	1.122	1.113

## A.8 Network Configuration Details

### A.8.1 AP & IP Credentials

Raspberry Pi access point: 192.168.43.100 (pi:raspberry)

Wi-Fi (AP) SSID: Pi3-AP

Wi-Fi (AP) password: springmielie; provides the range of IPs: 192.168.42.1 etc.

Logging into any Edison module: ssh root@192.168.42.X (where X is the Kli-Pi number)

Tablet static (Ethernet) IP: 192.168.43.200 (pi:raspberry)

### A.8.2 AP Configuration

The following packages and dependencies were installed for the AP (Raspbian – Stretch) to configure the network:

- Python-pip –y
- pssh
- dnsmasq
- hostapd
- matchbox-keyboard

The following highlights the necessary configuration file contents:

#### /etc/network/interfaces

```
source-directory /etc/network/interfaces.d
```

#### /etc/dnsmasq.conf

```
interface=wlan0
```

```
listen-address=192.168.42.100
```

```
bind-interfaces
```

```
server=8.8.8.8
```

```
domain-needed
```

```
bogus-priv
```

```
dhcp-range=192.168.42.10,192.168.42.50,144h
```

```
# all the MAC addresses goes here; Klippie 1 through 4
dhcp-host=90:b6:86:10:6d:3e,192.168.42.1
dhcp-host=fc:db:b3:95:8a:f3,192.168.42.2
dhcp-host=fc:db:b3:98:5a:b3,192.168.42.3
dhcp-host=fc:db:b3:9a:7a:3d,192.168.42.4
```

**/etc/hostapd/hostapd.conf**

```
# This is the name of the Wi-Fi interface we configured above
interface=wlan0

# Use the n180211 driver with the brcmfmac driver
driver=n180211

# This is the name of the network
ssid=Pi3-AP

# Use the 2.4 GHz band
hw_mode=g

# Use channel 6
channel=6

# Enable 802.11n
ieee80211n=1

# Enable WMM
wmm_enabled=1

# Enable 40MHz channels with 20ns guard interval
ht_capab=[HT40][SHORT-GI-20][DSSS_CCK-40]

# Accept all the MAC addresses
macaddr_acl=0

# Use WPA authentication
auth_algs=1

# require clients to know the network name
ignore_broadcast_ssid=0

# Use WPA2
```

```
wpa=2

# Use a pre-shared key

wpa_key_mgmt=WPA-PSK

# The network passphrase

wpa_passphrase=springmielie

# Use AES, instead of TKIP

Rsn_pairwise=CCMP
```

### **/etc/dhcpd.conf**

Add the 'denyinterfaces wlan0' before any use of 'interface' in this file.

### **/etc/rc.local**

Add the following to the file BEFORE EXIT 0 is called:

```
sleep 30

sudo ip link set wlan0 down

sudo ip addr add 192.168.42.100/24 dev wlan0

sudo ip link set wlan0 up

sleep 30

sudo service hostapd start

sudo service dnsmasq start

# Now the exit line is called:

exit 0
```

### **/boot/config.txt**

```
lcd_rotate=2
```

### **/etc/dhcpd.conf**

*#Add the following in the file:*

```
interface eth0

static ip_address=192.168.43.200
```

### A.8.3 USB AP Peripheral

In the event that an external W-Fi AP is used (for a stronger antenna gain), replace all `wlan0` instances as outlined in Appendix A.8.3 with `wlan1`. In addition, comment out the `driver=n180211` line as this is only applicable for the default Wi-Fi hardware of the Raspberry Pi.

### A.8.4 Ubilinux AP & Non-AP Mode Selection

In certain cases it is preferable for the Kli-Pi to boot and function in AP. The AP mode by default is disabled and will instead search for the predefined network SSID.

To enable the service:

```
systemctl enable APMoDe.service
```

To disable the service (default operating mode):

```
systemctl disable APMoDe.service
```

In the event that contact cannot be established with the Kli-Pi in either of these modes, the user must remove the Edison board from the stack and establish direct communications using a serial connection (with the UART shield). This can be accomplished using Ubuntu with:

```
sudo screen /dev/ttyUSB0 115200
```

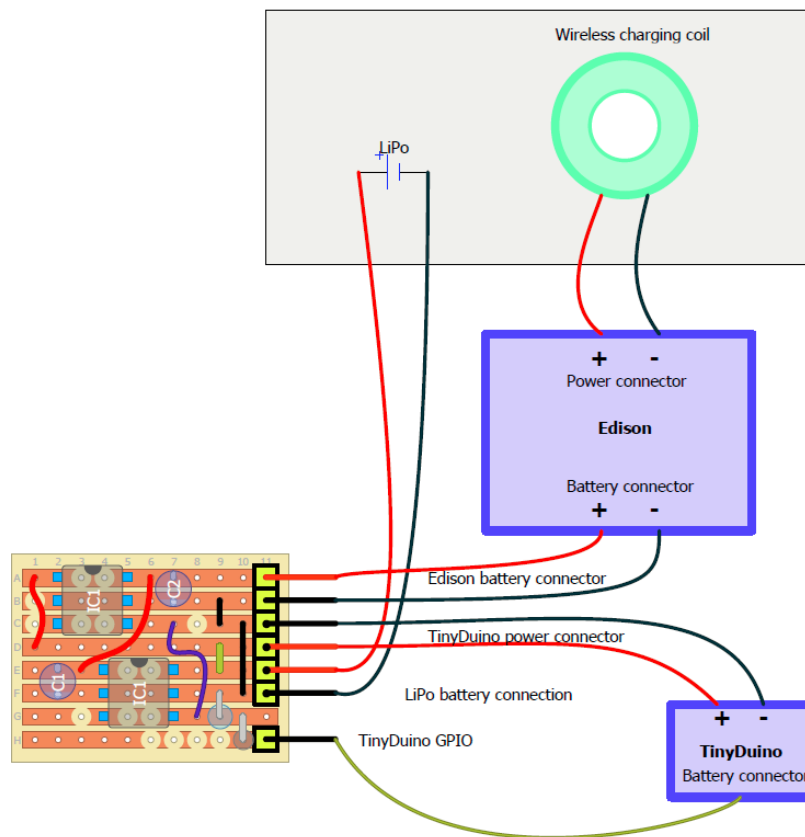
### A.8.5 Ubilinux system time

Due to the absence of a real-time clock (RTC) on the Raspberry Pi, the user is able to manually override the system time and date that is included in the output data files. This command must be sent using the `pssh` functionality to synchronize all the active Kli-Pi instruments. The date and time is specified in full as a string.

```
timedatectl set-time "2018-11-13 13:35:00"
```

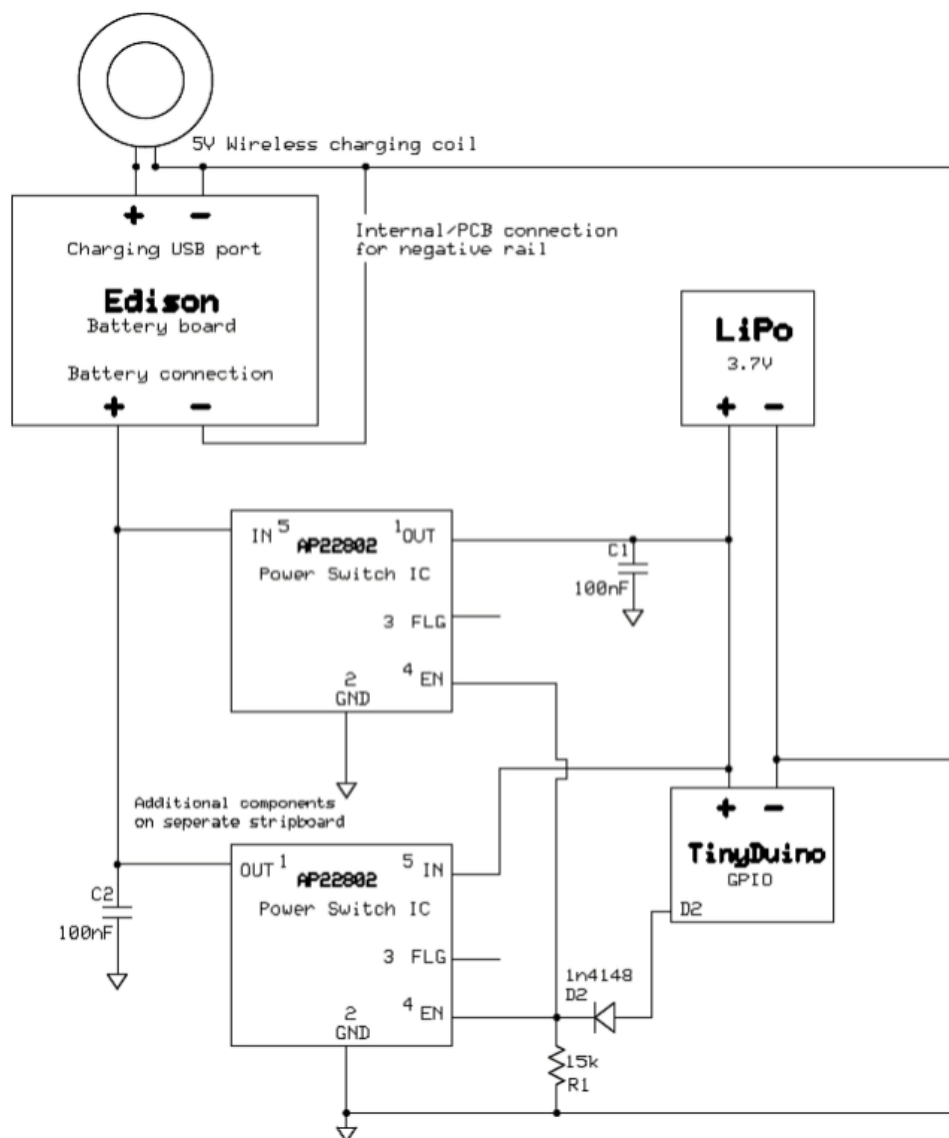
## A.9 Electrical Configuration

Figure A-80 illustrates the connections for each component to the interface board, including the polarity that should be strictly followed. Note that the orientation of the installed interface board is in a different orientation to that illustrated. Normally the only connectors that required configuration on a regular basis are that of the battery during prolonged periods of inactivity.



**Figure A-80: Electrical connectors for the interface board**

The electrical design of the interface board is illustrated (Figure A-81). A single channel, low-power, current-limited power switch IC (AP22802) controls the current flow to the Edison stack. The enable switch is controlled through the GPIO pin from the TinyDuino. The second AP22802 IC provides bi-directional current flow for recharging capabilities of the battery. Any 5V power supply (500 mA) provides sufficient charging capabilities. In the event of over-discharged batteries, either a jump-start is required using a USB cable via the TinyDuino or an external battery charger can be utilized.



**Figure A-81: Electrical design of the interface board**

This page is intentionally left blank.